

A quantum dot in a microcavity as a coherent spin-photon interface

Inauguraldissertation

ZUR

Erlangung der Würde eines Doktors der Philosophie
vorgelegt der
Philosophisch-Naturwissenschaftlichen Fakultät
der Universität Basel

VON

Nadia Olympia Antoniadis

2024

The original document is saved on the University of Basel document server
<http://edoc.unibas.ch>



This work is licensed under a Creative Commons
Attribution-NonCommercial-NoDerivatives 4.0 International License.

The complete text may be reviewed here:

<http://creativecommons.org/licenses/by-nc-nd/4.0/>

Genehmigt von der Philosophisch-Naturwissenschaftlichen Fakultät
auf Antrag von

Erstbetreuer: Prof. Dr. Richard J. Warburton

Zweitbetreuer: Prof. Dr. Philipp Treutlein

Externer Experte: Prof. Dr. Alexander Kubanek

Basel, den 17.10.2023

Prof. Dr. Marcel Mayor
Dekan

*To my family,
for their endless love, encouragement and belief in me.*

Abstract

Single photons can encode and transmit information at the speed of light and, hence, are the most promising candidates for flying qubits in quantum networks and measurement-based quantum computation. Although photons do not naturally interact with each another, spin-photon interfaces can mediate the necessary interaction or entanglement between them. An ideal platform combines high-rate photon emission with a coherent spin in an efficient interface.

Semiconductor quantum dots coupled to optical cavities are excellent single-photon sources. Due to the ability to charge a single electron or hole onto a quantum dot, they can further be used to engineer strong spin-photon interfaces. The key challenge is achieving high quantum dot-cavity coupling and a coherent spin while being able to coherently manipulate the spin state in the cavity.

In this thesis, we address these demands by employing a single InAs quantum dot in a tunable open microcavity – a system that has already reported a record-high single-photon source efficiency.

First, we implement a highly-efficient light-matter interface – a one-dimensional atom. We observe an extinction in photon transmission of 99.2% resulting in a photon bunching of close to 600. This showcases the nonlinearity of the system at level of single photons: a near-perfect transmission of the two-photon component and reflection of single photons. The open nature of the cavity allows for *in-situ* tuning of the quantum dots's coupling efficiency to the cavity, resulting in full control over the photon statistics from bunching to anti-bunching. Furthermore, we implement a chiral interface and measure directional transmission with an isolation of 10.7 dB, the highest non-reciprocal response recorded with a single quantum emitter. Lastly, we operate in the back-reflection regime and directly observe a photon-number dependent time-delay upon scattering of a laser pulse: single-, two-, and three-photon components incur a different time delay of 144.02 ps, 66.45 ps and 45.51 ps, respectively. This is a fingerprint of stimulated emission at the level of a few photons.

In the second part, we establish a spin-photon interface. We achieve fast single-shot readout of an electron spin within 3 ns with a fidelity of 95.2%. For the first time, this allows readout faster than the quantum dot relaxation and dephasing times. Further, we observe time-resolved quantum jumps in the spin state using many readout repetitions and predict that single-shot readout should be achievable with 89.9% fidelity in Voigt geometry. Finally, we implement coherent control of a hole spin in the microcavity. We observe hole-spin Rabi oscillations with frequencies up to 1 GHz. The spin mediates interaction with the host nuclear spins, narrowing the nuclear spin distribution – an effect which has not yet been exploited on the hole. The nuclear cooling results in an enhancement of the spin coherence time from 30 ns to 500 ns.

In summary, a quantum dot in a microcavity can combine the best of all worlds in the same system: coherent single photons, a coherent spin, an interface for high efficiency spin-photon interaction, and fast manipulation and readout of a spin state. The results pave the way for the implementation of two-qubit gates between photons, high rate spin-photon entanglement and ultimately the generation of photonic cluster states.

Contents

Dedication	iii
Abstract	iv
I An introduction to a quantum dot in a tunable microcavity	1
1 Introduction	2
2 Background	5
2.1 Self-assembled quantum dots	5
2.1.1 Structure and optical properties	5
2.1.2 Electron and hole spins	9
2.2 An emitter in a tunable open microcavity	11
2.2.1 Cavity quantum electrodynamics	11
2.2.2 An efficient single-photon source	14
2.2.3 The perfect coupling case: a one-dimensional atom	15
II A quantum dot in a microcavity as a one-dimensional atom	18
3 A tunable, coherent and efficient light-matter interface	19
3.1 Summary	19
3.2 Introduction	19
3.3 Experimental and theoretical description	20
3.4 Results	22
3.4.1 Strong extinction	22
3.4.2 Giant and tunable nonlinearity	23
3.4.3 Back-reflection mode	25
3.5 Discussion	26
4 A chiral one-dimensional atom	27
4.1 Summary	27
4.2 Introduction	28
4.3 The working principle of the single-photon diode	28
4.4 Experimental details and characterisation of the diode	30
4.4.1 Cavity characterisation	30
4.4.2 Insertion losses	31
4.4.3 Quantum dot characterisation	32
4.4.4 Wavelength dependence of β -factor and highest observable contrast	33
4.5 Results	34
4.5.1 Tuning the β -factor to the ideal limit	34
4.5.2 Non-reciprocal transmission of the single-photon diode	35
4.5.3 Nonlinearity of the single-photon diode	36
4.6 Discussion	38

5	Photon bound-state dynamics	39
5.1	Summary	39
5.2	Introduction	40
5.3	Concept: Scattering dynamics via correlation functions	40
5.4	Results	41
5.4.1	One- and two-photon scattering eigenstates	41
5.4.2	Experimental implementation	42
5.4.3	Pulse delay induced by the cavity	43
5.4.4	Direct observation of photon-number dependent scattering dynamics	44
5.4.5	Two-photon bound states as a function of pulse-width	49
5.5	Conclusions	51
III	Readout and manipulation of a single spin in a microcavity	52
6	Cavity-enhanced single-shot readout	53
6.1	Summary	53
6.2	Introduction	54
6.3	Fast single-shot readout	55
6.3.1	High efficiency photon collection	55
6.3.2	Single-shot spin readout	56
6.3.3	Cavity suppression in a 2T out-of-plane magnetic field	58
6.3.4	Readout fidelity estimation	59
6.3.5	Predictions for optimised system and Voigt geometry	61
6.3.6	Repeated readout and quantum jumps	62
6.3.7	Continuous wave quantum jumps measurements	63
6.4	System analysis via autocorrelation functions	64
6.4.1	Extraction of spin lifetime from $\mathbf{g}^{(2)}(\tau)$	64
6.4.2	Spin initialisation by optical pumping	66
6.5	Discussion	68
7	Fast optical manipulation of a coherent hole spin	70
7.1	Summary	70
7.2	Introduction	70
7.3	Experimental Setup	72
7.4	Spin control in a microcavity	73
7.4.1	Coherent control of a hole spin	73
7.4.2	Hole lifetime and spin characteristics	75
7.4.3	Spin initialisation fidelity	77
7.4.4	Laser-induced spin-flips	78
7.5	Nuclear spin cooling via a hole spin	79
7.6	Discussion	81
IV	Conclusions and outlook	82
8	Conclusions	83

9 Outlook	85
Appendices	87
A Quantum dot-cavity-system and experimental setup	87
A.1 Description and fabrication of the coupled system	87
A.1.1 Heterostructure and growth	87
A.1.2 Curved mirror fabrication	90
A.1.3 Microcavity characterisation	90
A.1.4 Numerical simulations of the microcavity	92
A.2 Experimental setup	94
A.2.1 Optical setups	94
A.2.2 Lasers and pulse generation	97
A.2.3 Use and calibration of detectors	97
B Theory: A chiral one-dimensional atom	99
B.1 Transmission of a two-level emitter in a one-sided cavity	99
B.2 Second-order correlation function	103
C Off-resonant drive through the top mirror of the open microcavity	105
Bibliography	108
Acknowledgement	118
List of publications	121
Curriculum vitae	123

Part **I**

An introduction to a quantum dot in
a tunable microcavity

1

Introduction

Just over a century ago, physicists believed nature to be almost fully understood. Then however, with the development of quantum mechanics, the world they knew was turned upside down.¹ Nature is not classical, it is non-local and much more complex than long assumed.^{2,3} This *first quantum revolution* opened up a full new range of research expanding into various fields from electronics and atomic physics up to the detection of gravitational waves. The understanding of quantum mechanics on a fundamental level has kept physicists excited until today. In the present, the idea of applying the concepts of quantum mechanics to technological applications has emerged. This led to the *second quantum revolution* which already today enables first applications as true random number generators⁴ and sensors with radically enhanced sensitivity, e.g. in magnetometry^{5,6} and interferometry.^{7,8} It further promises a range of advancements in the near future. Secure communication can be assured using the concepts of entanglement and teleportation distribution over long distances resulting in a large scale quantum network.⁹⁻¹² Ultimately, a powerful quantum computer built on the concepts of quantum mechanics is predicted to massively speed up future computations of specific problems.¹³

A quantum computer is built of operating units called *quantum bits* (qubits). Contrary to a classical bit, a qubit can not only be in state 0 or 1, but in a superposition state $|\Psi\rangle = \alpha|0\rangle + \beta|1\rangle$ (where $|\alpha|^2, |\beta|^2$ are the probabilities to measure the corresponding state), and can be entangled with other qubits. Generally, two types of qubits can be distinguished: *flying qubits* and *stationary qubits*. For a quantum network or computer, both are crucial. For example, in gate-based quantum computing the operating qubits are stationary qubits which store information and are manipulated via applied electrical gates, while flying qubits are used to transport information between different qubits. Contrary, in a photonic processor the operating qubits are the flying qubits. In that case, in order to achieve universal quantum computation, the qubits need to be manipulated or interfered. This can be done by the implementation of high fidelity one- and two-qubit gates, typically via stationary qubits.

An alternative approach to quantum computing is measurement-based quantum computation.^{14,15} It requires a grid of qubits where each qubit is entangled with all direct neighbours and computation is performed by measurements on specific qubits in a certain order. The two approaches to quantum computing can be mapped onto each other and can in principle perform the exact same computations. However, measurement-based computation only

requires one-qubit operations. The complexity of the computation is therefore shifted to the generation of entangled cluster-states.^{16,17}

One of the key demands in the development of quantum computers in either of these approaches is to find a suitable physical system to host the qubits. There are many platforms explored to implement a quantum computer – superconducting circuits,¹⁸ semiconductor quantum dots (QDs),^{19,20} atomic systems,^{21,22} photons²³ and many more – without a clear leading candidate. Every physical system comes with its strengths and weaknesses, and it is most likely that there will be no clear victor to solve all tasks, but rather different qubits that suit the specific demand at hand. Either way, optical single photons are a very promising candidate for a flying qubit for both approaches to quantum computing.^{17,24–26} They can encode and transmit information at the speed of light with low noise and high coherence, even at room temperature. Optical fibres can be used for long distance transmission of information similar to classical communication – an established network already exists and builds the backbone of the internet. Furthermore, the technology for single qubit operations on photons is easy: mirrors and wave-plates are available and well established. But, as photons do not naturally interact with each other, stationary matter qubits can enable light-matter interaction for gate operations or entanglement generation between successive photons.²⁷

In photonic quantum applications, a stationary qubit needs to fulfil two main requirements: it should generate photons at high rates and be highly coherent to mediate interaction between photons. Optical emitters are ideal for the first demand. Their structure typically exhibits an excited and a ground state where the excited state relaxation results in the generation of a single photon. While a fast radiative decay favours a single-photon source, it makes optical emitters poor candidates for qubit operations requiring long lived qubit states. Optical emitters containing a single spin offer the best of both worlds. They exhibit both an optical transition for fast photon generation and a stable ground state spin qubit for manipulations.²⁸

Several platforms have been examined as spin-photon interfaces and the different possible emitters bring various benefits and challenges. For example, due to their good spin properties, NV centres in diamond have been the leading platform in the field of quantum networks.^{3,11,29} Yet, they have poor optical properties leading to low photon count rates. Other defects in diamond are also emerging,^{30,31} promising to overcome some of the issues associated with NV centres. Similarly, rare-earth ions have been established with promising spin properties but exhibiting poor optical properties.³² On the other hand, atoms^{21,33–36} or ions^{22,37} exhibit low noise due to an isolated environment, have long emitter lifetimes but can only be trapped with a lot of effort.

Contrary to most emitters, self-assembled semiconductor QD have excellent optical properties and are the leading platform for the generation of single-photons.^{19,23} Furthermore, a QD can be loaded with a single electron or hole, providing a spin degree of freedom.^{38,39} However, due to the hyperfine interaction of an electron or hole spin with the semiconductor environment, QDs typically exhibit poor spin coherence. While for an electron spin, recent schemes have demonstrated cooling of the nuclear spin environment resulting in enhanced electron spin coherence times,^{40–44} nuclear cooling has not yet been exploited on a hole.

Besides the demand of enhanced spin coherence, it is important to engineer the photonic environment of QDs in order to enhance the light-matter interaction and specifically route photons. This can be achieved by embedding them into photonic crystal waveguides,⁴⁵

micropillars^{46,47} or microcavities.^{19,48,49} Ideally, light-matter coupling is strong enough that every single photon interacts with the emitter. In other words, the quantum node can be optimised to be a close-to-lossless one-dimensional (1D) atom.^{50,51} Furthermore, a light-matter interface can be designed to be chiral.⁵² This means that emission is directional into specific optical modes, which is necessary for large-scale quantum networks.

The challenge in realising a coherent spin-photon interface with QDs in cavities is two-fold: achieving high QD-cavity couplings in combination with high fidelity rotations of the QD spin and by that nuclear spin cooling in the cavity.

In this thesis we address these challenges by employing a single InAs QD in an open and tunable microcavity.

This thesis is structured as follows:

Part I gives an introduction and the relevant background to the topics of this thesis. Ch. 2 introduces semiconductor QDs and optical cavities, and discusses two specific applications of a QD coupled to a microcavity. In particular, a main prior result of the system – an efficient single-photon source – is described.

Part II presents an implementation of a highly-coherent light-matter interface – a 1D atom. Ch. 3 discusses how a QD coupled to a microcavity can be turned into a 1D atom. A large coupling efficiency is observed resulting in a high extinction in photon transmission and strong bunching in the photon statistics. The chapter establishes the platform as a coherent interface for single photon - single emitter interaction with tunable photon statistics and gives a brief outlook into the physics of a one-sided cavity. Ch. 4 presents an implementation of a chiral 1D atom at a specific condition of the coupling efficiency $\beta = 0.5$. It demonstrates strong nonreciprocal absorption – a diode for single photons. The results in Ch. 5 mimic a chiral system in the limit of a large coupling efficiency ($\beta \simeq 1$). The dynamics of photonic bound states are investigated and their existence is directly observed.

Part III focuses on the implementation of the QD coupled to the cavity as a spin-photon interface. Ch. 6 discusses single-shot readout of an electron spin in the cavity. Single-shot readout faster than the QD relaxation and dephasing times is achieved with high fidelity allowing for the direct observation of quantum jumps in the spin state. Ch. 7 presents coherent and fast manipulation of a hole spin in a cavity. The coherent interaction allows for cooling of the host nuclear spins resulting in an enhanced coherence time of the hole spin.

Lastly, part IV concludes on the results presented in Ch. 3-7 (Ch. 8) and discusses future prospects (Ch. 9) towards the realisation of universal quantum computing.

2

Background

This introductory chapter provides the relevant background to semiconductor quantum dots (QDs) and cavity quantum electrodynamics (QED). It gives an overview of the most important parameters and some of the main applications of a single QD coupled to an optical cavity. The open microcavity system that is key to all the results presented in this thesis is also introduced and described.

2.1 Self-assembled quantum dots

Coherent optical emitters are a crucial requirement for the realisation of optical networks and single-photon sources.^{19,23} There exists an entire zoo of optical emitters, including atoms,^{33,36} ions,^{32,37} defects in diamond,^{3,53} molecules⁵⁴ and optically active QDs.⁵⁵ The implementation of these emitters as a qubit bring different advantages and challenges with them. Semiconductor QDs provide excellent optical properties and are the most promising candidate for applications involving high photon generation rates.⁵⁶ The ability to load a QD with a single electron or hole spin enables their operation as a spin qubit.³⁹ As a QD is naturally embedded in a solid-state environment, the spin will interact with its environment, potentially leading to low spin coherence times. In order to overcome this decoherence process and realise QDs as qubits, their structure and interactions with the environment have to be understood.

2.1.1 Structure and optical properties

Self-assembled InAs/GaAs QDs are nano-sized semiconductor heterostructures grown by molecular beam epitaxy (MBE) or metal-organic vapor phase epitaxy (MOVPE). In MBE, layers of material can be grown with a precision down to monolayer thicknesses. Using a specific method called Stranski-Krastanov growth,⁵⁷ a few layers of InAs are grown on top of a GaAs substrate. Due to a lattice mismatch of $\sim 7\%$ between the two materials, strain relaxation causes InAs islands consisting of $\sim 10^5$ atoms to form on top of the initial InAs layer (wetting layer). Additional layers of GaAs cap the QDs in order to protect them from surface charges. This island formation is a stochastic process, so that the position, size, and hence the emission wavelength, varies from QD to QD. Typically, a QD has a width of ~ 20 nm and height of ~ 8 nm as can be seen on a transmission electron microscopy (TEM) image in Fig. 2.1a.

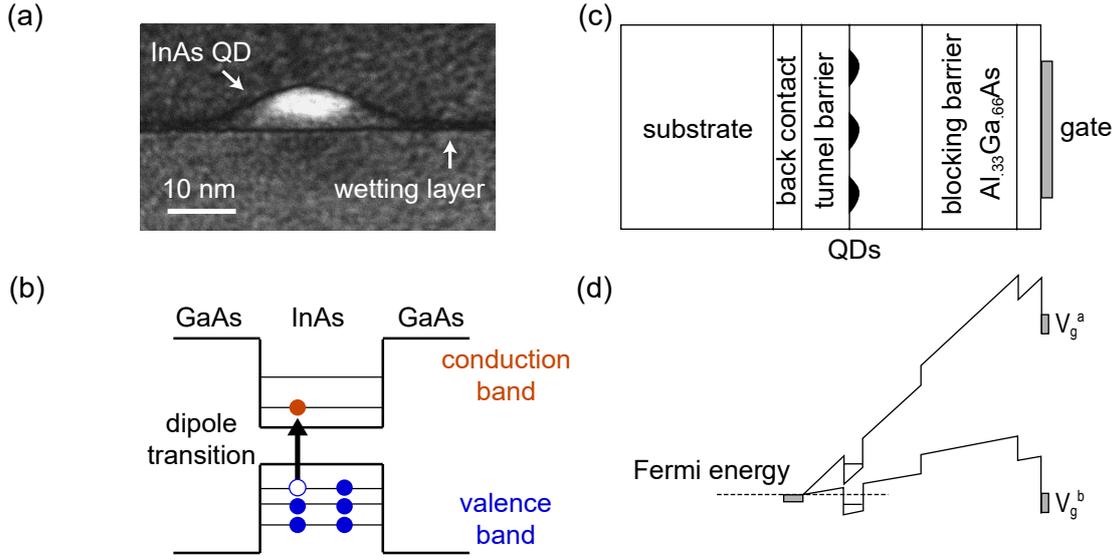


Figure 2.1: Self-assembled InAs QDs (a) Dark-field TEM image of an InAs QD embedded in a GaAs matrix. The QD has an approximate width of 20 nm and height of 8 nm. Image courtesy of Jean-Michel Chauveau and Arne Ludwig. (b) Schematic of the QD energy structure. The lower bandgap of InAs compared to GaAs acts as a confining potential for electrons and holes. An exciton is formed via a strong optical dipole transition. (c) Example of a gated semiconductor heterostructure with the capability to tune the QD energy level with respect to the Fermi sea of the back-gate. (d) Conduction band edge for two different applied voltages ($V_g^{a/b}$). (c) and (d) are reproduced and modified from Ref. ³⁸

The three-dimensional confinement on a nano-scale has immense consequences for the QD electronic and optical properties. In bulk, the band-structure of a semiconductor material can be derived from a tight-binding model.^{58,59} The conduction band is constructed from s-wave Bloch-states ($S, S_z = 1/2, \pm 1/2$). On the other hand, the valence band is six fold degenerate ($J, J_z = 1/2, \pm 1/2; J_z = 3/2, \pm 3/2, \pm 1/2$) with a p-wave character arising from the atoms of the host material. The spin-orbit interaction splits off the $J_z = 1/2$ Bloch-states by an energy Δ_{SO} . The different effective masses and therefore different confinement of the heavy-hole (HH) ($J, J_z = 3/2, \pm 3/2$) and light hole (LH) ($J, J_z = 3/2, \pm 1/2$) states as well as strain in the semiconductor further lift their degeneracy.⁶⁰ The HH has the lowest energy of the three components and hence builds the highest valence band. These energy level splittings are maintained even with strong confinement of the semiconductor as in the case of a QD. The nano-sized island of InAs between the GaAs substrate leads to a potential energy barrier, a trapping potential for electrons in the conduction and holes in the valence band, respectively, with discrete energy levels³⁸ (Fig. 2.1b). Due to their atom-like quantised energy levels, QDs are often referred to as *artificial atoms*, while in contrast to atoms, QDs are naturally trapped in space⁶¹ by the semiconductor crystal. Moreover, the band-structure of InAs has a direct bandgap, leading to a strong optical transitions. InAs QDs have been shown to have very high oscillator strengths,³⁹ and hence, fast radiative decay rates in comparison to other emitters. That is one reason QDs are promising candidates for applications like high-rate single-photon sources.

If a light pulse excites a single electron from the valence to the conduction band, it leaves behind a hole creating a bound electron-hole pair called an exciton.⁶² Upon recombination of an exciton, one single photon at a wavelength matching the recombination energy is emitted.

There are different types of excitons (shown in Fig. 2.2). When the QD is empty before excitation, a neutral exciton, consisting of one electron and one hole, is created. However, QDs can be charged with one single electron (hole) ahead of excitation. In this case, a negatively (positively) charged trion is created, containing two electrons (holes) and one hole (electron).⁵⁵

A gated structure (shown in Fig. 2.1c) allows tuning of the QD energy levels with respect to the Fermi sea. This enables deterministic tunneling of individual charge carriers into the QD via the Coulomb blockade effect.^{38,63} While tunneling is suppressed in this regime, a higher order term, co-tunnelling, survives.⁶⁴ Additionally, gating of the QDs allows for tuning of the transition energies via the DC Stark effect. Furthermore, it has been shown that gates reduce charge noise in QDs, resulting in optical linewidths close to the transform-limit ($\gamma_R = 1/\tau_R$, with τ_R being the radiative lifetime and $\gamma_R/(2\pi)$ the optical linewidth).⁶⁵

Coherence of the exciton

Due to the solid-state environment of a QD, the exciton coherence is limited. The three main sources of noise in the semiconductor are nuclear spins, fluctuating charges⁶⁶ or lattice vibrations (phonons).⁶⁷ While charge noise can be suppressed via a diode structure as discussed above, phonon effects are more difficult to circumvent. Phonon-exciton interactions do however have an important impact on single-photon indistinguishability and the performance of the QD as ideal two-level systems (TLSs). As an effect of the phonons coupling to the optical transitions, the QD transition energy fluctuates resulting in a reduction of the exciton coherence. It has been shown, that phonon effects can be mitigated (but not eliminated) by coupling QDs to a intermediate to high Q cavity (optical cavities are introduced in Sec. 2.2) by reducing the radiative lifetime on resonance with the TLS.^{67,68} Although these phonon process can be mitigated to a large degree, they are still the major contributor to the homogeneous linewidth broadening of QDs and by that to the indistinguishability of single photons.

Optical selection rules

In order to address the different excitons in an optical experiment, it is important to understand the individual selection rules.⁵⁵ The neutral exciton, X^0 , consists of one electron and one hole. Thus, there are four possible spin configurations: $|\uparrow, \downarrow\rangle, |\downarrow, \uparrow\rangle, |\uparrow, \uparrow\rangle, |\downarrow, \downarrow\rangle$. In an optical transition, the angular momentum must be conserved, which is reflected in the photon polarisation ($\Delta J = \pm 1 \equiv$ circular polarisation σ^+, σ^- ; $\Delta J = 0 \equiv$ linear polarisation x, y). The change in total angular momentum for these four spin combinations is $\Delta J = \pm 1$ or $\Delta J = \pm 2$. Consequently, the latter two combinations do not conserve angular momentum, and are thus optically forbidden, turning them into dark excitons, while the first two combinations ($|\uparrow, \downarrow\rangle, |\downarrow, \uparrow\rangle$) are optically allowed and circularly polarised. However, in reality uniaxial strain anisotropy in the semiconductor and the strong vertical confinement lead to an exchange interaction. This results in effective pseudo-spin excitons that are slightly fine-structure split in energy. These excitons are superpositions of the spins in the quantisation axis (z-direction) with the bright states being $|X^{a/b}\rangle = (1/\sqrt{2})(|\uparrow, \downarrow\rangle \pm |\downarrow, \uparrow\rangle)$. Consequently, these exciton transitions have linear polarisations with perpendicular axes as seen in Fig. 2.2a.^{69,70} For charged excitons however, the exchange interaction vanishes due to Kramer's theorem, which claims that a system with an odd number of fermions in the absence of magnetic fields is at least two-fold degenerate.⁷¹ Both the negative (Fig. 2.2b)

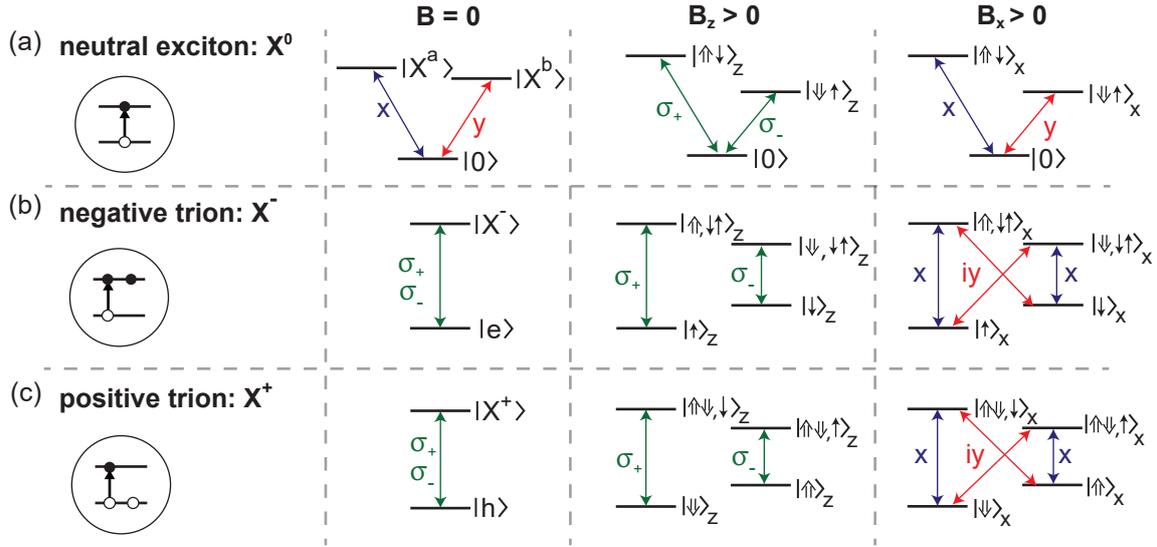


Figure 2.2: Transition rules of different exciton types at $B = 0$ (left) and ($B > 0$) (middle: Faraday; right: Voigt). (a) The neutral exciton (X^0) is a V-level system with one ground state (empty QD) and two excited states (excitons), with linearly polarised transitions x, y . In a Faraday field, the transitions become circularly polarised while in a Voigt field they remain linearly polarised. (b) The negatively charged trion (X^-) is degenerate at 0 T with the ground state being a single electron and the excited state being the charged trion. These transitions are circularly polarised. In a magnetic field, the transitions split into a four-level system. In Faraday geometry, the diagonal transitions are forbidden and the vertical transitions circularly polarised. In Voigt geometry, all four transitions are equally allowed and linearly polarised. The diagonal transitions are perpedicularly polarised and shifted by a π phase with respect to the vertical transitions. (c) The positively charged trion (X^+) is degenerate at 0 T with a single hole in the ground state and a charged trion as excited state. The selection rules are identical to the negative trion.

and positive (Fig. 2.2c) trion have two-fold degenerate energy levels where the ground state is a single electron or hole and the transitions are circularly polarised according to angular momentum conservation.

Most of the experiments performed in this work require the ability to modify the selection rules and address individual states. In particular, employing the electron or hole spin requires the spin orientations ($|\uparrow\rangle, |\downarrow\rangle$) to be split in frequency. A magnetic field (\mathbf{B}) can split transitions by interacting with the magnetic moment of an electron or hole. As a result, the potential energy changes by $\mu\mathbf{B}$, where $\mu_i = -\frac{1}{2}g_i\sigma_i\mu_B$, g_i is the g-factor, μ_B the Bohr magneton and σ_i the Pauli operator. This leads to a total splitting between the two spin states of $Z = g_i\mu_B B$ according to the Zeeman-effect.^{72,73} Typical g-factors for electron spins in InAs QDs are $g_e \sim -0.5$ to -0.8 ⁷⁴ while the hole g-factor varies a lot depending on the specific QD and the magnetic field orientation. Despite this variation in strength of the hole g-factor, the sign is typically positive, as opposed to the electron. Furthermore, the magnetic field orientation has a strong influence on the transition rules.^{39,75}

For an out-of-plane magnet (B-field in z -direction, the so-called Faraday configuration), the Zeeman effect splits the spin states in frequency with respect to the quantisation axis (z -direction) and the transition rules can be determined purely by the conservation of spin angular momentum for all three exciton types. As a result, all allowed transitions become circularly polarised (Fig. 2.2b,c). In particular, for X^0 for large magnetic fields, the Zeeman effect dominates over the exchange interaction making the transitions circularly polarised.

In case of the charged excitons, the vertical transitions are allowed while the diagonal ones are forbidden. However, due to HH-LH-mixing, the forbidden diagonal transitions become partially allowed.⁷⁶

An in-plane magnet (B-field in x-direction, the so-called Voigt geometry) changes the transition rules. Now, the quantisation axis points in the in-plane direction and accordingly, the new pseudo-spin states are a superposition of the z-basis spin states: $|\uparrow\rangle_x = (1/\sqrt{2})(|\uparrow\rangle_z + |\downarrow\rangle_z)$; $|\downarrow\rangle_x = (1/\sqrt{2})(|\uparrow\rangle_z - |\downarrow\rangle_z)$ (and equivalently for the hole spin). The consequences are linear transition rules for all three excitons as shown in Fig. 2.2 with equally strong vertical and diagonal transitions, but with perpendicular polarisation between them.

The two magnet configurations have exactly opposite advantages and challenges for spin experiments. The weakly allowed diagonal transitions in the Faraday configuration are advantageous for spin readout, as they allow for several cycles of the readout before back-action. Spin manipulation, however, requires the diagonal and vertical transitions to be similarly strong. Hence, the Voigt geometry is ideal for spin rotations. Combining readout and manipulation on the same experimental configuration is an ongoing challenge that is addressed in Ch. 6.

2.1.2 Electron and hole spins

While QDs are known for their excellent optical properties, spin coherence is relatively poor due to their interaction with the environment, in particular the hyperfine interaction with the host nuclear spins. This main source of decoherence arises since the wave-function of an electron or hole spin within the QD overlaps with many nuclear spins of the host. The wave-function extent is illustrated in Fig. 2.3a. Each of the 10^5 nuclei of the host has non-zero nuclear spins ($I_{\text{In}} = 9/2$, $I_{\text{Ga}} = I_{\text{As}} = 3/2$), which specifically for InAs QDs lead to a strong hyperfine interaction. The Hamiltonian describing the hyperfine interaction between a spin and multiple nuclei consists of two main components:⁷⁷ the contact hyperfine term and the dipole-dipole term. Understanding the hyperfine interaction allows overcoming it, for example via decoupling schemes,⁷⁸ dynamic nuclear polarisation^{79,80} or by narrowing of the nuclear spin distribution⁴³ as is further discussed in Ch. 7. Interestingly, even though electron and hole spins follow the same selection rules, they differ significantly in their hyperfine interaction.

The electron spin

The conduction band is constructed from s-like orbitals which are localised at the positions of the nuclei (see in Fig. 2.3b). This results in a strong contact hyperfine interaction between the electron spin and each nucleus of the host material. The contact hyperfine interaction can be described by⁸¹

$$H_C \approx \Omega \sum_i A_i^e |\Psi_i|^2 \mathbf{I}_i \cdot \mathbf{S} \simeq \mu_B \hat{g}_e \mathbf{B}_N \cdot \mathbf{S}, \quad (2.1)$$

with A_i^e being the coupling coefficient with nuclear spin i , \mathbf{I}_i the nuclear spin vector, Ψ_i the electron envelope function, Ω the unit cell volume, \mathbf{S} the electron spin operator and \hat{g}_e the electron g-factor. The individual nuclear spins interact with the electron via an effective magnetic field which for N nuclear spins does not fully cancel, leaving a residual factor proportional $1/\sqrt{N}$. The remaining Overhauser field for InAs QDs is about $B_N \approx 20$ mT.³⁹ Fluctuations of this field lead to decoherence. Furthermore, the part of B_N fluctuating

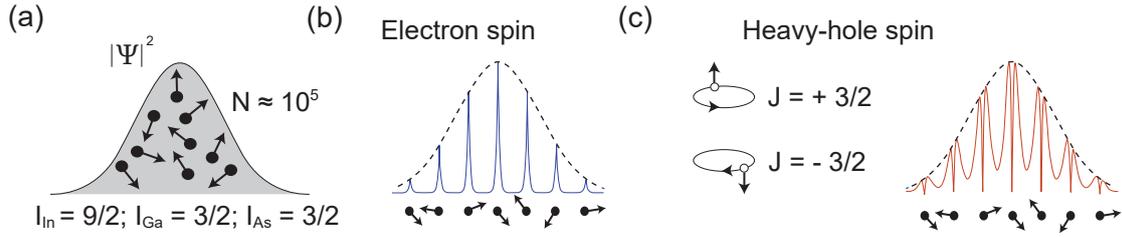


Figure 2.3: Hyperfine interaction of an electron and heavy-hole spin (a) The wave-function of an electron or hole extends over a few nanometers in all directions. It overlaps with $\sim 10^5$ atoms in the host material, where each host atom has non-zero nuclear spin. (b) The conduction band is constructed of atomic s -orbitals that are localised at the position of the nuclei. (c) The valence band is predominantly constructed from atomic p -orbitals, where the amplitude of the wave-function is small at the position of the nuclei. The magnetic dipole moment of the heavy-hole can be illustrated as a circulating current pointing in the $\pm z$ direction. This figure has been modified and adapted from Ref.³⁹

perpendicular to the applied magnetic field is responsible for a spin flip-flop process, a process that can be suppressed by applying high enough magnetic fields. Attempts to overcome the decoherence times of electrons have been made, including narrowing of the spin distribution of the nuclear ensemble.⁴³ As s -orbitals have spherical symmetry, the dipole hyperfine interaction is zero. Note that the quadrupolar term of the interaction Hamiltonian can give rise to non-collinear terms,⁸² which are relevant for more recent cooling schemes.⁴⁴

Despite their low coherence times ($T_2^* \sim 1-3$ ns;^{83,84} $T_2^* \sim 296$ ns with cooling^{43,44}), electron spins have been fully implemented as qubits with fast initialisation⁸⁵ and manipulation.⁸⁶ Readout of the spin state faster than the coherence time is important for quantum applications and is presented in Ch. 6.

The hole spin

Due to higher coherence times ($T_2^* \sim 20-30$ ns⁸⁷), hole spins present an interesting alternative to electrons for spin qubits. Valence band states are constructed of p -like orbitals that show suppressed interaction at the contact point as can be seen in their wave-function in Fig. 2.3c. Consequently, the contact hyperfine interaction is suppressed.⁸⁸ As a result of the p -wave symmetry of the Bloch function, the dipole part remains. For a pure HH state and a magnetic dipole along the z -direction, the Hamiltonian takes a simple Ising form:⁸⁸

$$H_{\text{dipole}}^{\text{HH}} \approx \Omega \sum_i A_i^{h,z} |\Psi_i|^2 I_i^z \cdot J^z \simeq \mu_B \hat{g}_h B_N^h J^z \quad (2.2)$$

with A_i^h the coupling of the HH to nuclear spin i , I_i^z the z -component of the nuclear spin, Ψ_i the hole envelope function, J^z the z -component of the hole spin vector and \hat{g}_h the hole g -factor. A_i^h is typically only 10% of A_i^e , which might be the reason for the difference in coherence times between electrons and holes.⁸⁹ According to Eq. 2.2, there is an anisotropy in the Overhauser field as $\mathbf{B}_{\text{tot}} = \mathbf{B} + B_{N,z}^h$ and the HH only experiences a fluctuating Overhauser field in z -direction. For a strong in-plane magnetic field, these fluctuations are suppressed. However, these predictions only hold for a pure HH state. As mentioned above, in reality the valence band is a mixture of HH and LH (approximately 5-10% of hole state is LH⁹⁰), which gives rise to non-vanishing components in the hyperfine interaction. The extended interaction Hamiltonian for a real hole spin is no longer of Ising form and includes

relevant non-collinear terms:⁹¹

$$H_{\text{dipole}}^{\text{HH/LH}} \approx \Omega \sum_i |\Psi_i|^2 (A_i^{h,z} I_i^z \cdot J^z + A_i^{h,\perp} (I_i^+ \cdot J^- + I_i^- \cdot J^+) + A_i^{h,nc} (I_i^+ \cdot J^z + I_i^- \cdot J^z)) + \dots \quad (2.3)$$

with ladder operators $J^\pm = J^x \pm iJ^y$ and $I_i^\pm = I_i^x \pm iI_i^y$ for hole spins and for nuclear spins, respectively, $A_i^{h,\perp}$ the transverse part of the hyperfine coupling and $A_i^{h,nc}$ the non-collinear coupling. Note that non-collinear interaction is unusual but hides a lot of interesting QD physics. For example for electrons, it enables coherent feedback cooling.⁴⁴ This means that they are crucial to understand how cooling protocols can be implemented using hole spins as discussed in Ch. 7. It is, however, not fully understood how each of the non-HH components influences the coherence of the hole spins in InAs QDs.

Until here, the physics of QDs have been discussed on a bulk sample only. However, in all experiments presented in this thesis, the QDs are coupled to a microcavity. This can radically change the transition rules and decay rates.

2.2 An emitter in a tunable open microcavity

Owing to the high refractive index of GaAs, the coupling of photons emitted by a QD out of the bulk material is low. Furthermore, spontaneous emission of photons is directed into all possible free space modes. This makes it difficult to collect a large percentage of emitted photons (<1% of photons are collected), severely limiting the usefulness of QD photons for quantum technologies. However, embedding QDs (or other emitters) into photonic engineered micro-structures, for example photonic crystal cavities^{92,93} or microcavities,^{19,46,48} can overcome these issues. These structures act as a resonator for light-matter interaction and, thus, can increase the photon emission rate while funnelling the emitted photons into the direction of the resonant cavity mode. The full interaction of a single emitter with a cavity is described by cavity-QED. Optimisation of the relevant parameters of the optical cavity, the emitter as well as the coupling between them can increase the photon counting rate immensely.

2.2.1 Cavity quantum electrodynamics

Typically, light-matter interaction can be boosted by placing an emitter in an optical resonator. Although different types of optical resonators exist, the physics is most easily explained by a simple optical Fabry-Pérot cavity consisting of two flat mirrors with reflectivities R_1 and R_2 placed at a distance L apart. The two mirrors act as a standing wave resonator.⁹⁴ Due to interference effects, wavelengths resonant with the cavity frequency are enhanced, while all other wavelengths are suppressed. The general working principle of a cavity is based on a small mode volume V between the mirrors confining the electric vacuum field E_{vac} by modulating the density of photonic states.⁹⁴ Three main parameters of cavity-QED are introduced in order to describe a cavity and its interaction with a TLS at resonance condition⁹⁴ (Fig. 2.4a).

Firstly, the cavity-photon loss rate κ describes all losses due to transmission, scattering and absorption and is typically dominated by losses through the cavity mirrors:

$$\kappa = \frac{1}{\tau_{\text{cav}}} = 2\pi \frac{c}{nL} \frac{1 - R_1 R_2}{\sqrt{R_1 R_2}} = \frac{\omega}{Q}, \quad (2.4)$$

where τ_{cav} is the lifetime of a photon in the cavity. Furthermore, κ is inversely proportional

to the quality factor Q of a cavity, which depends on the resonance frequency ω . The cavity-photon loss rate κ can be extracted from the linewidth of a cavity resonance (as is demonstrated in Sec. 2.2.2).

Secondly, a TLS consists of a ground $|g\rangle$ and an excited state $|e\rangle$. Upon decay of the excited state ($|e\rangle \rightarrow |g\rangle$), a photon at angular frequency ω is released as described in Sec. 2.1.1. For a transform-limited TLS, the emission is dominated by the radiative decay rate $\gamma = \gamma_R$, which is given by:

$$\gamma = \frac{1}{\tau_R} = \frac{n\omega^3}{3\pi\epsilon_0\hbar c^3} \cdot \mu^2, \quad (2.5)$$

with μ the transition dipole moment of the emitter.

Thirdly, the coherent coupling rate g describes the interaction if the polarisation of the vacuum electric field amplitude E_{vac} aligns with the transition dipole moment μ :

$$g = \frac{\mu E_{\text{vac}}}{\hbar} = \sqrt{\frac{\omega}{2\hbar\epsilon_0 n^2}} \cdot \frac{\mu}{\sqrt{V}}. \quad (2.6)$$

Different regimes and properties of cavity-QED can be described by means of these three main parameters, κ , γ and g . In strong-coupling, where $g \gg \kappa, \gamma$, the emitted photons are reabsorbed faster than they can escape the mirrors. Although strong coupling is useful for studying coherent light-matter interactions, it is not the optimal regime for maximum photon collection efficiency. Hence, in order to collect all photons, the weak coupling regime is preferable. Specifically for optimisation of photon collection efficiencies, $\kappa > g > \gamma$ is ideal. In this regime, the spontaneous emission rate, γ , is modified by the Purcell factor

$$F_P = \frac{4g^2}{\kappa\gamma}, \quad (2.7)$$

which means that we can define a cavity-enhanced emission rate $\Gamma = F_P \cdot \gamma$. Hence, for a $F_P > 1$, the emitter decay rate is increased, which is important for high-rate single-photon sources. We can define another important parameter, the β -factor. It describes the coupling efficiency of the optical cavity mode and the emitter and is given by⁹⁴

$$\beta = \frac{F_P}{1 + F_P} = \frac{g^2}{g^2 + \kappa\gamma/4}. \quad (2.8)$$

A high $\beta \simeq 1$ means that the optical mode is close-to-perfectly coupled to the emitter, e.g. no photons are lost, neither when coupling to the emitter nor being emitted into the cavity mode. This efficient light-matter coupling results in a preferred direction of spontaneous emission into the coupled cavity mode. This is important for efficient single-photon sources, but also coherent photon-emitter interfaces. Ideally, β is as high as possible. However, for the goal of achieving high photon collection efficiency, it is important to avoid the strong coupling regime, and out-couple the photon through the cavity mirror before it is reabsorbed by the emitter. Accordingly, the outcoupling efficiency, defining how many photons are coupled out through the cavity mirrors once being in the cavity mode, is a relevant parameter:

$$\eta_{\text{out}} = \frac{\kappa}{\kappa + \gamma}. \quad (2.9)$$

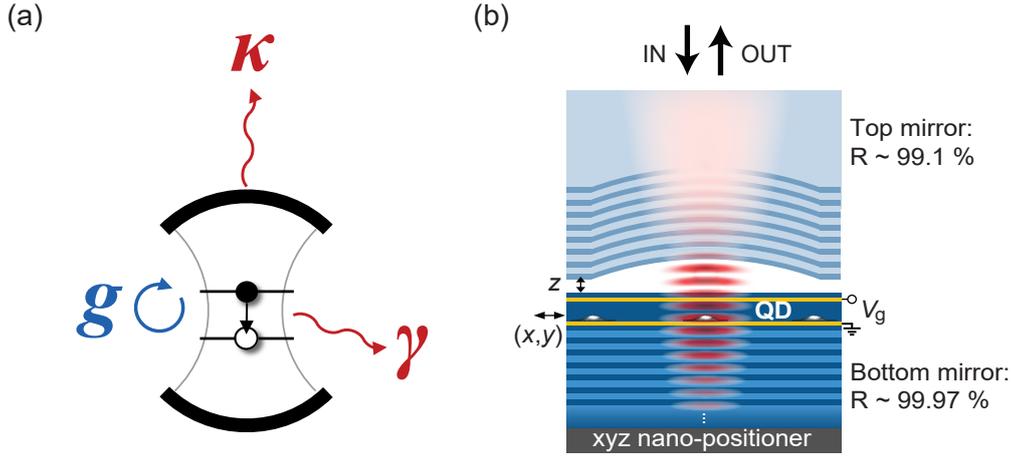


Figure 2.4: Cavity-QED parameters and one-sided cavity (a) The three relevant parameters of cavity-QED are depicted in a schematic of a TLS in a cavity: the cavity photon loss rate κ , the TLS decay rate γ and the coupling rate g between the TLS and the cavity vacuum field. (b) Schematic of the used cavity-QED system where the bottom mirror is a semiconductor heterostructure including the QDs and the top mirror a much less reflective curved silica mirror. Due to the reflectivity difference of the mirrors, the cavity operates in the one-sided regime, where $\kappa_{\text{top}} \gg \kappa_{\text{bottom}}$. (b) has been modified and adapted from Ref. ¹⁹

In order to optimise photon collection, one can define the so-called quantum efficiency η :⁹⁵

$$\eta = \beta \cdot \eta_{\text{out}} = \frac{g^2}{g^2 + \kappa\gamma/4} \cdot \frac{\kappa}{\kappa + \gamma}. \quad (2.10)$$

It describes the probability with which a QD photon is emitted into the cavity mode and subsequently leaves through the mirror. Tuning the cavity parameters to the optimum, hence, can maximise the quantum efficiency. While it is not easy to engineer γ and g in a Fabry-Pérot cavity, κ can easily be modified by varying the reflectivities of the mirrors, for example by reducing the number of distributed Bragg reflector (DBR) layers in a mirror. The quantum efficiency η can be maximised by tuning κ to the condition $\kappa = 2g$.⁴⁸

A tunable one-sided cavity coupled to an InAs quantum dot

In the scope of this work, a very specific cavity system¹⁹ is coupled to InAs QDs (described in Sec. 2.1). A schematic of the system is shown in Fig. 2.4b. The cavity is a tunable open microcavity consisting of a flat semiconductor DBR mirror (46 $\lambda/4$ layer pairs of AlAs/GaAs with central wavelength $\lambda = 917$ nm) that includes the gated QDs embedded in a n-i-p diode structure and a curved silica DBR (8 $\lambda/4$ layer pairs of Ta₂O₅/SiO₂; radius of curvature $R=12$ μm) that is much less reflective (all details on the experimental setup can be found in App. A). Consequently, all light is sent in and collected via the top mirror such that $\kappa = \kappa_{\text{top}} + \kappa_{\text{loss}}$ (κ_{loss} includes losses to side channels κ_{side} and the bottom mirror κ_{bottom}). In that case, $\eta_{\text{out}} = \kappa_{\text{top}}/(\kappa + \gamma)$. This changes the condition for optimal quantum efficiency to:

$$\kappa_{\text{top}} = \sqrt{(1 + \kappa_{\text{loss}}/\gamma)(4g^2 + \kappa_{\text{loss}}\gamma)}. \quad (2.11)$$

Subsequently, the tuning knob for κ_{top} is the number of DBR layer-pairs in the top mirror.

Moreover, the open microcavity has several *in-situ* tuning capabilities. As the two mirrors are completely separated in space, the bottom mirror including the QDs can be moved with

respect to the top mirror. This way, the cavity resonance can be adjusted via the length of the cavity (z), but also the coupling, g , can be tuned by moving a QD out of the cavity mode (x, y), and thus, β can be modified. Furthermore, the described properties of the gated QD structures (see Sec. 2.1.1) provide tuneability of the QD transitions.

This type of well coupled cavity-emitter system has various applications in quantum technologies. This chapter focuses on two main aspects. Firstly, a QD is an excellent source of single photons. Optimising the quantum efficiency by engineering of the microcavity is promising for maximal increase of photon collection rates. Secondly, a close-to-ideal interface for photons can be achieved by combining a high single-photon rate, a noise free emitter and high β -factors.

2.2.2 An efficient single-photon source

Optimising a coupled emitter-cavity system for high quantum efficiencies is an important step in achieving an efficient single-photon source. However, this is not the end of the story. For any application it is essential to be able to collect the generated photons, ideally into a single-mode optical fibre. Hence a measure of the usable photon rate is crucial. This is captured in the end-to-end efficiency Σ .¹⁹ In addition to the quantum efficiency η , the optical losses from directly outside the cavity mirror through all optical elements into an optical fibre must be taken into account. Furthermore, it is essential that the probability to excite the TLS is evaluated and included. In the open microcavity system described above, the biggest losses are optical losses. However, the losses have been minimised as described in App. A, enabling the system to be the most efficient source of single photons to date.^{19,49} With this system, an end-to-end efficiency of $(57 \pm 3)\%$ has been measured by sending picosecond pulses at a rate of 76.3 MHz and collecting the single-photon counts on a detector (Fig. 2.5a). For reference, the efficiency of QD single photon sources with no cavity enhancement is $<1\%$ and the previous state-of-the-art for QD-cavity sources was 24%.⁴⁷ Importantly, many quantum technological applications scale exponentially with the source efficiency. The end-to-end efficiency is defined by:

$$\Sigma = \beta_H \cdot \frac{\kappa_{\text{top}}}{\kappa + \gamma} \cdot \Pi \cdot \eta_{\text{optics}}. \quad (2.12)$$

where Π is the π -pulse efficiency for optical excitation of the TLS, β_H the β -factor of the H-polarised cavity mode and η_{optics} the efficiency of the throughput of the optical elements.

The tunability of the system allows for a direct extraction of the β -factor by measuring the decay rate of the QD as a function of the cavity length as shown in Figure 2.5b. Two frequency-split cavity modes (details described in App. A) can be observed. From the change in decay rate on and out of resonance with the cavity modes a Purcell factor of $F_p = 10$ is obtained and hence $\beta = 91\%$ (more specifically for the H mode, $\beta_H = 87\%$). The cavity-photon loss rate – which is now dominated by the losses through the top mirror κ_{top} – can be extracted from the cavity linewidth, κ , and is found to be $\eta_{\text{out}} = 96.2\%$. Furthermore, Π is derived from the theory model derived in Ref.,¹⁹ $\Pi = 96.3\%$, and $\eta_{\text{optics}} = 69.0\%$ is measured by duplicating the optical system with a mirror instead of the cavity and measuring its throughput. In summary, all extracted efficiencies multiply together to the measured end-to-end efficiency. Thus, the described system is well understood.

Moreover, the purity and coherence of the photons are very high in this system. Measurements of the $g^{(2)}(\tau)$ and the Hong-Ou-Mandel interference V are shown in Fig. 2.5c,d

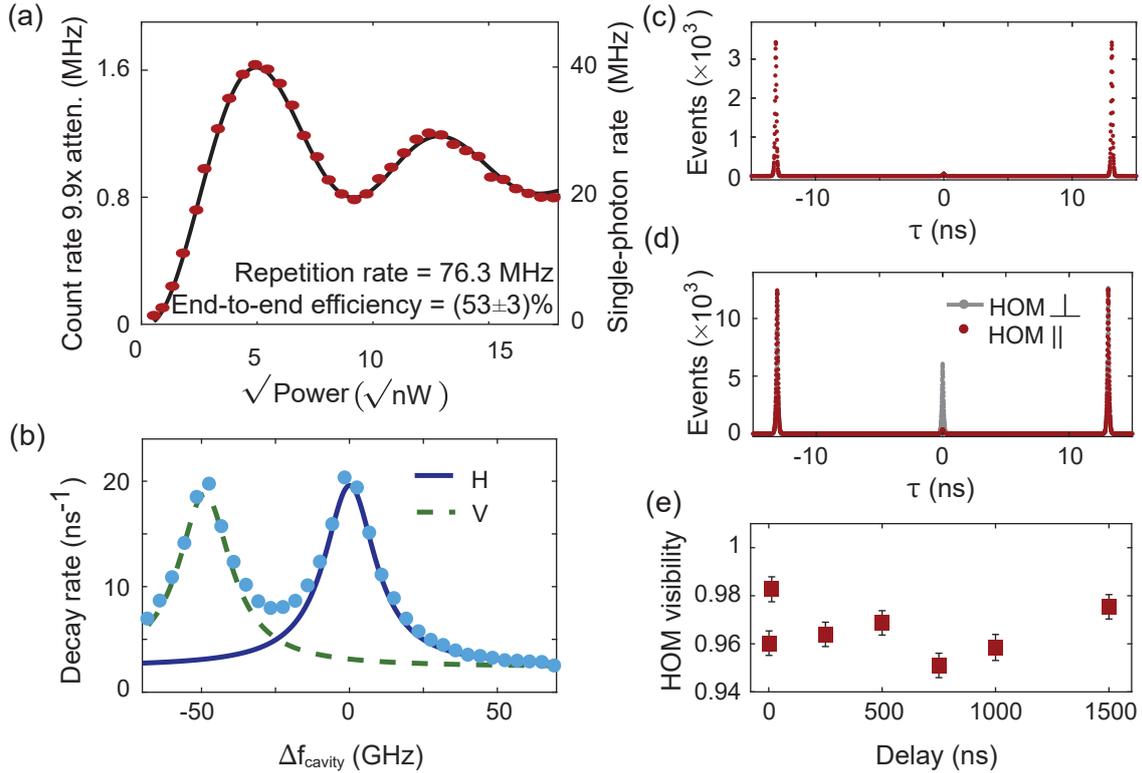


Figure 2.5: A bright source of coherent single photons (a) Measured signal versus square root of the laser power. The pulsed laser repetition frequency is 76.3 MHz. The signal is deliberately attenuated by a factor 9.9 to avoid saturation of the detector (left y-axis). The right axis shows the expected signal without attenuation and with a perfect detector. The solid line is the theory model discussed in Ref. ¹⁹ (b) Radiative decay rate versus cavity detuning. The total Purcell factor is determined to be 10, implying $\beta = 91\%$. (c) Autocorrelation $g^{(2)}$ versus delay τ : $g^{(2)}(0) = (2.1 \pm 0.1)\%$. (d) HOM experiment showing two-photon interference from photons created at $1.5 \mu\text{s}$ apart in time: $V = (97.5 \pm 0.5)\%$. (e) HOM visibility V vs delay in the interferometer. This figure has been modified and adapted from Ref. ¹⁹

demonstrating a $g^{(2)}(0) = (2.1 \pm 0.1)\%$ and $V = (97.5 \pm 0.5)\%$. This is important for any application of photonic qubits. Furthermore, V , and hence the photon coherence, is equally high for photons generated by the same source at different time delays, from short ($\sim 1 \text{ ns}$) to long ($\sim 1.5 \mu\text{s}$) delays (Fig. 2.5e). Using a technique called photon-correlation Fourier spectroscopy (PCFS),⁹⁶ the coherence length of the photons was probed up to even longer timescales and no decay is observed up to a time of $\sim 200 \text{ ms}$. Consequently, strings of at least 100,000 indistinguishable, usable photons can be generated before the source dephases.

These results are relevant for all the experiments presented in this thesis. Apart from speeding up any experiment with high photon count rates, the optimisation of the system has enabled fast spin state manipulation and readout of spin states and a coherent interface of photons.

2.2.3 The perfect coupling case: a one-dimensional atom

A high coupling efficiency, β , is a prerequisite for a concept called a one-dimensional (1D) atom,²⁶ where one single optical mode is perfectly coupled to one single emitter. Since quantum gates require emitters acting as strong photon-photon interfaces, 1D atoms become crucial for the implementation of quantum computational nodes.⁹ A 1D atom can be realised

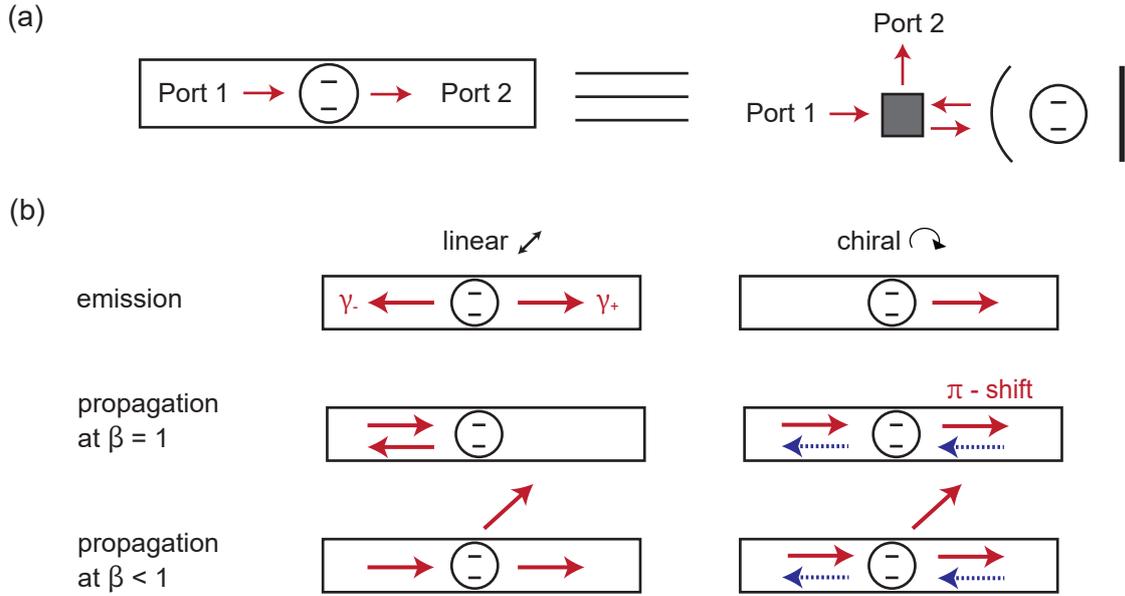


Figure 2.6: A 1D atom (a) A TLS coupled to a single optical mode, a 1D atom, can be implemented in a waveguide (left) or in a one-sided cavity using a set of optical elements (right; dark box consists of beam-splitters and wave-plates). The physics is identical and two ports can be defined for simplification. (b) Two different regimes in 1D atoms. In a linear regime (linear dipole transition or light polarisation), a TLS emits into both ports, while in the chiral regime (circularly polarised dipole transition *and* photons) it emits only into one port. Light propagation is hence dependent on the regime and the coupling efficiency β . While in the linear regime, all interactions are reciprocal, a chiral emitter only interacts with incident photons from a specific direction.

using different types of resonators. For simplicity, all concepts are discussed on a waveguide. Note however, that a one-sided cavity as in our case (App. A) in combination with some basic optical elements can mimic precisely the same conditions (Fig. 2.6a) as is further discussed in Chs. 3,4. Furthermore, owing to the cavity mode splitting in the one-sided cavity (details on the exact setup can be found in App. A), the one-sided cavity can mimic a two-sided cavity by making use of the orthogonal polarisations and the optical elements (compare with Ch. 3).

One important requirement for a quantum network consisting of several nodes is a clear photon propagation direction. This means that a photon travelling from port 1 in Fig. 2.6a propagates only forwards to port 2 and is not back-scattered to its origin, even upon interaction with the emitter. Example for elements requiring direction dependent behaviour are isolators, circulators, diodes or cascaded systems.^{97–99} The answer to these challenges is the concept of chiral emitters. It is important to distinguish between linear and chiral emitters as they behave very differently.

In order to achieve chiral coupling, both the emitter as well as the photons must possess circular polarisation. Consequently, if one of the two is linearly polarised, the interaction will be in what is called the linear regime and the interaction will not be chiral. While circularly polarised light in waveguides results from tight transverse confinement,⁵² optical wave-plates and a polarising beam-splitters can be used in the open cavity case in order to obtain it.¹⁰⁰ The emitters' transition rules can be set by choosing an appropriate exciton in a specific magnetic field orientation (compare to Fig. 2.2).

The difference between the two regimes (chiral or linear light propagation) can be under-

stood by looking at the emission properties of an emitter in a waveguide.⁵² In the linear regime, photons will be emitted to both port 1 and port 2 with equal probability. In the chiral regime, however, the emitted photons only go to one side. Therefore, in a chiral emitter $\gamma_+ \neq \gamma_-$ as is illustrated in Fig. 2.6b. Directional emission implies a directional coupling efficiency β_{\pm} of travelling photons as

$$\beta_{\pm} = \frac{\gamma_{\pm}}{\gamma_+ + \gamma_- + \gamma_{\text{loss}}}, \quad (2.13)$$

and hence, $\beta_+ \neq \beta_-$ (with $\beta = \beta_+ + \beta_-$). In the most extreme chiral case, $\beta_- = 0$ while $\beta_+ = 1$. Furthermore, directional coupling changes the transmission and reflection properties of the emitter in comparison to the linear regime as can be seen in Fig. 2.6b. The transmission and reflection coefficients for both regimes are given by

$$t_{\pm} = 1 - 2\beta_{\pm} \quad (2.14)$$

$$r_{\pm} = -2\sqrt{\beta_+\beta_-}, \quad (2.15)$$

resulting in an absorption $A_{\pm} = 1 - |t_{\pm}|^2 - |r_{\pm}|^2$.

There are two particularly interesting conditions.⁵² Firstly, the perfect coupling condition $\beta = 1$. In the linear case the emitter acts as a perfect mirror for single photons ($r = 1$, $t = 0$; more details in Ch. 3). It does so independent of the direction the photons come from. On the other hand, $t = -1$ in the chiral case: light travelling in one direction is transmitted acquiring a phase π (more details in Ch. 5). However, if photons arrive from the opposite direction, they won't interact, but will be transmitted resulting in a non-reciprocal phase shift. Further, for $\beta < 1$, reflection, transmission and absorption change according to Eqs. 2.14, 2.15. As long as $\beta > 0.5$, the emitter's dynamics will dominate the coupling to the waveguide mode.⁵² The second interesting case is at condition $\beta = 0.5$, where in the chiral case, absorption goes to unity for one direction ($t = 0$), while light propagating in the other direction is entirely transmitted ($t = 1$; more details in Ch. 4). This condition leads to a non-reciprocal transmission which can be used to realise optical diodes.

Alongside these different regimes and interesting configurations, a 1D atom generally enables strong optical nonlinearities at the single photon level to be observed.^{9, 26} Due to the two-level nature of an emitter, the response is different upon incidence of one or two photons. This nonlinearity in photon number arises because only one photon can interact with the TLS within the radiative lifetime of the emitter. At higher photon numbers within the lifetime, the TLS saturates. Particularly coupled to chiral emitters, a giant nonlinearity can have several applications in quantum and classical information technology.^{101, 102}

In order to experimentally implement a 1D atom, the cavity-QED parameters described in Sec. 2.2.1 (g , κ and γ) need to be optimised. The radiative decay rate γ (which here is included in γ_{loss}) is typically fixed and not equal to zero. In reality, this means β never reaches unity. However, β can be maximised by optimising κ and g to the same conditions as for a single-photon source and maximising the quantum efficiency. Importantly, all the descriptions in this section require a negligible upper-level dephasing (compare Sec. 2.1.1), which is a reasonable assumption for a modest Q -factor cavity as the one used in this thesis.⁶⁷

Part **II**

A quantum dot in a microcavity as
a one-dimensional atom

3

A tunable, coherent and efficient light-matter interface based on a single quantum emitter in a microcavityⁱ

3.1 Summary

A coherent and efficient light-matter interface at the level of single emitters and single photons, a one-dimensional (1D) atom, is the main requirement for photonic quantum gates. In a 1D atom, the photon-emitter coupling efficiency, β , determines the transmission amplitude and the phase of the scattered light. Observing high β in combination with a high photon collection efficiency and low dephasing has remained a challenge to date. Here we use a semiconductor quantum dot (QD) in an open microcavity to implement a 1D atom. We achieve an extinction of 99.2% in the transmission, resulting in a bunching in the photon statistics of $g^{(2)}(0) = 587$, showcasing the selective transmission of the two-photon component of the coherent input. The tunable nature of the microcavity allows β to be adjusted and gives control over the photon statistics – from strong bunching to anti-bunching – as well as over the phase of the transmitted photons. Our results are consistent with the observation of photonic bound states and pave the way for implementations of two-photon phase gates.

3.2 Introduction

The ability to generate and manipulate correlated and entangled photonic states at the few-photon level is imperative for the advancement of technologies promoting quantum information processing in the optical domain. The realisation of well-controlled quantum photonic gates requires a highly nonlinear medium, i.e. a medium that enables the strong and controlled interaction of few photons.^{103–105} A 1D atom, an emitter strongly coupled to a single optical mode, is the ideal candidate to provide these functionalities.^{50,106} Engineering a 1D atom is challenging, as it requires the β -factor to be nearly unity, without impairing decoherence or noise on the quantum emitter. One approach to enhance the coupling efficiency includes employing an ensemble of atoms^{99,107} that collectively behave as a super-

ⁱThe experiments in this chapter have been conducted in equal contribution with Natasha Tomm.

atom. Cavity quantum electrodynamics provides an alternative route to boost light-matter interaction by confining the vacuum electric field to small mode volumes, and placing a quantum emitter in the centre of the optical mode defined by the cavity. This approach has been successfully implemented with a number of emitters, such as atoms,^{108–110} ions,¹¹¹ molecules,¹¹² and solid-state systems for which very high atom-photon couplings have been achieved, for instance with semiconductor QDs.^{45, 48, 113–115}

Here, we embed a *single* low-noise QD in an open, one-sided microcavity, creating a system that acts as a 1D atom. An important feature of this design is the fact that the environment around the QD is a pristine crystal. With minimal disturbance and noise sources around the QD (circumvented charge noise and weak exciton dephasing via phonons as explained in Sec. 2.1), the highly coherent optical transitions that are present in the bulk sample are preserved. We showcase the low-noise performance of our implementation of a 1D atom by measuring its transmission and its nonlinearity. In the ideal case, the atom would act as a perfect mirror for single photons,^{50, 116, 117} i.e. single photons cannot be transmitted past the atom, but are 100% back-scattered. Our system shows an extinction of 99.2% of the *transmitted* light, when probed with a low-power laser. More importantly, the remaining transmitted state is highly bunched, $g^{(2)}(0) = 587$, which is a strong result of the nonlinearity at the single-photon level: a near-perfect transmission of the two-photon component. We also exploit the tunability of the cavity to tailor the photon statistics, transitioning from highly bunched to anti-bunched photonic states. The ability to modify the output photon statistics in a controlled manner paves the way for the formation and manipulation of exotic quantum states.⁹⁹ The observations in this work are consistent with the formation of photonic bound states^{118–120} and direction-dependent phase-shifts,⁵² important for the implementation of controlled phase-gates.

3.3 Experimental and theoretical description

The setup is schematically shown in Fig. 3.1a. The cavity is a highly miniaturised Fabry-Pérot type cavity: the bottom mirror is a highly reflective (reflectivity $R = 99.97\%$) semiconductor distributed Bragg reflector (DBR) which embeds a layer of InAs QDs within an n-i-p diode structure. This diode structure allows for the gating of the QD and hence stabilising and tuning of the transition frequency. The top mirror is a less reflective ($R = 99\%$) dielectric DBR ($\text{SiO}_2/\text{Ta}_2\text{O}_5$) on a silica substrate, where a microcrater is created by laser ablation. The much higher transmittance of the top mirror makes the cavity nearly one-sided: the top mirror of the cavity is the main access port for incoming and outgoing light, see App. A for more details on the system. The bottom mirror sits on a set of xyz-nanopositioners, which allows for full control over the length of the cavity (z) and the lateral position of the QD with respect to the centre of the cavity mode (xy). A combination of a polarising beam-splitter (PBS) and a half-wave plate (HWP) gives full control over the polarisation of the input (*excitation*) and output (*collection*) states. As seen on Fig. 3.1a, we name one of the ports of the polarising beam-splitter *port 1*, and the orthogonal side *port 2* for convenience. Additionally, the cavity mode is frequency-split by $\delta_{\text{cav}}/(2\pi) = (\Delta\omega_H - \Delta\omega_V)/(2\pi) \simeq 50$ GHz into two linearly- and orthogonally-polarised modes due to a small birefringence in the bottom mirror. We name these two polarisation orientations H and V , with detunings $\Delta\omega_{H/V} = \omega_{\text{laser}} - \omega_{H/V}$. The cavity modes have a loss rate $\kappa/(2\pi) = 28$ GHz.

In this work we use a neutral exciton, X^0 , in a QD. The level structure of the neutral exciton is shown in the top part of Fig. 3.1b. It has a V -level energy structure: one ground

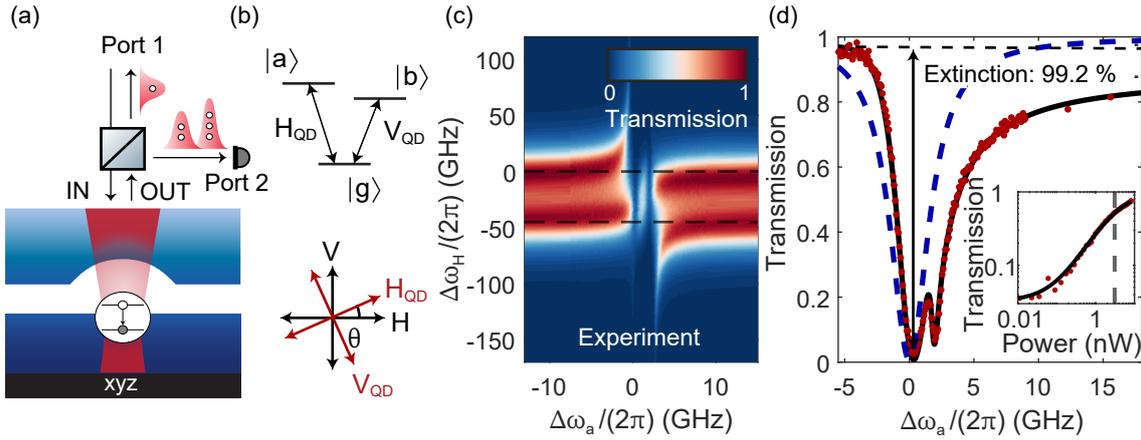


Figure 3.1: A 1D atom. (a) Experimental setup. A weak laser is sent onto an open, one-sided microcavity. The reflected light strikes a polarising beam-splitter. A HWP allows to set an angle between the incoming beam and the axes of the cavity. The sketch shows the optical path for photons in the transmission mode where the incoming beam is 45° polarised with respect to the cavity modes. At ideal coupling efficiency β , single-photon components are reflected into port 1 and higher-order components enter port 2. (b) Top: level structure of the neutral exciton (one ground state and two excited states). The two transitions have orthogonal linear polarisations. Bottom: the polarisation orientation of the horizontally (H) and vertically (V) polarised cavity modes and the QD transitions. (c) Transmission as a function of cavity and QD detuning. Horizontal lines indicate the two cavity resonances. (d) Transmission through the system as a function of the detuning of the QD. The transmission features two dips for the two dipoles. The stronger dipole shows an extinction of 99.2%. The black line is the theoretical prediction and matches the data very well. The dashed blue line shows the simplified scenario (one cavity, one TLS) and does not feature the second dip. The inset shows the power dependent transmission on resonance with the QD. The saturation power (indicated by the dashed grey line) is 3.1 nW.

state $|g\rangle$ with two excited states $|a\rangle$ and $|b\rangle$, with detunings $\Delta\omega_{a/b} = \omega_{a/b} - \omega_{\text{laser}}$. The two transitions are linearly polarised and orthogonal to one another. They are split in frequency by $\delta_{\text{QD}}/(2\pi) = (\Delta\omega_a - \Delta\omega_b)/(2\pi) = 2.3$ GHz. The polarisation axes of the QD lie at an angle of $\theta = 25.1^\circ$ with respect to the polarisation axes of the cavity, see the bottom panel in Fig. 3.1b. As a consequence, the H_{QD} transition $|a\rangle \leftrightarrow |g\rangle$ is more efficiently coupled to the H - than to the V -polarised cavity mode, and vice-versa for the V_{QD} transition $|b\rangle \leftrightarrow |g\rangle$. When H_{QD} is on resonance with the H -cavity mode, we achieve maximal coupling, presenting a Purcell-enhanced decay rate $\Gamma/(2\pi) = 3.0$ GHz (Purcell factor $F_P = 10$), resulting in a maximum dipole-cavity coupling efficiency of $\beta = F_P/(F_P + 1) = 92\%$.

We use two main experimental configurations termed *transmission* and *back-reflection* modes. We first focus on data acquired in the transmission mode experiments. In this setup, light with polarisation $P = 1/\sqrt{2}(H + V)$ is input from port 1 and interacts with the QD-cavity system. The output is collected in port 2 and probes the polarisation $M = 1/\sqrt{2}(H - V)$. We work with a drive strength, i.e. a unitless photon flux per time which is proportional to the optical laser power, $\varepsilon = \sqrt{\dot{n}_{\text{in}}}$, where \dot{n}_{in} is the input photon flux. The theoretical model used to compute transmission, back-reflection and intensity correlations in both transmission and back-reflection mode is similar to the model derived in App. B, but for a three-level system instead of a two-level system (TLS). The cavity-QD system dynamics are described through a Lindblad master equation and connected with measured quantities via the *input-output-theory*.^{121,122} Adiabatic elimination and perturbation theory in the

drive strength are employed to solve for the steady-state and obtain correlation functions.

3.4 Results

3.4.1 Strong extinction

The measured transmission from impinging P-polarised light to M-polarised light as a function of the QD detuning is shown in Fig. 3.1 d, illustrating an extinction of 99.2%, and showcasing the efficient coupling between the cavity and the QD.

We first consider the QD transition to be out of resonance with respect to the laser frequency (see the far left or far right in Fig. 3.1 c). When the resonance frequency of one cavity mode, say the V -mode, is swept across the resonant laser frequency, the phase of the reflected V -polarised light winds around 2π ⁱⁱ while the H polarisation does not pick up a phase upon reflection. On resonance, V -polarised light obtains a phase shift of π , thereby turning $P = 1/\sqrt{2}(H + V)$ light into $M = 1/\sqrt{2}(H - V)$ light and resulting in a transmission close to unity. This explains the peaks when the laser is on resonance with one of the cavity modes (while the QD is out of resonance). When the laser frequency is on resonance with one of the cavity modes, sweeping the QD frequency across the resonance results in a phase that winds twice across 2π ⁱⁱⁱ. On resonance, no phase is picked up and we expect a perfect extinction ($T = 0$) in the absence of dissipation ($\beta \simeq 1$) and upper-level dephasing.

Many of the qualitative features seen in the experiment can be understood by a simple model, which is obtained by setting $\theta = 0$ (ignoring the misalignment between the polarisations of the QD transitions and the cavity modes) and $|\delta_{\text{cav}}|/\kappa \rightarrow \infty$ (separating the resonances of the two cavity modes). In this case, when the laser is close to resonance with one mode, only light of the same polarisation may transmit into the cavity and interact with the TLS while the other polarisation is perfectly reflected. This simple model can thus be fully understood by a TLS coupled to a single cavity mode.^{122,123} Due to dissipation, the transmission on resonance in this model is reduced to $T = (1 - \beta)^2$.

The simple model may be mapped onto a two-sided cavity, where the P and M modes correspond to the two sides of a cavity^{iv}. In this case, T refers to the transmission through the cavity. Features of the transmission that are not captured by the simple model are the double dip structure in as well as the slight shift of the maximal extinction away from $\Delta\omega_a = 0$ in Fig. 3.1 d. Considering the full three-level system with an angle $\theta = 25.1^\circ$ between QD and cavity polarisation axes, the theory shows excellent agreement with these features. The transmission close to resonance with the QD is strongly dependent on the input power. With increasing laser power, the transmission dip disappears, see inset in Fig. 1c. This nonlinear response in the transmission is a consequence of the saturation of the quantum emitter. We extract a saturation power of $P_{\text{sat}} = 3.1$ nW, where power is measured at the input before the window to the cryostat. This saturation power corresponds to an average of 0.69 photons per lifetime of the QD on resonance with the cavity mode. From theory, we would expect an average photon number of $\langle n \rangle = 0.29$. The discrepancy likely arises due to an offset in the scaling between the power measured at the optical table and the actual power at the QD after optical losses.

ⁱⁱSimply derived by treating the cavity as a harmonic oscillator. Note that the factor of two difference in comparison to a classical oscillator arises from the fact that the light has to enter, and leave the cavity, resulting in twice a factor of π .

ⁱⁱⁱSame argument as for the cavity; the QD can be treated as a harmonic oscillator.

^{iv}The full theory model has been derived by Marcelo Janovitch and Patrick P. Potts

3.4.2 Giant and tunable nonlinearity

We now demonstrate the ability of this cavity-QED setup to manipulate the transmitted state of light. To this end, we consider the second-order correlation function $g^{(2)}(\tau)$, with τ being the delay between detection events. We observe very strong photon bunching of $g^{(2)}(\tau = 0) = 587$ (Fig. 3.2a) for very low input powers and an optimally-coupled QD. To our knowledge, this is the strongest photon bunching due to a non-linear effect observed to date. As discussed earlier, this bunching results from the atom reflecting the single-photon component in the quantum state. To achieve such a high bunching, all parameters of the system have to be close to ideal, i.e. very low dephasing, good coupling efficiency to the cavity, $\beta \simeq 1$, and very good overall detection efficiency^v. Our photon collection efficiency is high enough to further enable a high resolution measurement of a $g^{(3)}(\tau_1, \tau_2)$ as is shown in Fig. 3.2b. High bunching, i.e. coincidence clicks of three- and larger photon states, is observed for $\tau_1 = \tau_2 = \tau_3$. In addition to the high bunching obtained in $g^{(2)}(\tau)$, changing β allows us to tune from strong bunching to anti-bunching (Fig. 3.2c), demonstrating a large amount of control over the statistics of the transmitted light. In the experiment, control over β is achieved by controlling the lateral position of the QD with respect to the cavity centre.

The giant bunching and, more generally, the measurements of intensity correlations can be

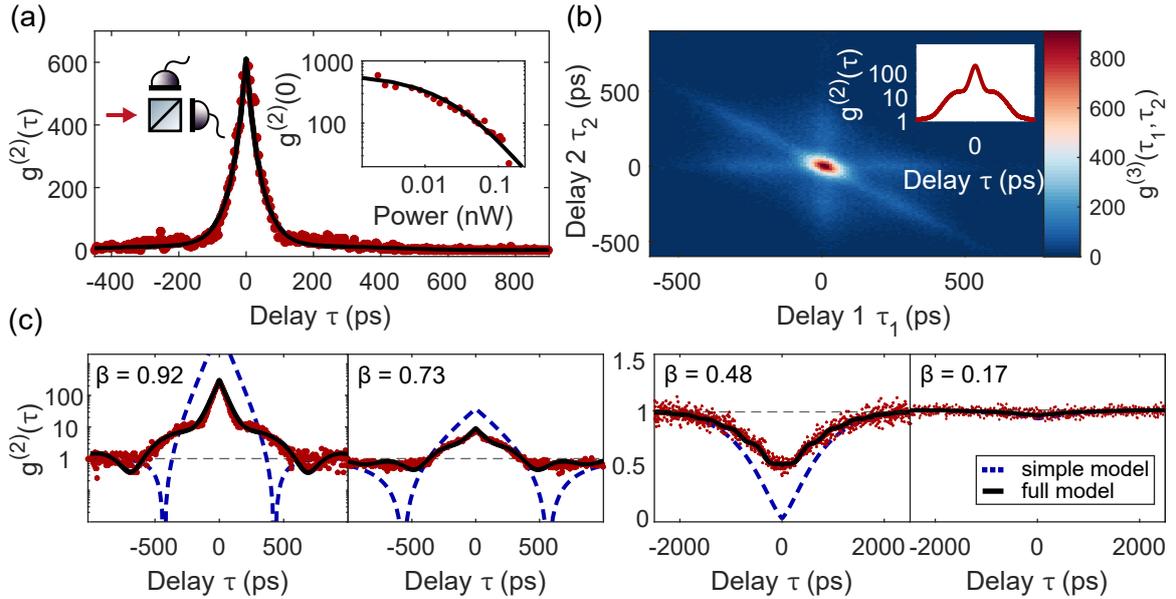


Figure 3.2: Strong modification of the transmitted photon statistics by the 1D atom. (a) Auto-correlation function $g^{(2)}(\tau)$ of the transmitted photonic state as a function of the delay between detectors τ . A bunching of 587 highlights the strong nonlinear response of the system. Inset shows the bunching at zero delay ($g^{(2)}(0)$) as a function of laser power. The black lines are the theoretical model. For these measurements the QD is positioned in the centre of the cavity ($\beta = 0.92$). (b) Third order correlation function $g^{(3)}(\tau_1, \tau_2)$ of the transmitted photonic state as a function of the delays between three detectors, τ_1, τ_2 . (c) $g^{(2)}(\tau)$ for different QD positions with respect to the cavity's anti-node, i.e. for decreasing β -factor. The bunching at the ideal coupling position turns into an anti-bunching at $\beta \simeq 0.5$, and disappears for $\beta \rightarrow 0$. The black line is the full model for a V-level structure and the dashed blue line is the theory for a TLS. The side bumps originate from the interaction with the second dipole.

^vThe latter might sound contradicting as $g^{(2)}(\tau)$ is independent of photon loss. However, the transmitted light is so low, that it can easily be polluted by uncoupled laser reflection.

explained by the evolution of the M-polarised cavity field after photo-detection, $\tau = 0$, back to the steady-state $\tau \rightarrow \infty$. In the bad-cavity ($\kappa > g > \gamma$) and weak drive ($\varepsilon \ll 1$) limits, the cavity field can be described by a pure quantum state at all times^{121, 123, 124}

$$|\psi\rangle_\tau = |\alpha\rangle - i\sqrt{\frac{\Gamma}{2\kappa}}\langle\hat{\sigma}_M\rangle_\tau\hat{a}_M^\dagger|\alpha\rangle. \quad (3.1)$$

Here, $|\alpha\rangle$ denotes the coherent state describing the M-mode in the absence of the atom. The second term describes the effect of the atom, where \hat{a}_M^\dagger denotes the creation operator in the M-mode and $\hat{\sigma}_M$ the QD dipole which is more efficiently coupled to the M polarisation. Note that the second term of Eq. 3.1 vanishes as $\varepsilon \rightarrow 0$ since $\langle\hat{\sigma}_M\rangle_\tau$ and α are proportional to ε . The state in Eq. 3.1 provides the correct averages for any normal-ordered observable (involving the M-mode) to leading order in the external drive ε . We refer to this state as *Rice-Carmichael (RC) state* since such a description was first introduced by Rice and Carmichael.¹²³ Since the input is P-polarised, the RC state of the M-polarised cavity mode fully characterises the M-polarised output. The $g^{(2)}$ -function measured at port 2 may then be understood as follows: measuring a photon at $\tau = 0$ alters the field in the cavity. As time progresses, the field will evolve back to its steady state (the state before a photon was detected). It can be shown that this time-dependent average field value directly determines $g^{(2)}(\tau) = |\langle\hat{a}_M\rangle_\tau/\langle\hat{a}_M\rangle_\infty|^2$, where the average is taken w.r.t. $|\psi\rangle_\tau$.¹²⁴ Thus, $g^{(2)}(\tau)$ larger (smaller) than one is observed whenever the average field is stronger (weaker) than in steady state.

To explain the key qualitative aspects of the experimental results, we consider the RC state for the simplified model discussed above ($\delta_{\text{cav}} \rightarrow \infty$, $\theta = 0$). In this case, we find^{vi}

$$\frac{\langle\hat{a}_M\rangle_\tau}{\langle\hat{a}_M\rangle_\infty} = 1 - \frac{\beta^2}{(1-\beta)^2}e^{-\frac{\gamma\tau}{2(1-\beta)}}. \quad (3.2)$$

This shows that the photon statistics can be modified by tuning β : At $\beta \simeq 0$ the cavity field remains close to a coherent state while for $\beta \simeq 1$, the contribution to Eq. 3.2 stemming from the QD can yield an amplified number of photons as compared to steady state.

The described RC states can now be used to investigate the β -factor dependence of the $g^{(2)}(\tau)$. The experimental results demonstrating a transition from bunching to anti-bunching (Fig. 3.2c) may qualitatively be understood by considering the steady state in the Fock basis:

$$\langle n|\psi\rangle_\infty = \alpha^n(1-\beta n)/\sqrt{n!}. \quad (3.3)$$

At $\beta = 1$ the single-photon component in the cavity vanishes and is thus perfectly reflected (sketch Fig. 3.1a). Importantly, higher-number components of the state are present in the cavity, leading to bunching in the transmitted light. In contrast, for $\beta = 1/2$, the two-photon component in the cavity vanishes due to destructive interference (half the two-photon components get a π and the other half no phase shift), which results in perfect anti-bunching $g^{(2)}(0) = 0$. Similarly, tuning $\beta = 1/n$ allows for suppressing the n -photon component. From Eq. 3.2, we may furthermore infer that the average field strength in the cavity changes sign upon the detection of the first photon if $\beta > 1/2$. As time progresses, the field then crosses zero, which in the theoretical curves in Fig. 3.2c results in dips of the $g^{(2)}$ -function. As for

^{vi}These relations have been derived by Marcelo Janovitch and Patrick P. Potts

the transmission above, the simplified model cannot capture all features of the $g^{(2)}$ function. In particular, the experimental data exhibits shoulders Fig. 3.2c, which are related to the finite cavity and dipole splittings, $\delta_{\text{QD}/\text{cav}} \neq 0$. In addition, the anti-bunching is limited by the finite cavity-mode splitting $\delta_{\text{cav}} \neq 0$ and slightly due to the dipoles' misalignment, $\theta \neq 0$ such that $g^{(2)} \simeq 0.5$ at $\beta \simeq 0.5$. Our full theoretical model shows excellent agreement with these features.

3.4.3 Back-reflection mode

We now demonstrate the connection of a different scattering configuration with the recently reported formation of photon bound states.¹²⁰ To this end, we turn to the second experimental configuration termed back-reflection mode where we operate close to the one-sided cavity regime.^{52,100} In this configuration, the cavity is driven by H-polarized light and the reflected light in the same polarisation is measured. A 99:1 beam-splitter is used to separate the input light from the output. The measured light is a superposition of light that is directly reflected at the cavity and the light that leaks out of the cavity.¹²¹ Figure 3.3a shows the reflected signal as a function of the cavity and the QD detuning. The input field, off-resonant to the cavity and the QD, maintains its polarisation and ends up at the detectors, hence, back-reflection is near unity for all the frequency ranges. On resonance with the cavity, the QD is efficiently coupled to the one cavity mode of interest ($\beta_H = 0.89$). Contrary to transmission mode measurements, the output signal does not go to zero on resonance with the QD ($R_{\leftarrow} = 62\%$), in unison with the idealised scenario, in which $R_{\leftarrow} = (1 - 2\beta)^2$.

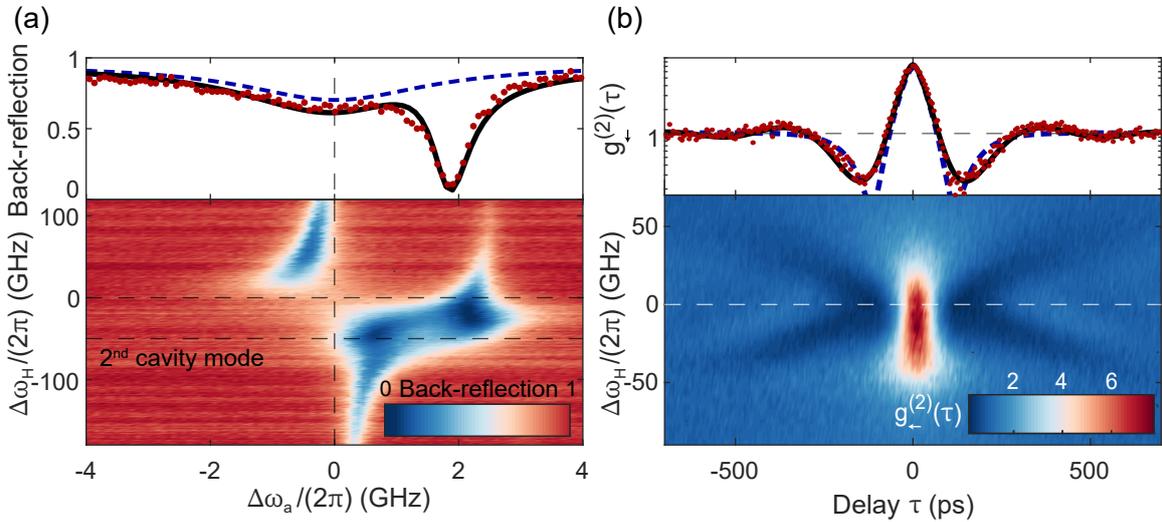


Figure 3.3: Back-reflection mode (a) Top: back-reflection signal as a function of QD detuning at resonance with the cavity H . The absence of a deep dip when the strongly coupled dipole $|a\rangle \leftrightarrow |g\rangle$ is resonant is a signature of chiral coupling. The deep dip appears off-resonant due to reduced coupling efficiency ($\beta \sim 0.5$). The dashed blue line is the simplified model for comparison. Bottom: back-reflection signal as a function of QD and cavity detuning. The dashed vertical line shows the QD resonance and is used for the measurements in (b). The horizontal lines indicate the two cavity modes. (b) Top: second-order correlation function $g_{\pm}^{(2)}(\tau)$ as a function of τ at the resonance of H . Anti-bunching is observed at ± 133 ps delay and bunching at zero delay, a signature of photons strongly correlated in time. The dashed blue line is the simplified model for comparison. Bottom: $g_{\pm}^{(2)}(\tau)$ measurement as a function of τ and the cavity detuning. The highest bunching is slightly off-resonant to the cavity due to the influence of the second cavity mode. The dashed line marks the cavity resonance, at which the cut-through is extracted.

Away from the cavity and QD resonances, in Fig. 3.3a, the back-reflection can still vanish as a consequence of reduced β -factor ($\beta \simeq 0.5$),¹⁰⁰ losses and coupling to the V cavity mode and QD transition.

We now turn to the correlation function $g_{\zeta}^{(2)}(\tau)$, in Fig. 3.3b which shows bunching at zero delay $g_{\zeta}^{(2)}(0) = 7.3$ followed by anti-bunching at finite delay $g_{\zeta}^{(2)}(\tau_0 = 133\text{ps}) = 0.25$. Here, the anti-bunched statistics have a different origin than the ones observed in the transmission mode experiments. The observation of an exponential decay of $g_{\zeta}^{(2)}$ in Fig. 3.3b are consistent with the formation of bound states further discussed in Ch. 5: a few photons are pulled together in time to form a highly correlated photonic state.^{120,125} Similar to the transmission mode experiment, the intensity correlations can be described using a RC state for the field in the cavity, displaced by the light that is directly reflected by the cavity. This results in $g_{\zeta}^{(2)}(\tau) = |\langle \hat{b}_{\text{H}} \rangle_{\tau} / \langle \hat{b}_{\text{H}} \rangle_{\infty}|^2$, where the averages are computed from the RC state and $\hat{b}_{\text{H}} = \hat{a}_{\text{H}} - i\varepsilon/\sqrt{\kappa}$. A simplified scenario with $\theta = 0$ again allows the qualitative features of the data to be understood. The simplified model reduces to a TLS in a single mode, single port cavity and we find

$$\frac{\langle \hat{b}_{\text{H}} \rangle_{\tau}}{\langle \hat{b}_{\text{H}} \rangle_{\infty}} = 1 - \frac{(2\beta)^2}{(1-2\beta)^2} e^{-\frac{\gamma\tau}{2(1-\beta)}}. \quad (3.4)$$

Thus, the observed field changes sign upon detecting a photon if $\beta > 1/4$. When going back to steady state, the output field vanishes at time $\gamma\tau_0 = 2(1-\beta) \ln\left(\frac{(2\beta)^2}{(1-2\beta)^2}\right)$. Figure 3.3b also contrasts the simplified scenario (dashed-blue), with the complete theoretical model (solid-black) and indicates that the reduced anti-bunching and the oscillations are due to the coupling to the V-mode, which makes the splittings $\delta_{\text{cav/QD}}$ relevant and introduces loss channels. Away from $\Delta\omega_{\text{H}} = 0$, the slight asymmetry between positive and negative cavity detuning in the bottom of Fig. 3.3b has its origin in the second cavity mode and the total Purcell factor being different depending on the direction of the detuning. The anti-bunched regions are pushed to higher time delays for a detuned cavity.

3.5 Discussion

We have established efficient coupling between a QD and a microcavity by virtue of which this system acts as an atom with giant optical cross-section. The consequence of such a large cross-section is that the QD behaves radically differently depending on the number of photons that interact with it within its lifetime. This is reflected in the very strong bunching of photons in the transmission mode measurements, where mainly multi-photon states are allowed to pass through the QD, while single-photon states are routed to other optical modes. Such a photon-number discriminating interaction enables photon-photon interactions at the fundamental limit of single photons to be studied and may find application in studying many-body phenomena¹²⁶ in a controllable setting. The overall transmission of the setup, from the input fibre to the output fibre is high, about 57%, and can allow these systems to be cascaded to study the interaction between photons mediated by multiple artificial atoms in series. One practical implementation could be to use time-delayed feedback of photons to mimic the interaction between photons and multiple quantum emitters, which can enable generating exotic bound states involving many photons.¹²⁵ Another potential application of this system is building blocks such as photon sorters^{102,127-129} and quantum gates between photons.^{130,131}

4

A chiral one-dimensional atom using a quantum dot in an open microcavity

Adapted from:

N. O. Antoniadis, N. Tomm, T. Jakubczyk, R. Schott, S. R. Valentin, A. D. Wieck, A. Ludwig, R. J. Warburton and A. Javadi
“**A chiral one-dimensional atom using a quantum dot in an open microcavity**”,
npj Quantum Inf. **8**, 27 (2022) ⁱ

4.1 Summary

In a chiral one-dimensional (1D) atom, a photon propagating in one direction interacts with the atom; a photon propagating in the other direction does not. Chiral quantum optics has applications in creating nanoscopic single-photon routers, circulators, phase-shifters and two-photon gates. Here, we implement chiral quantum optics using a low-noise quantum dot (QD) in an open microcavity. We demonstrate the non-reciprocal absorption of single photons, a single-photon diode. The non-reciprocity, the ratio of the transmission in the forward-direction to the transmission in the reverse direction, is as high as 10.7 dB. This is achieved by tuning the photon-emitter coupling *in situ* to the optimal operating condition ($\beta = 0.5$). Proof that the non-reciprocity arises from a single quantum emitter lies in the photon statistics – ultralow-power laser light propagating in the diode’s reverse direction results in a highly bunched output ($g^{(2)}(0) = 101$), showing that the single-photon component is largely removed.

ⁱN.O.A. carried out the experiments with help from N.T. and A.J. R.S., A.D.W., and A.L. designed and drew the semiconductor heterostructure. N.T. fabricated the top mirror, passivated the sample, and assembled the cavity setup. N.T. and T.J. characterised the top mirror. NOA developed the theoretical model and analysed the data. A.J. and R.J.W. conceived the idea and supervised the project. N.O.A., A.J., and R.J.W. wrote the manuscript with input from all the authors

4.2 Introduction

In a non-chiral 1D atom, an atom is coupled equally to a right-propagating and to a left-propagating mode in a single-mode waveguide. There are two input/output ports, one on the left (port 1) and one on the right (port 2). In the ideal limit (perfect atom with $\beta = 1$, where β is the probability that the excited atom emits a photon into the waveguide mode, a single photon at the input in resonance with the atom and upper-level dephasing of the two-level atom is negligible), the atom acts as a perfect mirror: the reflectivity is $R = 1$; the transmission $T = 0$.^{51,122} This changes completely in a chiral 1D atom: R and T depend on the propagation direction, left-to-right ($1 \rightarrow 2$) or right-to-left ($2 \rightarrow 1$), i.e. the system exhibits non-reciprocity ($T_{1 \rightarrow 2} \neq T_{2 \rightarrow 1}$). There are two simple cases.⁵² First, for $\beta \simeq 1$, the atom now becomes perfectly transparent ($T_{1 \rightarrow 2} = 1$, $T_{2 \rightarrow 1} = 1$, $R_{1 \rightarrow 1} = 0$, $R_{2 \rightarrow 2} = 0$). In one direction, the $2 \rightarrow 1$ -direction, say, the photon is phase-shifted by π via the interaction with the atom; in the other direction, $1 \rightarrow 2$, the photon phase-shift is zero. Second, for $\beta = \frac{1}{2}$, in the $2 \rightarrow 1$ -direction, the photon is scattered by the atom into non-waveguide modes – the photon is absorbed – such that $T_{2 \rightarrow 1} = 0$ and $R_{2 \rightarrow 2} = 0$, whereas in the $1 \rightarrow 2$ -direction, the photon does not interact with the atom, $T_{1 \rightarrow 2} = 1$ and $R_{1 \rightarrow 1} = 0$.

Chiral quantum optics has been implemented by using a single emitter in a nano-engineered waveguide, for instance a Rb atom in the evanescent field of a dielectric nanofibre,^{97,132} or a semiconductor QD in a waveguide.^{133–135} In the semiconductor case, β -factors can be high in nano-beam structures and particularly high in photonic-crystal waveguides. The system becomes chiral provided the QD is located off-centre in a nano-beam;¹³⁵ and at the centre of an inversion-asymmetric photonic-crystal waveguide.¹³³

We report here a different approach to engineering a chiral 1D atom. A single-mode optical fibre constitutes the waveguide on the *left* of the QD; another single-mode optical fibre constitutes the waveguide on the *right* of the QD; the atom itself is a QD in a low-volume one-sided microcavity, where the microcavity is coupled with high efficiency to the single-mode fibres. Chirality is induced by applying a magnetic field to a neutral QD: the QD's σ^+ -transition couples to the microcavity and is addressed with σ^+ -polarised photons. The advantage of this approach is that the resonant microcavity boosts the light-matter interaction in a controllable way: the β -factor can be tuned from small to extremely high values (99.7% has been achieved⁴⁸). Also, the good mode-matching¹⁹ implies that a high-efficiency, fibre-coupled platform for chiral quantum optics can be constructed.

Here, we implement the chiral scheme with $\beta = \frac{1}{2}$. In one direction, a single photon is transmitted; in the other direction, the photon is absorbed, Fig. 4.1a. We call this device a *single-photon diode* in analogy to its electronic counterpart. The challenge is twofold: to achieve exactly the right β ; and to achieve a close-to-perfect (transform-limited) QD. These challenges were met: we achieve an isolation of 10.7 dB, the highest non-reciprocal response recorded with a single quantum emitter. In addition, the high overall efficiency¹⁹ enables us to observe optical nonlinearities already at an input power of just 100 pW. The quantum nature of this nonlinearity is validated by observation of photon bunching by a factor of 101 compared to that of a laser field.

4.3 The working principle of the single-photon diode

Figure 4.1b shows a schematic of the setup and the operation principle of the diode. The optical setup consists of a polarising beam-splitter (PBS) and a quarter-wave plate (QWP,

$\lambda/4$) set at 45° with respect to the polarising beam-splitter axes. Consequently, light propagating in the forward direction is mapped to a left-handed field at the input of the microcavity, while light propagating in the backward direction is mapped to a right-handed field at the microcavity input, thereby creating the spin-momentum locking. The microcavity (Fig. 4.1b) comprises a highly reflective *bottom* mirror and a much less reflective *top* mirror.¹⁹ The top mirror is a dielectric distributed-Bragg-reflector deposited on a crater in a silica substrate with a radius-of-curvature of $11\ \mu\text{m}$. The bottom mirror is a semiconductor distributed-Bragg-reflector on top of which InAs QDs are embedded in an n-i-p diode in the heterostructure. The open nature of the microcavity allows the lateral position of the QDs to be controlled precisely with respect to the anti-node of the microcavity. The cavity mode has a Gaussian intensity profile centred around the crater. The coupling between the cavity and the QD is maximum when the QD is placed at the centre of the cavity mode. Figure. 4.1c shows the resonance fluorescence of a QD as a function of its lateral position.

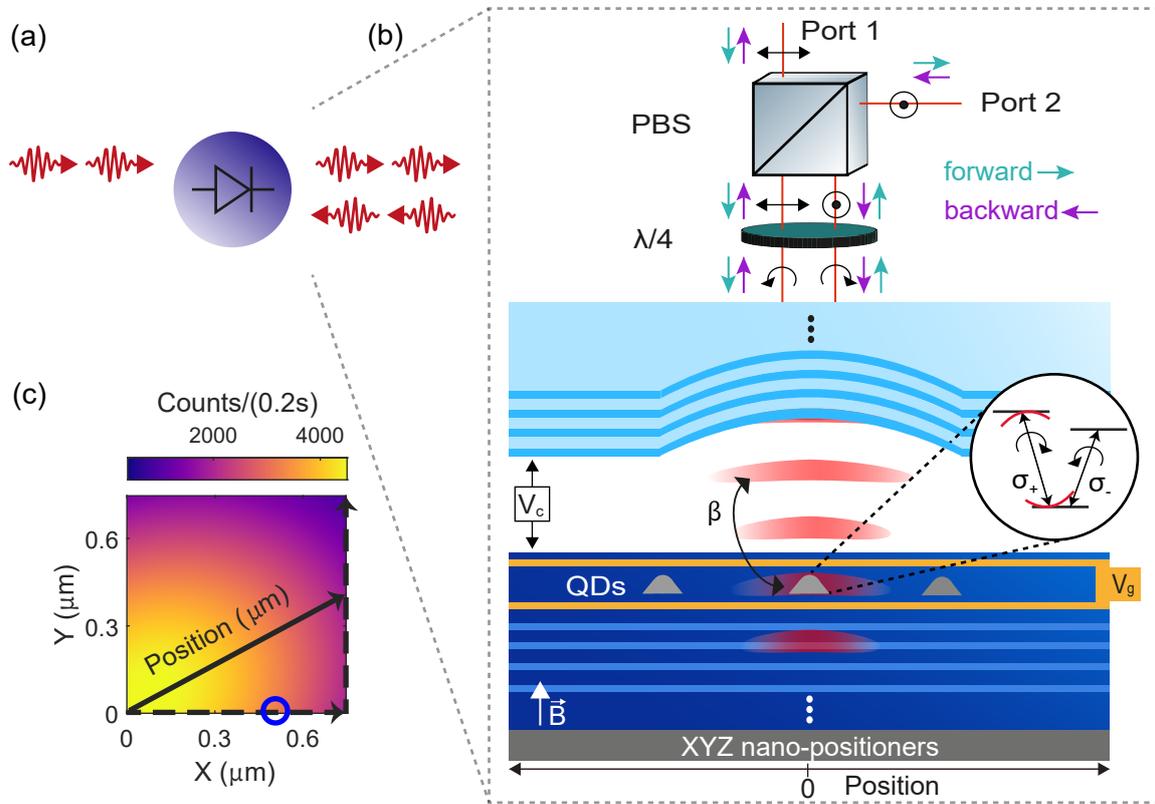


Figure 4.1: Schematic and operating principle of the chiral 1D atom (a) The optical system showing the two input/output ports. (b) Illustration of the open microcavity. The heterostructure consists of a GaAs/AlAs distributed Bragg reflector (the *bottom* mirror) and self-assembled InAs QDs embedded in an n-i-p diode. Nano-positioners allow precise tuning of both microcavity frequency (via z) and also the β -factor by positioning the QDs with respect to the anti-node of the microcavity (via xy). An external magnetic field of 2.0 T splits the neutral QD into two circularly-polarised transitions. The polarisation of the light is controlled by a PBS and a QWP in the microscope. The σ^+ -polarised exciton creates a photon in the microcavity with probability β . (c) Intensity of resonance fluorescence as a function of the displacement of the QD from the cavity mode centre. The position is defined as the distance from the anti-node with respect to the top mirror of the cavity, i.e. $r = \sqrt{X^2 + Y^2}$. We apply a bias to the x and y nanopositioners to move the semiconductor sample. The applied voltages are translated to distance using the specifications from the manufacturer (attocube systems AG). The position used in most of the measurements of this chapter ($\beta \approx 0.5$) is indicated with a blue circle.

The origin of the coordinate system corresponds to the centre of the cavity mode. The fluorescence from the QD drops as it is displaced from the origin, which shows that the coupling efficiency between the cavity and the QD is reduced. Therefore, the tunability of the lateral position of the QD with respect to the cavity anti-node allows *in situ* tuning of the β -factor. This position dependence can be used to achieve $\beta = 0.5$ with high precision. A position with $\beta = 0.5$, used in most measurements, is indicated by the blue circle in Fig. 4.1c. Furthermore, adjusting the distance between the bottom mirror and the top mirror provides precise control over the microcavity's frequency, enabling the QD's σ^+ -polarised exciton and the microcavity to be brought into spectral resonance.

We define the transmission as the propagation through the entire diode, i.e. from port 1 to 2 (2 to 1) in the forward (backward) direction. Ideally, the transmission in the forward direction $T_{1 \rightarrow 2}$ is unity as the left-handed optical field is orthogonal to the dipole-moment of the QD, i.e. there is no interaction. In the backward direction, the transmission amplitude is given by $t_{2 \rightarrow 1} = 1 - 2\beta$ where β is the β -factor describing the interaction of the σ^+ -polarised exciton with an empty microcavity. The full transmission in the backward direction is $T_{2 \rightarrow 1} = |t_{2 \rightarrow 1}|^2 = |1 - 2\beta|^2$. In the over-coupled regime, $\beta \approx 1$, the backwards-propagating photons receive a π -phase shift as they transit through the coupled system. At the critical coupling, $\beta = 0.5$, the light reflected by the QD interferes destructively with the light directly reflected from the microcavity and the transmission through the system vanishes; instead, the photons are scattered into non-microcavity modes.

4.4 Experimental details and characterisation of the diode

4.4.1 Cavity characterisation

For the described scheme to operate, the microcavity itself should not rotate the polarisation. However, the fundamental microcavity mode is typically split into two modes with orthogonal

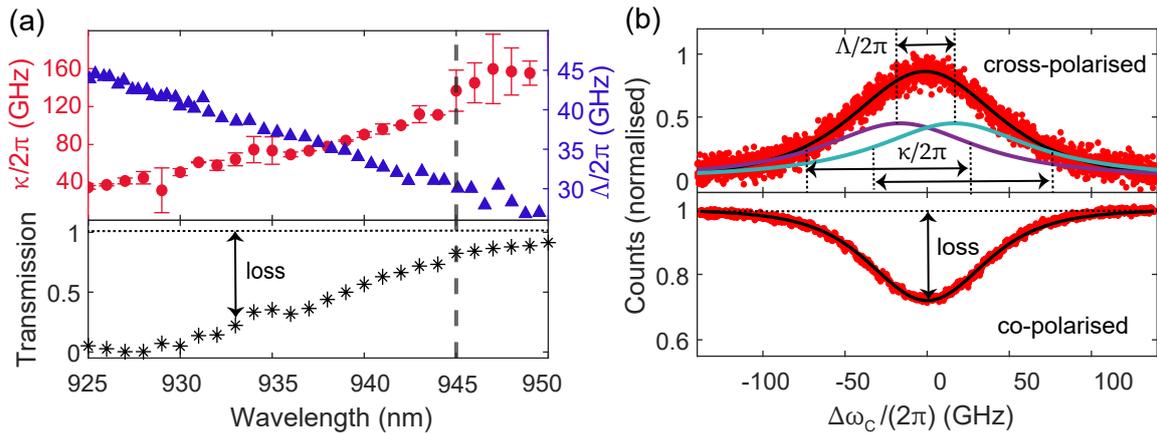


Figure 4.2: Characterisation of the cavity parameters without a QD. (a) Measured cavity decay rate ($\kappa/(2\pi)$, red circles) and mode-splitting ($\Delta/(2\pi)$, blue triangles) versus wavelength. The transmission through the one-sided cavity on resonance with the cavity mode (black stars) is calculated with these two parameters and Eq. 4.1. The transmission increases, i.e. the loss decreases, with increasing wavelength. (b) The measured transmission through the cavity mode in the cross- (top) and co-polarised (bottom) configuration at a wavelength of 945 nm versus the detuning of the cavity frequency. The peak in cross-polarisation is fitted with the response of the two linear cavity modes (H and V) that are plotted in purple and turquoise. The cavity dip was modelled using the parameters from (a).

linear polarisations, a consequence of a birefringence in the semiconductor heterostructure.¹³⁶ This means, we should work in a regime, where in order to maximise the overlap of the two cavity modes, this mode-splitting is minimised while the cavity linewidth is enhanced. By measuring the cross-polarised¹³⁷ transmission through the bare cavity setup (from port 2 to port 1 in Fig. 4.1b) and fitting a square of a double-Lorentzian to the data, we can characterise the decay rate, $\kappa/(2\pi)$, and the mode-splitting, $\Lambda/(2\pi)$, of the cavity; see the top panel in Fig. 4.2b for an example of the transmission spectrum. The top panel in Fig. 4.2a shows κ and Λ as a function of wavelength; Λ decreases for higher wavelength while κ increases.¹³⁶

We operate at a wavelength of 945 nm where the mode-splitting is on the order of 29 GHz and $\kappa/(2\pi) = 102$ GHz such that the mode-splitting is much smaller than the linewidth of the microcavity, and the microcavity mode is nearly degenerate. The microcavity losses are dominated by the transmission through the top mirror, i.e. $\kappa_{\text{top}} \gg \kappa_{\text{bottom}}$, an effect that we evaluate by comparing κ to the cavity losses reported in Ref. ¹³⁸ which were measured with the same bottom mirror but with a highly reflective top mirror. We conclude that $\kappa \approx \kappa_{\text{top}}$, i.e. close to all losses arise via transmission through top mirror for all wavelengths, assuring that the cavity is indeed one-sided in the full range of wavelengths presented.

4.4.2 Insertion losses

It is important to note, that in the described regime, the residual mode-splitting acts as an overall loss channel and does not limit the non-reciprocity of the system; it mostly affects the insertion loss of the system (here 1.5 dB). In order to optimise the operation of the diode, we evaluate the insertion losses induced by the cavity mode-splitting as a function of wavelength.

Neglecting interaction terms in Eq. B.10 in App. B.2, we can calculate the transmission through both cavity modes in the co-polarised configuration as:

$$T = \left| 1 - \frac{1}{1 + 2i(\Delta\omega + \Lambda/2)/\kappa} - \frac{1}{1 + 2i(\Delta\omega - \Lambda/2)/\kappa} \right|^2. \quad (4.1)$$

Using Eq. 4.1 and κ and Λ extracted above (shown in the top panel of Fig. 4.2a), we calculate the transmission from port 2 to port 1 for circularly polarised light at different laser frequencies for $\Delta\omega = 0$, i.e. the laser frequency lies exactly between the two cavity modes (bottom panel of Fig. 4.2a). We observe that the mode-splitting induces an overall loss in the transmission, which increases for decreasing frequency, i.e. decreases with increasing wavelength. Eventually, the transmission reaches unity at low frequencies (high wavelengths).

In order to reduce the insertion loss, working at high wavelengths, i.e. above 950 nm, seems obvious. However, as is explained in more detail in Fig 4.5, we are limited by the maximum achievable β -factor in a specific QD, which as well is depending on the emission wavelength of the QD. Given these constraints, we determined 945 nm to be an ideal wavelength to carry out the experiments. Figure 4.2b shows the cross-(top) and co-polarised (bottom) cavity transmission for this optimised operation-wavelength. The co-polarised data could be reconstructed using the extracted cavity parameters of Fig. 4.2a and Eq. 4.1.

4.4.3 Quantum dot characterisation

The Purcell factor, F_p , is a critical parameter characterising the operation of our diode. It is defined through $\Gamma_{\text{tot}} = (1 + F_p)\gamma$, where Γ is the overall linewidth of the QD, and γ is the linewidth of the QD outside the cavity. The linewidth of a bare QD is typically $\gamma/(2\pi) \approx 300$ MHz, as measured in Ref. ¹⁹ We estimate the Purcell-enhanced linewidth of the QD by measuring the resonance fluorescence spectrum from the QD. Figure 4.3a shows a sample spectrum from a QD placed in the centre of the cavity. We extract $\Gamma_{\text{tot}}/(2\pi) = 1.2$ GHz by fitting two Lorentzians to the data. The observed Purcell factor is $F_p = 3$, matching predictions from COMSOL simulations shown in Fig. 4.5.

The two peaks in Fig 4.3a show the fine-structure splitting of the optical transition. Under a magnetic field along the growth direction (Faraday geometry), the transitions become circular (see inset in Fig. 4.1a for the level structure). An out-of-plane magnetic field of 2.0 T splits the right-handed and left-handed transitions by 63 GHz, enough that only one transition interacts with the laser; here, the right-handed dipole σ^+ , as seen in Fig. 4.3b. The two curves in Fig. 4.3b show the photoluminescence signal of the QD for different positions of the QWP, hence, for different detection polarisations. The purple (turquoise) line represents the QWP setting where the incoming light matches the lower (higher)-wavelength transition. Therefore, only signal from the corresponding transition is collected. The data in Fig. 4.3b were taken on a different QD to that used in the rest of this chapter, but they show the principle of operation.

While operating in a magnetic field, we observed a nuclear-spin related effect in the transmission data, see Fig. 4.4. We found that the transmission depends on the scanning direction of the gate voltage and is asymmetric around the resonance of the QD. In order to overcome these so-called dragging and anti-dragging effects, the gate voltage was switched rapidly (100 Hz) between the resonance voltage and the co-tunnelling voltage using a square function from an arbitrary waveform generator. In the co-tunnelling regime, an QD electron is exchanged with an electron in the Fermi sea, randomising the electron's spin state and eliminating the spin polarisation of the nuclei.⁸⁰ Transmission data were acquired only when

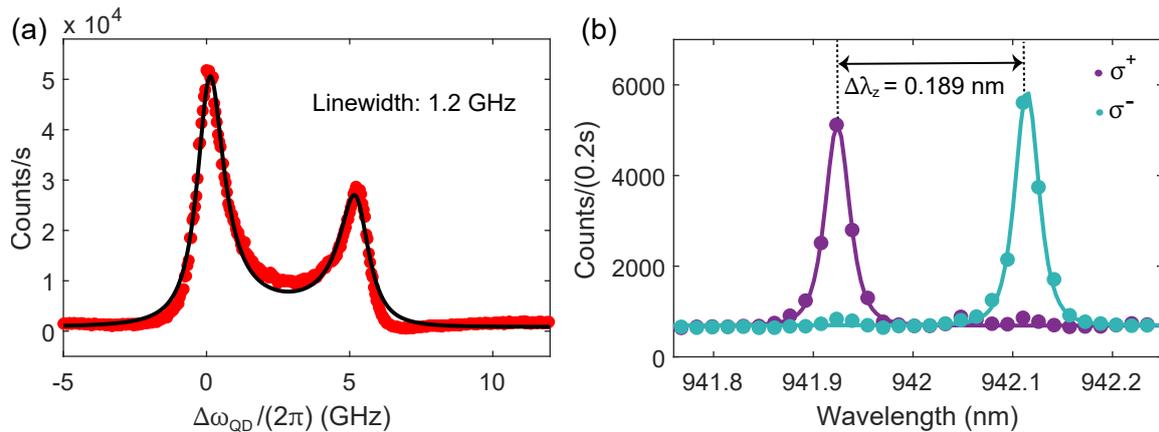


Figure 4.3: Characterisation of the QD (a) Resonance fluorescence from an over-coupled QD in the microcavity in the cross-polarised configuration at 0.0 T. The Purcell-enhanced linewidth is 1.2 GHz, corresponding to $\beta = 0.72$. (b) Photoluminescence spectrum of the QD in a magnetic field of 2.0 T. A Zeeman splitting of 0.189 nm (63 GHz) is observed. The lower wavelength (purple), i.e. higher frequency, transition was used for all measurements. The two curves were measured by changing the angle of the QWP between the two circular configurations.

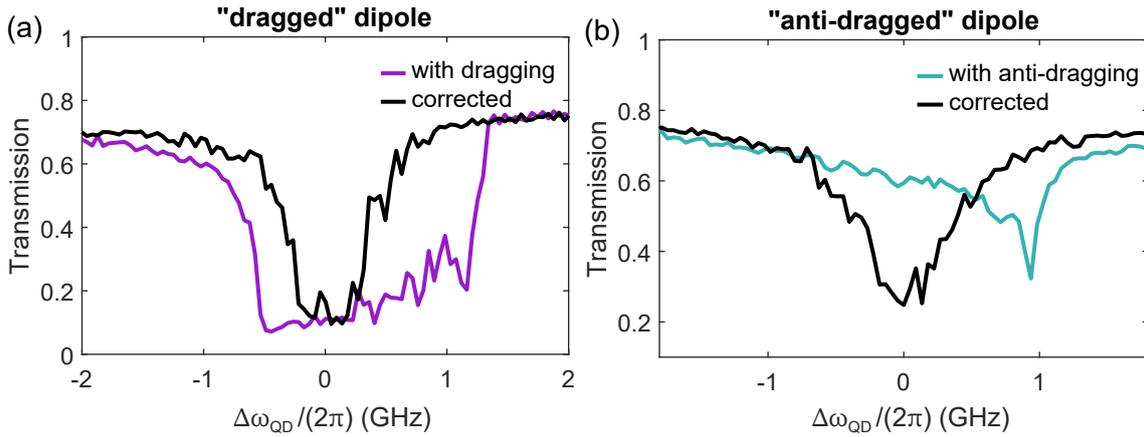


Figure 4.4: Overcoming nuclear spin induced effects (a)/(b) Transmission through the diode as a function of QD detuning for the high/low energy transition. The so-called *dragging* and *anti-dragging* effects (purple/turquoise lines) are overcome (black lines) by jumping back and forth between the measurement voltage and a voltage in the co-tunnelling regime.

the gate voltage was at the resonance voltage. The procedure to overcome nuclear spin effects was applied for all transmission data shown in this chapter.

4.4.4 Wavelength dependence of β -factor and highest observable contrast

The coupling efficiency between the QD and the cavity mode is given by the β -factor that has a wavelength dependence arising from the dispersion of the top and the bottom mirrors. We simulate this dependence by calculating the mode volume and the quality factor of the

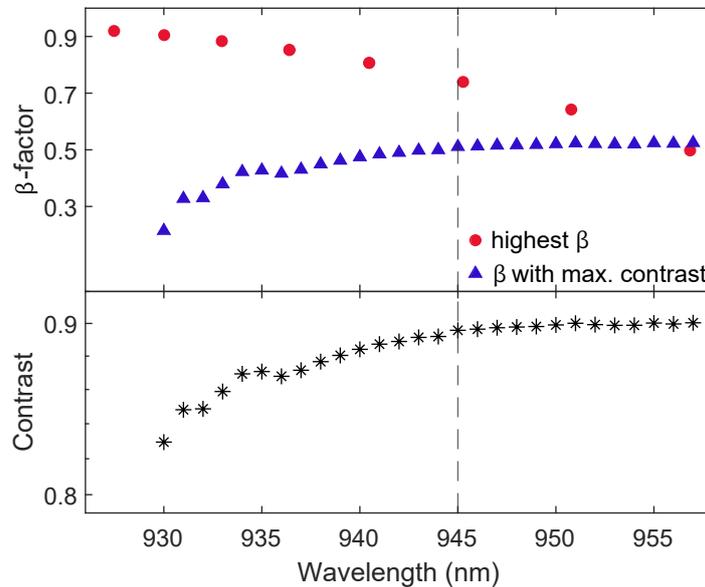


Figure 4.5: Wavelength dependence of the β -factor. COMSOL simulations (red circles) show the maximum achievable β for a QD positioned in the centre of the cavity. At wavelengths above 955 nm, the critical β of 0.5 is not reachable. Calculations using the model in App.B.1 enable us to predict the maximal contrast achievable for different wavelengths (black stars) and the optimal β -factor to observe the strongest contrast (blue triangles). The range between 945 and 955 has the highest contrast at $\beta = 0.5$ and is therefore ideal. The experiments in the main text were carried out at 945 nm (vertical line).

cavity in COMSOL. The results are shown in Fig. 4.5. The β -factor for a central QD drops with increasing wavelength and falls below 0.5 at a wavelength of 955 nm. This effect arises from the fact that the centre of the stop-band for the top and the bottom mirrors are 920 nm. Away from 920 nm the reflection of the top mirror drops and results in a reduced quality factor and, hence, a reduction in the β -factor.

Using the model derived in App. B.1, Λ and κ extracted above, and leaving β a free parameter, we estimate the highest observable contrast $(1 - T^0/T^\infty)$ for each wavelength (bottom part of Fig. 4.5) and extract the β at which it is maximised (top panel in Fig. 4.5). The achievable contrast is nearly constant between 945 and 955 nm, giving a broad range of QDs to work with. This also shows that the insertion losses do not influence the isolation (as mentioned above), i.e. non-reciprocity, of the system, but only describe overall losses. We chose an emitter at 945 nm, as the maximum β is above the critical value of 0.5, and the position dependence of β can be exploited to tune the system into the critical coupling conditions.

4.5 Results

4.5.1 Tuning the β -factor to the ideal limit

The transmission of the diode is probed with coherent laser light at very low powers, a regime dominated by single-photon components. We exploit the β -factor's dependence on the lateral position of the QD with respect to the centre of the microcavity to tune the system to the critical-coupling condition. Figure 4.6 shows the transmission in the backward direction, $T_{2 \rightarrow 1}$, as a function of the QD frequency for three different positions, i.e. three different β -factors. The orange data points show the transmission for the QD centred in the

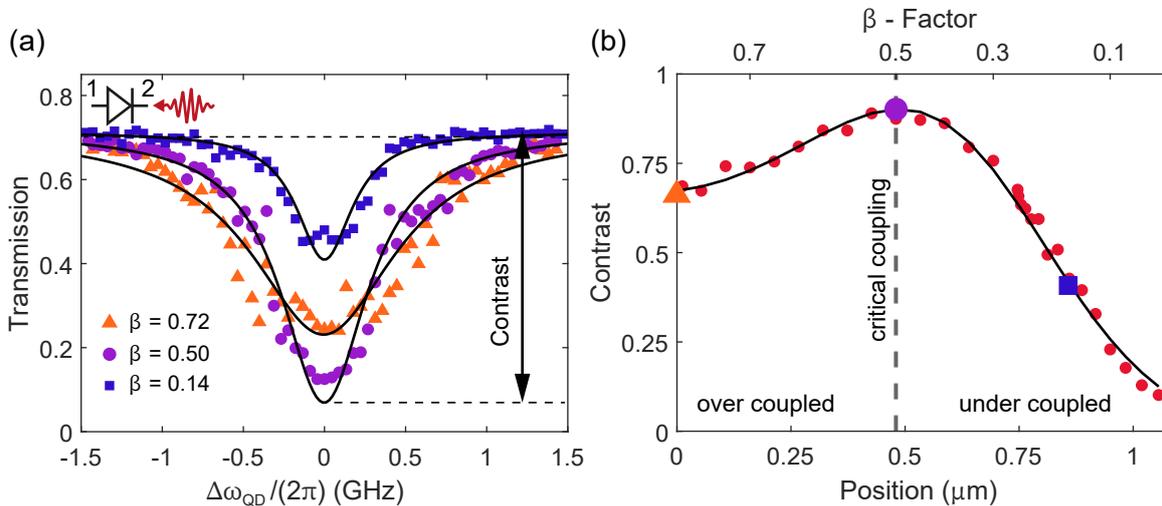


Figure 4.6: Schematic and operating principle of the chiral 1D atom (a) Transmission from port 1 to port 2 versus QD detuning for three different lateral positions of the QD: orange triangles ($\beta \approx 0.72$), purple circles ($\beta \approx 0.50$) and blue rectangles ($\beta \approx 0.12$). The solid lines are theory curves. The off-resonant transmission is limited to 0.7 by the residual non-degeneracy of the microcavity. The transmission is defined without taking into account the losses in the optical setup. The overall end-to-end throughput of the setup, taking into account all the optical elements and the fibre-coupling, is 56%: this corresponds to $T = 1$. (b) Contrast in the transmission as a function of the lateral position. Coloured data-points indicate the positions used in (b). The black solid line is the theory.

microcavity. For this position we extract $\beta = 0.72$, matching well the theoretical expectations for the maximum achievable β at this wavelength.

The β -factor is evaluated via the linewidth and the contrast of the dip. When the QD is laterally displaced such that $\beta = 0.50$ (purple data points), the $T_{2 \rightarrow 1}$ is lowest: $T_{2 \rightarrow 1} = 0.07$. Also, the linewidth of the QD transition decreases with decreasing β due to a reduced Purcell-enhancement. We define the transmission contrast as one minus the ratio between transmission on resonance and the transmission far off-resonance with the QD ($1 - \frac{T_{2 \rightarrow 1}^0}{T_{2 \rightarrow 1}^\infty}$). The transmission contrast is measured while scanning the lateral position of the QD relative to the microcavity's optical axis (Fig. 4.6b). For a well-centred position, the contrast in the transmission is around 0.67, increasing to a value of 0.9 as β approaches 0.5, and decreasing as β is further reduced. The solid black lines in Fig. 4.6a,b are the theoretically expected behaviour. (A comprehensive model for transmission through a two-level system coupled to a non-degenerate one-sided microcavity is derived and discussed in detail in App. B.1.) An average spectral fluctuation of the QD of 40 MHz was found by comparing the theoretical model and the measurements.⁶⁶

4.5.2 Non-reciprocal transmission of the single-photon diode

The non-reciprocal nature of the diode is demonstrated by measuring the transmission in both directions at the over-coupled and critical-coupling conditions. The top panels of Fig. 4.7 shows the transmission through the diode in the backward direction as a function of the microcavity detuning and the QD detuning.

In the over-coupled situation (Fig. 4.7a), the strongest contrast appears when the QD is spectrally detuned from the cavity resonance (contrast 0.89, red circles); the Purcell factor, F_p , hence also β , decrease as a function of cavity detuning. In this case, the isolation resulting from the detuned QD-cavity system is 11.2 (10.5 dB).

Figure 4.7b shows the diode configuration, i.e. the critical coupling condition. The transmission contrast shown in these maps decreases with microcavity detuning on account

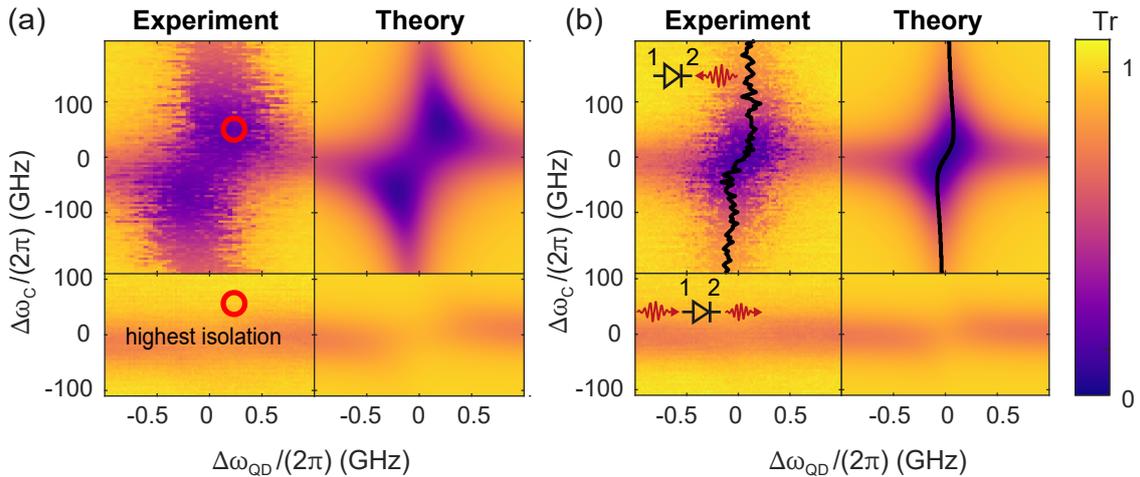


Figure 4.7: Non-reciprocal response of the diode. Transmission through the system versus QD and microcavity detuning for the backward (top panels, port 1 to 2) and forward (bottom panels, port 2 to 1) directions for $\beta = 0.72$ (a) and $\beta = 0.5$ (b). Experimental data (left) and theory (right) show an excellent match. The black lines show the Lamb shift of the QD resonance induced by the vacuum field of the microcavity.

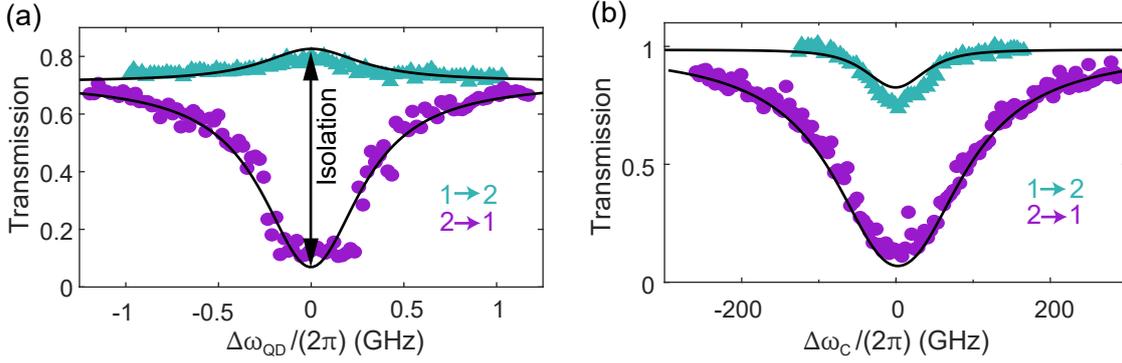


Figure 4.8: Non-reciprocal response of the diode. (c),(d) Transmission through the diode on resonance with the microcavity/QD in the forward and the backward direction versus QD/cavity detuning. The purple and turquoise data are cut-throughs of (a) (2→1) and (b) (1→2). The black solid lines are the theory

of a reduced β -factor. On the contrary, the transmission in the forward direction (Fig. 4.7, bottom panels) presents an almost flat behaviour independent of the detuning from the QD's resonance. The panels on the right side of Fig. 4.7a,b show the theoretically predicted behaviour from our model (App. B.2) A comparison of the transmission in the forward and backward directions at critical coupling as a function of the QD (microcavity) detuning is shown in Fig. 4.8a,b. At resonance, the transmission in the forward direction is around 0.82. The slight increase in the transmission signal in the forward direction is attributed to the mode-splitting based on the theoretical model (see App. Fig B.1). A figure of merit for a diode is the isolation. It is defined as $T_{1\rightarrow 2}/T_{2\rightarrow 1}$ and found to be a factor 11.9 (corresponding to 10.7 dB).

4.5.3 Nonlinearity of the single-photon diode

To prove that the non-reciprocity arises from a single emitter, we probe both the power dependence and the photon statistics of the output. In the power dependence, we find a striking nonlinearity of the transmission in the backward direction. Figure. 4.9a shows the transmission in the backward direction as a function of the optical power and detuning from the QD's resonance. On resonance with the QD (Fig. 4.9b), the backward transmission increases with a power-law dependence with a slope of one and is described by $T_{2\rightarrow 1}^0 = \frac{P/P_C}{1+P/P_C}$, where P is the input optical power and P_C the critical power. The experimental data in Fig. 3b match this behaviour very well for $P_C = 213$ pW. This behaviour is characteristic of the saturation of a two-level system – while the interaction between the input field and the QD is linear in power at very low powers, the QD saturates at higher input powers, which leads to a strong power-dependent transmission. The critical power is very close to the theoretically expected value of 198 pW (Eq. B.9 in App.B.2) This power level corresponds to an average photon flux of $\langle n \rangle = 0.27$ at the input of the microcavity per lifetime of the QD ($\tau_{\text{QD}} = 0.26$ ns).

The very low onset of the nonlinearity implies that the quantum statistics of the output field are affected by interaction with the QD.¹²³ We verify this by measuring the second-order auto-correlation function, $g^{(2)}(\tau)$, of the backward transmitted light.^{109, 112, 139, 140} The $g^{(2)}(\tau)$ was measured for three different powers (Fig. 4.10a). At the lowest power (5 pW), a very strong bunching of 101 is observed, proving that the single-photon components of the laser have been largely removed by the QD. With increasing power, the bunching

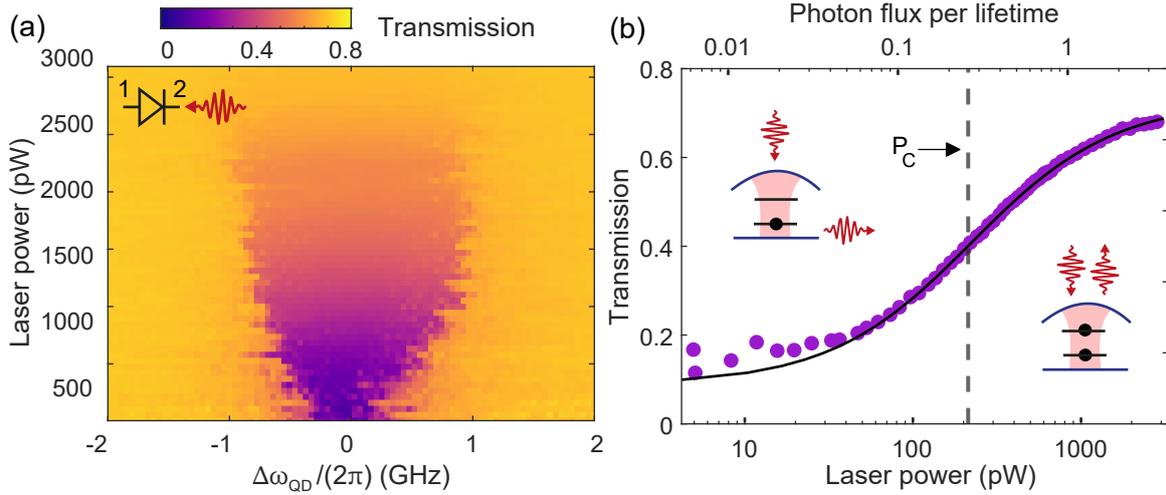


Figure 4.9: Nonlinear response of the diode. (a) Transmission on resonance with the microcavity versus QD detuning and optical input power. The transmission saturates at 0.7 on increasing the power. (b) Power dependence of the transmission on resonance with the QD. The black solid line corresponds to the theory. The insets illustrate absorption by the QD at small powers, and transmission at higher powers due to the increasing transparency of the emitter. The critical power is indicated with a vertical line.

decreases exponentially (inset Fig. 4.10a), corresponding exactly to the expected behaviour on saturating the QD: at high powers, most of the laser light is transmitted without interaction, resulting in $g^{(2)}(\tau) = 1$, the auto-correlation function of the laser light. Additionally, the auto-correlation function of the transmission in the forward direction is constant and unitary – this confirms the non-reciprocal transmission in the system (Fig. 4.10b). The measurements were modelled (see App. B.2) and the results are depicted as a solid black line in Fig. 4.10.

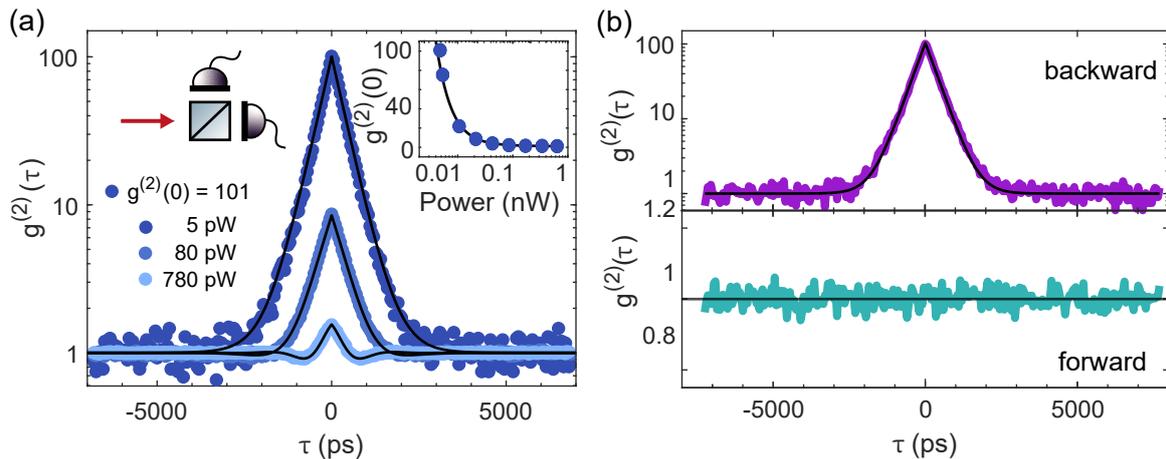


Figure 4.10: Nonlinear response of the diode. (a) Autocorrelation function of the backwards propagating light for three different input optical powers. At the lowest optical power (5 pW) a bunching of 101 is observed. As the power increases the bunching decreases exponentially (inset). (b) Auto-correlation function $g^{(2)}(\tau)$ for a critically-coupled QD-cavity system for the two propagation directions. Top: Backward direction showing a high bunching of 101. Bottom: Forward direction showing a flat curve indicating that in the forward direction there is no interaction between the photons and the QD such that the light remains coherent after passing through the cavity. The input power is around 5 pW. The black, solid lines are based on the model in Eq. B.18.

We emphasise that all the data in Figs. 4.7, 4.8, 4.9, 4.10 are modelled with the same set of parameters, in particular $\beta = 0.72$ or $\beta = 0.50$, a free-space decay rate $\gamma_0/(2\pi) = 300$ MHz, $\kappa/(2\pi) = 102$ GHz, $\Lambda/(2\pi) = 29$ GHz, and a spectral fluctuation of $\delta_{\text{sf}}/(2\pi) = 35$ MHz.

4.6 Discussion

The reported experiments reveal a strong non-reciprocal and highly nonlinear transport of optical photons through a QD-microcavity system. Model calculations based on the canonical chiral 1D atom describe the system extremely well. The single-photon diode is realised with a modest emitter-microcavity coupling, $\beta = 0.5$. We can foresee a range of applications. For example, the non-reciprocal behaviour can be dynamically controlled by driving the σ^- transition, by using the spin-state of a charge carrier in the QD, or by fast Stark tuning of the QD, opening possibilities for optical switches and transistors.^{102,117,129,141,142} Theory predicts that the strong bunching of the photons in the transmission of the system presages the formation of a two-photon bound state – it is a first step in creating exotic photonic states and simulating many-body dynamics using photons^{126,143–145} as is demonstrated and further discussed in Ch. 5. The performance of the system can be further improved by eliminating the mode-splitting of the microcavity. The mode-splitting can be minimised, perhaps eliminated, by exploiting the electro-optic effect¹⁴⁶ or by applying uni-axial stress to the semiconductor heterostructure.¹³⁶ This would not only reduce the insertion losses but also bring the regime $\beta = 1$ within range. Such a device would be ideal for achieving a single-photon phase-shifter and has a strong potential for deterministic two-photon quantum gates, either by using spin-state of the QD or by exploiting photonic bound states.^{125,127}

5

Photon bound-state dynamics from a single artificial atom

Adapted from:

N. Tomm*, S. Mahmoodian*, [N. O. Antoniadis](#), R. Schott, S. R. Valentin, A. D. Wieck, A. Ludwig, A. Javadi and R. J. Warburton

“Photon bound-state dynamics from a single artificial atom”,
Nat. Phys. **19**, 857-862 (2023) ⁱ

5.1 Summary

The interaction between photons and a single two-level atom constitutes a fundamental paradigm in quantum physics. The nonlinearity provided by the atom leads to a strong dependence of the light-matter interface on the number of photons interacting with the two-level system within its emission lifetime. This nonlinearity unveils strongly correlated quasi-particles known as photon bound states, giving rise to key physical processes such as stimulated emission and soliton propagation. While signatures consistent with the existence of photon bound states have been measured in strongly interacting Rydberg gases, their hallmark excitation-number-dependent dispersion and propagation velocity have not yet been observed. Here, we report the direct observation of a photon-number-dependent time delay in the scattering off a single artificial atom — a semiconductor quantum dot (QD) coupled to an optical cavity. By scattering a weak coherent pulse off the cavity-QED system and measuring the time-dependent output power and correlation functions, we show that single photons, and two- and three-photon bound states incur different time delays, becoming shorter for higher photon numbers. This reduced time delay is a fingerprint of stimulated emission, where the arrival of two photons within the lifetime of an emitter causes one photon to stimulate the emission of another.

ⁱN.T., S.M., A.J. and R.J.W. designed the research and experiments. N.T. and N.O.A carried out the experiments. S.M. developed the theoretical model and simulations. N.T. and S.M. analysed the data. R.S., S.R.V., A.D.W. and A.L. fabricated the semiconductor device. N.T., S.M. and R.J.W. wrote the paper with input from all authors.

5.2 Introduction

Photons do not easily interact with one another. This property is commonly exploited to communicate over long distances using optical fibres. Interaction between photons is desired however for classical and quantum information processing, but requires a highly nonlinear medium. Optical nonlinear processes are employed in a range of photonic applications such as frequency conversion, optical modulation, light amplification, and sensing.^{104,147,148} In the limit where the optical nonlinearity is significant on the scale of a few photons, one can observe quantum nonlinear phenomena, for instance via the optical correlation functions.^{104–106} One manifestation of the nonlinearity is the presence of two and higher-order photon bound states. Photons in these bound states are strongly correlated such that the likelihood of observing a photon at any one time is fixed, but once one photon is detected, the arrival of another is much more likely than at a random time. We emphasise that photon bound states are distinct from bunched photon states as photon bound states are quasiparticles that have their own dispersion relation and are eigenstates of the underlying Hamiltonian that describes the nonlinear medium. It has recently been predicted theoretically that the photon-number-dependent propagation velocity of photon bound states can lead to the formation of highly-entangled, ordered states of light.¹²⁵ Photon bound states have been predicted to exist in a number of systems such as unidirectional waveguide quantum electrodynamics (QED)^{50,149,150} and strongly correlated Rydberg gases.¹⁴⁵ In the latter case, experimental observations consistent with their presence have been reported.^{118,119,151} A direct observation of their dynamics is however lacking. To observe directly the dynamics of photon bound states we examine the unidirectional propagation of few-photon wavepackets strongly interacting with a single atom, in practice a semiconductor QD coupled to a one-sided cavity.

5.3 Concept: Scattering dynamics via correlation functions

The experimental setup is schematically depicted in Fig. 5.1a: Gaussian pulses of light are guided via a circulator to the one-sided QD-cavity system. The light is back-scattered and redirected by the circulator towards a Hanbury Brown-Twiss (HBT) setup equipped with single-photon detectors that record the time of arrival τ of individual photons. By launching a weak coherent pulse with average photon number $\bar{n} \ll 1$, one can probe directly the scattering dynamics of single-photon pulses via power measurements $P(\tau) = G^{(1)}(\tau)$, which is proportional to the single-photon wavefunction $|\psi_1(\tau)|^2$. Conversely, the second-order correlation function $G^{(2)}(\tau_{ch1}, \tau_{ch2})$ is insensitive to the single-photon Fock component and is used to study two-photon scattering dynamics.¹⁵² $G^{(2)}(\tau_{ch1}, \tau_{ch2})$ is proportional to the squared amplitude of the two-photon wavefunction, $|\psi_2(\tau_{ch1}, \tau_{ch2})|^2$. We also measure the third-order correlation function $G^{(3)}(\tau_{ch1}, \tau_{ch2}, \tau_{ch3})$ to probe the dynamics of the three-photon component. For higher-order correlation functions, we can determine the equal-time correlators, i.e. when $\tau_{ch1} = \tau_{ch2} = \dots = \tau_{chn}$. For the coherent state the equal-time correlator is $G^{(n)}(\tau, \tau, \dots, \tau) = P(\tau)^n$. Deviations from this indicate that the photons undergo a nonlinear scattering process.

5.4 Results

5.4.1 One- and two-photon scattering eigenstates

Single-photon states and two-photon states undergo distinct dynamics when scattering off the cavity-QED system. We can understand these dynamics by examining the one- and two-photon scattering eigenstates. In our cavity-QED setup the QD couples almost perfectly to the cavity ($\beta = 93\%$, compare discussion Ch. 3), which in turn has small undesired losses ($\leq 5\%$; arising from losses via the bottom mirror, absorption and scattering losses¹³⁸) and we thus model our system as being lossless. The single-photon scattering eigenstates are plane waves that are transmitted through the system with a transmission coefficient^{122, 153, 154}

$$t_1(\Delta_L, \Delta_C) = \frac{\Delta_L - \Delta_C - g^2/\Delta_L - i\kappa/2}{\Delta_L - \Delta_C - g^2/\Delta_L + i\kappa/2}, \quad (5.1)$$

where $\Delta_L = \omega_L - \omega_{\text{QD}}$ is the angular frequency detuning of the photon and the QD, $\Delta_C = \omega_C - \omega_{\text{QD}}$ the detuning between the cavity resonance and the QD, g the atom-cavity coupling, and κ the cavity loss rate. Under the lossless assumption ($\kappa = 0$) the scattering amplitude is unitary, $|t_1| = 1$, but scattering imparts a frequency-dependent phase on the photon. The importance of the frequency-dependent phase is highlighted when scattering Gaussian pulses off the cavity-QED system. Defining $e^{i\phi_1} = t_1$ we then have $\phi_1 = -i \ln(t_1)$. As in standard Gaussian pulse propagation,¹⁵⁵ the first to third derivatives of ϕ_1 then give the delay $\Delta\tau_1(\Delta_L, \Delta_C)$, broadening and chirp, and distortion $d_1(\Delta_L, \Delta_C)$ of the Gaussian pulse upon scattering off the quantum system, respectively. On resonance ($\Delta_L = 0, \Delta_C = 0$), the delay is $\Delta\tau_1(0, 0) = 4/\Gamma$, where $\Gamma = 4g^2/\kappa$ is the Purcell-enhanced decay rate. The distortion is given by $d_1(0, 0) = -32(1 - 3\Gamma/\kappa)/\Gamma^3$.¹²⁰

The physics of two-photon scattering is richer as the energy of the individual photons is not necessarily conserved, which leads to photon correlations. The two-photon scattering matrix has previously been computed,^{153, 156} but here, we diagonalise the scattering matrix and show that the two-photon eigenstates contain a subspace of two-photon bound states (photonic dimers), see Ref.¹²⁰ for the full calculation. We find general semi-analytic forms for these states, but in the limit where κ is larger than all other rates and detunings in the system, the bound eigenstates have the simple form

$$\psi_E(x_c, x) = N e^{iEx_c} \left[e^{-\frac{\Gamma}{2v_g}(1+\frac{\Gamma}{\kappa})|x|} - \frac{\Gamma}{\kappa} e^{-\frac{\kappa}{2v_g}|x|} \right] + O\left(\frac{1}{\kappa^2}\right), \quad (5.2)$$

where N is a normalisation constant, v_g the group velocity of the bound state and $O(1/\kappa^2)$ indicates terms of order $1/\kappa^2$ and higher. The state is not separable and the two photons composing the bound state are entangled with each other. In the relative two-photon coordinate $x = x_1 - x_2$ (the distance between the two photons), the photons are exponentially localised; however, since the two-photon energy is conserved, they take the form of a plane wave e^{iEx_c} in the two-photon centre-of-mass coordinate $x_c = (x_1 + x_2)/2$ with a common two-photon frequency E . The exponential localisation in the relative coordinates evidences the strong correlation of the two photons in the bound state. In contrast to the waveguide QED bound states,¹²⁵ the presence of the cavity results in the second term that removes the cusp at $x = 0$ such that the function is smooth.

The strong localisation within a time $1/\Gamma$ in the difference coordinate means that the two photons in the bound state excite and stimulate the emission of the atom. This distinctly

correlated interaction between the photons leads to this eigenstate having its own distinct transmission coefficient $t_B(E)$ and dispersion in comparison to the single-photon eigenstate and therefore undergoes different delays, broadening and distortion. We compute the general form of $t_B(E)$ numerically, but in the limit of a broadband cavity, the transmission coefficient of the two-photon bound states is

$$t_B(E) = \frac{E(\kappa + 2\Gamma) - 2i\Gamma(\kappa - \Gamma - E^2/\Gamma)}{E(\kappa + 2\Gamma) + 2i\Gamma(\kappa - \Gamma - E^2/\Gamma)} + O\left(\frac{1}{\kappa^2}\right). \quad (5.3)$$

Similar to single-photon scattering, by taking respectively the first and third derivatives of $\phi_B = -i \ln(t_B(E))$, we find that the delay of the two-photon bound state in the centre-of-mass coordinate is $\Delta\tau_2(0,0) = 1/\Gamma + 3/\kappa$ and the distortion is $d_2(0,0) = -(1 - 3\Gamma/\kappa)/(2\Gamma^3)$. In comparison to the single-photon state, the bound state therefore undergoes both a reduced delay and a factor of 64 less distortion. The reduction in distortion was shown to be related to soliton propagation in waveguide QED.¹²⁵

5.4.2 Experimental implementation

In order to fulfil experimentally the two criteria to study the photon-number-dependent scattering dynamics, namely unidirectional light propagation and a strong atom-photon interaction, we employ not a real atom but an artificial atom, a single QD, which is described in detail in App. A. The QD is embedded in a Fabry-Pérot microcavity. The cavity suppresses the effects of phonons such that the QD mimics a two-level system precisely.⁶⁷ The epitaxially grown InAs QDs are part of a semiconductor heterostructure comprising an n-i-p diode and a GaAs/AlAs Bragg reflector, the *bottom mirror*. The *top mirror* consists of a concave, dielectric Bragg mirror fabricated into a silica substrate. The reflectivity of the bottom mirror is significantly higher than that of the top mirror. With the aid of xyz-nanopositioners, one can position a QD in the sample relative to the cavity mode and one can tune the resonance frequency of the cavity to that of the QD's emission. Essential for the unidirectionality condition, the cavity should have only one port. In this system, undesired losses (losses via the bottom mirror, absorption and scattering losses¹³⁸) account for $\kappa_{\text{loss}}/(2\pi) = (0.72 \pm 0.07)$ GHz,¹⁹ while the total cavity linewidth is $\kappa/(2\pi) = (20.1 \pm 1.5)$ GHz, indicating that $\sim 96\%$ of the light is back-reflected via the one port of the microcavity, namely the top mirror. The QDs in this sample present a close-to-transform-limited linewidth $\gamma/(2\pi) = 0.30$ GHz. We use the transitions of a neutral exciton X^0 , which exhibits a so-called fine-structure splitting (FSS): there are two non-degenerate, linearly-polarised dipole moments. In order to work with one transition only, we search for a highly strained region in the sample in which both the FSS of the QD and the mode-splitting of the cavity are large. We select a QD with a starting linear frequency splitting $\text{FSS} = (7.6 \pm 0.1)$ GHz. We apply an out-of-plane magnetic field $B=0.5$ T, large enough to push the transitions further apart via the Zeeman effect, but not large enough to influence significantly the selection rules. (In a large magnetic field, the Zeeman splitting becomes much larger than the FSS such that the transitions become circularly polarised as discussed in Sec. 2.1.1.) With this magnetic field strength, we finally have $\text{FSS} = (11.0 \pm 0.1)$ GHz. We focus the rest of the discussion on the lower-frequency transition. When QD and cavity are coupled, the Purcell-enhanced QD linewidth $\Gamma = F_P \cdot \gamma$ becomes $\Gamma/(2\pi) = 4.24$ GHz, where $F_P = 14.1$ is the Purcell factor. The lifetime of the emitter becomes $\tau_{\text{QD}} = 37.5$ ps and the QD-cavity coupling rate $g/(2\pi) = 4.62$ GHz. The strong atom-photon interaction and near-lossless

operation result in a near-unitary probability of emission from the QD into the cavity mode, $\beta = F_P/(F_P + 1) = 0.93$. Further experimental details are provided in App. A.

5.4.3 Pulse delay induced by the cavity

The elastic scattering of a wavepacket by a resonator is not an instantaneous process. It was shown by E.P. Wigner in 1955 that the scattered wave propagates with a time delay with respect to an unscattered wave.¹⁵⁷ The so-called *Wigner delay* is given by the derivative of the phase shift acquired by the wave with respect to its frequency.¹⁵⁸ The delay is frequency dependent. In the case of a one-sided optical cavity with an inverse lifetime κ the Wigner delay inherited by the interacting pulse is given by

$$\Delta\tau_C(\omega_L, \omega_C) = \frac{4}{\kappa} \frac{1}{1 + 4 \left(\frac{\omega_L - \omega_C}{\kappa} \right)^2}. \quad (5.4)$$

It is easy to see that at resonance ($\omega_L = \omega_C$) the Wigner delay reduces to $\Delta\tau_C(0, 0) = 4/\kappa$. For our cavity, the expected Wigner delay at resonance is $\Delta\tau_C(0, 0) = 4/\kappa = (31.7 \pm 2.4)$ ps.

We study the dynamical response of a ~ 135 ps Gaussian pulse scattered by the one-sided cavity. We work in *back-reflection* mode, such that the input light only interacts with the H cavity mode. Figure 5.1b shows the time of arrival of the pulse $G^{(1)}(\tau)$ as a function of detuning between the laser and the cavity resonance. Even for the shortest pulses used here, the scattered pulse is shape-maintaining over the entire spectrum. We evaluate the delay of the pulse peak $\Delta\tau$ for one- (red dots) and two-photon components (blue dots) as

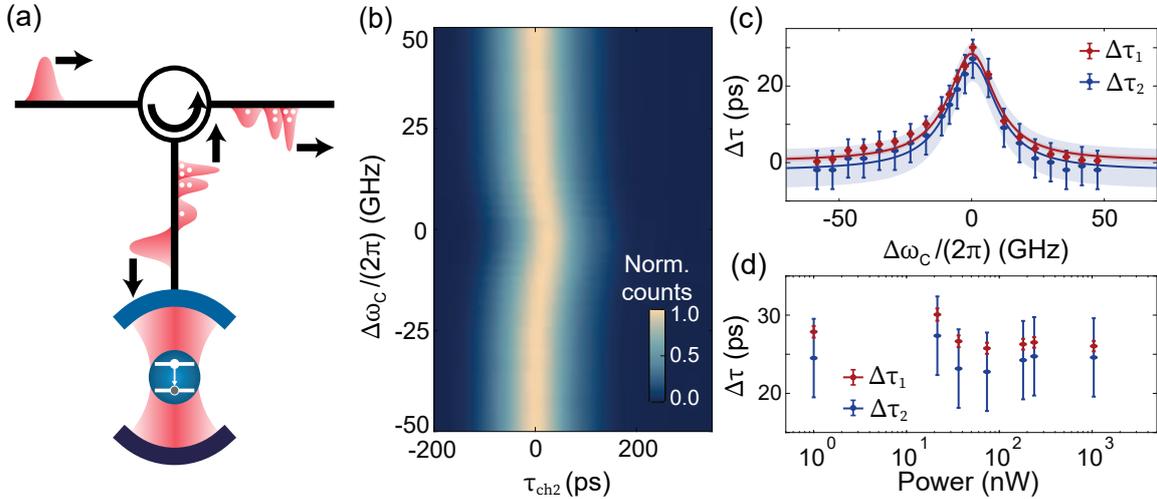


Figure 5.1: Schematic and Wigner delay induced by a one-sided cavity. (a) A Gaussian pulse of light is launched into a circulator, which guides the pulse towards a QD, coupled to a one-sided microcavity. Upon interaction with the QD-cavity system, states of light with different photon-number are transported through the system with different time delays. (b) Measured $G^{(1)}(\tau)$ histogram as a function of cavity detuning. (c) Measured pulse peak delay $\Delta\tau$ of $G^{(1)}$ (red data points) and $G^{(2)}$ (blue data points) as a function of cavity detuning. For an optical cavity, the Wigner delay is photon-number independent, and at resonance equal to $\Delta\tau_C = 4/\kappa$ for a one-sided cavity. By fitting Eq. 5.4 (solid lines) we determine $\kappa_{\text{fit}}/(2\pi) = (21.6 \pm 0.2)$ GHz. Error bars in data points arise from fitting residual standard error, and error bars in fit arise from accounting for experimental error bars in the fitting process. (d) The Wigner delay for single-photon states (red data points) and two-photon states (blue data points) at resonance measured for different laser powers: the delay is independent of the power. Error bars in data points arise from residual standard error.

a function of detuning (Fig. 5.1c). The delay experienced in both cases is the same, and described by Eq. 5.4, which we fit to the data (red and blue solid lines) allowing us to retrieve the cavity linewidth $\kappa_{\text{fit}}/(2\pi) = (21.6 \pm 0.2)$ GHz. This value is the same (within the error bars) as the value of κ determined via the intensity measurement described in App. A, $\kappa/(2\pi) = (20.1 \pm 1.5)$. The photon lifetime in the cavity is $\tau_C = 1/\kappa_{\text{fit}} = (7.3 \pm 0.1)$ ps, leading to a Wigner delay at resonance of $\Delta\tau_C(0, 0) = 4/\kappa_{\text{fit}} = (29.2 \pm 0.4)$ ps. Finally, we show in Fig. 5.1d that the Wigner delay for a resonator is linear, i.e. independent of input laser power. For the experiments in the following sections, we use the average of the delays extracted in this measurement as the *classical* (i.e. cavity-only) baseline.

5.4.4 Direct observation of photon-number dependent scattering dynamics

The direct observation of photon-number-dependent scattering dynamics is presented in Fig. 5.2a. A weak, coherent Gaussian pulse of temporal full-width-at-half-maximum (FWHM) 135 ps – about twice the lifetime of the QD, $\sigma\Gamma = 2.2$ – is launched into the input of the optical system. Without any interaction with the cavity-QED system, it propagates through the optical system and arrives at the single-photon detectors at time $\tau = 0$ (the pulse peak is represented by the grey dashed line).

Upon resonant interaction with the cavity, but in the absence of the quantum emitter, the Gaussian pulse undergoes a linear transmission, and is delayed by $\Delta\tau_C = (29.2 \pm 0.4)$ ps (the centre of the Gaussian pulse is represented by the black dashed line). This delay matches the predicted delay for a one-sided cavity $\Delta\tau_C = 4/\kappa = (31.7 \pm 2.4)$ ps (see Sec. 5.4.3). The delay imparted via the elastic scattering of a wavepacket by a resonator is often referred to as a Wigner delay.¹⁵⁷

In the presence of the QD, i.e. when the QD is tuned into resonance with the cavity, we observe that the scattered n -photon pulse reveals an n -dependent *quantum Wigner delay*. We inspect the dynamics under full resonant conditions, $\Delta_L = \Delta_C = 0$, via the n^{th} equal-time correlators. The single-photon scattering is given by a power measurement, $G^{(1)}(\tau)$, presented as red dots in Fig. 5.2a, and shows how the output pulse is delayed relative to the input pulse, a result previously observed also for other quantum systems.^{158–160} The scattered pulse is non-Gaussian in shape. This distortion causes the peak of the pulse to be delayed by a value different from $\Delta\tau_1 = 4/\Gamma$ (see Fig. 5.3). The distortion arises from the fact that the spectral components of the pulse probe a sizeable fraction of the components making up the resonance of the cavity-QED system. The observed dynamics in $G^{(1)}(\tau)$ are well captured by the theoretical model (red solid line). The scattering of two-photon states is examined via $G^{(2)}(\tau, \tau)$, Fig. 5.2a blue dots (theory, solid blue line). We find experimentally that both the delay and distortion in $G^{(2)}(\tau, \tau)$ are significantly reduced compared to those of $G^{(1)}(\tau)$. The theory accounts for the measured $G^{(2)}(\tau, \tau)$ very convincingly. This constitutes a clear observation of two-photon bound states. We interrogate also the third-order equal-time correlator, $G^{(3)}(\tau, \tau, \tau)$, given by the green dots (the green solid line is a Gaussian fit). Both the peak delay and temporal width of the $G^{(3)}(\tau, \tau, \tau)$ curve are reduced further, consistent with the observation of three-photon bound states.

The finite spectral width of the pulses probes the frequency- and photon-number-dependent phase imparted on different photon-number states. For a coherent input pulse we examine the delay experienced by an n -photon pulse by comparing the delay at the peak of the scattered pulse $\Delta\tau_n := \max(G^{(n)}(\tau, \tau, \dots, \tau))$ (Fig. 5.4d). Since longer pulses undergo significantly reduced distortion, for $n = 1, 2$ we extract the peak delay from measurements with ten

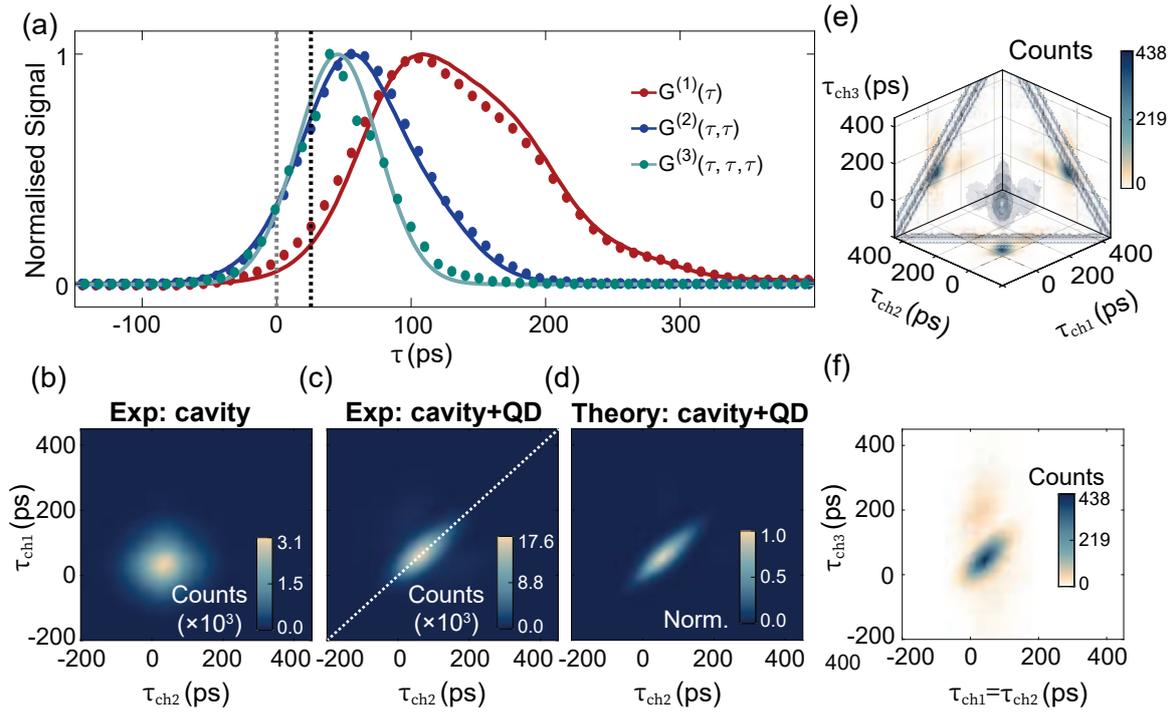


Figure 5.2: Photon-number-dependent pulse scattering. (a) Normalised photon-counts versus delay. For a Gaussian pulse ($\sigma\Gamma = 2.2$) launched at time $\tau = 0$ (dashed grey line), the propagated pulse undergoes a Wigner delay in the presence of the optical cavity alone (dashed black line). Scattering off the QD-cavity system, the single-photon components $G^{(1)}(\tau)$ – red points experiment, red solid line theoretical model – undergo pulse reshaping and arrive with a larger delay than the two-photon bound states $G^{(2)}(\tau, \tau)$ – blue points experiment, blue solid line theoretical model – which in turn undergo a larger delay than three-photon states $G^{(3)}(\tau, \tau, \tau)$ – green points experiment, green solid line Gaussian fit. (b) Auto-correlation map $G^{(2)}(\tau_{ch1}, \tau_{ch2})$ of the pulse following propagation through the entire system in resonance with the optical cavity but in absence of the QD, and (c) in the presence of the QD. The white dashed line represents the equal-time correlation. (d) Simulation of normalised $|\psi_2(\tau_{ch1}, \tau_{ch2})|^2$. (e) Auto-correlation map $G^{(3)}(\tau_{ch1}, \tau_{ch2}, \tau_{ch3})$. The volumes in the 3-dimensional space depict the isosurfaces at 0.05, 0.20, 0.50, 0.75 and 0.90 of the normalised counts, and the projections on each axis are plotted on setting one of the detection times to zero. (f) Cut-through of $G^{(3)}$ at times τ_{ch3} and $\tau_{ch1} = \tau_{ch2}$.

different pulse widths ($1.3 \leq \sigma\Gamma \leq 26.0$). The one- and two-photon delays correspond well to the theoretical predictions (red and blue dashed lines respectively). The single-photon wavepackets undergo a delay $\Delta\tau_1 = (144.02 \pm 26.90)$ ps; two-photon wavepackets undergo a reduced delay $\Delta\tau_2 = (66.45 \pm 5.97)$ ps. The reduced delay is a consequence of stimulated emission: the first photon excites the atom, the second photon stimulates the emission of the atom, thereby reducing the total time in which the photons interact with the atom. The three-photon delay is $\Delta\tau_3 = (45.51 \pm 0.09)$ ps, a further reduction. This measurement of the quantum Wigner delay therefore unveils the existence of few-photon bound states. Key to success is the strong nonlinear and unidirectional scattering off the single quantum emitter.

We proceed to examine the auto-correlation functions of the scattered pulses. Figure 5.2b shows the two-photon auto-correlation map $G^{(2)}(\tau_{ch1}, \tau_{ch2})$ of the weak Gaussian pulses scattered off the optical cavity, but in absence of the quantum emitter. The linear response of the cavity displaces the two-dimensional Gaussian pulse shape by $\Delta\tau_C$ along the equal-time-of-arrival line ($\tau_{ch1} = \tau_{ch2}$) with respect to the Gaussian structure of the non-interacting

pulse centred at $(\tau_{ch1}, \tau_{ch2}) = (0, 0)$. As shown experimentally (theoretically) in Fig. 5.2c(d), when the pulse interacts with the QD-cavity system the correlated counts are drawn towards the diagonal of the $G^{(2)}$ -map (white dashed line), and can no longer be described by a linear transformation of the response to the bare cavity. We examine also the three-photon auto-correlation map $G^{(3)}(\tau_{ch1}, \tau_{ch2}, \tau_{ch3})$ in Fig. 5.2e, where the volumetric isosurfaces at 0.05, 0.2, 0.5, 0.75 and 0.90 of the normalised counts are shown. The projections on the axes are the cut-through planes in each of the detection channels at time $\tau = 0$. As in the $G^{(2)}$ measurements, there is a strong peak along the diagonal revealing highly correlated three-photon states, as well as faint lateral lobes away from the diagonal.¹⁶¹ Figure 5.2f displays a cut-through along the plane defined by $\tau_{ch1} = \tau_{ch2}$ and τ_{ch3} where the clustering of the coincidence counts along the diagonal are prominently revealed. In all likelihood, this manifests the propagation of three-photon bound states (photonic trimers).

Dependence of delay distortion on pulse width

The scattered light dynamics depend on the input pulse shape and temporal width. Shorter pulses in time, a few times the lifetime of the emitter, undergo higher-order distortion as more spectral components interact with the two-level system (TLS). Much longer pulses are spectrally narrow and the continuous-wave (CW) limit is appropriate in which only a

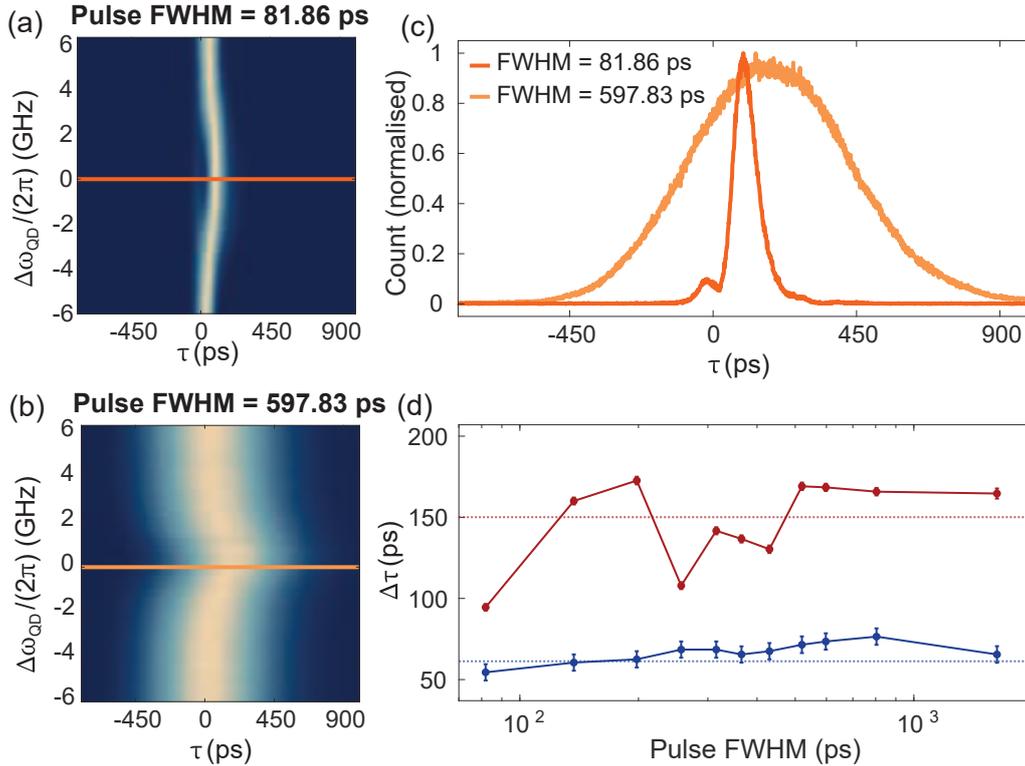


Figure 5.3: Input pulse width and input-power dependent dynamics. Time of arrival τ of the propagated pulse power $G^{(1)}(\tau_{ch1})$ as a function of QD detuning from the laser resonance $\Delta_{QD}/(2\pi)$ for a short (pulse FWHM = 81.86 ps, (a)) and a long (pulse FWHM = 597.83 ps, (b)) input Gaussian pulse. (c) Line cut-through of (a) at resonance, showing the pulse deformation for short pulses. (d) Peak delay $\Delta\tau$ as a function of input pulse width for one (red) and two photons (blue). The red and blue horizontal dashed lines represent the theoretical values in the infinite-pulse-width limit. Data point centres and error bars in (d) are the maximum of fitted Gaussian distribution and residual standard errors from fitting, respectively.

delay (phase shift) is impinged onto the pulse. In Fig. 5.3, the normalised power $G^{(1)}(\tau)$ as a function of QD-laser detuning ($\Delta\omega_{\text{QD}} = \omega_{\text{QD}} - \omega_{\text{L}}$) is shown. The laser is in resonance with the cavity. We show the one-photon scattering response for two pulse widths, a shorter one ((a)), pulse intensity-FWHM of 81.86 ps, corresponding to $\sigma\Gamma = 1.3$) and a longer one ((b), pulse intensity-FWHM = 597.83 ps, corresponding to $\sigma\Gamma = 9.6$). In both cases, far from resonance, the pulse is delayed by the delay of the cavity alone and does not present any reshaping. In the shorter-pulse limit, the transmitted pulse is distorted near the resonance and no longer corresponds to a Gaussian pulse, as is seen in Fig. 5.3c. The distortion of the pulse results in a deviation of the peak delay $\Delta\tau$ in shorter pulses compared to the infinite-pulse limit, in which the distortion is negligible. The two-photon auto-correlation maps for these pulse widths are discussed in Sec. 5.4.5. We further probe the peak delay at resonance for single photons $\Delta\tau_1$ and for two-photon states $\Delta\tau_2$ as a function of the pulse FWHM, displayed in Fig. 5.3d, where the red and blue dashed lines correspond to the theoretical prediction neglecting the effects of distortion. We point out that the single-photon scattering dynamics are more sensitive to dispersion effects (see Fig. 5.5) than the dynamics of the two-photon bound states; this explains the larger variance in $\Delta\tau_1$ in this analysis.

Power dependence

The response of a single TLS is highly susceptible to the number of photons impinging on it, as the TLS saturates upon absorption of a single photon.^{117,122} This results in a strong nonlinear response even at very low input laser powers. We expect the few-photon nonlinearity to fade with strong coherent fields, as in this regime a large fraction of the pulse is scattered without interacting with the saturated TLS. Figure 5.4a presents the normalised power-time response as a function of QD-detuning from the laser-cavity resonance for a pulse with ~ 135 ps FWHM in the case of a low-power (2.89 nW, left) and high-power (73.64 nW, right) input. These laser powers translate to an average photon-number per lifetime of $\bar{n} = 0.0052$ and $\bar{n} = 0.1313$ at the cavity, respectively. The QD saturates at the critical photon number¹⁰⁰ $\bar{n}_c = 1/(8\beta^2) = 0.143$. In the latter measurement, the reduced delay at resonance testifies to the saturation of the QD. The fingerprints of two-photon correlated states (clustering and delay of coincidence counts along the diagonal) also diminish (Fig. 5.4b). We present in Fig. 5.4c the peak delay observed for one (red) and two photons (blue) as a function of average photon number per lifetime. At low photon-number, the measurements correspond well to the simulated $\Delta\tau$ for this pulse width (red and blue dashed lines), converging gradually as the laser power increases to the limit where only the delay induced by the cavity alone remains (black dashed line). The delay response for both one- and two-photon states correspond well to a TLS-saturation power law like function,

$$\Delta\tau(\bar{n}) = 1 - (1 - \Delta\tau^\infty/\Delta\tau^0) \cdot \frac{\bar{n}/\bar{n}_c}{1 + \bar{n}/\bar{n}_c}, \quad (5.5)$$

where $\Delta\tau^0$ and $\Delta\tau^\infty$ are the peak delays measured in the limits of zero and infinite input photons, respectively. The fits are depicted with red and blue solid lines in the plot.

Next, we evaluate $G^{(1)}(\tau)$ and the diagonals of the auto-correlation functions $G^{(2)}(\tau, \tau)$ and $G^{(3)}(\tau, \tau, \tau)$ and determine the dynamical properties of the photon-number dependent scattering. We present in Fig. 5.4d,e the values of peak delay $\Delta\tau$ and relative pulse width $\sigma_n/\sigma_{|in\rangle}$ as a function of photon-number n . For each n , these values are extracted from $G^{(1)}(\tau)$, $G^{(2)}(\tau, \tau)$ and $G^{(3)}(\tau, \tau, \tau)$. Here, we extract the average and variance from all

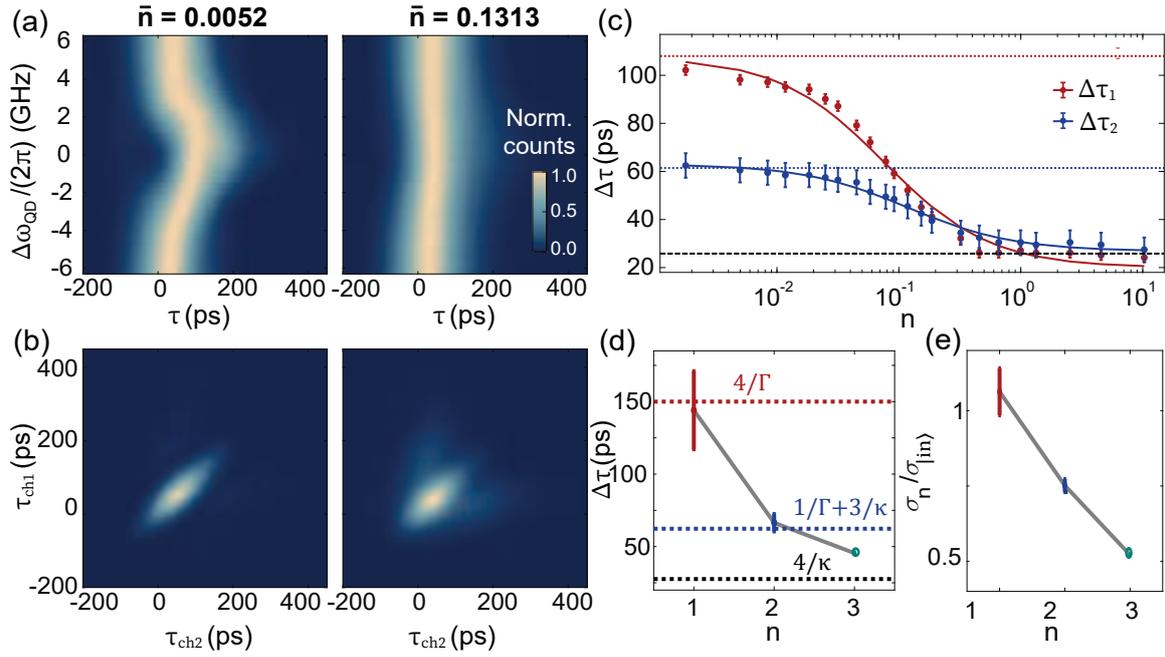


Figure 5.4: Photon-number-dependent scattering dynamics. (a) Time of arrival τ of the propagated pulse power $G^{(1)}(\tau_{\text{ch1}})$ for a 135 ps Gaussian pulse as a function of QD detuning from the laser resonance for an average input photon number $\bar{n} = 0.0052$ (left) and $\bar{n} = 0.1313$ (right), and (b) respective $G^{(2)}(\tau_{\text{ch1}}, \tau_{\text{ch2}})$ maps at resonance. (c) Peak delay as a function of average input photon number for one- (red) and two-photon (blue) states. Solid lines are fits to the TLS-saturation relation, with critical photon number $\bar{n}_c = 0.1338$. The red and blue dashed lines show the modelled $\Delta\tau$ for one- and two-photon states for a 135 ps Gaussian pulse in the low power limit, and the black dashed line is the delay of the cavity alone. Data point centres and error bars in (c) are the maximum of fitted Gaussian distribution and residual standard errors from fitting, respectively. (d) Average peak delay of the scattered pulse $\Delta\tau$, and (e) average ratio of the measured pulse width after scattering (σ_n) to the input pulse width $\sigma_{|in}$), for different photon-numbers n . The values are extracted by averaging over all the low-power resonant experiments carried out in the course of this work (including differing pulse widths), probed via $G^{(1)}$, $G^{(2)}(\tau, \tau)$ and $G^{(3)}(\tau, \tau, \tau)$.

experiments presented in the course of this work under low-power resonant conditions.

The single-photon components undergo a delay $\Delta\tau_1 = (144.02 \pm 27.90)$ ps, in good agreement with the predicted value of $\Delta\tau_1^{\text{theory}} = 4/\Gamma = 150.00$ ps. The large error stems from the sensitivity of the peak delay to distortions, as discussed above; the distortions depend sensitively on the exact detunings which can drift slightly. We determine the two- and three-photon delays to be $\Delta\tau_2 = (66.48 \pm 5.97)$ ps and $\Delta\tau_3 = (45.51 \pm 0.09)$ ps. The two-photon delay corresponds well to the prediction of $\Delta\tau_2^{\text{theory}} = 1/\Gamma + 3/\kappa = 61.3$ ps. We note that as we approach the classical limit of $n \rightarrow \infty$, the delay converges to the value induced by the cavity alone (see Sec. 5.4.3). Finally, we compare the Gaussian width of the interacting n -photon output pulse and the input pulse and determine $\sigma_1/\sigma_{|in} = 1.06 \pm 0.08$, $\sigma_2/\sigma_{|in} = 0.75 \pm 0.02$ and $\sigma_3/\sigma_{|in} = 0.52 \pm 0.00$. This is consistent with the n^{th} correlation function being proportional to the electric field to the power of n and hence σ being reduced by a factor of \sqrt{n} .

Delay dispersion

Next, we investigate the behaviour of the single- and two-photon scattering dynamics as a function of the central frequency of the photons. Figure 5.5a,b show, respectively, the

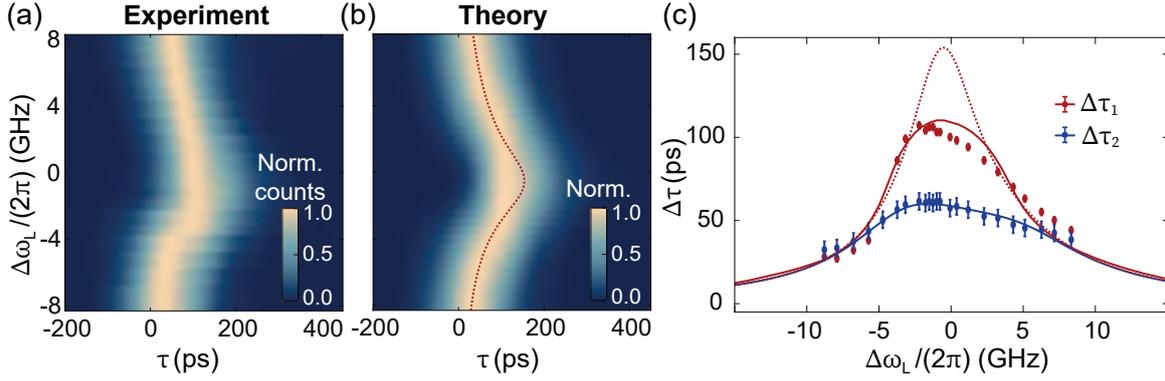


Figure 5.5: Single-photon and two-photon bound state delay dispersion. (a) Experimental $G^{(1)}(\tau)$ as a function of laser detuning $\Delta_L/(2\pi)$ for a cavity-QD detuning of $\Delta_C/(2\pi) = 1.0$ GHz and for an input pulse with intensity FWHM of ~ 135 ps, and (b) respective simulation, where the red dotted line indicates the single-photon component delay in the continuous wave limit. (c) Peak delay $\Delta\tau$ as a function of laser detuning for single photons (red) and two-photon bound states (blue). The solid lines are the numerically simulated peak delays for the single- and two-photon bound states. The red dotted line shows the calculated pulse delay $\Delta\tau_1$ neglecting distortion. In this system, the two-photon bound state propagates without noticeable distortion. Error-bars arise from fitting residual standard error.

experimental and simulated power signal of the scattered pulse (FWHM = 135 ps) as a function of laser detuning from the QD's resonance $\Delta_L/(2\pi)$. The red dashed line in the theoretical model shows where the pulse maximum would occur if distortion effects were disregarded. Here, the cavity is slightly detuned from the QD, $\Delta_C/(2\pi) = 1.0$ GHz, which induces a slight spectral asymmetry to the one- and two-photon peak delays presented in Fig.5.5c (red and blue dots, respectively). The results are in good agreement with the simulations and validate the theoretical model. We calculate numerically the dispersion of the peak delays $\Delta\tau_1$ and $\Delta\tau_2$ (red and blue solid lines). The results describe the experimental observations very well. Here too, the red dashed line corresponds to the single-photon case neglecting pulse distortion. The results demonstrate that two-photon bound states experience a much reduced distortion, imperceptible in this system.

5.4.5 Two-photon bound states as a function of pulse-width

The interaction of the two-photon wavefunction with the cavity-QED system strongly depends on the Gaussian pulse width. In Fig.5.6a we explore this dependence, where we present on the top row the experimental $G^{(2)}$ -map for three different pulse widths, FWHM=(81.86, 256.72, 597.83) ps – equivalently $\sigma\Gamma = (1.3, 4.1, 9.6)$. We compare the experimental results to the simulated absolute-square of the full two-photon wavefunction (middle row), which contains contributions from both two-photon bound states and extended states. The total contribution of the bound states alone is shown in the bottom row: the appearance of just the diagonals is evidence that the bound states contribute to the diagonal of the correlation maps; the extended states contribute to the lobes away from the diagonals. Details of the model are elucidated in Ref.¹²⁰ The nodal line (absence of coincidence events) that occurs between the diagonal (contribution from the bound states) and lobes (contribution from the extended states) occurs due to the different phase the two states obtain after scattering. The phase approaches π for the bound state and is 0 for the extended states. For $\sigma\Gamma = 1.3$, the lobes are very weak in both the experiment and accompanying theory: in Fig.5.6b,

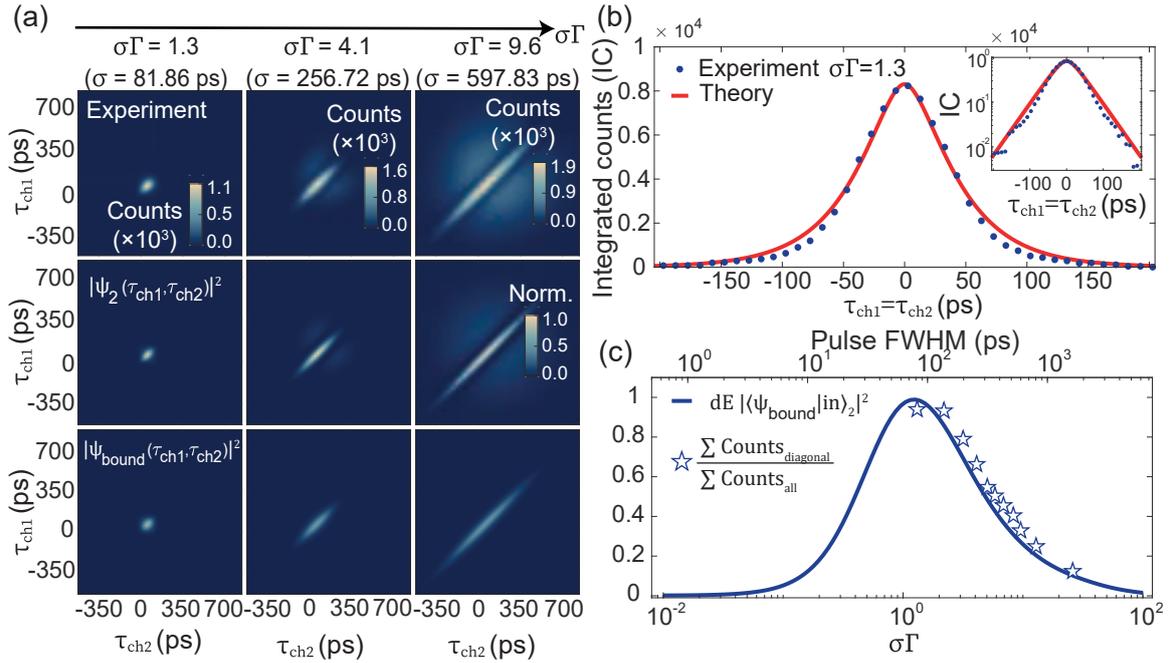


Figure 5.6: Observation of two-photon bound states as a function of input pulse width. (a) Experimental (top row) and simulated (middle row) $G^{(2)}(\tau_{ch1}, \tau_{ch2})$, as well as two-photon bound-state contribution (bottom row) for increasing relative pulse widths $\sigma\Gamma = (1.3, 4.1, 9.6)$ (left to right). (b) Integrated counts versus $\tau_{ch1} - \tau_{ch2}$ for $\sigma\Gamma = 1.3$ (blue circles) along with the theoretical result (red curve) for the two-photon bound states. Inset shows the same, but on a log-scale. Apart from the signal amplitude at $\tau_{ch1} - \tau_{ch2} = 0$, there are no fit parameters. (c) Theory: calculated overlap of the two-photon bound state and an input state $|\text{in}\rangle$, a two-photon Gaussian pulse of width σ . Experiment: integrated counts over the diagonal divided by the total integrated counts in each $G^{(2)}$ -map. The nodal line, clearly visible in the $G^{(2)}$ -map for $\sigma\Gamma = 9.6$, is used to define the integration area for the diagonal; the same area is used for each $\sigma\Gamma$. Both theory and experiment are plotted as a function of pulse width (intensity FWHM, top x-axis) and relative pulse width normalised to the decay rate Γ (bottom x-axis), which has units of $(s \cdot s^{-1})$.

we sum the counts in the $G^{(2)}$ -map over successive stripes parallel to the diagonal, i.e. for successive values of $\tau_{ch1} - \tau_{ch2}$. This procedure is equivalent to performing a conventional correlation measurement $g^{(2)}(\tau_{ch1} - \tau_{ch2})$ with CW excitation, except unnormalised. We find an exponential dependence of $G^{(2)}$ on $(\tau_{ch1} - \tau_{ch2})$ (inset Fig. 5.6b). This reveals experimentally the exponential decay of the two-photon bound-state wavefunction. The exponential dependence of the bound states as revealed in the experiments is well described by the theoretical model: we evaluate the absolute value squared of Eq. 5.2, taking the parameters established from the spectroscopy experiments, and find excellent agreement with the experiment (Fig. 5.6b red solid line). Finally, the total fraction of the scattered wavefunction in the bound-state subspace depends on the overlap of the two-photon bound states with the two-photon input pulse. The theory shows that this overlap has a strong dependence on the input Gaussian pulse duration relative to the lifetime of the quantum emitter, and is largest and very close to unity when the input pulse has a duration $\sim 1/\Gamma$, as shown in Fig. 5.6c, solid blue line. Experimentally, we estimate the bound-state fraction by evaluating the ratio of the counts in the diagonal to the total counts in each $G^{(2)}$ -map. The results (blue stars) follow the theoretical prediction convincingly.

5.5 Conclusions

We demonstrate here the ability to manipulate and identify highly correlated photonic states in time. The results reveal stimulated emission in its most canonical description, a single quantum emitter interacting with single photons.¹⁵⁶ This achievement represents an important landmark in the development of a variety of quantum technologies. Stimulated emission plays a central role for instance in approximate-quantum cloning of photons,¹⁶² a key technology for quantum information processing and networking. The strong dependence of the propagated pulse on photon number can be enhanced by cascading such cavity-QED systems and enables a variety of important applications, such as photon sorting, photon-number-resolving detectors and Bell measurements.^{102,127,128} The revealing of two-photon bound states upon interaction with a single atom is an appealing resource for the realisation of high-fidelity two-qubit photonic gates, such as controlled-phase gates.¹³⁰ Furthermore, the systematic generation of photonic dimers paves the way for significant advances in quantum metrology,¹⁶³ and quantum-enhanced microscopy and lithography.^{164,165}

Part **III**

Readout and manipulation of
a single spin in a microcavity

6

Cavity-enhanced single-shot readout of a quantum dot spin within 3 nanoseconds

Adapted from:

N. O. Antoniadis*, M. R. Hogg*, W. F. Stehl, A. Javadi, N. Tomm, R. Schott, S. R. Valentin, A. D. Wieck, A. Ludwig and R. J. Warburton
“**Cavity-enhanced single-shot readout of a quantum dot spin within 3 nanoseconds**”,
Nat. Commun. **14**, 3977 (2023) ⁱ

6.1 Summary

Rapid, high-fidelity single-shot readout of quantum states is a ubiquitous requirement in quantum information technologies. For emitters with a spin-preserving optical transition, spin readout can be achieved by driving the transition with a laser and detecting the emitted photons. The speed and fidelity of this approach is typically limited by low photon collection rates and measurement back-action. Here we use an open microcavity to enhance the optical readout signal from a semiconductor quantum dot (QD) spin state, largely overcoming these limitations. We achieve single-shot readout of an electron spin in only 3 nanoseconds with a fidelity of $(95.2 \pm 0.7)\%$, and observe quantum jumps using repeated single-shot measurements. Owing to the speed of our readout, errors resulting from measurement-induced back-action have minimal impact. Our work reduces the spin readout-time well below both the achievable spin relaxation and dephasing times in semiconductor QDs, opening up new possibilities for their use in quantum technologies.

ⁱN.O.A., M.R.H. and W.F.S. performed the experiments with input from A.J. and R.J.W. N.T. assembled the cavity structure and fabricated the silica top mirror. R.S., S.R.V., A.D.W. and A.L. fabricated and processed the semiconductor device. N.O.A. and M.R.H. performed the analysis with input from A.J. and R.J.W. N.O.A., M.R.H. and R.J.W. wrote the paper with input from all authors.

6.2 Introduction

The ability to perform a projective measurement of a quantum state in a single measurement (single-shot readout) is an enabling technique in quantum technologies.^{166,167} Single-shot readout is necessary in quantum computation in order to extract information at the end of the protocol, as well as in error detection and correction as the quantum processor runs.¹⁶⁸ Additionally, single-shot readout is necessary to close the fair-sampling loophole in tests of quantum non-locality, and was a key ingredient in recent demonstrations of loophole-free Bell inequality violations.³ The ideal single-shot readout protocol achieves high-fidelity qubit readout in the shortest time possible; readout within the qubit dephasing time is essential for quantum error correction, and enables measurement-based quantum feedback.^{169,170}

The spin states of semiconductor QDs show exceptional promise in quantum technology.^{171–173} Optically-active QDs, established bright and fast sources of coherent single photons,^{19,46,92,174} can be occupied with a single electron and the electron spin can be initialised^{175,176} and rotated on the Bloch sphere^{86,177} on nanosecond timescales using all-optical techniques. Theoretical proposals^{178,179} and recent experiments^{180–182} have established the spin-photon interface provided by the InAs platform as a leading contender for creating photonic cluster states, an important resource for quantum repeaters¹⁸³ and measurement-based quantum computation.¹⁸⁴ The dephasing time of the electron spin in optically-active QDs is limited by magnetic noise arising from the nuclear spins. However, there are powerful mitigating strategies. A double-QD can be used to create a clock-transition;¹⁸⁵ a switch to a hole spin suppresses the effect of the magnetic noise particularly in an in-plane magnetic field;^{87,186} and the noise can be almost eliminated by laser-cooling the nuclei.^{43,44} In the context of cluster states, spin readout is necessary in order to disentangle the spin from the photons, thereby releasing an entirely photonic entangled state. To date, single-shot spin readout on a timescale comparable to the rapid spin initialisation and manipulation times has remained elusive.

Spin readout with an optical technique typically proceeds by applying a magnetic field to a QD containing a single electron, resonantly driving one of the Zeeman-split trion transitions, then collecting the spin-dependent resonance fluorescence.¹⁸⁷ However, during readout, the applied laser can induce an unwanted spin flip,^{188,189} a process known as *back-action*. The key challenge for spin readout is to collect enough photons to determine reliably the spin state before the back-action flips the spin. Of the small number of previous experiments to achieve single-shot readout of InAs QD spin states,^{190–192} the most rapid to date achieved a fidelity of 82% in a readout time of 800 ns.¹⁹¹ This 800 ns readout time was similar to the back-action timescale, and is significantly longer than the dephasing time for an electron spin bound to an InAs QD ($T_2^* = 296$ ns following nuclear bath cooling^{43,44}).

In this chapter, we report nanosecond-timescale, all-optical, single-shot spin readout. We use an open microcavity to boost the photon collection efficiency in order to reduce the spin readout time. We achieve single-shot readout in only 3 nanoseconds with a fidelity of $(95.5 \pm 0.7)\%$, an improvement in readout speed of more than two orders of magnitude with respect to previous experiments. To the best of our knowledge, this is the fastest single-shot readout of a quantum state ever achieved across any material platform. Our approach brings the readout time well below the dephasing time for an electron spin in this system. Cavity enhancement is a powerful tool for improving optical single-shot spin readout in other systems; photonic crystal cavities have been successfully used with defect centres in

diamond¹⁹³ and rare-earth ions.^{194, 195} Importantly our open microcavity approach is not specific to QD samples, and can be used to enhance optical spin readout in other material platforms.¹⁹⁶

6.3 Fast single-shot readout

6.3.1 High efficiency photon collection

A schematic of the setup used in our experiments is shown in Fig. 6.1 a. Our sample is a gated, charge-tunable InAs/GaAs device, with a highly reflective Bragg mirror integrated into the semiconductor heterostructure as described in detail in App. A. The gate structure allows the charge occupancy of the QD to be set, as well as fine tuning of the emission frequency via the quantum-confined Stark effect. We operate with a single electron occupying the QD, which is our spin readout target. A miniaturised Fabry-Pérot cavity is created between the semiconductor bottom mirror and a free-standing concave top mirror. The QD sample is attached to an xyz nano-positioning stage. This flexibility of the open microcavity design allows the cavity to be re-positioned to address a chosen QD. Once a QD is positioned at the anti-node of the cavity field (xy positioning), its frequency can be matched to one of the QD transitions (z positioning).

Figure 6.1 c demonstrates the high photon collection efficiency of our microcavity system and its potential for rapid spin readout. A photon emitted by the QD exits the output facet

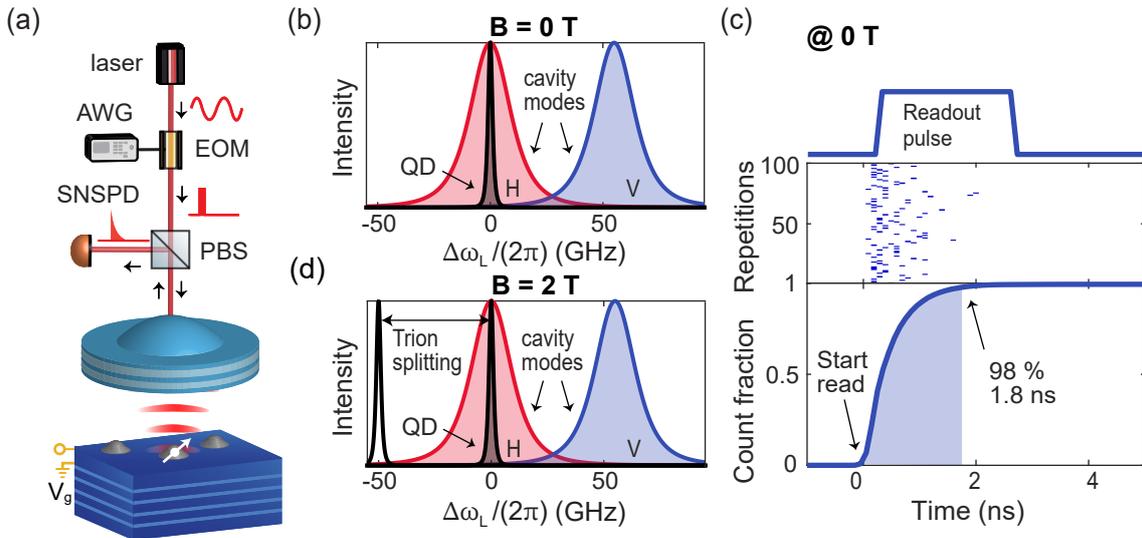


Figure 6.1: Experimental setup and system efficiency. (a) Resonant laser pulses with variable intensity and duration are sent to the QD using an electro-optic modulator (EOM) driven by a fast arbitrary waveform generator (AWG). The photons emitted by the QD are collected in the output arm of the cross-polarised microscope and measured on a superconducting nanowire single photon detector (SNSPD). (b) Frequency configuration of the QD and mode-split cavity with respect to the laser at zero magnetic field. (c) Readout characterisation at zero magnetic field: here, the readout pulses are set to a duration of 2.0 ns (top panel) with a repetition time of 100 ns. Photons emitted by the QD are detected and the arrival times registered for 100,000 repetitions of the pulse sequence; 100 example traces are depicted in the middle panel where the blue dots represent a photon detection event. In 98% of the repetitions a photon is detected within 1.8 ns. (d) Frequency configuration of the two QD transitions and mode-split cavity with respect to the laser. With a 2.0 T magnetic field, only one trion transition is resonant with the H-polarised cavity mode, resulting in spin-selective Purcell enhancement.

of the collection single-mode fibre with 57% probability.¹⁹ The overall system efficiency, η , the probability that an exciton in the QD results in a click on the detector, includes losses on fibre-couplers and the detectors efficiency and results in 37%. Initially, we set the magnetic field to zero, such that the optical transitions for both electron spin states are degenerate. In this scenario, a resonant laser pulse excites the QD optical transition regardless of the electron spin state. The readout pulse drives the optical transition, and the QD emits photons at a rate set by the (Purcell-enhanced) optical decay rate. The time required for a photon emitted from the QD to be registered by the detector depends on the overall system efficiency; for high efficiencies a photon is rapidly detected. We apply a train of 2 ns readout pulses (approximately square temporal shape limited by the 350 ps AWG rise time, separated by 100 ns, with a peak optical power equal to six times the QD saturation power) to the QD, and monitor the collected photons on a single photon detector (a SNSPD). The SNSPD has a dead time of ~ 12 ns, meaning that after one photon has been detected another detection event stemming from the same pulse is extremely unlikely. Thus, although the QD emits at a constant rate during the 2 ns readout pulse, a maximum of one photon detection event occurs. We repeat the pulse sequence 100,000 times, and analyse the fraction of pulses in which a photon was detected as a function of the readout duration. Our detector registers the precise arrival time of each photon detected during the 2 ns readout pulse, which we use to plot the probability of detecting a photon as a function of elapsed readout pulse duration (see bottom panel Fig. 6.1c). We find that for 98% of the traces, a photon is detected within 1.8 ns. When the same pulse sequence is repeated with the QD detuned out of resonance with the readout laser, we detect a photon (due to laser leakage within the cross-polarised setup) for $< 0.1\%$ of the pulses, demonstrating that the photons we detect are almost exclusively created by the QD.

6.3.2 Single-shot spin readout

To perform single-shot spin readout, we apply a magnetic field of 2.0 T along the growth direction of the sample (Faraday configuration), which creates a four-level system in which the two strongly allowed trion transitions with linewidth $\Gamma/(2\pi) = 2.8$ GHz (that corresponds to the transform limit) are split by 55 GHz (the sum of the electron and hole Zeeman splittings, 6.8 GHz/T and 20.7 GHz/T respectively). Spin readout is achieved by tuning the cavity into resonance with one of the strongly allowed transitions, as shown in Fig. 6.1d. The readout pulse sequence is then similar to that shown in Fig. 6.1b, but photon emission is now only enhanced for the trion transition resonant with the cavity. Figure 6.2a shows example single-shot readout traces: here, we apply a train of readout pulses (5 ns duration with a repetition time of 100 ns) resonant with the cavity-enhanced $|\uparrow\rangle \leftrightarrow |\uparrow, \uparrow\downarrow\rangle$ trion transition. We note that for this experiment, the frequency alignment of cavity modes and trion transitions is identical to that shown in Fig. 6.1 d. If the electron is projected into the $|\uparrow\rangle$ spin state, Purcell-enhanced fluorescence from the $|\uparrow\rangle \leftrightarrow |\uparrow, \uparrow\downarrow\rangle$ trion will be rapidly registered by the detector. The spin is thus projected into the bright state, and detecting a single photon emitted by the QD during the readout pulse constitutes a measurement of the spin state. Conversely, if the electron is projected into the $|\downarrow\rangle$ (dark) spin state no fluorescence is detected, as the $|\downarrow\rangle \leftrightarrow |\downarrow, \uparrow\downarrow\rangle$ trion is out of resonance with the readout laser. In this case, the absence of a detector event during the readout pulse indicates that the spin was projected into the dark state. We stress again that the readout time is less than the dead time of the detector: a maximum of one photon can be measured during the readout process.

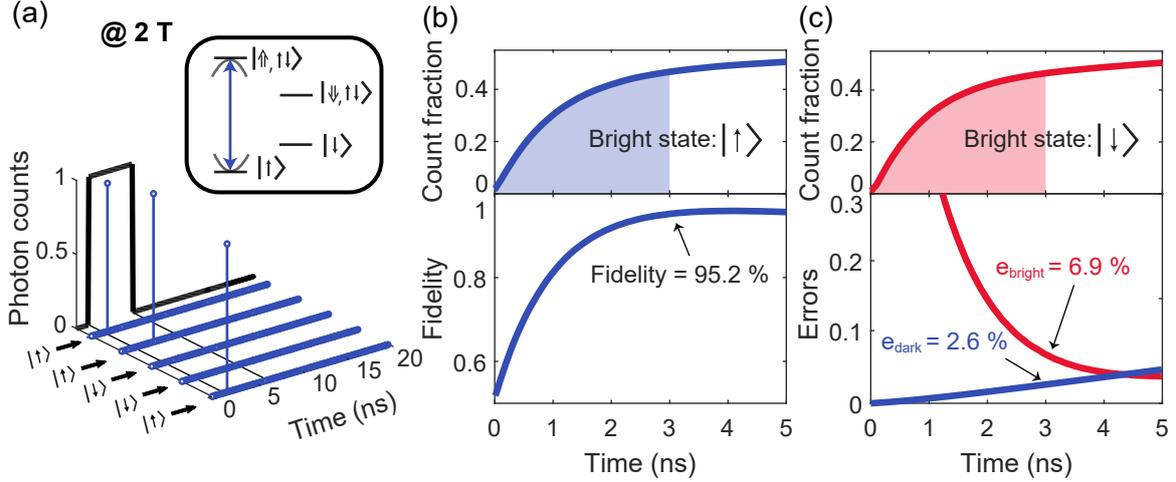


Figure 6.2: Single-shot readout of the QD spin at 2.0 T. (a) Example single-shot readout traces. If a photon is detected during the readout pulse, the state of the QD is assigned to the bright state (here, spin up $|\uparrow\rangle$). Repetitions with no detected photon are assigned to the dark state (here, spin down $|\downarrow\rangle$). Schematic of the QD energy levels in a magnetic field, indicating the readout transition (here, bright state $|\uparrow\rangle$, blue arrow) and the cavity frequency. (b),(c) Experimental count fraction (top) and corresponding readout fidelity/errors (bottom) as a function of readout time for the bright state being up/down. Here, readout pulses with a duration of 5 ns are used. The pulse sequence is repeated 100,000 times. We achieve a readout fidelity of 95.2% for a readout time of 3 ns.

Furthermore, the overall system efficiency is high enough that the absence of a detected photon contains significant information: it denotes that the spin was projected into the dark state. The detection is thus binary: detection of one photon corresponds to the $|\uparrow\rangle$ state, and zero photons to the $|\downarrow\rangle$ state. Equivalently, our photon number threshold for discriminating the spin states is one single photon. We repeated the spin-readout measurements with the cavity and readout laser tuned such that either $|\uparrow\rangle$ or $|\downarrow\rangle$ is the bright transition. In Fig. 6.2 b we show the results of 100,000 repetitions of the spin readout pulse sequence with $|\uparrow\rangle$ set as the bright state (the configuration shown in Fig. 6.1 d). We plot the fraction of readout traces containing one photon, i.e. the fraction of traces we assign the electron spin state to be $|\uparrow\rangle$. We observe a rapid increase in the count fraction (on a timescale of a few nanoseconds) as a function of the readout time. Compared to the 0 T results in Fig. 6.1 c, the maxima of the count fractions now saturate close to 50%: each spin state is almost equally likely. The reason is that the spin is not initialised in these experiments. Instead, before readout, the spin is in a mixed state as co-tunnelling between the QD and the Fermi sea of the back contact regularly randomises the spin state (on a timescale of ~ 150 ns) during the 100,000 readout pulse repetitions, such that both $|\uparrow\rangle$ and $|\downarrow\rangle$ spin states have approximately equal probabilities. We note that spin initialisation via optical pumping was possible in our experiment, albeit with a modest fidelity of approximately 67% due to the relatively rapid co-tunneling rate (Sec. 6.4.2). Figure 6.2 c shows data for 100,000 repetitions of the readout pulse sequence, now with the readout laser resonant with the low frequency trion transition, $|\downarrow\rangle \leftrightarrow |\downarrow\uparrow\rangle$ (thus making the $|\downarrow\rangle$ state the bright state and $|\uparrow\rangle$ the dark state). Compared to the 0 T readout in Fig. 6.1c, the readout speed is slightly slower (high-fidelity readout is achieved in 3 ns rather than 1.8 ns). The reason for this slower readout is that at 2.0 T we operate with the laser on resonance with the QD but detuned by 7.5 GHz from the actual cavity resonance, where we observe optimal laser suppression at the cost of a reduced Purcell

factor (as explained in Sec. 6.3.3).

6.3.3 Cavity suppression in a 2T out-of-plane magnetic field

In order to readout the spin-state correctly, the excitation laser has to be suppressed well enough to minimise spurious counts on the detector due to laser leakage. Otherwise, there is a significant probability that the readout pulse projects the spin into the dark spin-state yet the outcome is recorded falsely as the bright spin-state. A cross-polarisation setup is used to prevent laser light from entering the detection fibre.¹³⁷ This works extremely well at zero magnetic field. However, in an applied magnetic field, the background suppression works slightly less well. This effect likely arises from a Faraday effect in the top mirror of the cavity and/or objective lens. A normalised background signal showing the counts due to laser leakage as a function of cavity detuning is shown in Fig. 6.3a. Unfortunately, the point of maximum laser suppression is not aligned with the cavity resonance, but detuned by 7.5 GHz. At the cavity resonance, the background is high enough to give a spurious count on the detector in 80% of the readout pulse repetitions, making this regime impractical for the readout. The 2 T measurements are therefore performed at the cavity detuning where the background is a minimum. At this cavity detuning, the probability of detecting a photon via laser leakage reduces to 1.4% for a 3 ns readout pulse.

An important parameter for the spin-readout is the β -factor which itself depends on the Purcell factor, F_P : $\beta = F_P/(F_P + 1)$. Cavity-enhanced spin readout depends on achieving β -factors as close as possible to one, equivalently large Purcell factors. We extract the Purcell-factor as a function of cavity detuning by measuring the lifetime of the QD at each cavity detuning and deriving it via $\Gamma = F_P \cdot \gamma$, where Γ is the Purcell-enhanced decay rate and γ is the bare decay rate ($\gamma \approx 0.3$ GHz). (The decay rate is the inverse of the lifetime, $\gamma = 1/\tau$.) On resonance with the cavity, $F_P = 8.5$. At the detuning for which the laser suppression works best, the Purcell factor is slightly lower, $F_P = 6.1$. The corresponding decay curves following excitation with a few-ps laser pulse are shown in Fig. 6.3b. The spin read-out experiments were carried out at $F_P = 6.1$. Consequently, the readout speed is

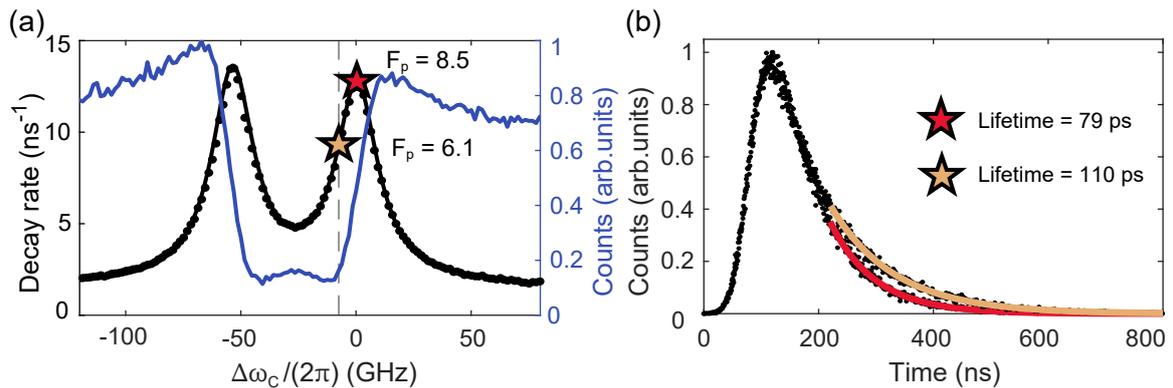


Figure 6.3: (a) Laser leakage into the collection channel (blue) and decay rate of the QD (black) as a function of cavity detuning $\Delta\omega_C/(2\pi)$. The laser leakage shows two minima and neither aligns perfectly with the cavity resonance. At the cavity resonance, the Purcell factor is $F_P = 8.5$; at the lowest laser leakage, $F_P = 6.1$. (b) Time-resolved lifetime measurement on resonance with the cavity (red) and at the detuning for minimum laser leakage (yellow). The response of the QD to a short excitation pulse (few ps) is measured and reveals an exponential decay (black). The lifetime is extracted from an exponential fit and is 79 ps at resonance and 110 ps at minimum laser leakage.

slightly reduced compared to 0 T. However, we still achieve high-fidelity single-shot spin readout within 3 ns.

6.3.4 Readout fidelity estimation

Our single-shot readout results are modelled using a Monte-Carlo approach in order to determine the readout fidelity.

Simulation of readout count fractions

The simulations of the count fractions are based on a Monte-Carlo method in which the (simulated) readout outcome is recorded many times (100,000 repetitions) in order to mimic the experiment. The readout pulse is considerably longer than the Purcell-enhanced radiative lifetime. The power is also well above the saturation power. These two factors mean that should the spin be projected into the bright state, the exciton population is close to 0.5. The photon emission rate is the occupation of the bright state divided by the lifetime. Each photon is detected with a certain probability, the overall system efficiency. In other words, the detection rate is the emission rate multiplied by the overall system efficiency, η . A readout cycle is repeated until a photon is detected and the detection time is recorded. Summing up over all repetitions leads to count fractions as in the measurements in Fig. 6.2b. The model has four input parameters: the overall system efficiency η (the probability that an exciton in the QD results in a click on the detector), the Purcell factor F_P , the spin-flip time τ_{SF} , and the probability of detecting a laser photon (to simulate the laser background, see analysis in Sec. 6.3.3). The spin $T_1 = 158$ ns was measured via the quantum jump experiments discussed in the Sec. 6.3.6.

The dependence of the readout on the overall system efficiency is shown in Fig. 6.4a. The higher the efficiency, the sooner the spin-state can be read out, and the lower the probability of incorrectly assigning the spin state. In practice, the overall system efficiency η is known based on the analysis in Ref. ¹⁹ the properties of the fibre couplers, and the quantum efficiency of the detector:

$$\eta = \beta \cdot \frac{\kappa_{\text{top}}}{\kappa + \gamma} \cdot \eta_{\text{optics}} \cdot \eta_{\text{coupler}} \cdot \eta_{\text{detector}} \quad (6.1)$$

where β is the probability that an exciton creates a photon in the H-polarised cavity mode; $\kappa_{\text{top}}/(\kappa + \gamma) = 96\%$ is the probability that a photon in the cavity exits the top mirror; and $\eta_{\text{optics}} = 69\%$ represents the throughput of the optical system from microcavity to the output of the final output fibre (as defined and measured in Ref. ¹⁹ and discussed in Sec. 2.2.2). The output of this fibre is coupled to the detector with an optical coupler (in practice, two fibre-couplers) with efficiency $\eta_{\text{coupler}} = 80\%$. Finally, the detector has a quantum efficiency of $\eta_{\text{detector}} = 82\%$.

At $B = 0$, $\beta = 86\%$ such that $\eta = 37\%$. We stress that this is the predicted overall system efficiency based on the analysis of all the individual contributions, including the detector efficiency. In practice, this predicted value of η describes the experimental results extremely well.

At $B = 2$ T, $\beta = 80\%$, resulting in a predicted overall efficiency of $\eta = 35\%$. In practice, a slightly lower η is required to describe quantitatively the experimental results, $\eta = 25\%$. The origin of this slight reduction in η with respect to $B = 0$ is unknown. For the cavity alignment with $F_p = 6.1$ used in our experiments (shown in Fig. 6.3 a) the Purcell factor

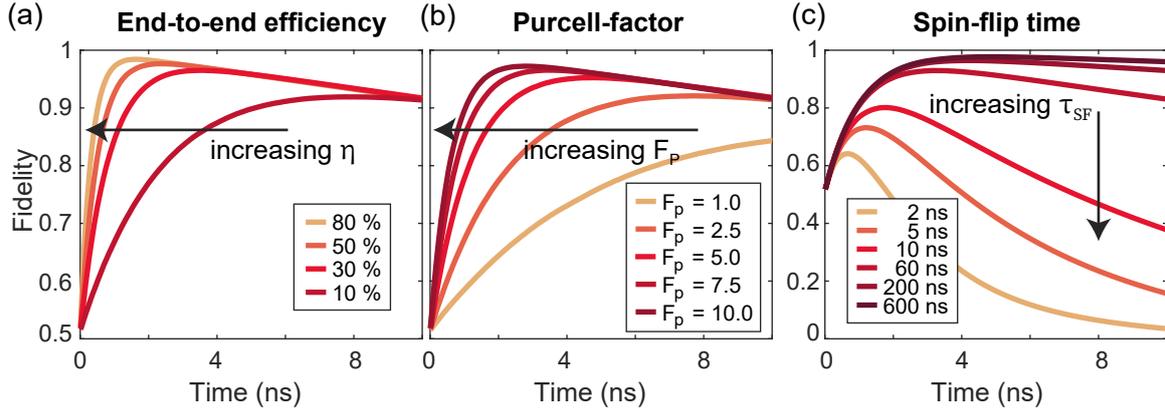


Figure 6.4: Simulation of the fidelity as a function of readout time for different (a) overall efficiencies, (b) Purcell factors and (c) spin-flip times. While one of the parameters is varied, the other two are set to the experimental conditions: $\eta = 25\%$, $F_P = 6.1$, and $\tau_{SF} = 158$ ns. All simulations are performed at six times the saturation power including 1.4% laser leakage at 3 ns readout duration.

is very sensitive to the exact cavity detuning; a small shift could result in a slightly lower Purcell factor. The effect of a lower Purcell factor in our simulations is similar to that of a lower efficiency. Other explanations could be a deterioration in either the in-coupling efficiency (such that the power exceeds the saturation power by a smaller margin than at $B = 0$) or the optical alignment thereby reducing the product $\eta_{\text{optics}} \cdot \eta_{\text{coupler}}$. We stress that this slight discrepancy between the predicted overall efficiency and the overall efficiency that matches best our experimental data has no impact on our readout fidelity analysis.

Calculation of the readout fidelity

The fidelity of the spin-readout is defined as¹⁹⁰

$$\mathcal{F}(t) = 1 - p_{\text{bright}} \cdot e_{\text{bright}}(t) - p_{\text{dark}} \cdot e_{\text{dark}}(t), \quad (6.2)$$

where p_{bright} (p_{dark}) is the occupation probability of the bright (dark) state. The spin occupation probability distribution depends on the spin-flip rates, as well as the readout pulse duration and repetition rate; for our experiments it is approximately 50:50 ($\rho_{\uparrow\uparrow} : \rho_{\downarrow\downarrow}$, with ρ the density matrix of the spin).

The readout projects the spin into either the bright state or the dark state; the readout process records an outcome, either bright or dark. If the spin is projected into the bright (dark) state but readout as dark (bright) then the error is e_{bright} (e_{dark}). These error probabilities are time-dependent in that they depend on the duration of the readout pulse.

The errors in the readout have several origins. The bright spin state is correctly assigned if a photon is measured. Therefore, photon loss is an important source of readout error. The overall system efficiency η therefore contributes to e_{bright} . This source of error can be quantified by isolating this loss process in a simulation which takes the experimental value of η but without back-action and without a spin-flip process. This results in $C(t)$, the cumulative distribution function for collecting a count as a function of time induced by a readout pulse starting at $t = 0$. Another source of error for the bright state readout is a spin flip during the readout process: the QD can be projected into the bright state by the readout pulse but if it flips to the dark state before a photon is detected the spin is assigned

incorrectly. These combined contributions to e_{bright} result in:

$$e_{\text{bright}}(t) = 1 - C(t) + C(t) \cdot [1 - \exp(-t/\tau_{SF})] = 1 - C(t) \cdot \exp(-t/\tau_{SF}), \quad (6.3)$$

where τ_{SF} is the spin-flip time. In our experiments the error probability $e_{\text{bright}} = 6.9\%$ at 3 ns, as shown in Fig. 6.2c.

The dark state readout error also has two origins. First, the readout can project the spin into the dark state yet be recorded as the bright state should a laser photon leak into the collection channel and be detected. This error can be estimated and taken into account by measuring the count fraction $C_d(t)$ on turning off the QD, i.e. detuning the QD with respect to the readout laser (in practice via the gate voltage). Second, as for the bright state, a spin-flip can lead to an error: the readout can project the spin into the dark state yet be recorded as bright if a spin-flip from dark-to-bright state occurs followed by photon detection. The analysis of the second error is more complicated than that of the first. If the spin flips from the dark to the bright state, a photon can be emitted and counted. This takes place with the same time-dependence as $C(t)$, but shifted in time by the location in time of the spin-flip. This effect can be taken into account by a convolution of the shifted count fraction with the spin-flip probability. The combined readout error is therefore:

$$e_{\text{dark}}(t) = C_d(t) + \frac{1}{t} \int_0^t C(t - \tau) \cdot [1 - \exp(-t/\tau_{SF})] \cdot d\tau. \quad (6.4)$$

For a 3 ns readout pulse, the error probability $e_{\text{dark}} = 2.6\%$. For short readout times, the error in reading out the state e_{bright} is high, as not enough time has elapsed to ensure that one of the QD photon is detected by the detector. For longer readout times, the probability of a spin-flip increases, and hence the probability of detecting a photon from the dark state via a spin flip to the bright state (e_{dark}) increases. Hence, there is an optimal readout time for which the fidelity can be maximised. By plugging Eq. 6.3 and 6.4 into Eq. 6.2, we can calculate the fidelity of the readout as a function of the readout time; this is shown in Fig. 6.2b. We carry out this calculation on tuning the cavity to the higher-frequency trion and, separately, on tuning the cavity to the lower-frequency trion. The simulated count fractions show very good agreement with our experimental results and allow us to extract a maximum readout fidelity of $(95.2 \pm 0.7)\%$ in 3 ns. The calculated readout fidelity as a function of readout-time for the configurations with $|\uparrow\rangle$ and with $|\downarrow\rangle$ as the bright state is plotted in Figs. 6.2b and c, respectively.

Figure 6.4 shows the dependence of the fidelity on the end-to-end efficiency (Fig. 6.4 a), Purcell factor (Fig. 6.4 b) and spin-flip time ((Fig. 6.4 c). In Fig. 6.4 when one of the parameters is varied, the others are set to match our present experimental conditions. However, for realistic improvements to all of these parameters simultaneously the readout can be significantly improved, as we now discuss.

6.3.5 Predictions for optimised system and Voigt geometry

Based on the success of the Monte-Carlo method in describing the experimental results, we can estimate the achievable fidelity for an optimised system as well as for single-shot readout in the Voigt geometry. We assume that the issue of imperfect laser suppression at the exact cavity resonance (Sec. 6.3.3) can be overcome. We assume also that another QD can be selected – we note that other QDs in the same sample show higher Purcell factors¹⁹

than the QD used in these experiments – so that the Purcell factor can be increased from 6.1 to 12 without any modifications to the cavity. By reducing optical losses we estimate that $\eta_{\text{optics}} \cdot \eta_{\text{coupler}}$ can be increased from 55.2% to 90%. Finally, single-photon detectors with quantum efficiency $\eta_{\text{detector}} = 95\%$ (instead of 82%) are commercially available, and could also be used. These improvements would lead to $\eta = 76\%$ and would allow single-shot readout in less than 1 ns with a readout fidelity of 99.5%.

Although our readout speed is extremely fast, a key question is whether we can read the spin state fast enough to overcome the back-action in the Voigt geometry (in-plane magnetic field) as this is the configuration required for spin control. With $F_P = 12$, the branching ratio is 92.3%. In the optimised case ($\eta = 76\%$), we expect we can achieve single-shot readout with a fidelity of 89.9% below 1 ns, while for our present experimental conditions, single-shot readout should already be possible with a fidelity as high as 77.4% in 3 ns. These readout fidelities are extremely promising. Our approach can thus overcome a key outstanding challenge, namely combining spin control and spin readout in one and the same QD spin.

6.3.6 Repeated readout and quantum jumps

The fast spin readout enables us to probe the electron spin dynamics. By repeated single-shot measurements of the spin state, we can determine the spin-flip time from the correlation between sequential measurements. Additionally, we can track the electron spin state in real time, observing quantum jumps as the spin flips. In Fig. 6.5 a we perform a pulse sequence consisting of two readout pulses separated by a time τ . Here we fix the length of both readout pulses to be 3 ns, and the pulse repetition time to be 400 ns. The first readout pulse is a projective measurement of the spin state: in effect, the spin is initialised at $\tau = 0$ with a fidelity given by either e_{bright} or e_{dark} . This approach of initialisation-by-readout provides an alternative to spin initialisation via optical pumping, and in our experiments

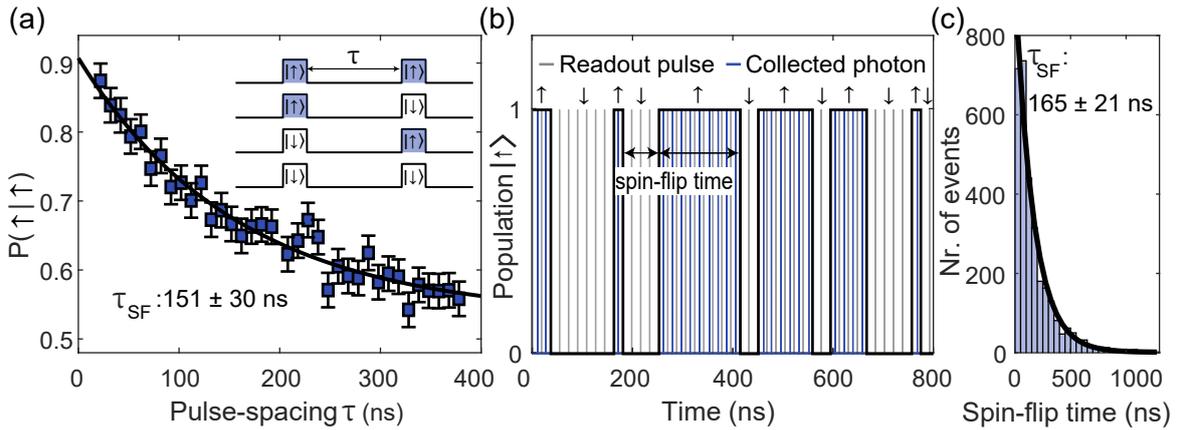


Figure 6.5: Repeated single-shot measurements and quantum jumps. (a) Conditional probability of measuring $|\uparrow\rangle$ given that the first measurement returned $|\uparrow\rangle$ for two sequential (3 ns duration) readout pulses as a function of τ , the delay between the pulses (the errorbars are one standard deviation). For short values of τ , the second measurement outcome is correlated with the first; for longer values of τ , the probability to acquire the same outcome decreases exponentially, revealing a spin-flip rate of about 151 ± 30 ns. (b) By repeatedly measuring the spin state with excitation pulses spaced by 15 ns (above the detector’s dead time), we observe quantum jumps of the spin state. (c) The time between the spin flip events in (b) are extracted for a total measurement time of 2.4 ms and are summarised in a histogram. The distribution of the events reveals a spin-flip time of 165 ns, matching well the result of the two-pulse measurements in (a).

results in a higher spin initialisation fidelity ($F_{\text{init}}^{|\uparrow\rangle} = 93.1\%$ and $F_{\text{init}}^{|\downarrow\rangle} = 97.4\%$ with $|\uparrow\rangle$ as the bright state, compared to $F_{\text{init}}^{|\uparrow\rangle,|\downarrow\rangle} \sim 67\%$ for optical pumping). The second readout pulse can then be used to determine the spin state at $\tau > 0$ allowing us to measure the correlation between the two measurement outcomes as a function of τ . Figure 6.5 a shows the conditional probability of measuring spin $|\uparrow\rangle$ in the second pulse (as a function of τ), given that the first read result returned $|\uparrow\rangle$. We note that the minimum spacing between the two pulses is limited to $\tau \gtrsim 15$ ns by the dead time of the detector. Increasing τ decreases the probability of reading out the same spin state for both pulses due to spin flips, and for large τ the second read is completely uncorrelated with the first. By fitting an exponential decay to the data in Fig. 6.5 a, we extract a spin-flip time of 150 ± 30 ns. Furthermore, the limit as $\tau \rightarrow 0$ of this conditional probability is approximately $1 - e_{\text{bright}}$, confirming the value of e_{bright} determined from the Monte Carlo simulations. Similarly, a measurement of the dark-dark conditional probability confirms the value of e_{dark} .

Given that our readout sequence is much shorter than the spin lifetime, we can use repeated single-shot measurements to detect real-time quantum jumps of the electron spin state. For that purpose, we send in a train of 3 ns readout pulses spaced by 15 ns, slightly above the minimum allowed by the detector's dead time. We observe quantum jumps in the spin state, as shown in Fig. 6.5b. (In the original quantum jump experiment, the quantum jumps between the bright and dark states were driven with weak coherent excitation.¹⁹⁷ Here, the jumps are driven by a dissipative process, energy exchange with the Fermi sea via co-tunneling.) The time between spin-flip events during a 2.4 ms total acquisition period is extracted and summarised in the histogram in Fig. 6.5c. From the exponential decay in the number of events per flip time, we can extract the spin-flip time to be approximately 165 ns, consistent with the results from the double-pulse experiment in Fig. 6.5a.

6.3.7 Continuous wave quantum jumps measurements

Complementary to the experiments demonstrating quantum jumps using rapidly repeated readout pulses shown in Fig. 6.5b, we also observed quantum jumps using continuous wave

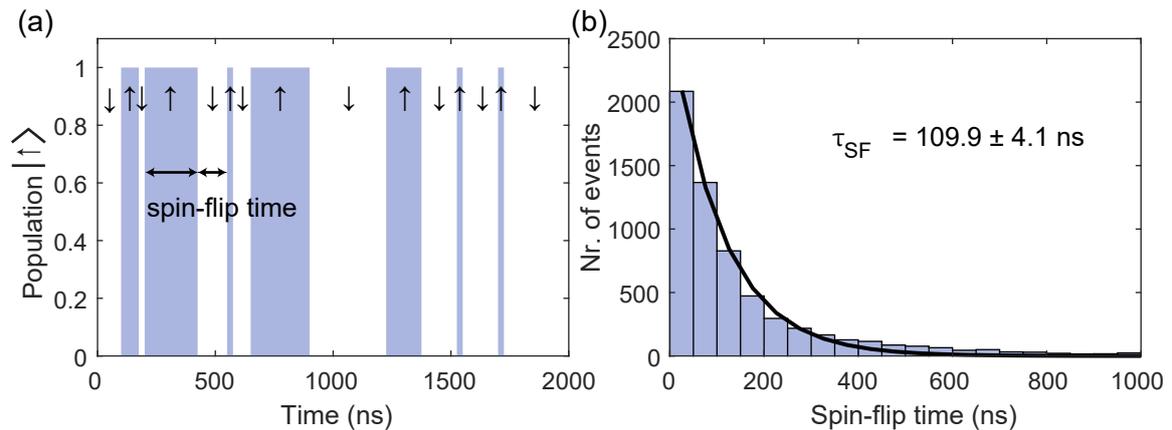


Figure 6.6: CW quantum jumps (a) Normalised photon counts as a function of detection time. The quantum jumps between the two spin states can be observed and the time over which the spin remains the same can be extracted. (b) Histogram of the extracted times between spin-flip events reveals an exponential decay. The spin-flip time is extracted from an exponential fit to be (109.9 ± 4.1) ns.

(CW) excitation. A CW laser set to four times the saturation power of the bright state transition was used, and the emitted photons were routed (via cascaded 50:50 beam splitters) to four SNSPD detectors. In contrast to the pulsed single-shot readout experiments in Sec. 6.3.6 (where only one SNSPD detector was used), we used four detectors to mitigate partially the impact of the detectors' dead time. We note that the addition of the cascaded beam splitters reduces the overall system efficiency. We measured the signal on all four detectors simultaneously, and the resulting counts registered by the four detectors were then added together. If at least one photon is measured in a time-bin, the state is assigned spin up ($|\uparrow\rangle$). If no photon is detected, the state is assigned spin down ($|\downarrow\rangle$). A fraction of these quantum jumps is shown in Fig. 6.6a.

The CW quantum jumps we observe provide an additional method to characterise the spin-flip rates in our system, as τ_{SF} can be directly extracted from the waiting-time distributions for $|\uparrow\rangle$ and $|\downarrow\rangle$. The time over which the spin state remains the same is extracted over an experiment of 50 ms duration, and its distribution is shown as a histogram in Fig. 6.6b. By fitting the decay in the histogram we determine a spin-flip time of $\tau_{\text{SF}} = 109.9.9 \pm 4.1$ ns. The result is slightly lower (although broadly consistent) with the spin-flip time extracted from the $g^{(2)}(\tau)$ recorded using the same laser power (Sec. 6.4.1); the present experiment was performed slightly offset from the exact charge plateau centre, which may explain the difference. Due to partial spin-pumping with CW excitation (see Sec. 6.4.2), the observed spin-flip time is slightly smaller than that measured with pulsed excitation (165 ns, Sec. 6.3.6).

6.4 System analysis via autocorrelation functions

6.4.1 Extraction of spin lifetime from $g^{(2)}(\tau)$

We can characterise the spin-flip rate in our experiment by measuring the second-order correlation function of the resonance fluorescence $g^{(2)}(\tau)$. By driving only one of the Zeeman-split trion states, spin-flips are observed as blinking in the QD fluorescence as the spin state switches between the on-resonance (bright) and off-resonance (dark) states. This blinking

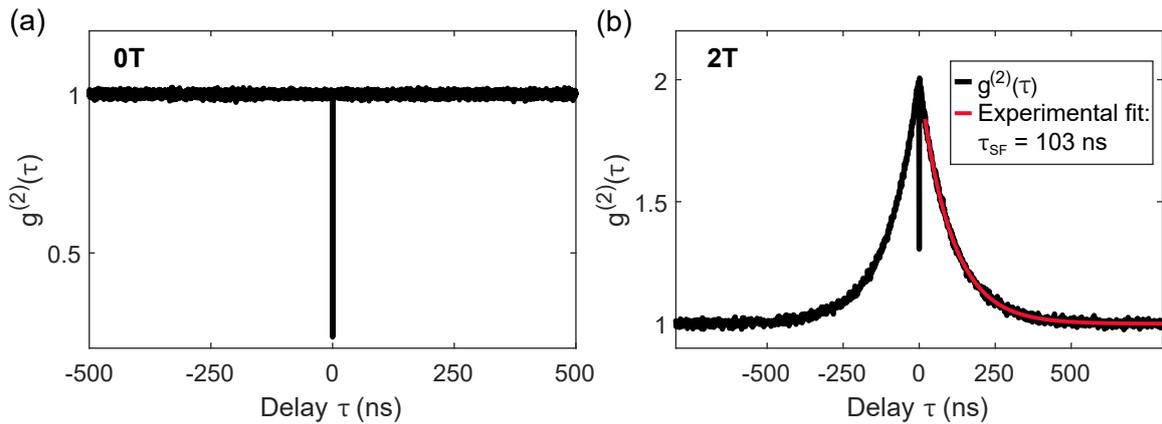


Figure 6.7: Second-order correlation function at 0 T and 2 T. (a) At $B = 0$ T the $g^{(2)}(\tau)$ features anti-bunching at $\tau = 0$ but no bunching out to $\tau = 500$ ns, demonstrating that the QD emission is stable on this timescale. (b) $g^{(2)}(\tau)$ at $B = 2$ T while resonantly driving the higher-frequency trion state. The QD emission shows clear bunching. We fit the $g^{(2)}(\tau)$ with an exponential decay to determine the spin-flip rate. The data shown here is acquired with a laser power equal to the QD saturation power; from the fit we extract $\tau_{\text{SF}} = 103$ ns. The maximum bunching $g_{\text{max}}^{(2)} \sim 2$ means that the spin resides in each state for approximately half the time.

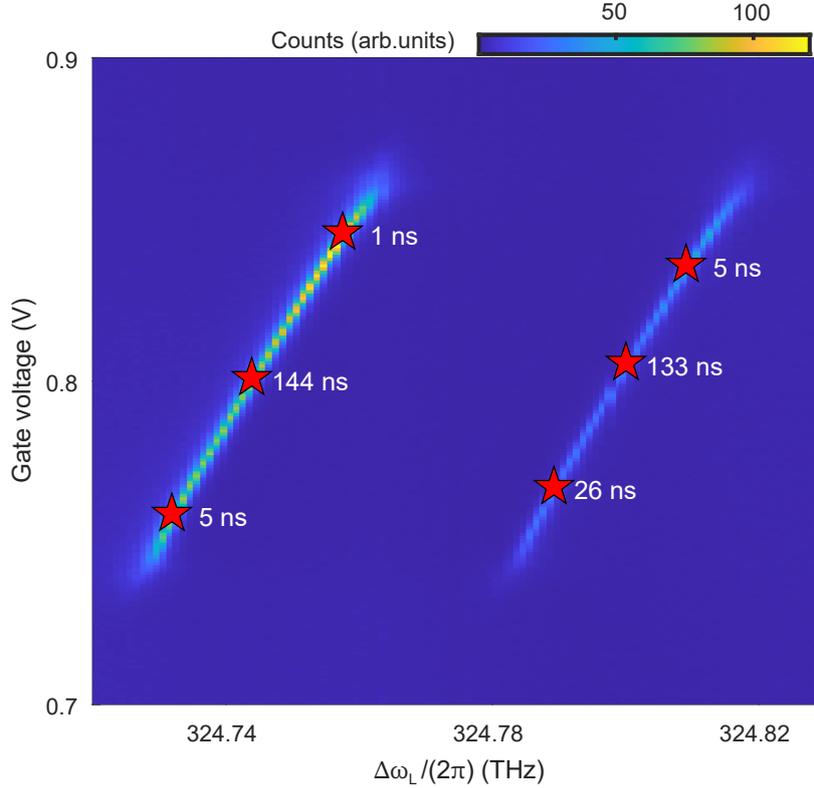


Figure 6.8: Spin lifetime as a function of position within the charge plateau. To map out the charge plateaus, the QD fluorescence was collected as a function of excitation laser frequency ($\Delta\omega_L/(2\pi)$) and gate voltage applied across the diode structure. The applied magnetic field is 2.0 T, resulting in a splitting of ~ 55 GHz between the two vertical optical transitions. The red stars indicate positions on the Zeeman-split plateaus for which the spin lifetime was measured (as described in Fig. 6.7b). The spin lifetime decreases at the plateau edges to very small values, a clear sign of co-tunnelling. However, even in the plateau centre the longest spin lifetime time we observe is 144 ns, also determined by co-tunnelling. We note that to acquire this data we adjust the cavity length when the laser frequency is stepped such that the laser remains on resonance with the cavity.

results in bunching of the $g^{(2)}(\tau)$ -function.¹⁹⁸ This blinking is not present at zero magnetic field, where the trion states are degenerate such that both spin states are driven with a resonant linearly-polarised laser. Figure 6.7a shows $g^{(2)}(\tau)$ measured at zero magnetic field for the X^- transition of the QD used in our experiments. As expected for a single emitter, anti-bunching is observed at $\tau = 0$. Away from $\tau = 0$, the $g^{(2)}(\tau)$ is flat with no significant bunching observed, indicating that the QD emission is stable.

Figure 6.7b shows a similar $g^{(2)}(\tau)$ -measurement, now for an out-of-plane magnetic field $B = 2.0$ T. Here, the laser drives the higher-frequency trion state, and clear bunching is observed. By fitting the measured $g^{(2)}(\tau)$ to an exponential decay, we can extract the characteristic timescale on which the QD emission switches on and off. Because the switching between bright and dark states occurs purely due to spin flips, the timescale of the bunching decay is a direct measurement of the spin lifetime, τ_{SF} .¹⁹⁹

We measured the $g^{(2)}(\tau)$ and extracted τ_{SF} for several different positions on the X^- charge plateau. The results are summarised in Fig. 6.8, where the red stars indicate the charge plateau position at which each experiment was performed. The data in Fig. 6.8 were acquired using low laser powers, significantly below the saturation power. The spin lifetime is very short, a few nanoseconds, at the edges of the charging plateau, and reaches a modest value,

~ 140 ns, at the centre of the plateau. These are the hallmarks of co-tunneling,^{64,200} a process in which a combined tunnelling process swaps an electron confined to the QD with an electron close to the Fermi energy in the Fermi sea. From the measured spin lifetimes, it is clear that co-tunneling determines the spin lifetime even at the centre of the plateau. The observed maximum spin lifetime of 144 ns is orders-of-magnitude less than the expected intrinsic spin lifetime via a phonon-mediated process at this magnetic field: previous experiments using InAs QDs have demonstrated ~ 20 ms at similar magnetic field strengths.^{187,200} The relatively fast co-tunneling is a consequence of the 25 nm-thick tunnel barrier, the distance separating the back contact and QD-layer in the heterostructure.

We note that due to the high speed at which we can perform single-shot spin readout, the relatively short co-tunneling induced spin-flip time that we observe is not the limiting factor for the readout fidelity. For a readout time of 3 ns, we would expect a spin flip during the readout pulse in only $1 - \exp(-3/144) \sim 2\%$ of readout attempts.

For the low powers used in Fig. 6.8, we do not observe spin pumping, for which the typical signature is a region of decreased signal at the centre of the charge plateau: in spin pumping, the excitation results in occupation of the dark spin state.^{141,175} The absence of a spin pumping signature in Fig. 6.8 indicates that the spin pumping rate is significantly smaller than the spin flip rate. Spin pumping arises via spin-nonconserving spontaneous emission, a diagonal transition, Fig. 6.2a. (The spin-conserving recombination is the vertical transition, Fig. 6.2a.) The branching ratio is the ratio of the diagonal to vertical recombination times. It can be inferred from the $g^{(2)}(\tau)$ recorded with optical driving powers above saturation power. Specifically, the branching ratio can be extracted from $g^{(2)}(\tau)$ by solving the incoherent part of the optical Bloch equations, i.e. the rate equations describing the populations of the three relevant QD levels.²⁰¹ Following this process, we extract a branching ratio of $\Gamma_s/\gamma_d = 600 \pm 200$ (where Γ_s is the vertical spin-conserving decay rate, and γ_d the diagonal spin-nonconserving rate). This branching ratio applies to the experimental conditions for the readout process in which one of the vertical transitions is in resonance with the cavity.

Spin-nonconserving spontaneous emission is the origin of back-action in the spin readout process and is weakly allowed due to heavy-hole light-hole mixing in the QD as is discussed in Ch. 2.1.1. For single-shot readout, the branching ratio must be high enough for the spin state to be assigned with high fidelity before a laser-induced spin-flip transition occurs. This is the case here. In fact, the branching ratio is sufficiently high that back-action is a negligible source of readout error in these experiments.

6.4.2 Spin initialisation by optical pumping

One strategy for demonstrating single-shot spin readout is to first initialise the spin in a known state, then perform the readout sequence. By comparing the spin state attributed during readout with the initially prepared state, the readout fidelity can be quantified. This method relies on the ability to initialise the spin state with high fidelity. In our experiments, the combination of a modest spin lifetime together with a large branching ratio make the initialisation of a known spin state via optical pumping challenging. The maximum spin pumping rate that we were able to achieve was comparable to the co-tunnelling rate in the centre of the plateau. Figure 6.9a shows a plateau map similar to Fig. 6.8 using a significantly higher excitation laser power (approximately twice the saturation power). We now observe decreased fluorescence intensity in the plateau centre, consistent with spin pumping. However, rather than near-complete extinction of the fluorescence, the signal at the plateau centre is

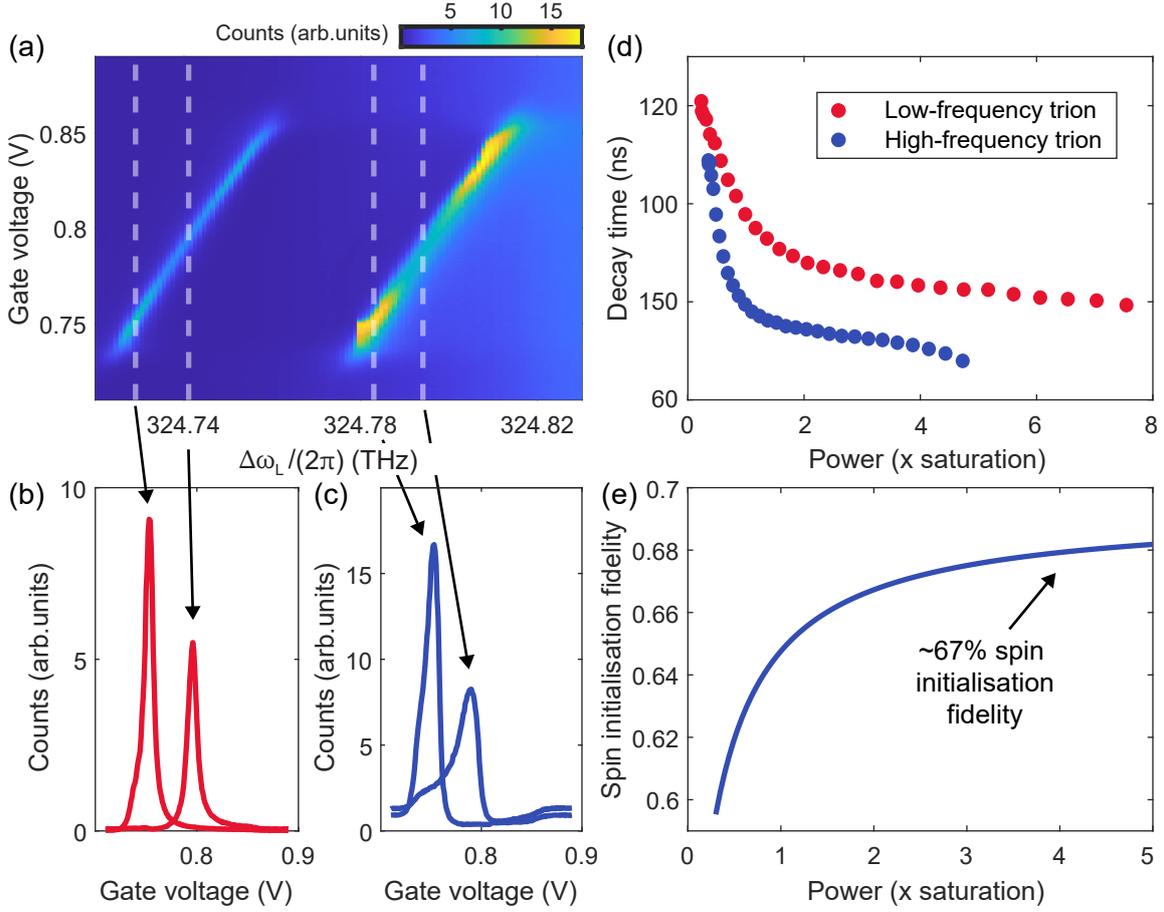


Figure 6.9: Partial optical spin initialisation. (a) Plateau map acquired with a laser power twice the saturation power. We observe a reduction in signal at the plateau centre, consistent with optical spin pumping. However, comparing the signal in the centre of plateau with that at the edges in the fast co-tunnelling regime suggests a poor spin initialisation fidelity. (b) Comparison of fluorescence signal for the low-frequency trion in the fast co-tunnelling regime (left, lower gate voltage) and in the plateau centre (right, higher gate voltage). (c) Similar to (b) but for the high-frequency trion. (d) Spin-flip times as a function of excitation laser power measured at the centre of the charge plateau, resonantly driving the low-frequency trion (blue data points) or the high-frequency trion (red data points). (e) Estimated spin initialisation fidelity from solving the rate equations using spin-flip rates extracted from (d). Based on this analysis, a maximum spin initialisation fidelity of $\sim 67\%$ is expected.

reduced by only a factor of about two (Figs. 6.9b,c) compared to at the edges where rapid co-tunnelling prohibits spin pumping. The incomplete suppression of fluorescence in the centre of the charge plateau indicates that our spin initialisation fidelity using optical spin pumping is likely to be modest. To quantify the achievable spin initialisation fidelity, we measured the spin-flip rate near the centre of the charge plateau as a function of laser power. The result is shown in Fig. 6.9d; the two curves show τ_{SF} for the laser resonant with the high-frequency trion transition or the lower-frequency trion transition.

We solve the incoherent part of the optical Bloch equations to estimate the population of the spin initialisation target state (equivalent to the initialisation fidelity) as a function of the initialisation laser power, shown in Fig. 6.9e. We find that the achievable initialisation fidelity saturates to a rather low value; for a laser power of four times the QD saturation power, the initialisation fidelity (defined as $|\langle\psi_{\text{actual}}|\psi_{\text{target}}\rangle|^2$) is approximately 67%.

With such a low initialisation fidelity, a measurement sequence of first initialising the spin before readout is impractical, as the initialisation fidelity would dominate the total sequence fidelity and obscure the actual readout error. Instead, to characterise our single-shot readout fidelity we repeat our readout sequence with a delay comparable to the plateau-centre spin lifetime, which results in an approximately 50:50 spin state occupation probability over the course of a large number of sequential readout sequences. As discussed in Sec. 6.3.4, by characterising each readout error process individually we can determine the overall readout fidelity.

We stress that the inability to initialise the spin with high fidelity in these experiments is a consequence of the tunnel barrier thickness and does not represent a limitation of the scheme itself. High initialisation fidelities can be achieved by suppressing the co-tunneling at the plateau centre using a larger tunnel barrier.¹⁷⁵

6.5 Discussion

We have demonstrated that the frequency-selective Purcell enhancement provided by our optical microcavity enables us to perform single-shot readout of a QD spin state within a few nanoseconds, with a fidelity as high as 95%. Our results bring the spin readout time for semiconductor QDs close to the short optical spin manipulation times,^{86,177} and well below previously demonstrated relaxation (T_1)²⁰⁰ and dephasing (T_2^*) times.^{43,44,177} For recent loophole-free Bell tests, entangled nitrogen vacancy (NV) centres were positioned 1.28 km apart to allow 4.27 μs for the Bell sequence to be performed such that the NVs are space-like separated.³ Of this 4.27 μs , 3.7 μs (corresponding to 1.1 km in free space) was used for the single-shot spin readout. Our rapid spin readout indicates that similar Bell tests could be performed using semiconductor QDs located significantly closer together, mitigating the challenge of synchronising experiments between different buildings; the separation distance enforced by our readout time is less than one metre. By combining the highly indistinguishable photons created by remote semiconductor QDs,²⁰² the high system efficiency of our microcavity,¹⁹ along with T_2^* -enhancement via cooling of the nuclear spins,^{43,44} high-fidelity spin-spin entanglement generation rates of a few tens of MHz are feasible.

We can foresee several ways to improve the readout time in our experiment even further. Most simply, the overall system efficiency can be increased by improving the detector system (fibre couplers and detector itself). Furthermore, it should be possible to operate at the true cavity resonance in an applied magnetic field, thereby at maximum Purcell factor. Our Monte-Carlo simulations show that these changes would allow single-shot readout with a fidelity of 99.5% in less than one nanosecond to be achieved.

We also note that although spin initialisation via optical pumping was not required for our present experiments, the ability to initialise the spin in a specific target state is important for future quantum technological applications. Spin initialisation via optical pumping has been achieved with fidelities $\gtrsim 99.8\%$ in similar QD samples,¹⁷⁵ and should be achievable in our system by increasing the tunnel barrier thickness between the QD layer and the n-doped Fermi sea to reduce the co-tunneling rate, which limited our initialisation fidelity to approximately 67% in the present experiments. Future experiments using devices with a larger tunnel barrier are strictly necessary to verify that high-fidelity spin initialisation can be combined with cavity-enhanced single-shot readout. Based on the detailed understanding of co-tunneling,²⁰⁰ chances of success are very high.

Given the efficient generation of single photons, fast spin initialisation and rotation, and now fast single-shot spin readout, the next step is the implementation of coherent manipulation of the spin-state together with spin readout. Fast spin manipulation relies on a Raman transition that is naturally established in an in-plane magnetic field (Voigt configuration). In this case, the four transitions (Fig. 6.2a) have equal optical dipole moments such that readout back-action is maximal: spin readout becomes challenging. With our approach, this longstanding problem, spin readout in the Voigt geometry, can be solved: the resonant cavity restores a spin-conserving process, i.e. a cycling transition; the high overall system efficiency enables a readout outcome before back-action occurs. Our simulations show that in the Voigt configuration, readout on the same timescale with a fidelity of up to 89.9% is feasible.

Coherent spin control of InAs QDs typically uses a Raman laser detuned by $\gtrsim 200$ GHz from the QD resonance; in our cavity system this laser can access the QDs via a waveguide-like mode propagating perpendicular to the cavity axis along the sample surface. This side-excitation strategy has previously been used to demonstrate resonance fluorescence in similar QD samples,²⁰³ and is conceptually similar to the side-access control used in trapped atom cavity systems.²⁰⁴ Alternatively the Raman transition can be driven directly through the cavity; field enhancement inside the cavity is proportional to \sqrt{F} (where $F = 506$ is the cavity finesse), and for our one-sided cavity the intra-cavity field is enhanced out to detunings of $2\kappa\sqrt{F}/\pi = 468$ GHz (where $\kappa = 25$ GHz is the cavity linewidth), suitable for coherent spin control as is demonstrated in Ch. 7, where coherent manipulation of a hole spin via a Raman transition is achieved. Our cavity platform is thus capable of integrating rapid QD spin control, readout and photon emission simultaneously, and is an exceptional platform for spin-photon technologies such as the generation of photonic cluster states.

7

Fast optical manipulation of a coherent hole spin in a microcavityⁱ

7.1 Summary

The implementation of an optimal spin-photon interface is one of the key challenges for the development of quantum networks. Physical platforms under investigation span the range of modern experimental physics, from ultra-cold atoms to solid-state physics. However, it is not easy to implement an ideal spin-photon interface that successfully combines fast, high-quality and high-efficiency photon emission with a highly coherent spin. Here we show an interface that combines state-of-the-art photonic emission with a highly coherent spin. Our system is based on an InAs quantum dot (QD) coupled to an optical microcavity; the same system has previously demonstrated a single-photon source with GHz repetition rates and 57% end-to-end efficiency. By imprinting a microwave (MW) signal onto two Raman fields we achieve coherent rotations of a QD hole spin around an arbitrary Bloch sphere axis, achieving a maximum π -pulse fidelity of 98.26%. Furthermore, we observe ultra-fast Rabi frequencies of up to 1 GHz. We demonstrate all-optical cooling of the QD nuclear spin ensemble via the QD hole spin, extending the T_2^* time from 30 ns to 500 ns. The hole spin T_2^* times are measured via Ramsey interferometry; we observe a transition in the Ramsey decay envelope from Gaussian to exponential as we cool the nuclear ensemble. Finally, we show that we can access collective magnon states of the QD nuclear ensemble via the hole spin. Our system shows exceptional promise for a wide range of key tasks in quantum information science, from the generation of entangled multi-photon graph states to the development of an efficient nuclear memory.

7.2 Introduction

The ability to generate entanglement between flying photonic qubits and stationary matter qubits (such as a coherent spin) is a key challenge in quantum information science.^{9,205} Spin-photon entanglement provides the basis for a distributed quantum network; entangled multi-photon graph states can also be generated using the stationary qubit as an entangling mediator for sequentially emitted photons.^{17,178,204} Such graph states are the central resource

ⁱThe content in this chapter has been measured and analysed in equal contribution with Mark R. Hogg.

for optical measurement-based quantum computing,^{14,206,207} as well as all-optical quantum repeaters.^{208,209}

Typical schemes for creating spin-photon entanglement rely on spin-dependent optical selection rules, which allows quantum correlations between the spin and a photonic degree of freedom to be generated. Promising platforms for generating spin-photon entanglement include trapped atoms,^{34,35} defects in diamond^{31,210,211} and semiconductor QDs.^{180–182,212,213} In all cases extracting coherent photons from the emitter with high efficiency is crucial to generate large entangled resource states. Additionally fast photon emission is desired to increase the transmission rate in quantum networks.

Semiconductor QDs stand out as having exceptional photonic properties. Highly indistinguishable photons have been demonstrated from individual^{19,46} and remote²⁰² QDs; by using optical microcavities to Purcell enhance the QD emission single photon sources with GHz repetition rates and end-to-end efficiencies exceeding 50% have been demonstrated.¹⁹ However, the poor electron spin coherence ($T_2^* \sim 1\text{-}3\text{ ns}$) represents a long-standing challenge for spin-photon entangled technologies, leading to poor fidelities and limiting the size of photonic graph states that can be produced.¹⁸²

QD spin coherence can be improved by using a hole spin,^{87,186} for which the lack of a contact hyperfine interaction reduces the sensitivity to magnetic noise from the host nuclei,⁸⁸ the main source of spin dephasing. The hyperfine interaction for a hole spin in an InAs QD depends on the composition of the valence states: for a pure heavy-hole (HH) spin, the hyperfine interaction can be suppressed with an in-plane magnetic field.^{88,186} A wide range of hole spin T_2^* times have been reported in the literature, ranging from 2.3 ns²¹⁴ to 460 ns.¹⁸⁶ The most direct method for measuring the hole spin T_2^* time is via Ramsey interferometry; experiments using this technique have typically found T_2^* times of 30-50 ns,²¹⁵ an order of magnitude longer than for the electron spin. The reason for the large variation of reported literature values could be related to spin decoherence via electrical noise varying between differently grown devices, but it generally remains an open question.

More recently, strategies to improve QD spin coherence by cooling the host nuclear spins to a reduced-entropy state have been developed,^{43,44,216} resulting in electron spin T_2^* times of up to 600 ns.²¹⁷ The narrowing of the Overhauser field has enabled the observation and coherent manipulation of collective nuclear magnon modes via the electron spin.^{43,218} However, such nuclear cooling strategies rely on flexible coherent control of the central electron spin with precisely tunable Rabi frequencies, which has been achieved with two optical fields red-detuned from the QD resonance to drive a two-photon Raman process.¹⁷⁷ Combining coherent control of a QD spin with the resonant optical microcavities required for high-efficiency photon extraction is an important outstanding challenge. Additionally, all previous single-QD nuclear cooling experiments used an electron spin;^{43,44} cooling via a hole spin (possessing a more complex hyperfine interaction) has yet to be demonstrated.

Here we achieve the best of all possible worlds: we implement high-fidelity coherent control of a QD hole spin integrated into an optical microcavity with an extremely high photon collection efficiency. We demonstrate coherent optical control of the hole spin using a two-photon Raman process; we show that coherent control is compatible with our efficient microcavity architecture without major modifications to the cavity setup. We show that the cavity can be used to enhance the Raman fields, and demonstrate coherent control of a QD hole spin with Rabi frequencies of up to 1 GHz ($\sim 17\%$ of the Larmor frequency, towards the breakdown of the rotating wave approximation). The flexible coherent spin

control is an enabling technique to access interactions between the central hole spin and the host nuclear spins; we use this capability to perform all-optical cooling of the host nuclear ensemble, extending our hole spin T_2^* time from 30 ns to 500 ns. Interestingly we observe a transition from a Gaussian to an exponential Ramsey decay as the nuclear ensemble is cooled, suggesting our T_2^* time might no longer be limited by slow non-Markovian Overhauser field fluctuations.²¹⁹ We then show that a hole spin can also be used to generate collective magnon states of the host nuclear ensemble.

Our results demonstrate that a QD coupled to an optical microcavity is an ideal platform for spin-photon entangled technologies, combining exceptional optical properties with high-fidelity spin control.

7.3 Experimental Setup

Our system consists of an InAs QD device coupled to a tunable optical Fabry–Pérot microcavity (see App. A for further details of the device and cavity construction). The bottom cavity mirror is integrated into the QD device heterostructure, separated by an air-gap from the free-standing top mirror. Importantly the cavity mode position can be moved using xy nanopositioners to select an arbitrary QD on the sample, and the resonance frequency of the cavity can be tuned by changing the cavity length with a z-positioner. Furthermore, the cavity is split in frequency (by ~ 50 GHz) into two linearly polarised cavity mode that are orthogonal to one another (H - and V -polarised modes). The same cavity-coupled QD device has previously been used to demonstrate a single-photon source with an end-to-end efficiency of 57% and GHz repetition rates.¹⁹ A magnetic field of 2.9 T is applied perpendicular to the growth direction of the QDs (Voigt geometry). Figure 7.1a shows a schematic of the cavity setup and Fig. 7.1b the level structure of the QD in the given configuration. The magnetic field splits the ground state into two hole spin states $|\uparrow\rangle, |\downarrow\rangle$ with Zeeman splitting $Z_h = 5.8$ GHz at 2.9 T. This corresponds to a hole g-factor of $g_h = 0.143$ (defined as a hole pseudospin with spin $\pm \frac{1}{2}$). The vertical and diagonal transitions are H and V polarised, respectively (compare selection rules Ch. 2.1). Using the quarter-wave plate (QWP) in the microscope head (compare App A), the QD and cavity polarisations can be aligned such that the collection cavity polarisation, i.e. the cavity mode with the polarisation matching the

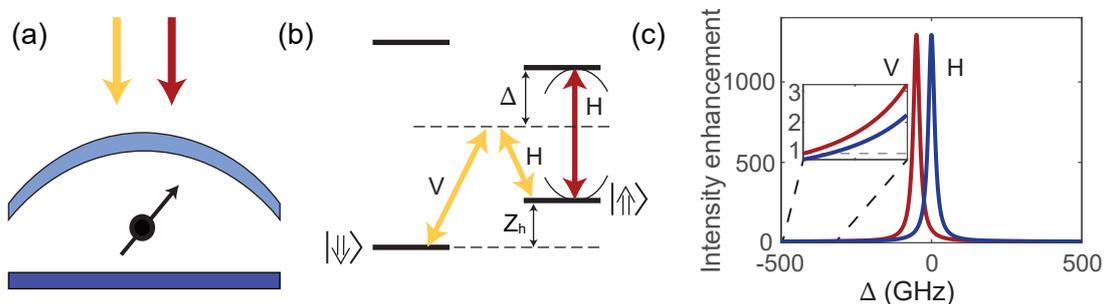


Figure 7.1: Coherent control of a hole spin in a microcavity. (a), (b) Illustration of spin control in a one-sided cavity. A laser resonant with the collection cavity (H -polarised, red) is used for spin initialisation and readout and a detuned laser (circularly-polarised, yellow) for coherent control of a hole spin via a Raman transition. (a) Schematic of the cavity. (b) QD energy level structure. (c) Calculated optical intensity enhancement factor inside the two cavity modes as a function of the laser detuning Δ . At a detuning of 448 GHz (498 GHz), the $H(V)$ -cavity field intensity equals the input field intensity.

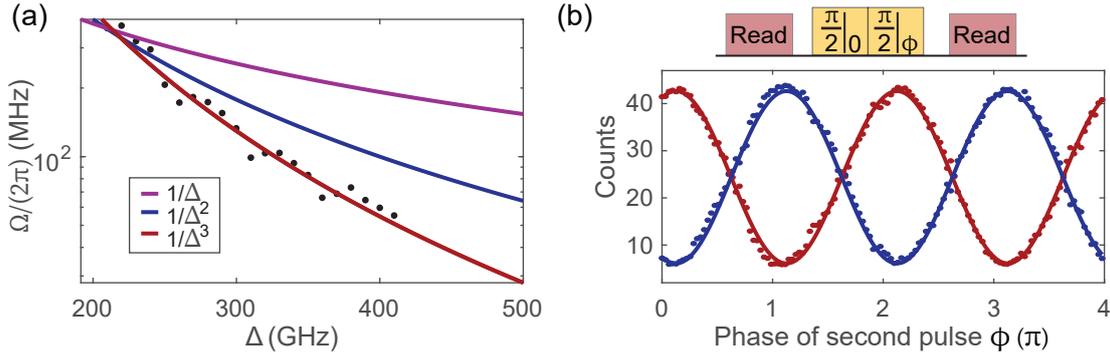


Figure 7.2: Coherent control of a hole spin in a microcavity. (a) Experimental Rabi frequency Ω as a function of the Raman laser detuning Δ . Theory curves for $1/\Delta^n$ with $n = 1, 2, 3$ confirms the $1/\Delta^3$ dependence of Ω as expected from the quadratic dependence of the cavity enhancement. (b) Top: pulse sequence for multi-axis phase control. Two $\pi/2$ pulses are sent right after each other. The phase of the second pulse is swept from 0 to 2π . Bottom: readout signal as a function of the phase ϕ of the second pulse for the initial pulse having phase 0 (red) and π (blue). The signal oscillates with a period of π .

collection arm of the dark-field microscope,¹³⁷ is perpendicular to the polarisation of the vertical transition that is used for spin readout.

A laser resonant with both the H -cavity and the lowest frequency vertical exciton transition (red arrow) is used to initialise the spin to $|\downarrow\rangle$ via optical pumping and to probe the $|\uparrow\rangle$ population for spin readout. The spin can be rotated by a two-frequency Raman pulse that is red-detuned from the resonant laser. It is generated by amplitude-modulation of circularly-polarised light with an electro-optic modulator (EOM) driven by an AWG and provides multi-axis control of the spin state in the Bloch sphere¹⁷⁷ as demonstrated in Fig. 7.2b.

7.4 Spin control in a microcavity

7.4.1 Coherent control of a hole spin

The cavity has a linewidth of $\kappa = 25$ GHz and a finesse $F = 506$. For optimal photon collection efficiency, the cavity must be resonant with one of the QD transitions. However, coherent control of the QD spin requires Raman laser detunings satisfying the criteria $\Delta \gg \Omega_R/(2\pi)$ to avoid populating the trion states, which randomises the spin when the trion decays (here Δ is the Raman laser detuning and Ω_R is the optical Rabi coupling of the two Raman fields, assumed to be equal). In practice, Raman detunings of $\sim 100 - 1000$ GHz are typically used. A challenge for spin control in a cavity is thus how to couple the detuned Raman fields to the resonantly coupled QD. Fortunately we find that the optimal cavity parameters for efficient photon collection are also well suited to driving spin rotations: the Raman fields can be coupled in via the detuned *tails* of the Lorentzian cavity mode. On resonance a cavity mode enhances the input optical intensity by a factor of $\approx 8F/\pi = 1285$ for our $F = 506$. As a function of detuning from the cavity resonance, the intensity enhancement follows a Lorentzian profile that depends on the cavity linewidth. For our cavity parameters the optical intensity of the Raman lasers is still enhanced out to detunings of $\Delta \sim 448$ GHz (Fig. 7.1c), perfectly suitable for coherent spin control. For Raman detunings ≥ 448 GHz the cavity begins to suppress the input optical field as $1/\Delta^2$. However, for $\Delta \lesssim 448$ GHz the cavity actually enhances the Raman fields with the same quadratic dependence, allowing for

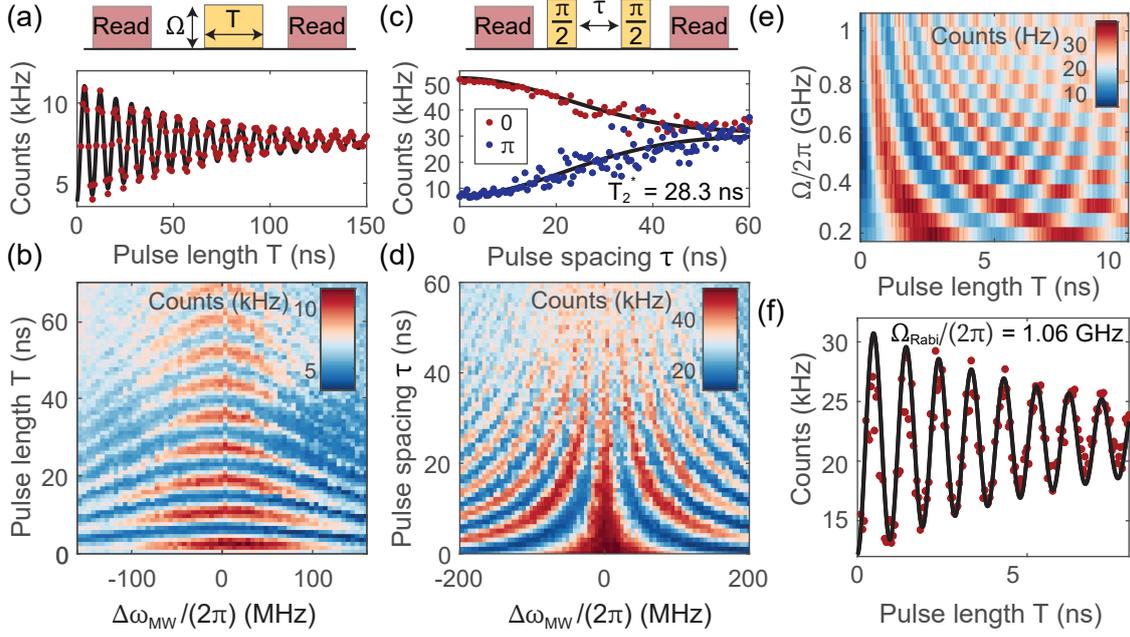


Figure 7.3: Fast spin manipulation. (a) Readout signal as a function of rotation pulse length T shows Rabi oscillations. (b) Rabi oscillations as a function of the MW detuning ($\Delta\omega_{\text{MW}}/(2\pi)$), i.e. the detuning of the Raman drive from the Zeemann splitting Z_h . (c) Ramsey interferometry of the readout signal as a function of pulse spacing τ between two $\pi/2$ pulses with a zero- (red) and a π -phase on the second pulse. A T_2^* of 28.3 ns is measured. (d) Ramsey interferometry as a function of $\Delta\omega_{\text{MW}}/(2\pi)$. (e) Rabi oscillations as a function of the Rabi frequency $\Omega/(2\pi)$ for high laser powers. (f) Rabi oscillations at $\Delta = 170$ GHz. Fast oscillations at 1.06 GHz oscillation frequency are measured.

ultra-fast coherent spin control in comparison to QDs not coupled to a microcavity. The full derivation of the field enhancement can be found in App. C.

All of this is true for both the H - and V polarised cavity modes. This is important as the circularly polarised rotation pulse couples into the cavity via the tails of both cavity modes. As the mode-splitting is smaller than the laser Raman laser detuning, both polarisations of the Raman laser couple in via one of the two cavity modes with similar enhancement as can be observed in Fig. 7.1c. The slight asymmetry in intensity enhancement can be compensated by having a slightly elliptical drive (achieved by rotation of the QWP).

We drive coherent rotations between $|\uparrow\rangle$ and $|\downarrow\rangle$ by optically driving the hole spin resonance (Fig. 7.3a) with Raman pulses of increasing pulse length T . We observe clear Rabi oscillations: when driving the Rabi oscillations as a function of the MW detuning $\Delta\omega_{\text{MW}}/(2\pi)$ (Fig. 7.3b) we observe a chevron pattern expected for a two-level system. However, the chevron features a MW-detuning-independent modulation at a frequency of ~ 26 MHz in the pulse length. This oscillation frequency closely matches the expected indium Larmor frequency,²²⁰ suggesting an interaction between the hole spin with the nuclei of the host material.

We measure the hole spin T_2^* time with a Ramsey sequence, extracting the $\pi/2$ -pulse length from the Rabi oscillations. Figure 7.3c shows the pulse scheme and the measured decay corresponding to a coherence time of $T_2^* = 28.3$ ns. To avoid nuclear polarisation effects, we repeat each Ramsey sequence twice, once with a phase of $\phi = 0$ applied to the second $\pi/2$ pulse and once with a phase of $\phi = \pi$.¹⁷⁷ Using this scheme, the polarisation of the hole spin throughout the pulse sequence is averaged out, mitigating the buildup of

nuclear polarisation. With increasing $\Delta\omega_{\text{MW}}/(2\pi)$ (Fig. 7.3d), we observe oscillations in the Ramsey signal exactly at the difference between the hole Zeeman frequency and our drive frequency, as expected for a qubit precessing relative to the rotating frame defined by the MW control signal.

Our T_2^* time is comparable to previous reports at similar magnetic fields (with exception of Ref. ¹⁸⁶), which attributed the coherence to be limited by the interaction with the host nuclear spins.²¹⁵ The Hamiltonian for the hole spin is given by⁹¹ (compare with discussion on origin in Ch. 2.1.2)

$$H \approx \Omega \sum_i |\Psi_i|^2 (A_i^{h,z} I_i^z \cdot J^z + A_i^{h,\perp} (I_i^+ \cdot J^- + I_i^- \cdot J^+) + A_i^{h,nc} (I_i^+ \cdot J^z + I_i^- \cdot J^z)) + \dots, \quad (7.1)$$

with A_i^h the coupling of hole to nuclear spin i , I_i the nuclear spin, Ψ_i the hole envelope function, J the the hole spin and Ω the unit cell volume. We define the ladder operators $J^\pm = J^x \pm iJ^y$ and $I_i^\pm = I_i^x \pm iI_i^y$ for hole spins and for nuclear spins, respectively, and $A_i^{h,\perp}$ and $A_i^{h,nc}$ are the transverse and non-collinear parts of the hyperfine coupling.

The magnitude of the hyperfine components is of key importance for hole spin coherence, with significantly different values being reported for transverse and non-collinear terms in both the experimental and theoretical literature.^{186,215,221,222} There is, however, agreement on the leading term being Ising-like.⁸⁹

The Rabi frequency of the oscillations, Ω , depends on the Raman laser field experienced by the QD, which in our system depends on Δ (the detuning from the QD transition which is equal to the cavity detuning). Without the cavity, the Rabi frequency scales inversely with Δ ($\Omega \propto 1/\Delta$). In the cavity however, the $1/\Delta^2$ scaling of the field enhancement needs to be taken into account. This leads to a scaling of $\Omega \propto 1/\Delta^3$. We confirm this experimentally. Figure 7.2a shows the Rabi frequency Ω as a function of the Raman detuning Δ . Ω clearly follows a $1/\Delta^3$ dependence. We can increase the Rabi frequency significantly by reducing Δ , thereby cavity-enhancing the Raman fields experienced by the QD. Figure 7.3e shows Rabi oscillations as a function of the Raman laser power for $\Delta = 170$ GHz. The Rabi frequency can be extracted; we observe coherent oscillations with Rabi frequencies of up to $\Omega/2\pi = 1.06$ GHz, i.e. a π -rotation in 0.5 ns is possible. In principle we can increase the Rabi frequency even further by reducing Δ , allowing for coherent control beyond the rotating wave approximation. We observe a quality factor of the Rabi oscillations ($Q = 2 \cdot T_2^{\text{Rabi}} \cdot f_{\text{Rabi}}$) of $Q = 14.5 \pm 0.1$; which is within errorbars of the quality factor of the Rabi oscillations at lower Ω in Fig. 7.3a, where $Q = 15.7 \pm 1.1$.

7.4.2 Hole lifetime and spin characteristics

The device used in this work is an electron device, featuring a Fermi sea for electrons. As discussed in Ch. 6, the tunnel barrier is relatively thin (25 nm), leading to short T_1 times for the electron spin (~ 150 ns). The hole on the other hand, is metastable in this device. This is why the hole was not used for single-shot readout in Ch. 6. While the hole resides in the QD most of the time, it spends a certain amount of time in some unknown trapped states, leaving the QD empty. The *tunneling* behaviour of the hole between an occupied and empty state can be analysed via the auto-correlation function, a $g^{(2)}$ -measurement at zero magnetic field. Figure 7.4a shows the $g^{(2)}$ as a function of time delay τ between two detector events. It shows a slight bunching of $g^{(2)}(0) = 1.26$ around zero delay. The dynamics of this bunching

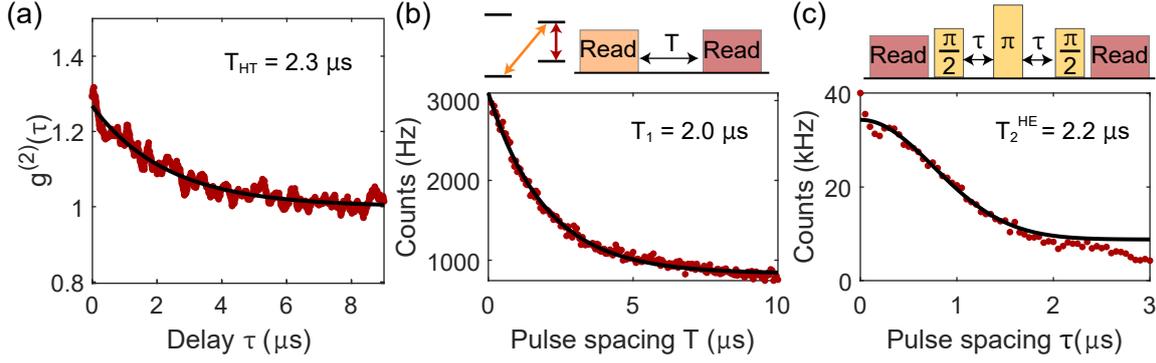


Figure 7.4: Hole tunneling, T_1 and Hahn-echo (a) $g^{(2)}(\tau)$ at 0 T and a laser power far below saturation shows slight bunching around zero time delay τ . The decay time is equivalent to the hole tunneling time. In this QD, the hole is present for biggest part of the time but tunnels in and out the QD at a timescale of $T_{\text{HT}} = 2.3 \mu\text{s}$. (b) Measurement of the hole spin T_1 via a two laser experiment. One laser initialises the spin $|\uparrow\rangle$ (orange) and the second pulse reads out the state (red) as a function of the splitting between the two pulses T . $T_1 = 2.0 \mu\text{s}$ is extracted from a fit to the exponential decay. This shows, that the T_1 -measurement of the spin is limited by the hole lifetime. (c) A Hahn-echo experiment is performed by using a pulse sequence of a $\pi/2$ a π and another $\pi/2$ pulse followed by a readout pulse while sweeping the spacing between the three pulses. This decouples the spin from nuclear spin noise and increases its coherence time to $T_2^{\text{HE}} = 2.2 \mu\text{s}$. The coherence time can hence also not be measured beyond the lifetime of the hole.

effect reveals the timing of the process. We extract an exponential decay corresponding to the time the hole spends in the QD of $T_{\text{HT}} = 2.3 \mu\text{s}$. The small bunching indicates, that the hole resides in the QD $\sim 80\%$ of the time. This hole tunneling processⁱⁱ is a limiting factor for experiments performed on the hole spin, as within this characteristic time, the hole will disappear from the QD. Additionally, this process prevents single-shot readout of the hole spin similar to Ch. 6, as for an absence of a photon in a readout pulse, one can not precisely determine between a spin in the dark state or an empty QD.

One important parameter for spin characterisation is the lifetime of the spin state, the relaxation time T_1 . It can be measured using a two-laser spin-pumping experiment as depicted in a schematic in Fig. 7.4b. A first laser is pumping the spin state which is then read out. The counts during the second pulse are integrated over the relevant area as a function of the delay between the two pulses T . This reveals a characteristic exponential decay from which T_1 can be extracted. From the data in Fig. 7.4b we get $T_1 = 2.0 \mu\text{s}$. The close match with T_{HT} indicates that T_1 is likely limited by the hole tunneling time, as a disappearing hole destroys the count rates in our analysis leading to the same decay.

The second characteristic spin parameter is the coherence time T_2^* . One method to increase the coherence time relies on decoupling the spin from nuclear noise. Decoupling is typically done via a Hahn-echo refocusing sequence as is shown in Fig. 7.4c. By reading the counts at the end of a sequence as a function of the spacing between the three pulses, τ , we can extract $T_2^{\text{HE}} = 2.2 \mu\text{s}$ from the exponential decay in the signal. Again, we see that this measurement is likely limited by the hole tunneling behaviour and we cannot determine a coherence beyond the hole lifetime. Therefore for this specific device, implementing more advanced schemes, e.g. CPMG, becomes redundant.

Note that even though the spin characteristics and single-shot experiments are limited by

ⁱⁱWe call this process tunneling, but we do not have a full understanding and microscopic model of the process to confirm it.

the tunneling of the hole, the observed time-scale still allows all presented spin experiments as $T_2^{\text{HE}} \gg T_2^*$ and we are T_2^* limited as usual, and experiments can be performed by integrating over many repetitions such that the short-time absence of the hole is negligible for experiments in this chapter.

7.4.3 Spin initialisation fidelity

All pulse sequences used in this chapter start with a pulse that initialises the spin state, typically to spin up $|\uparrow\rangle$. The fidelity with which this initialisation step is performed is part of the overall qubit operation fidelity. A lower bound to this initialisation fidelity can be estimated by looking at the form of a histogram of counts collected over many repetitions of an initialisation pulse (which at the same time acts as a readout pulse) as the one shown in Fig. 7.5a. Prior to the pulse, a preparation pulse brings the spin state into the read out state. During the initialisation pulse, a high intensity peak I_{peak} of counts is observed at first, exponentially decaying to a steady-state level I_{SS} . The values of I_{SS} and I_{peak} can be extracted from an exponential fit. The initialisation fidelity is then given by:²²³

$$F = 1 - \rho_{11}(0) \cdot \frac{I_{\text{SS}}}{I_{\text{peak}}} + \rho_{11}(0) \cdot \Theta \cdot \frac{\gamma_x}{\gamma_0} \frac{I_{\text{SS}}}{I_{\text{peak}}}, \quad (7.2)$$

where $\rho_{11}(0) = e^{-\tau_{\text{spacing}}/T_1}$ is the population of the read out state $|1\rangle$ ($\equiv |\uparrow\rangle$) at time zero (start of pulse), $\gamma_{x,y}$ the emission rates from an excited state into $|1\rangle$, $|2\rangle$ ($\equiv |\downarrow\rangle$), $\gamma_0 = \gamma_x + \gamma_y$ and $\Theta = \frac{\rho_{22}}{\rho_{11} + \rho_{22}}$. The fidelity therefore depends on the population of the read out state which can be determined from the preparation fidelity, the time since the last initialisation pulse, τ_{spacing} , and the T_1 of the spin. Hence, in reality, the population of the read out spin state $|\uparrow\rangle$ will be $\rho_{11}(0) < 1$ at the beginning of the readout pulse ($t = 0$). Assuming a perfect π -rotation, i.e. ideal pulse preparation, and neglecting the second term of Eq. 7.2, a lower bound of the initialisation fidelity can be calculated.

The initialisation fidelity strongly depends on the readout power. At low laser powers, the spin is never fully pumped and does not reach a steady state I_{SS} during the finite pulse

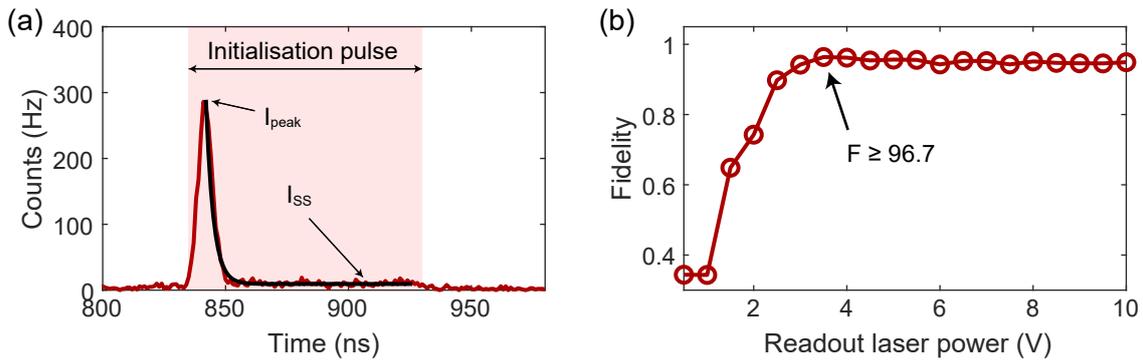


Figure 7.5: Spin initialisation fidelity (a) Histogram of an initialisation pulse. A preparation pulse 300 ns prior the initialisation pulse pumps the spin to the readout state. The initialisation pulse pumps the spin back to the original state. The initially high counts I_{peak} decay exponentially to a steady-state level I_{SS} . A lower bound to the initialisation fidelity can be calculated from I_{peak} and I_{SS} . An initialisation time of about 3 ns is extracted from the exponential decay. (b) Initialisation fidelity F for different laser powers (in units of the PID voltage to stabilise the laser). A lower bound of $F \geq 96.7\%$ is extracted. At even lower powers than in this figure, the fidelity would go towards zero.

duration. After reaching a maximum with increasing power, the fidelity stays more or less constant for a range of powers. However, for even higher powers, the fidelity reduces again, likely due to optical re-pumping, i.e. the power broadened pulse simultaneously pumps both the diagonal and the vertical transition resulting in the spin state being pumped back and forth between $|\uparrow\rangle$ and $|\downarrow\rangle$. The lower bound of the fidelity for different readout powers is calculated via Eq. 7.2 and is shown in Fig. 7.5b. A maximum lower bound fidelity of the initialisation of $F \geq 96.7\%$ is found. At this specific power, the exponential decay reveals a fast initialisation time of ~ 3 ns.

7.4.4 Laser-induced spin-flips

The detuned rotation laser induces incoherent spin flips. This effect can be quantified by comparing integrated counts on a Rabi drive as a function of the rotation laser duration for the MW drive being on- and off-resonant to the hole Zeeman splitting. Figures 7.6a, b and c show the on- and off-resonant ($\Delta\omega_{\text{MW}}/(2\pi) = 300$ MHz) counts for 18.5 MHz, 31.1 MHz and 51.7 MHz Rabi frequency, respectively, each at a rotation laser detuning of 320 GHz. For large rotation pulse durations the counts increase even in the off-resonant curve, resulting in incoherent spin-flips. This process limits the Q-factor of the Rabi oscillations for high rotation laser powers. The spin-flip rate can be extracted from an exponential fit to the off-resonant signal and yields $\kappa = 0.0012 \text{ ns}^{-1}$, $\kappa = 0.0017 \text{ ns}^{-1}$, and $\kappa = 0.0025 \text{ ns}^{-1}$, respectively, for the three Rabi frequencies above. A linear dependence of the spin-flip rate on the Rabi frequency can be extracted yielding a slope of $0.6 \cdot 10^{-4} \text{ ns}^{-1}/\text{MHz}$. This slope, however, scales differently depending on the detuning of the rotation laser and increases to $1.2 \cdot 10^{-4} \text{ ns}^{-1}/\text{MHz}$ for a laser detuning of 170 GHz, possibly as a consequence of enhanced excited state population. The mechanism leading to these incoherent spin-flips is not understood. It is possible, that either the Raman laser ejects a hole from the QD while a new one enters with random spin, or that phonon processes could be involved resulting in incoherent spin-flips. However, we can neither confirm nor exclude these possible explanations experimentally.

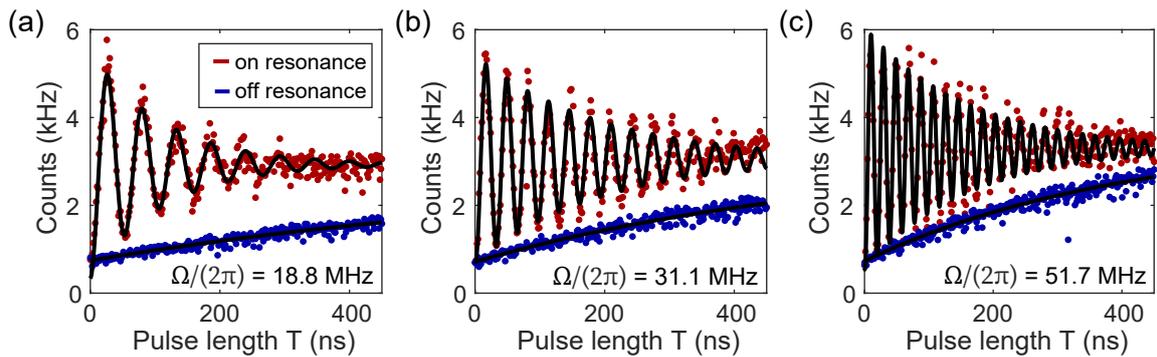


Figure 7.6: Incoherent rotation laser-induced spin flips Readout signal as a function of Rabi pulse length T on-(red) and off-(blue) resonant to the hole Zeeman transition at a rotation laser detuning of 320 GHz at Rabi frequencies of (a) $\Omega = 18.5$ MHz, (b) $\Omega = 31.1$ MHz, and (c) $\Omega = 51.7$ MHz. For higher power as well as lower rotation laser detuning, the off-resonant curve approaches the envelope of the resonant Rabi oscillations, meaning that the incoherent spin-flip process becomes a limiting factor to the spin rotation fidelity.

7.5 Nuclear spin cooling via a hole spin

Our cavity-enhanced Raman control strategy allows for spin control with Rabi frequencies that can be precisely tuned over two orders of magnitude (Figs. 7.3e and 7.7b). In addition to ultra-fast spin control, we can drive the hole spin with Rabi frequencies comparable to the host nuclear Larmor frequencies ($\omega_n/2\pi \approx 20 - 50$ MHz). The Q -factor of Rabi oscillations shows a non-trivial dependence on the Rabi frequency. When the hole spin is driven close to the nuclear Larmor frequencies $\omega_n/(2\pi)$ (Fig. 7.7c), the Q -factor drops. This effect has been previously observed for electron spins in QD devices,^{177,217} where it was attributed to a Hartmann-Hahn resonance between the electron and nuclear spins. For an electron spin, driving spin rotations with a Rabi frequency matching a nuclear Larmor frequency has been demonstrated to cool the nuclei, narrowing the Overhauser field distribution and extending the coherence time. We observe similar behaviour for the hole spin, increasing the T_2^* from $T_{2,\text{bare}}^* = 28.3$ ns to $T_{2,\text{Rabi-cooling}}^* = 120.8$ ns when measuring a Ramsey sequence after driving such a nuclear resonance (Figs. 7.7e,g). Furthermore, Rabi oscillations measured following a cooling sequence are shown in Figs. 7.7d,f (using a cooling Rabi frequency of $\Omega_C \sim 26$ MHz and a chevron Rabi frequency of $\Omega \sim 68$ MHz). The MW-detuning-independent periodic modulation in pulse length observed for hole spin rotation without nuclear cooling

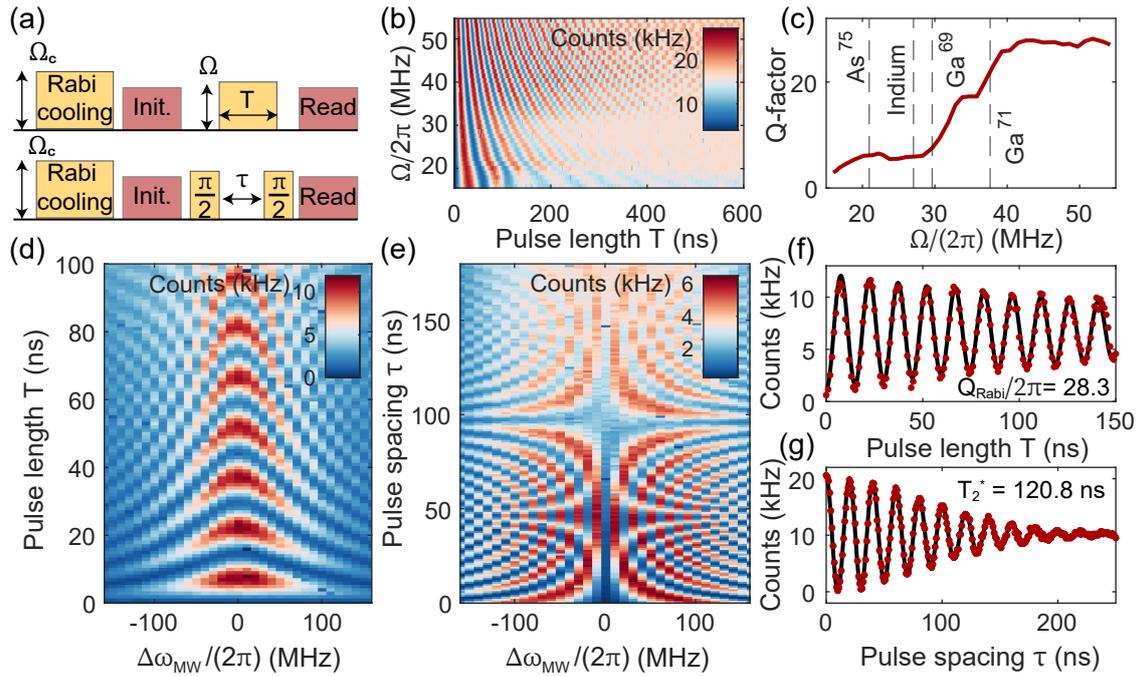


Figure 7.7: Rabi cooling of the nuclear spins (a) Pulse sequence for Rabi cooling. A Raman drive at the cooling Rabi frequency Ω_C narrows the nuclei distribution. A Rabi or Ramsey sequence can follow after the cooling pulse. (b) Rabi oscillations as a function of the Rabi frequency Ω for low laser powers. The visibility of the oscillations strongly depends on Ω . (c) The Rabi oscillation Q -factor as a function of the Rabi frequency Ω . The data is extracted from the oscillations in (b). The Q -factor drops at the Larmor frequencies of indium and arsenic. A Rabi frequency for the cooling pulse Ω_C is set to the indium resonance. (d) Rabi oscillations as a function of the $\Delta\omega_{\text{MW}}/(2\pi)$ after cooling of the nuclei with a 80 ns long Rabi pulse at $\Omega_C \sim 26$ MHz. (e) Ramsey interferometry as a function of the $\Delta\omega_{\text{MW}}/(2\pi)$ after cooling of the nuclei. (f) Rabi oscillation linecut of (d) at MW resonance. A Rabi oscillation Q -factor of 28.3 is extracted from the fit. (g) Ramsey interferometry at MW resonance with a serrodyne frequency of 125 MHz yielding a T_2^* of 120.8 ns.

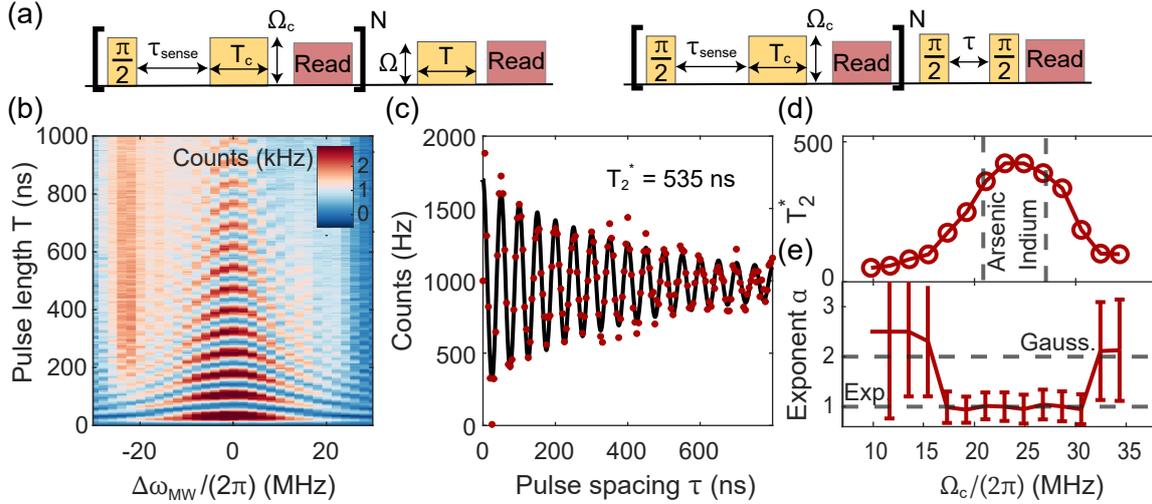


Figure 7.8: Optimal nuclei cooling mediated by a hole spin (a) Schematic of the pulse sequence. The nuclei are cooled via feedback cooling that consists on N repetitions of a sequence with a $\pi/2$ Rabi rotation followed by a sensing time τ_{sense} , a Rabi drive at the indium Larmor frequency Ω_C and a reset/readout pulse. After cooling of the nuclei, Rabi oscillations and Ramsey interferometry are performed. (b) Rabi oscillations as a function of MW frequency after an optimal cooling sequence. The side-bands indicate coupling to collective nuclear excitations. The asymmetry of the side-bands is likely arising from fluctuations in the laser power over the long measurement time, resulting in a changed cooling Rabi frequency and, hence, a shift in the cooling performance. (c) Ramsey interferometry after nuclei cooling. The coherence time is enhanced up to $T_2^* = 535$ ns. (d) T_2^* as a function of the cooling Rabi frequency Ω_C . The maximum coherence time is observed close to the indium and arsenic Larmor frequency. (e) The exponent of the fit to the Ramsey decays, α , as a function of the cooling Rabi frequency Ω_C . Close to the optimal parameters for cooling, the envelope follows an exponential decay curve ($\alpha = 1$) rather than a Gaussian ($\alpha = 2$).

(Fig. 7.3b) have disappeared, resulting in a textbook chevron. The Rabi Q-factor increases to a maximum of 28.3, leading to an upper-bound π -pulse fidelity of 98.3%.

The nuclei can be cooled even further using a recently developed technique, a quantum-sensing based cooling scheme.⁴⁴ Figure 7.8a shows the three-step protocol of this cooling scheme: First, the hole spin is initialised and rotated by a $\pi/2$ Raman pulse. The hole then senses the Overhauser field fluctuations during a sensing period of τ_{sense} . Second, a hole-nuclei non-collinear flip-flop process is driven via a Hartmann-Hahn resonance, which flips a nuclear spin with a direction dependent on the phase accumulated by the hole spin during the sensing phase. In this way, Overhauser field fluctuations away from the target value are corrected in a quantum sensing-based feedback loop.⁴⁴ Third, an optical projective readout measurement removes entropy from the nuclei. This cycle is repeated N times with linearly increasing sensing time τ_{sense} . This way, the feedback function is narrowed with each cycle and sensitivity is increased. The optimal parameters were determined experimentally and in our case are $N=35$ with τ_{sense} increasing from $\tau_{\text{min}} = 10$ ns to $\tau_{\text{max}} = 450$ ns, a Hartmann-Hahn drive with pulse length $T_C = 60$ ns at Rabi frequency ~ 26 MHz and a readout pulse of 90 ns length. This preparation sequence is repeated in front of every measurement of Rabi oscillations or of a Ramsey cycle. The chevron observed after the cooling sequence (Fig. 7.8b), similar to Rabi-cooling, no longer shows the MW-detuning-independent periodic modulation in pulse length in comparison to the non-cooled chevron (Fig. 7.3c). Interestingly, in addition to a textbook chevron, Fig. 7.8b features side-bands at around $\Delta\omega_{\text{MW}}/(2\pi) \pm 24$ MHz. This

is an indication for collective nuclear excitations, similar to what has been observed for electrons.⁴³ In contrast to the results with electrons, however, we only observe the first nuclear transitions.

The Ramsey sequence shows a dramatic increase in coherence time from $T_{2,\text{bare}}^* = 28.3$ ns to $T_{2,\text{feedback-cooling}}^* = 535$ ns (Fig. 7.8c). The cooling protocol strongly depends on the Rabi frequency used during the non-collinear flip-flop drive Ω_C , as is seen in Fig. 7.8d, where the T_2^* is shown as a function of Ω_C . The coherence time is clearly maximised for specific cooling Rabi frequencies close to the indium and arsenic Larmor frequency, very similar to the Rabi cooling. Figure 7.8e shows the exponent of the fitted decay α (fit function is $\cos(\omega_{\text{serr}}\tau) \cdot \exp(-\tau/T_2^*)^\alpha$) with $\omega_{\text{serr}} = 20$ MHz) as a function of Ω_C . The exponent of the decay drops from close to 2 (with larger errorbars) to 1 (with smaller errorbars and better fit quality) in the region of enhanced T_2^* , indicating a transition from Gaussian to exponential decay in the envelope of the decay function. This change from Gaussian to exponential decay is predicted for optimal cooling of nuclei,²¹⁹ but has not been observed to date.

We further measure the nuclear spin diffusion by checking the T_2^* as a function of waiting time after the optimal cooling sequence. Up to 1.2 ms – a technical limit for our experiments – we see no decrease in the coherence time.

7.6 Discussion

Our results show that the cooling strategies used to manipulate QD nuclear spin states via the electron spin^{43,44} are also effective for hole spins. The fact that the feedback protocol successfully cools the nuclear spins is clear evidence that the hole spin possesses a non-collinear term in its hyperfine interaction, and that our uncooled T_2^* time of 28.3 ns is limited by Overhauser field fluctuations. The QD hole spin hyperfine interaction has been the subject of significant investigation and theory and experiments typically agree that the Ising form is crucial and that the magnitude of hole hyperfine coupling constant along the QD growth direction (A_z^h) is $\sim 10\%$ of the electron coupling constant.⁸⁹ However, significant discrepancies emerge with regard to the transverse coupling constant, A_x^h . Coherent population trapping experiments on low-noise QD devices have estimated $A_x^h/A_z^h < 1\%$,^{88,186} whereas Ramsey experiments indicate that A_x^h and A_z^h may be of comparable magnitudes.^{215,222}

To conclude, we have demonstrated coherent spin control of a hole spin in an optical microcavity with Rabi frequencies up to 1 GHz. For the first time, we implement nuclear cooling schemes on a hole, extending the hole spin T_2^* to 535 ns and observe a transition to an exponential decay envelope of the Ramsey signal. These high spin coherence times in combination with high photon collection efficiencies, fast spin manipulation and fast initialisation highlights the potential of our platform as an efficient spin-photon interface and a resource of entangled cluster states, especially in combination with the fast single-shot spin readout that was implemented in Ch. 6 and that should be achievable in a p-type device. Furthermore, the system has potential as a hole-mediated nuclear memory via the creation of collective nuclear excitations.⁴³

Part **IV**

Conclusions and outlook

8

Conclusions

This work builds on years of previous successful development of both semiconductor quantum dots (QDs) and open microcavities. QDs have already been established as bright single-photon sources. The open microcavity that is used here has however increased photon collection rates to a record-value efficiency with more than every second photon ending up at the detector. As a consequence, at least 100,000 highly coherent photons can be generated by a single QD before loss of coherence. In this thesis we reported on various experiments profiting from this high collection efficiency. Furthermore, we presented optimisations towards usage of the microcavity-QD system as a coherent spin-photon interface.

The first part of this thesis focused on the cavity as a coherent light-matter interface. The overall goal was to achieve high coupling efficiencies $\beta \simeq 1$ in order to implement a one-dimensional (1D) atom for quantum networks. Ideally, in order to route photons, the light-matter interaction in a 1D atom should be direction-dependent. We have implemented a strong photon-emitter interface by optimising the cavity-QD coupling. The interaction is strong enough to result in radically different behaviour for different photon numbers – a strong nonlinearity is observed. An extinction in light transmission due to interaction with the QD of 99.2% is achieved resulting in a bunching of 587, both record values. The tunability of the microcavity allows *in-situ* tuning of the photon statistics from bunching to anti-bunching. Additionally, true directional light-matter interaction is achieved at one of the interesting chiral conditions, $\beta = 0.5$. We measured a strong non-reciprocal absorption with an isolation of 10.7 dB – an implementation of a *single-photon diode*. The second interesting case of $\beta \simeq 1$ is however impossible to achieve with the given configuration of the system. In order to nevertheless examine this regime, we investigated the *back-reflection* mode at high β . This mimics a chiral system well (or a true *one-sided* cavity). We observed the dynamics of photon bound states, which exhibit an interesting behaviour. Different photon number states result in different emitter-induced delays of 144.02 ps, 66.45 ps and 45.51 ps for one-, two-, and three-photon states, respectively. This can be understood in terms of stimulated emission at the level of single photons. In summary we have demonstrated both a strong photon-emitter interface as well as clear directional dynamics using an open microcavity system.

The second part of this thesis established a cavity-enhanced QD as a spin-photon interface. It addressed all relevant requirements for a spin-qubit. Firstly, we made use of the high

photon collection efficiency of the system and radically increased the readout speed of the spin state by demonstrating single-shot readout of an electron spin in 3 ns with a fidelity of 95.2%. For the first time, the readout speed has been brought well below the T_1 and T_2^* times for semiconductor QDs. The achieved readout speed also predicts fast, high-fidelity readout in Voigt geometry, allowing combination of single-shot readout with manipulation of a spin state. Moreover, we observed time-resolved quantum jumps of the electron spin state by repeatedly applying single-shot readout. By changing to Voigt geometry, we demonstrated all-optical manipulation of a hole spin inside a cavity. The electric field enhancement of the rotation laser through the cavity allows for Rabi oscillations at frequencies up to 1 GHz. A maximum π -pulse fidelity of 98.26% was observed. Furthermore, the nuclear spins were cooled by optically driving the hole spin, leading to an increased T_2^* from ~ 30 ns to above 500 ns. Lastly, fast spin initialisation within 3 ns is observed with a fidelity of 96.7%. As a conclusion, we have established a fully operational spin-qubit with ultra-fast and high fidelity initialisation, rotation and readout as well as a largely increased coherence of the hole spin.

Overall, the work results in a highly optimised platform. The presented QD-in-microcavity system can generate coherent photons with high efficiency, represents a coherent and directional interface at the level of single photons and possesses a coherent spin that can be read out and manipulated at ultra-fast speed. This combination of the relevant techniques with high rates and fidelity paves the way for using QDs in microcavities for a large variety of applications in quantum technologies.

9

Outlook

Plenty of photons, fast readout and manipulation of coherent spins, and a strong (and directional) light-matter interface – the overall results of this thesis demonstrate important progress towards the requirements for an ideal spin-photon interface. They pave the way for many exciting paths ranging from immediate experiments to applications in quantum technologies.

A major part of the advancement in this work is owed to careful design of the microcavity and its tunability. Of course, our microcavity approach is directly applicable to other emitters as other types of quantum dots (QDs) – e.g. GaAs QDs,²²⁴ where photons at wavelengths about 795 nm can be matched with rubidium memories or QDs at telecom wavelengths²²⁵ for smaller losses in fibre networks – colour centres in diamond^{226,227} or molecules.⁴⁷

Even though the end-to-end efficiency is record-high, there is still room to improve the system. At the moment, the largest source of photon loss is at optical interfaces. These losses could be overcome by implementing an *atom-drive*,²⁰³ i.e. by driving the QDs from the side through a waveguide mode, and hence, making several elements of the optical microscope head redundant. This could improve end-to-end efficiencies up to 80%. Undoubtedly, a higher collection efficiency would directly reflect on the single-shot readout speed and potential spin-photon entanglement rates.

Several optimisations could be achieved by slight modifications to the growth of the semiconductor heterostructure material. In this thesis, a device designed to host electrons is used. The short tunnel barrier leads to short electron spin-flip times T_1 . Growing a larger tunnel barrier in a next generation device would increase the electron T_1 allowing for spin control experiments on the electron. On the other hand, a specific hole sample could be designed in order to work with a stable hole spin. This way, single-shot experiments could be performed on a hole.

While the cavity mode splitting is optimal for single-photon collection, a degenerate cavity would allow for the combination of high β -factors and chirality. In that case, circularly polarised light could enter and leave the cavity without optical losses. The splitting can be tuned via application of electrical bias¹⁴⁶ or strain¹³⁶ to the semiconductor heterostructure or by designing an elliptical top cavity mirror to counteract the present mode-splitting. The implementation of a chiral one-dimensional (1D) atom at $\beta \simeq 1$ would furthermore allow for the realisation of directional bound-states, quantum networks based on chiral emitters⁹⁸ and

two-qubit gates.¹²⁷

The biggest milestone of this thesis, however, is the implementation of spin manipulation of a hole spin with enhanced coherence inside a cavity. It allows for a full new chapter of possible experiments and applications. First results in this thesis suggest an efficient coupling to magnons⁴³ – collective excitations of the nuclear spins – which have a strong potential as memories and quantum nodes. Furthermore, the cavity-enhancement of the Raman laser field allows for the achievement of high powers at the QD, giving insight into spin rotations beyond the rotating-wave approximation.²²⁸ This could be interesting in order to implement even faster spin control, but is also particularly interesting from the fundamental point of view. Another interesting prospect is the generation of designer photons – photons where the wave-package can be shaped by using spin control and the cavity.²²⁹ This is especially interesting when combined with GaAs QDs and would enable bandwidth-matching of the QD-photons to rubidium memories.

Ultimately, the most promising path of our platform leads towards the generation of photonic cluster-states. The high photon collection rates combined with the strong interface, the low noise performance and fast spin rotations and readout will enable a high rate of spin-photon entanglement and eventually an efficient generation of 1D-cluster and GHZ states.^{15,178,179} Based on the results in this thesis, we predict three-photon GHZ states generation at rates of tens of MHz with high fidelity without any changes to the system. In this sense, this work marks the stepping stone for this highest-efficiency single-photon source to also become the highest-efficiency cluster-state source.

A

The quantum dot-cavity system: characterisation and experimental setup

Adapted fromⁱ:

N. Tamm*, A. Javadi*, N. O. Antoniadis, D. Najer, M. C. Löbel, A. R. Korsch, R. Schott, S. R. Valentin, A. D. Wieck, A. Ludwig and R. J. Warburton
“A bright and fast source of coherent single photons”,
Nat. Nanotechnol. **16**, 399-403 (2021)

A.1 Description and fabrication of the coupled system

A.1.1 Heterostructure and growth

The heterostructure is grown by molecular beam epitaxy (MBE) and consists of an n-i-p diode with embedded self-assembled InAs quantum dots (QDs). This design allows for QD frequency tuning via the dc Stark effect as well as QD charging via Coulomb blockade. The n-i-p diode is grown on top of a semiconductor distributed Bragg reflector (DBR), a planar *bottom* mirror, composed of 46 pairs of AlAs (80.6 nm thick)/GaAs (67.9 nm thick) quarter-wave layers (QWLs) with a centre wavelength of nominally 940 nm (measured: 917 nm). Below the DBR, an AlAs/GaAs short-period superlattice composed of 18 periods of 2.0 nm AlAs and 2.0 nm GaAs is grown for stress-relief and surface-smoothing.

From bottom to top (see Fig. A.1a), the diode consists of an n-contact, 41.0 nm Si-doped GaAs, n⁺, doping concentration $2 \cdot 10^{18} \text{ cm}^{-3}$. A 25.0 nm layer of undoped GaAs acts as a tunnel barrier between the n-contact and the QDs. The self-assembled InAs QDs are grown by the Stranski-Krastanov process and the QD emission is blue-shifted via a flushing-step.²³¹ The QDs are capped by an 8.0 nm layer of GaAs. A blocking barrier, 190.4 nm of Al_{0.33}Ga_{0.67}As, reduces current flowing across the diode in forward-bias. The p-contact consists of 5.0 nm of C-doped GaAs, p⁺ (doping concentration $2 \cdot 10^{18} \text{ cm}^{-3}$) followed by 20.0 nm of p⁺⁺-GaAs (doping concentration $1 \cdot 10^{19} \text{ cm}^{-3}$). Finally, there is a 54.6 nm-thick GaAs capping layer.

ⁱThis is the main source, but some sentences were added from the methods sections of Refs. ^{100, 120, 230}

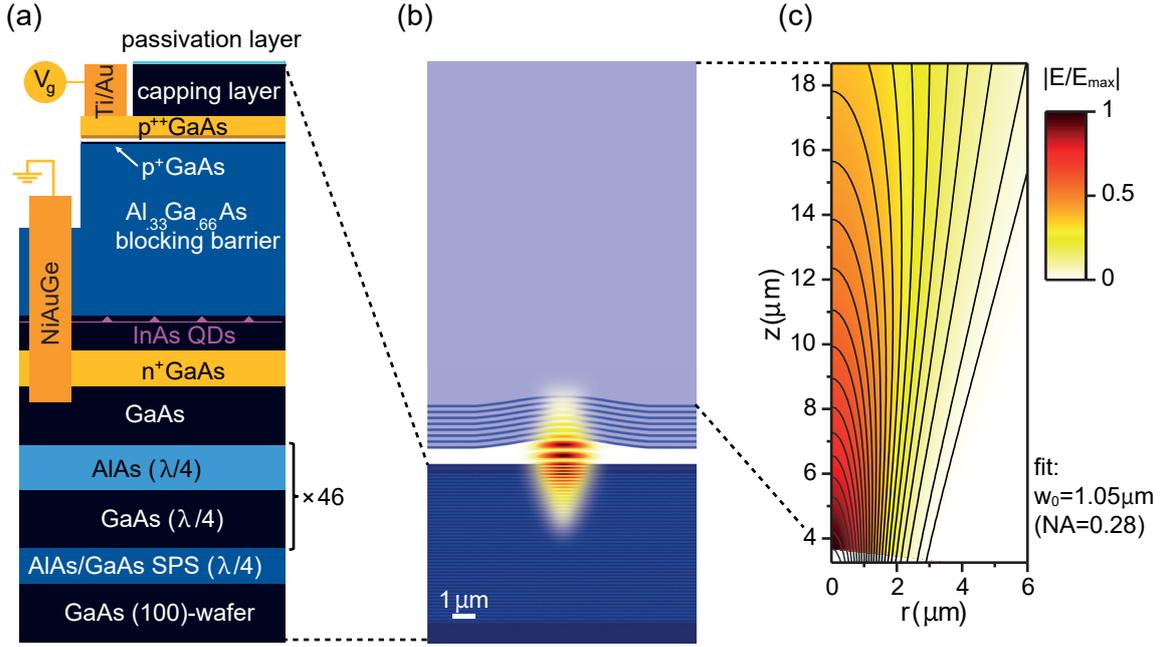


Figure A.1: Heterostructure design and numerical simulation of the microcavity. (a) The semiconductor heterostructure consists of a DBR and an n-i-p diode structure with embedded self-assembled InAs QDs. (b) Numerical simulation of the vacuum electric field $|E_{\text{vac}}|$ confined by the microcavity (image to scale). (c) Colour-scale plot: normalised electric field within the SiO_2 substrate supporting the *top* mirror. Contour lines: fit of a Gaussian beam to the calculated normalised electric field. The fit yields a beam waist of $w_0 = 1.05 \mu\text{m}$ corresponding to a numerical aperture of $\text{NA} = 0.279$. $|E_{\text{max}}|$ is the maximum electric field amplitude in this particular domain.

The layer thicknesses are chosen to position the QDs at an antinode of the vacuum electric field. The p-contact is centred around a node of the vacuum electric field to minimise free-carrier absorption in the p-doped GaAs. Coulomb blockade is established on times comparable to the radiative decay time for GaAs tunnel barriers typically $\lesssim 40 \text{ nm}$ thick. This is less than the thickness of a QWL thereby preventing the n-contact being positioned likewise at a node of the vacuum electric field. However, at a photon energy 200 meV below the bandgap,²³² the free-carrier absorption of n^+ -GaAs ($\alpha \approx 10 \text{ cm}^{-1}$) is almost an order-of-magnitude smaller than that of p^{++} -GaAs ($\alpha \approx 70 \text{ cm}^{-1}$). The weak free-carrier absorption of n^+ -GaAs is exploited in the design presented here by using a standard 25 nm thick tunnel barrier. The n-contact is positioned close to a vacuum field node, although not centred around the node itself.

After growth, individual $3.0 \times 2.5 \text{ mm}^2$ pieces are cleaved from the wafer. The QD density increases from zero to $\sim 10^{10} \text{ cm}^{-2}$ in a roughly centimetre-wide stripe across the wafer. The sample used in all experiments of this thesis was taken from this stripe. Its QD density, measured by photoluminescence imaging, is approximately $7 \times 10^6 \text{ cm}^{-2}$.

Separate ohmic contacts are made to the p^{++} and n^+ layers. For the n-contact, the capping layer, the p-doped layers and part of the blocking barrier are removed by a local etch in citric acid. On the new surface, NiAuGe is deposited by electron-beam physical vapour deposition (EBPVD). Low-resistance contacts form on thermal annealing. To contact the p-doped layer, the capping layer is removed by another local etch. On the new surface, a Ti/Au contact pad (100 nm thick) is deposited by EBPVD. Although this contact is not thermally annealed,

it provides a reasonably low-resistance contact to the top-gate on account of the very high p-doping (Fig. A.1a).

After fabricating the contacts to the n- and p-layers, the contacts are covered with photoresist and a passivation layer is deposited onto the sample surface. A thin native oxide layer on the surface is removed by etching a few nm of GaAs in HCl. Following a rinse in deionised water, the sample is immersed in a bath of ammonium sulphide $((\text{NH}_4)_2\text{S})$. Subsequently, the sample is transferred rapidly into the chamber of an atomic-layer deposition (ALD) setup. An 8 nm layer of Al_2O_3 is deposited using ALD at a temperature of 150°C . With the present heterostructure, this process is essential to reduce surface-related absorption: a low-loss microcavity is only achieved following surface-passivation.^{48,138} An advantage of the surface passivation lies in the fact that it prevents the native oxide of GaAs from re-forming after its removal: it provides a stable termination to the GaAs heterostructure.²³³ Following the surface-passivation procedure and photoresist stripping, the NiAuGe and Ti/Au films are wire-bonded to large Au pads on a sample holder. Using silver paint, macroscopic wires (twisted pairs) are connected to the Au pads.

When applying a voltage across the gates of this n-type device, the neutral exciton, X^0 , is observed at intermediate biases. The negatively-charged trion, X^- , is observed at more positive bias, and the positively-charged trion, X^+ at more negative voltages.

This particular device presents a small leakage current at the X^- voltage and a short tunnel barrier, leading to a spin T_1 limited by co-tunneling for X^- . On the other hand, the hole is not stable in this n-type device. It is, however, present even without a dedicated laser for photo-creation, which is unexpected. The origin of the hole in our sample is not fully understood and subject of further investigation.

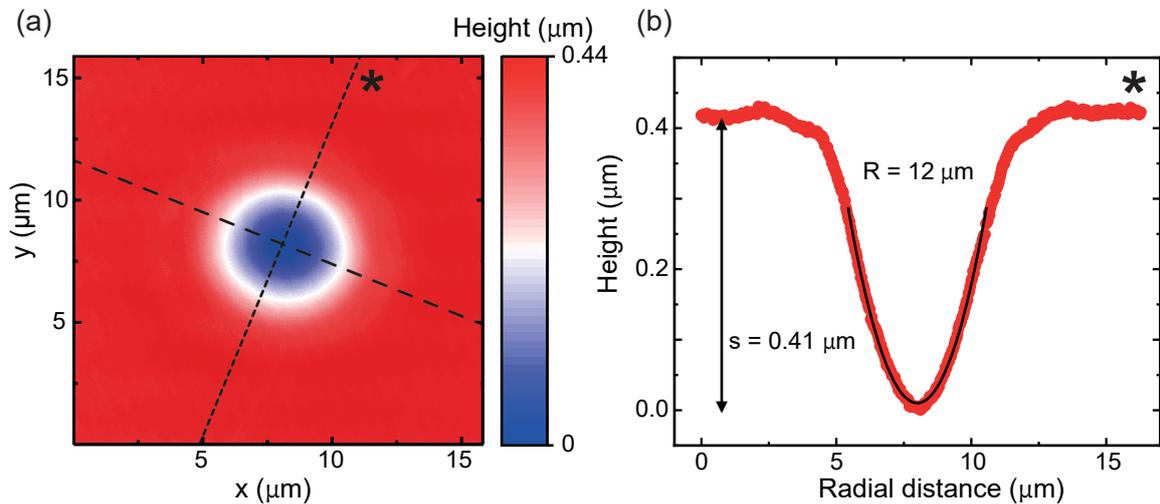


Figure A.2: Geometrical characterisation of the curved mirror. Following CO_2 -laser machining, the fabricated crater's profile is measured with a confocal laser scanning microscope. **(a)** Height map of the crater determined with sub-nm resolution. From the height map, the two principal planes are extracted by fitting a two-dimensional Gaussian function to the data. **(b)** By evaluating the height information along the two principal axes, it is possible to extract the crater's parameters such as the radius of curvature $R = (11.98 \pm 0.02) \mu\text{m}$, sagittal height $s = (0.41 \pm 0.01) \mu\text{m}$, and asymmetry of 4.5%. This is an example crater that has been used for the experiments in Ref.¹⁹ and Part II of this thesis. Other craters have been used for the experiments in Part III, but the results were very similar.

A.1.2 Curved mirror fabrication

The top mirror is fabricated in a 0.5 mm thick fused-silica substrate. An atomically-smooth crater is machined at the silica surface via CO₂-laser ablation.^{234,235} We achieve craters with a similar radius of curvature as described in Ref.,²³⁵ but with a shallower profile by substituting the focusing lens in the ablation setup by a lens with NA = 0.67.

The profile of the fabricated crater is measured by a confocal laser scanning microscope (Keyence Corporation), as shown in Fig. A.2a. From the two-dimensional height profile, two principal axes can be identified, and the profile parameters can be extracted (Fig. A.2b). The radius of curvature of this crater is $R = (11.98 \pm 0.02) \mu\text{m}$ and the sagittal height $s = (0.41 \pm 0.02) \mu\text{m}$. After laser ablation, the crater is coated with 8 QWL-pairs of Ta₂O₅ (refractive index $n = 2.09$ at $\lambda_0 = 920$ nm) and SiO₂ ($n = 1.48$ at $\lambda_0 = 920$ nm) layers (terminating with a layer of Ta₂O₅) by ion-beam sputtering at a commercial company (Laseroptik GmbH), see Fig. A.1b.

A.1.3 Microcavity characterisation

The microcavity is a highly miniaturised Fabry-Perot type resonator. A fundamental mode is resonant for a given laser frequency at a particular microcavity length. In order to determine the Q-factor of the microcavity, a dark-field measurement is performed, as shown in Fig. A.3a. Given the spectral tunability of the microcavity, its Q-factor can be determined for a wide wavelength range within the stopband of the mirrors, centred around $\lambda_0 \approx 917$ nm, as shown in Fig. A.3b.

Figure A.3a shows such a measurement performed on a fundamental mode at $\lambda_0 = 922$ nm.

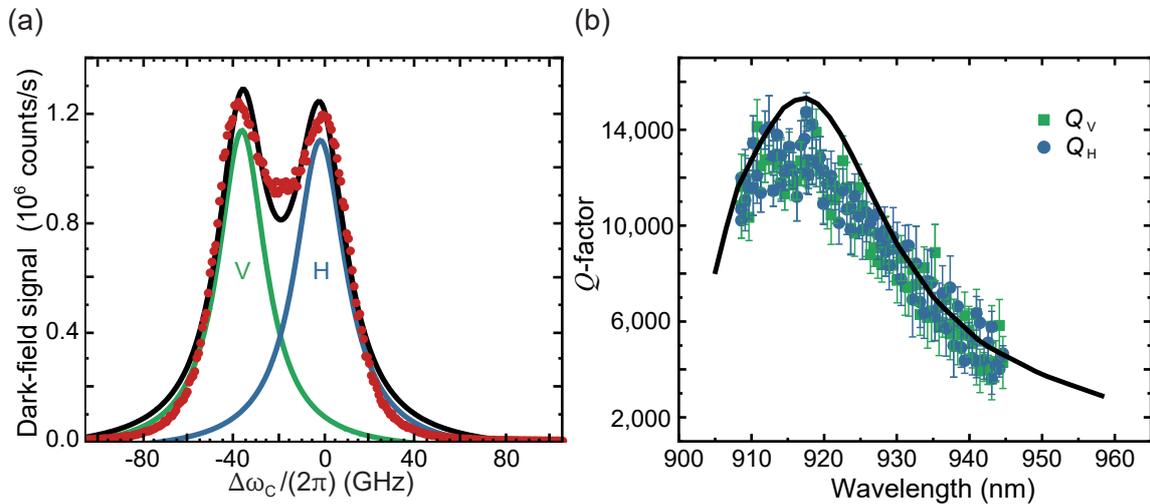


Figure A.3: Q-factor of the microcavity. (a) Signal versus optical frequency expressed as a detuning with respect to the upper-frequency resonance. The microscope operates in dark-field mode with principal axes lying at 45 degrees to the principal axes of the microcavity. The wavelength is $\lambda_0 = 922$ nm. The fundamental mode splits into two modes both with linear polarisation, one H-polarised, the other V-polarised. The H- and V-axes correspond to the crystal axes of the GaAs wafer. The transmission data (red dots) are fitted to a squared double-Lorentzian function (blue and green curves) yielding in this measurement Q-factors for the two polarised modes: $Q_H = 11,900 \pm 1,000$ and $Q_V = 12,800 \pm 1,000$. The mode-splitting is 34.6 GHz. (b) A measurement of Q_H (blue points) and Q_V (green points) can be extracted across a wide spectral range, demonstrating good agreement between calculated and experimental Q-factors. We note that there is no systematic difference between Q_H and Q_V .

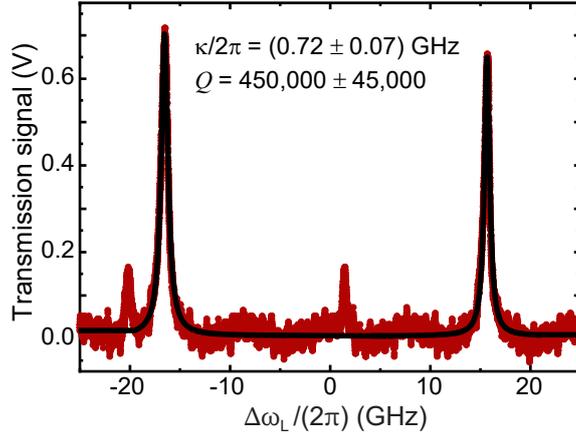


Figure A.4: Upper bound of κ_{loss} . A microcavity composed of the same semiconductor heterostructure and a high reflectivity top mirror (116 ppm transmission) yields a Q-factor $4.5 \cdot 10^5$ near the centre of the stopband ($\lambda_0 = 920$ nm), corresponding to $\kappa/(2\pi) = 0.72 \pm 0.07$ GHz. This value sets the upper bound of $\kappa_{\text{loss}}/(2\pi) \leq 0.72$ GHz in the experiment with the lower reflectivity top mirror, making $\kappa_{\text{loss}}/\kappa \leq 3\%$, where $\kappa = \kappa_{\text{top}} + \kappa_{\text{loss}}$.

The fundamental mode splits into two modes, each linearly polarised, with opposite polarisations, H and V. The mode-splitting is 34.6 GHz. The H and V axes align with the crystal axes of the semiconductor wafer. This points to the physical origin of the mode-splitting: a small birefringence in the semiconductor. The birefringence is probably induced by a very small uniaxial strain. The splitting of the fundamental microcavity mode into two separate modes together with the linear, orthogonal polarisations of these two modes are exploited in the experiment to achieve high efficiencies in our experiment, as discussed in Sec. A.2.1. The mode-splitting is, therefore, an important parameter. Performing this measurement at different locations on the sample yields a spread in mode-splittings. For the QDs investigated, the splitting lies between 34.6 and 58.8 GHz.

The Q-factors of both H- and V-polarised modes are extracted from the dark-field spectrum (exemplified in the green and blue curves in Fig. A.3a) yielding $Q = 12,600 \pm 1,000$ ($\kappa/(2\pi) = 25.9$ GHz) at $\lambda_0 = 917$ nm. The finesse is $\mathcal{F} = 506 \pm 50$. \mathcal{F} , determined by microcavity scanning at a fixed wavelength. Unlike the mode-splitting, the Q-factors have no variations within the error bar from position to position in the sample.

The microcavity does not have a monolithic design and is potentially susceptible to environmental noise, vibrations and acoustic noise. The microcavity is operated in a helium bath-cryostat. The cryostat is shielded from vibrational noise by an active damping stage and from air-borne acoustic noise by an acoustic enclosure. Using the microcavity itself as a noise sensor shows that environmental noise is significant only when operating with a finesse above 10,000,²³⁵ corresponding to a Q-factor of approximately 10^5 with the present design. Here, the Q-factor is approximately 10^4 and the experiment was not troubled by residual environmental noise.

Finally, the Q-factor can be limited by losses, such as undesired absorption in gated regions of the semiconductor heterostructure, surface-related absorption at the semiconductor-air interface, and scattering. This means that the total loss rate of the cavity κ has contributions from the preferred loss channel κ_{top} and the undesired channel κ_{loss} which accounts for all other losses: $\kappa = \kappa_{\text{top}} + \kappa_{\text{loss}}$. In order to determine κ_{loss} we probe a microcavity composed

of the same semiconductor heterostructure, but we use instead a top mirror with much lower transmittivity (116 ppm). We measure (at $\lambda_0 = 920$ nm) $Q = 450,000 \pm 45,000$, shown in Fig. A.4, corresponding to $\kappa/(2\pi) = (0.72 \pm 0.07)$ GHz. We argue that this measured quantity sets an upper bound for κ_{loss} in the experiments in this work $\kappa_{\text{loss}}/(2\pi) \leq 0.72$ GHz, as all losses – except κ_{top} – are maintained constant.

A.1.4 Numerical simulations of the microcavity

Calculation of the Q-factor

The microcavity Q-factor was calculated using a one-dimensional transfer matrix simulation (The Essential Macleod, Thin Film Center Inc.). The top mirror is described using the design parameters taking the manufacturer’s values for the refractive index (mirror design: silica-(HL)⁷H with H (L) a quarter-wave layer in the high- (low-) index material at wavelength 920 nm, refractive indices 2.09 (1.48)). The transmission loss per round trip of the top mirror is 10,300 ppm. The bottom mirror has a nominal design GaAs-(HL)⁴⁶-active layer with H (L) a quarter-wave layer in GaAs (AlAs) at wavelength 940 nm, as shown in Fig. A.1a. In practice, the layers become gradually thinner during growth. The wavelength of the stopband and the oscillations in reflectivity out with the stopband can be very well described by postulating a linear change in thickness during growth.⁴⁸ The losses in the entire semiconductor heterostructure (including the free-carrier absorption in active layer) can be assessed by measuring the Q-factors with an extremely reflective, extremely low-loss top mirror: the transmission loss is just 1 ppm per round trip; the absorption/scattering losses amount to 373 ppm per round-trip.⁴⁸ These losses are negligible compared to the transmission loss of the top mirror. The simulated Q-factor for the semiconductor DBR – GaAs active layer (6 QWLs) – air-gap (4 QWLs) – top mirror structure is about 15,200 at the centre of the stop-band, a value obtained for a cavity composed of two flat mirrors.

Another possible source of losses in a microcavity is diffraction losses at the DBR mirrors, also termed *side-losses* in the micropillar community.^{236,237} For tightly confined modes, the angular spread in k-space expands, increasing the losses in the DBR mirrors and reducing the Q-factor. We carried out numerical simulations to probe the effect of the radius of the curvature on the Q-factor. Figure A.5a shows the Q-factor as a function of the wavelength and R . Fig. A.5b shows a cut-through of the data close to the centre of the stopband at 920 nm. As expected, for small radii the Q-factor is a strong function of R and drops to 4,600 at $R = 2.3 \mu\text{m}$. At large radii ($R > 6 \mu\text{m}$), the Q-factor is a weak function of R , and saturates at a value of 15,200. We use a top mirror with $R = 11.98 \mu\text{m}$ in our experiments. We calculate a Q-factor of 15,000 for this R at the centre of the stopband, very close to the value at large radii. Hence, we conclude that side losses are negligible in our experiments.

When further taking into consideration contributions from $\kappa_{\text{loss}}/(2\pi) = 0.72$ GHz, bounded from below by the measurement described in Sec. A.1.3, the Q-factor calculated at the stop-band centre ($\lambda_0 \approx 917$ nm) with the exact top mirror used in the experiment reduces to approximately 14,500. This is very close to the measured value, $12,600 \pm 1,000$. The small difference between the calculated and experimental Q-factors may well arrive from imperfect knowledge of the optical thicknesses in the two DBRs.

Calculation of the QD-microcavity coupling

In order to estimate the QD-microcavity coupling, a finite-elements method (Wave-Optics Module of COMSOL Multiphysics) is used to compute the vacuum electric field amplitude

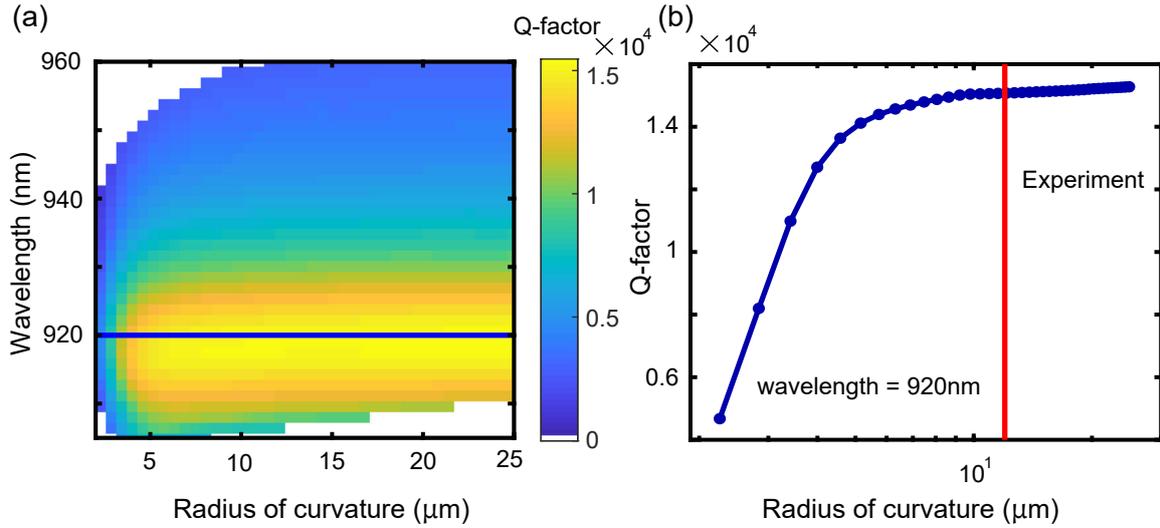


Figure A.5: Effect of diffraction losses on the Q-factor. (a) Calculated Q-factor as a function of the wavelength and the radius of the curvature of the top mirror. The Q-factor is maximum at the centre of the stopband (close to 920 nm). (b) A cut-through of the data at the wavelength of 920 nm corresponding to the blue line in part (a). The Q-factor drops significantly for radii smaller than 6 μm signalling diffraction losses. For larger radii the Q-factor approaches 15,200.

$|E_{\text{vac}}(r, z)|$ confined by the microcavity (Fig. A.1b). The model assumes axial symmetry about the optical axis ($(x, y) = 0$). We use a 1 μm thick perfectly index-matched layer at all outer boundaries of the simulation to prevent internal reflections. The model takes a top mirror with radius of curvature $R = 11.98 \mu\text{m}$ and sagittal height $s = 0.41 \mu\text{m}$, exactly the mirror used in the characterisation (see Sec. A.1.2). At the location of the QDs ($z = z_{\text{QD}}$) in the exact anti-node of the microcavity mode ($r = 0$), the field is $|E_{\text{vac}}(0, z_{\text{QD}})| = 35,000 \text{ V/m}$. A QD at these wavelengths has an optical dipole of $\mu/e = 0.71 \text{ nm}$ where e is the elementary charge.⁶³ The X^+ consists of two degenerate circularly-polarised dipole transitions (at zero magnetic field). We consider the interaction of one of these circularly-polarised dipoles with a linearly-polarised microcavity mode. The predicted QD-cavity coupling is therefore $\hbar g = \mu \cdot E_{\text{vac}}(0, z_{\text{QD}})/\sqrt{2}$ giving $g/(2\pi) = 4.2 \text{ GHz}$. (The same is true for X^- . For X^0 the dipoles are linearly polarised, in principle increasing the maximum achievable g by a factor of $\sqrt{2}$. However, in the case of X^0 the effective coupling will depend on the angle between the polarisation axes of the QD and the cavity modes, which is not controllable in our system and varies from QD to QD.) This dipole moment implies a natural radiative decay rate of 1.72 ns^{-1} , equivalently $\gamma/(2\pi) = 0.27 \text{ GHz}$ (assuming the dipole approximation in an unstructured medium). The calculated Purcell factor is therefore $F_{\text{P}} = 4g^2/(\kappa\gamma) = 11.4$.

The Purcell factor and coupling g can be determined from the experiment. The natural radiative decay γ rate can be determined by gradually tuning the microcavity out of resonance with the QD, extrapolating the decay rate to large detunings (Fig. 2.5b). This gives $\gamma/(2\pi) = 0.30 \text{ GHz}$. This agrees well with the estimate above. On resonance, the total decay rate increases to 3.33 GHz. In the experiment however, the polarisation-degeneracy of the microcavity is lifted (see Sec. A.1.3) and the QD exciton, an X^+ , interacts with both microcavity modes. We focus on the resonance with the H-polarised mode. We determine the contribution to the total decay rate from the presence of the V-polarised microcavity mode by fitting the total decay rate as a function of microcavity detuning to two Lorentzians

(Fig. 2.5b). We subtract the contribution from the V-polarised mode and the free-space modes at the resonance with the H-polarised mode, giving a decay rate of $\gamma_{\text{H}}/(2\pi) = 2.87$ GHz. This is the decay rate contribution we would expect if the V-polarised mode were highly detuned, in other words if the microcavity mode-splitting were very large. In this limit, a circularly-polarised dipole interacting with a single linearly-polarised microcavity mode, allows a comparison to be made with the calculated properties of the microcavity. The Purcell factor arising from the H-polarised mode alone is therefore $F_{\text{P}}^{\text{H}} = \gamma_{\text{H}}/\gamma = 9.6$, close to the calculated value (11.4). Using $F_{\text{P}}^{\text{H}} = 4g^2/(\gamma\kappa)$ and taking $\kappa/(2\pi) = 25.9$ GHz, we determine $g/(2\pi) = 4.3$ GHz, close to the calculated value. An exact agreement is not expected as the QD dipole fluctuates from QD to QD and therefore between the different experiments. We can conclude that, first, the vacuum field in the real microcavity is compatible with the value calculated from the microcavity's geometry; and second, that the lateral tuning of the microcavity enables the QD to be positioned at the anti-node of the vacuum field.

Properties of output mode

A simulation of the microcavity mode was used to determine the parameters of the output beam of the microcavity, notably the beam waist. The calculated beam in the SiO₂ substrate, i.e. in the region above the top mirror (Fig. A.1c), is fitted to a Gaussian beam²³⁸ of the form

$$|E(r, z)| = |E_0| \frac{w_0}{w(z)} e^{-r^2/w^2(z)} \quad (\text{A.1})$$

with waist radius at z given by

$$w^2(z) = w_0^2 \left(1 + \left(\frac{z}{z_{\text{R}}} \right)^2 \right). \quad (\text{A.2})$$

$z_{\text{R}} = n\pi w_0^2/\lambda_0$ is the Rayleigh range in the medium (refractive index $n = 1.4761$ is taken for SiO₂). The fit taking w_0 (and $|E_0|$) as fit parameters results in $w_0 = 1.05$ μm . This corresponds to a numerical aperture of $\text{NA} = \lambda_0/(\pi w_0) = 0.279$.

A.2 Experimental setup

A.2.1 Optical setups

In the experiment, the microcavity and one lens (the objective lens) are mounted in a helium bath-cryostat ($T = 4.2$ K) equipped with a superconducting solenoid magnet. There are two different magnets that can be placed in the cryostat prior a cool-down, either out-of-plane (0 – 9 T) or in-plane (0 – 3 T) with respect to the QD growth direction. A window enables free-space optical-beams to propagate from an optical setup at room temperature to the microcavity system at low temperature,^{48, 235, 239, 240} as shown in Fig. A.6. The top-mirror of the microcavity is fixed at the top of a titanium *cage*, inside which the sample, mounted on a piezo-driven xyz nano-positioner, is placed.^{48, 235, 239, 240} The nano-positioner allows for full *in situ* spatial (xy) and spectral (z) tuning of the microcavity. The titanium cage sits on another xyz nano-positioner, which allows for positioning of the microcavity relative to the objective lens, an aspheric lens of focal length $f_{\text{obj}} = 4.51$ mm (355230-B, NA = 0.55, Thorlabs Inc.), leading to close-to-perfect mode matching of the microcavity and the microscope. The microscope has a polarisation-based dark-field capability.¹³⁷ As shown in Fig. A.6, laser light is input into the microscope via a single-mode fibre, mostly via the excitation port. The

beam is collimated by a $f_{\text{fibre}} = 11$ mm aspheric lens (60FC-4-A11-02, Schäfter + Kirchhoff GmbH). A linear polariser (LP; Thorlabs Inc.) guarantees the polarisation-matching of the input beam to a polarising beam-splitter (PBS; Thorlabs Inc.) which reflects the light towards the microcavity. A half-wave plate (HWP/ $\lambda/2$, 946 nm zero, B. Halle) allows the axis of the polarisation to be rotated: the output state is chosen to match one of the principal axes of the microcavity, the V-axis. The light is then coupled into the microcavity by the objective lens. The same lens collects the microcavity output. H-polarised light is transmitted by the PBS and focussed by a lens (60FC-4-A11-02, Schäfter + Kirchhoff GmbH) into a single-mode optical fibre (780HP fibre, Thorlabs Inc). In the dark-field scheme, the suppression of V-polarised laser light is optimised by adjusting an additional quarter-wave plate (QWP/ $\lambda/4$, 946 nm zero, B. Halle) in the main beam-path. Confocal detection is crucial.²⁴¹ For continuous wave excitation, an extinction ratio up to 10^8 is achieved (for pulsed excitation, it is up to 10^6) and remains stable over many days of measurement.¹³⁷

We use the cross-polarised microscope setup to separate the resonant excitation laser light from the QD emission.¹³⁷ The mode splitting between the orthogonally polarised modes of our microcavity allows us to excite the QD using the Lorentzian *tail* of one mode and to collect via the other mode.^{19,47} The QD photons emitted from the cavity are then elliptically polarised, with the major polarisation axis orthogonal to the excitation laser polarisation. Using this technique, we overcome what would otherwise be a 50% loss of QD photons in the cross-polarisation optics.⁴⁷

Depending on the requirements of the individual experiment, the HWP and QWP can be modified. The microscope head in Fig. A.6 provides full tunability of the excitation and collection polarisation. The arms of the head (excitation/collection arm) can be used in different configurations. For most experiments, we define transmission from port 2 to port 1, as described above. But we can also measure *backwards* (port 1 to port 2) as discussed in Ch. 4 or in the so-called *back-reflection mode* (port 1 to port 1) as used in Ch. 3.5.

The estimation of the microcavity beam waist (Sec. A.1.4) was used to optimise the fibre-coupling efficiency by selecting an appropriate aspheric lens in front of the optical fibre. The objective lens (355230-B, NA = 0.55, Thorlabs Inc.) has a focal length $f_{\text{obj}} = 4.51$ mm. Its NA is considerably larger than the NA of the microcavity in order to minimise clipping losses. The lens coupling the output into the final optical fibre should be chosen to ensure mode-matching with the single-mode in the fibre. The fibre has a nominal mode-field radius of $w_1 = (2.71 \pm 0.27) \mu\text{m}$ at $\lambda_0 = 920$ nm (780HP fibre, Thorlabs Inc.). The focal length for optimum fibre-coupling is $f_{\text{fibre}} = f_{\text{obj}} \cdot w_1/w_0 = (11.6 \pm 1.2)$ mm. Thus, an $f_{\text{fibre}} = 11$ mm aspheric lens was chosen for the experiments.

In order to estimate the throughput of the optical system, i.e. η_{optics} , the following room-temperature experiment is conducted: a single-mode optical fibre (780HP fibre, Thorlabs Inc.) outputs laser light into free-space, which is collimated by an aspheric lens with effective focal length 18.40 mm (C280TMD-B, Thorlabs Inc.). We measure the power out-coupled from this fibre, P_1 . We then add all the optical components (Fig. A.6a) and couple the light optimally into a second optical fibre and measure the out-coupled power from this second fibre, P_2 . This gives us an estimation of losses in the microscope head: P_2/P_1 . This estimation gives the absorption losses in the full set-up: clipping losses, the reflection losses – the fibres lack anti-reflection coatings – and also any wavefront distortions which limit the in-coupling to the second fibre. We find $\eta_{\text{optics}} = (69.0 \pm 3.6)\%$.

For experiments in Ch. 7, the microscope head is slightly modified. As shown in Fig. A.6b in

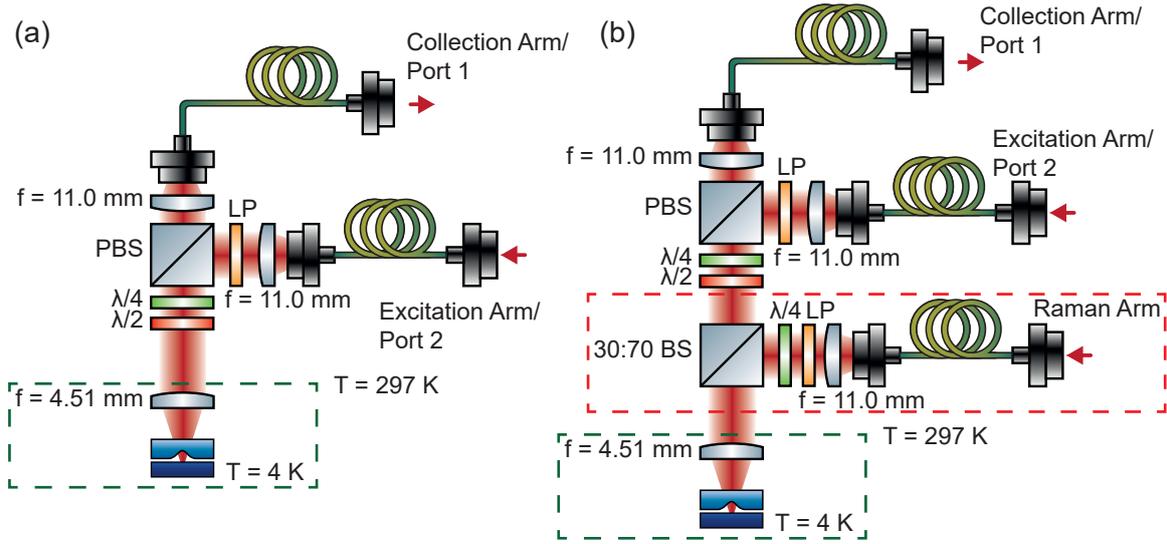


Figure A.6: The optical setup. (a) The microcavity system resides in a cryostat at $T = 4.2$ K. Light is coupled in and out of the microcavity with a polarisation-based dark-field microscope. The objective lens is placed inside the cryostat along with the microcavity; the rest of the microscope is located outside the cryostat. Laser light enters via a single-mode optical fibre and is collimated with an $f = 11$ mm lens, passing through a LP. The input is reflected by a PBS; the polarisation axis of the excitation, the V-axis, is set by the HWP. The PBS and a QWP suppress the coupling of unwanted back-reflected laser light into the collection arm. H-polarised light scattered by the emitter is transmitted through the PBS and focused into the final single-mode optical fibre. (b) The Raman arm (red marked part), including a 30:70 beam-splitter (BS), an LP and a QWP, is added for the spin-control experiments in Ch. 7 in order to additionally send circularly polarised light to the QD.

the red box, an additional arm (the Raman arm) is added, consisting of a 30:70 beam-splitter (BS; $T \sim (62 \pm 10)\%$, Thorlabs Inc.), a LP and a QWP. It is used to control the spin state via a Raman transition and is set such that in addition to the cross-polarised configuration, off-resonant, circularly-polarised light can be sent to the QD. As a consequence of the circularly-polarised light, 50 % of the Raman laser background will end up in the collection arm. In order to filter out the off-resonant light, we use a grating setup ($\sim 50\%$ efficiency, 900 lines/mm at 930 nm, Watatch Photonics). This addition of optical components has a major influence on the collection efficiency. Including the 30:70 BS and the grating setup leads to $\eta_{\text{optics}} = (21.55 \pm 4.55)\%$. Furthermore, any fibre-coupler used in the collection path from port 1 to the detector, will bring an extra loss of $\sim 20\%$ as becomes relevant in the analysis of Ch. 6.

When we measure in the *back-reflection* regime (as discussed in Ch. 3 and 5), the generated light pulses are sent into a 99:1 fibre beam-splitter, which we employ as an approximate optical circulator. We send 1% of the light intensity into the QD-cavity system. The light is back-scattered and 99% of it is sent to the detector.

In order to measure a $G^{(2)}$, a 50:50 fibre beam-splitter is put at the output of the collection arm sending the outputs onto two detectors. Further, in the experimental determination of a three-photon correlation function $G^{(3)}$, we divide the signal on one of the outputs of the beam-splitter once more with a second 50:50 fibre-beam splitter and use four detectors.

A.2.2 Lasers and pulse generation

For most experiments we use a tunable continuous-wave laser (CTL 950 or DL pro, TOPTICA Photonics A.G., Germany).

We generate short (1-10 ns close-to-square or Gaussian-shaped signals with a full-width-at-half-maximum (FWHM) between 75 ps and 2 ns) pulses using a high-bandwidth electro-optic modulator (EOM; EOSpace AZ-6S5-10-PFA-SFAP-950-R5-UL) driven by a high sampling-rate AWG (Tektronix 7122C or Tektronix 70002B). A trigger signal from the AWG is sent to a time-correlator to synchronise the experiment, and the analog output from the AWG is used to modulate the EOM. Similar to the EOM, an acousto-optic modulator (AOM; Gooch & Housgo 3200-1117) can also be used for pulse generation of longer pulses (≥ 10 ns) or for pulse-picking of short picosecond pulses. For the Raman drive (Ch. 7), an EOM is driven by the AWG to generate side-bands of the laser frequency in order to address the spin transitions. This is achieved by generating a sine signal with a oscillation period proportional to the Zeeman splitting of the spin transitions. By rapidly turning this sine signal on and off, spin control pulses at the transitions of the Raman frequency are generated.¹⁷⁷

For single-photon generation and measurement of the QD lifetime, we use a mode-locked laser (Mira 900-D picosecond mode, Coherent GmbH), which operates at a repetition rate of 76.3 MHz. The spectral width lies in the range between 60 and 100 GHz corresponding in the transform-limited case to temporal widths between 5 and 3 ps, respectively. The temporal width is the FWHM of the intensity.

For all lasers used we can select and stabilise the laser power sent to the system with an AOM controlled digitally by a PID-loop.

A.2.3 Use and calibration of detectors

Two photon-counting detectors were used to perform experiments in this work, a superconducting NbTiN-nanowire single-photon detector (SNSPD) unit (EOS 210 CS Closed-cycle, Single Quantum B.V.) optimised for operation at 950 nm; and a near-infrared optimised, fibre-coupled silicon avalanche photodiode (APD, model SPCM-NIR, Excelitas Technologies GmbH & Co. KG). In order to determine the overall collection efficiency, a careful calibration of the detectors' efficiencies was performed.

The measurement relies on a setup with a free-space laser beam (out-coupled from an optical fibre with angled facet), a set of calibrated neutral density filters (NDs) that can be placed in and out of the beam path, and a second optical fibre into which the beam is coupled (in-coupling via an angled facet). The frequency ν of the laser light is determined precisely prior to measurement with a interferometric device (HighFinesse Laser and Electronic Systems GmbH). For optical power P , the photon flux is $\frac{P}{h\nu}$ where h is Planck's constant.

With the NDs removed from the beam's path, the optical power emerging out of the second fibre is measured with a calibrated silicon photodiode (Sensor Model S130C, Power measuring console PM100D, Thorlabs Inc.). The attenuating NDs are subsequently placed into the beam's path in order to avoid saturating the photon-counting detectors. The photon rate out of the fibre is then measured using both the SNSPD and the APD. The efficiency of each detector is given by the ratio of the measured count-rate to the known photon flux.

The efficiency of the SNSPD is determined to be $\eta_{\text{SNSPD}} = (82 \pm 5)\%$. The efficiency of the APD is $\eta_{\text{APD}} = (42 \pm 3)\%$ with an angled facet directly in front of the detector (FC-APC type fibre). The efficiency is slightly higher, $\eta_{\text{APD}} = (44 \pm 3)\%$, with a flat facet directly in front of the detector (FC-PC type fibre).

All continuous-wave transmission measurements were performed using an APD. The $g^{(2)}(\tau)$ - and $g^{(3)}(\tau)$ -measurements as well as all time-resolved photon counting spin experiments and lifetime measurements were performed using the SNSPDs. The binning size can be modified (typically in a range of 1 – 100 ns) and depends on the specific experiment. Also, depending on the data size and type of a measurement, the time tags were recorded either full recording (e.g. in correlation, lifetime or resonance fluorescence measurements of all chapters) or scope mode (e.g. in the single-shot readout measurements in Ch. 6), where only the rising and falling edges on a channel are detected. The signals from the SNSPDs were analysed using a time tagger (Time Tagger Ultra, Swabian Instruments GmbH) with a timing jitter of 9 picoseconds.

B

Theory: A chiral one-dimensional atom

Adapted from:

N. O. Antoniadis, N. Tomm, T. Jakubczyk, R. Schott, S. R. Valentin,
A. D. Wieck, A. Ludwig, R. J. Warburton and A. Javadi

“A chiral one-dimensional atom using a quantum dot in an open microcavity”,
npj Quantum Inf. **8**, 27 (2022)

B.1 Transmission of a two-level emitter in a one-sided cavity

A model describing the transmission of a two-level system coupled to a one-sided cavity is derived based on the theory in Ref. ¹²² We consider the situation in Fig. B.1a. The cavity has two orthogonally polarised modes (H and V). Both modes are coupled to a one-dimensional waveguide. The Hamiltonian for the system is:

$$\begin{aligned} H = & \hbar\omega_0\sigma_z + \hbar(\omega_0 + \delta_H)a_H^\dagger a_H + \hbar(\omega_0 + \delta_V)a_V^\dagger a_V \\ & + i\hbar g_H(\sigma_+ a_H - \sigma_- a_H^\dagger) + i\hbar(g_V^* \sigma_+ a_V - g_V \sigma_- a_V^\dagger) \\ & + \sum_k \hbar\omega b_{kH}^\dagger b_{kH} + \sum_k \hbar\omega b_{kV}^\dagger b_{kV} \\ & + \sum_k \hbar\kappa_- (a_H b_{kH}^\dagger + a_H^\dagger b_{kH}) + \sum_k \hbar\kappa_+ (a_V b_{kV}^\dagger + a_V^\dagger b_{kV}). \end{aligned} \tag{B.1}$$

The cavity contains a single two-level system (TLS) with angular resonance frequency ω_0 . $a_{H/V}$ ($b_{kH/kV}$) describes the annihilation operator for the cavity mode (waveguide fields). $\omega_0 + \delta_{H/V}$ is the cavity angular frequency, ω is the laser angular frequency and $\Delta\omega = \omega_0 - \omega$. The atomic operators are given by $\sigma_z = \frac{1}{2}(|e\rangle\langle e| - |g\rangle\langle g|)$ and $\sigma_- = |g\rangle\langle e|$. The coupling strengths between the cavity modes and the TLS are given by $g_{H,V}$ where g_V can be complex. Applying the same procedure as Ref. ¹²² we end up with the following equations of motion

for the cavity modes and the atomic operators in the laser frame:

$$\begin{aligned}
\dot{a}_{\text{H/V}} &= -i(\Delta\omega + \delta_{\text{H/V}}) \cdot a_{\text{H/V}} - \frac{\kappa}{2} a_{\text{H/V}} - g_{\text{H/V}} \cdot \sigma_- + i\sqrt{\kappa} \cdot b_{\text{in,H/V}}, \\
\dot{\sigma}_- &= -i\Delta\omega\sigma_- - 2g_{\text{H}} \cdot \sigma_z \cdot a_{\text{H}} - 2g_{\text{V}}^* \cdot \sigma_z \cdot a_{\text{V}} - \gamma/2 \cdot \sigma_-, \\
\dot{\sigma}_z &= g_{\text{H}} \cdot (\sigma_+ a_{\text{H}} + a_{\text{H}}^\dagger \sigma_-) + (g_{\text{V}}^* \sigma_+ a_{\text{V}} + g_{\text{V}} a_{\text{V}}^\dagger \sigma_-) - \gamma \cdot \left(\sigma_z + \frac{1}{2}\right), \\
b_{\text{out,H/V}} &= b_{\text{in,H/V}} + i\sqrt{\kappa} \cdot a_{\text{H,V}},
\end{aligned} \tag{B.2}$$

where γ is the decay rate of the two-level system into non-cavity *leaky* modes and is introduced using a Lindblad operator, and κ is the photon decay rate through the top mirror. $b_{\text{in,H/V}}$ describe the horizontally/vertically polarised components of the input field, and $b_{\text{out,H/V}}$ describe the corresponding output fields.

Equations B.2 are the quantum coupled mode equations for the evolution of a TLS and a cavity driven by b_{in} . In the *bad cavity* regime ($\kappa \gg g \gg \gamma$), where the cavity is fast, the cavity mode can adiabatically be eliminated from the equations by setting $\dot{a} = 0$. This implies:

$$a_{\text{H,V}} = \frac{i\sqrt{\kappa} \cdot b_{\text{in,H,V}} - g_{\text{H,V}} \cdot \sigma_-}{\frac{\kappa}{2} + i(\Delta\omega + \delta_{\text{H,V}})}. \tag{B.3}$$

The linearly-polarised field at the input of the diode (the diode consists of the cavity, the TLS and the optical components, as shown in Fig. B.1a) b_{in} , is converted to a circularly polarised field at the input of the cavity, and $b_{\text{in,H}} = 1/\sqrt{2}b_{\text{in}}$ and $b_{\text{in,V}} = i/\sqrt{2}b_{\text{in}}$. Moreover, the TLS has a circularly-polarised optical dipole moment, hence, $g_{\text{V}} = ilg_{\text{H}}$, where $l = \pm 1$ sets the handedness of the optical dipole moment. In the following, we drop the subscript H, setting $g_{\text{H}} = g$. Equation B.3 may be written in a more compact form by using the definition $t_{\text{H,V}} = (1 + 2i(\Delta\omega + \delta_{\text{H,V}})/\kappa)^{-1}$:

$$\begin{aligned}
a_{\text{H}} &= \sqrt{\frac{2}{\kappa}} \left(ib_{\text{in}} - \sqrt{\frac{2g^2}{\kappa}} \sigma_- \right) t_{\text{H}}, \\
a_{\text{V}} &= i\sqrt{\frac{2}{\kappa}} \left(ib_{\text{in}} - l\sqrt{\frac{2g^2}{\kappa}} \sigma_- \right) t_{\text{V}}.
\end{aligned} \tag{B.4}$$

The output of the cavity passes a quarter wave-plate and is converted to a vertical field at the output of the diode, and hence, $b_{\text{out}} = \frac{1}{\sqrt{2}}(b_{\text{out,H}} - ib_{\text{out,V}})$. Combining this equation with the last term in Eq. B.2, the field amplitude at the output of the diode can be related to the input fields and the cavity operators as:

$$\begin{aligned}
b_{\text{out}} &= b_{\text{in}} + \sqrt{\frac{\kappa}{2}}(ia_{\text{H}} + a_{\text{V}}), \\
&= b_{\text{in}} - b_{\text{in}}(t_{\text{H}} + t_{\text{V}}) - i\sqrt{\frac{\Gamma_1}{2}}(t_{\text{H}} + lt_{\text{V}}) \cdot \sigma_-,
\end{aligned} \tag{B.5}$$

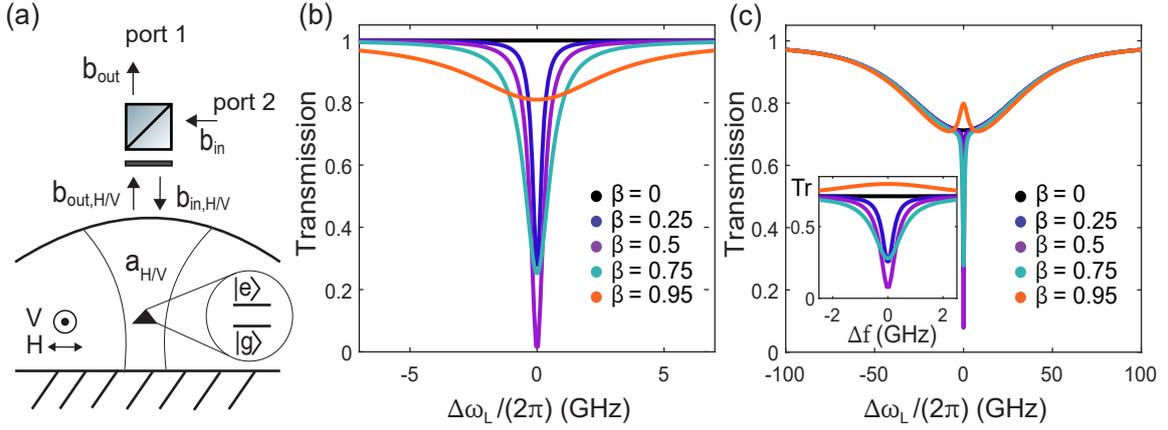


Figure B.1: (a) Illustration of the concept and definition of the parameters of a one-sided cavity with cavity modes a_H and a_V , and incoming (outgoing) field b_{in} (b_{out}). A two-level emitter with ground state $|g\rangle$ and excited state $|e\rangle$ is coupled to the cavity modes. (b) Transmission through the full system in (a) as a function of the laser frequency detuning, $\Delta f = \Delta\omega/(2\pi)$, for different β -factors in the simplified, ideal case: $\delta_H/(2\pi) = \delta_V/(2\pi) = 0$, without spectral fluctuation, $\kappa/(2\pi) = 102$ GHz and $\gamma/(2\pi) = 0.30$ GHz. (c) Transmission through the full system in (a) as a function of the laser frequency detuning, $\Delta f = \Delta\omega/(2\pi)$, for different β -factors under experimental conditions: $\delta_H/(2\pi) - \delta_V/(2\pi) = 29$ GHz, $\delta_{sf}/(2\pi) = 40$ MHz, $\kappa/(2\pi) = 102$ GHz and $\gamma/(2\pi) = 0.30$ GHz. The inset shows how the depth of the dip and the linewidth depend on the β -factor.

and the equations of motion become:

$$\begin{aligned} \dot{\sigma}_- &= -i\Delta\omega\sigma_- - \frac{\Gamma_1}{2} \left(t_H + t_V + \frac{1}{F_{p1}} \right) \sigma_- + ib_{in} \sqrt{\frac{\Gamma_1}{2}} (-2\sigma_z)(t_H + lt_V), \\ \dot{\sigma}_z &= -\Gamma_1 \left(\text{Re}(t_H + lt_V) + \frac{1}{F_{p1}} \right) \left(\sigma_z + \frac{1}{2} \right) + b_{in} \sqrt{\frac{\Gamma_1}{2}} (i(t_H + t_V)\sigma_+ + h.c.), \end{aligned} \quad (\text{B.6})$$

where $\Gamma_1 = \frac{4g^2}{\kappa}$, $F_{p1} = \frac{4g^2}{\kappa\gamma}$. Note that the decay rate of the TLS is $\Gamma = 2\Gamma_1$ when the cavity modes are degenerate. In this limit, the Purcell-factor is $F_p = 2F_{p1}$ as both cavity modes contribute to the total Purcell-factor.

Next, we solve the steady-state equations $\dot{\sigma}_- = \dot{\sigma}_z = 0$ for σ_z and σ_- . Following the Ehrenfest theorem, we can replace the operators in the steady state by their expectation values: $\langle \sigma_- \rangle = S_-$, $\langle \sigma_z \rangle = S_z$ and $\langle b_{in} \rangle = b_{in}$. We end up with:

$$\begin{aligned} S_- &= \frac{ib_{in} \sqrt{\frac{\Gamma_1}{4}} (-2S_z)(t_H + lt_V)}{-i\Delta\omega + \Gamma/4 \left(t_H + t_V + \frac{2}{F_p} \right)}, \\ S_z &= \frac{-1/2 \left(\text{Re}(t_H + lt_V) + \frac{2}{F_p} \right)}{\text{Re}(t_H + lt_V) + \frac{2}{F_p} + 2b_{in}^2 \text{Re} \left[\frac{(t_H + t_V)(t_H^* + lt_V^*)}{i\Delta\omega + \Gamma/4(t_H^* + t_V^* + 2/F_p)} \right]}. \end{aligned} \quad (\text{B.7})$$

For the simplified case of resonant excitation ($\Delta\omega = 0$) and degenerate cavity modes ($\delta_H = \delta_V$), S_z reduces to:

$$S_z = -\frac{1}{2} \frac{1}{1 + |b_{in}|^2/P_c} = -\frac{1}{2}\Pi, \quad (\text{B.8})$$

with critical power:

$$P_c = \frac{\Gamma}{8\beta^2} \cdot \hbar\omega. \quad (\text{B.9})$$

β is the coupling efficiency of the emitter to the cavity and is described by: $\beta = \frac{\Gamma}{\Gamma+\gamma} = \frac{F_p}{F_p+1}$. Plugging Eq. B.7 into Eq. B.5, we determine the full transmission coefficient of the cavity-emitter system via $b_{\text{out}} = t \cdot b_{\text{in}}$ to be:

$$t = 1 - t_H - t_V + \frac{\Pi}{\frac{\Gamma}{2(t_H+t_V)} + 1 + \frac{2}{F_p(t_H+t_V)}} \cdot \frac{(t_H + lt_V)^2}{(t_H + t_V)}. \quad (\text{B.10})$$

When $l = 1$, the optical dipole and the incoming light have the same handedness, while $l = -1$ for a non-interacting optical dipole. At low input powers, with the same simplified condition as in Eq. B.8 ($\Delta\omega = 0$, $\delta_H = \delta_V$) and $l = 1$, the reflection coefficient can be reduced to the simple form:

$$t(0) = -1 + 2\beta. \quad (\text{B.11})$$

In this case, $t(0) = 0$ at the critical coupling condition $\beta = 1/2$.

So far, t includes only the coherent part of the transmitted field. At higher excitation powers, the transmitted field is a sum of coherent and incoherent components. The incoherent component arises from the spontaneous emission of photons from the TLS. The incoherent part of the scattering (P_{incoh}) can be extracted by subtracting the coherent scattering of the TLS (both scattered into the cavity and into non-cavity modes) from the total power:⁹³

$$\frac{P_{\text{incoh}}}{|b_{\text{in}}|^2} = 1 - |t|^2 - \gamma \cdot \frac{|\langle S_- \rangle|^2}{|b_{\text{in}}|^2}. \quad (\text{B.12})$$

The intensity transmission from port 1 to port 2 (or vice versa) in Fig.4.1b is given by

$$T = |t|^2 + \beta \cdot \frac{P_{\text{incoh}}}{2 \cdot |b_{\text{in}}|^2}. \quad (\text{B.13})$$

In the simplest ideal case (resonance condition as in Eq. B.8 and $\beta = 0.5$), this leads to a power-dependent transmission of the form:

$$T = \frac{|b_{\text{in}}|^2/P_c}{(1 + |b_{\text{in}}|^2/P_c)}. \quad (\text{B.14})$$

The average photon flux per lifetime of the emitter is related to the input power via $\hbar\omega \langle n \rangle = |b_{\text{in}}|^2/(\Gamma + \gamma)$.

In order to match the conditions of the experiment, we include a spectral fluctuation. This is done by convoluting a Lorentzian distribution with the quantum dot (QD) transmission:⁶⁶

$$T_{\text{end}} = \int T(\Delta\omega_{\text{QD}} + \sigma) \cdot L(\sigma, \delta_{\text{sf}}) \cdot d\sigma. \quad (\text{B.15})$$

$L(\sigma, \delta_{\text{sf}})$ describes a Lorentzian distribution, σ is the standard deviation and δ_{sf} is the full-width half-maximum (FWHM) of this distribution, i.e. the spectral fluctuation.

Figures B.1b and c show the transmission T_{end} through the system as a function of the laser frequency for different values of the β -factor. We use $\kappa/(2\pi) = 102$ GHz and $\gamma/(2\pi) = 0.30$ GHz for both figures. In Fig. B.1b we show the simplified, ideal case without

mode-splitting and without spectral fluctuation ($\delta_H/(2\pi) = \delta_V/(2\pi) = 0$, $\delta_{sf}/(2\pi) = 0$). The transmission is unity in the case of zero coupling between TLS and cavity ($\beta = 0$). With increasing β , a dip appears on resonance with the TLS. This dip reaches zero at the critical coupling condition $\beta = 0.5$. Increasing β further reduces the depth of the dip again. In the strongly over-coupled regime ($\beta \approx 1$), the photons that interact with the TLS acquire a π -phase shift according to Eq. B.11. Figure B.1c shows the same plot after adapting the theory to the experimental conditions, $\delta_{sf}/(2\pi) = 40$ MHz and $\delta_H/(2\pi) - \delta_V/(2\pi) = 29$ GHz. With no TLS-cavity coupling ($\beta = 0$), the transmission through the system is governed by the two cavity modes and a dip of 30% arises due to the finite mode-splitting of the cavity. In the under-coupled regime ($\beta < 0.5$), a small dip is visible on resonance with the QD, similar to the ideal case. This dip reaches 90% for the critical-coupling condition ($\beta = 0.5$). At the critical-coupling condition, most of the photons impinging on the system are dissipated by the TLS to the non-cavity modes. Increasing β further results in a reduced dip size.

We model the transmission plots using Eq. B.15 with the same parameters as in Fig. B.1. The saturation power extracted by fitting Fig. 4.9b in Ch. 4 with Eq. B.14 is $P_c = 213$ pW, which is in agreement within the errorbar with the theoretical saturation power $P_c = 198$ pW that is expected from Eq. B.9.

B.2 Second-order correlation function

In order to model $g^{(2)}(\tau)$ of the backwards-propagating photons, we base ourselves on the derivation of Ref.¹²³ A comparison of the equations of motion in Ref.¹²³ to the ones in Eq. B.10 (resonance condition: $\Delta\omega = 0$, $\delta_{H/V} = 0 \rightarrow t_{H/V} = 1$) reveals that the equations of motion for a two-sided (2S) cavity are the same as the equations of motion for a one-sided (1S) cavity under the transformation:

$$\frac{1}{1/F_{p,2S} + 1} = \frac{2}{1/F_{p,1S} + 1}, \quad (\text{B.16})$$

where $F_{p,2S}$ is the Purcell factor as defined in Ref.¹²³ and $F_{p,1S}$ is the Purcell factor in Eq. B.10. This transformation is equivalent to transforming the β -factor as $\beta_{2S} = 2\beta_{1S}$. Note that this substitution can also be seen from the difference in the simplified transmission equations, which for a two-sided cavity is $T = |1 - \beta|^2$ and $T = |1 - 2\beta|^2$ for a one-sided cavity.

We use the result for $g^{(2)}(\tau)$ in Ref.¹²³ to model $g^{(2)}(\tau)$ in our experiments. The full formula for $g^{(2)}(\tau)$ is given by

$$g^{(2)}(\tau) = 1 + \left(\frac{\sqrt{2}F_{p,2S}}{1 + Y^2} \right)^2 \cdot e^{(3/4)\tau'} \cdot \left\{ \left(Y^2 + \frac{F_{p,2S}^2}{2} - 1 \right) \cdot \cosh(\Omega\tau') + \frac{1}{4\Omega} \cdot \left[Y^2 \cdot \frac{5 - F_{p,2S}}{1 + F_{p,2S}} - 1 - \frac{F_{p,2S}^2}{2} \right] \cdot \sinh(\Omega\tau') \right\}, \quad (\text{B.17})$$

with $\Omega = 1/4 \cdot \sqrt{1 - (8Y)^2 / ((1 + F_{p,2S})^2)}$; Y is the Rabi angular frequency in units of γ ($Y = \sqrt{\Gamma}/\sqrt{\gamma} \cdot b_{in}$); and τ' is a dimensionless delay, $\tau' = \gamma(1 + F_{p,2S}) \cdot \tau$. In the low power limit ($Y \ll 1$), this reduces to:

$$g^{(2)}(\tau) = (1 - F_{p,2S}^2 \cdot e^{-\tau'/2})^2, \quad (\text{B.18})$$

and

$$g^{(2)}(0) = (1 - F_{p,2S}^2)^2. \quad (\text{B.19})$$

The power dependence of the bunching is modelled by setting the time delay $\tau = 0$, resulting in:

$$g^{(2)}(0) = 1 + \left(\frac{\sqrt{2}F_{p,2S}}{1 + Y^2} \right)^2 \cdot \left(Y^2 + \frac{F_{p,2S}^2}{2} - 1 \right). \quad (\text{B.20})$$

These equations describe our measurements very well. Note that all the modelling for the correlation function was carried out for the case of a degenerate cavity for simplicity. We use $F_{p,1S} = 0.8$ to model our results in the backward direction. The discrepancy with the expected value of $F_{p,1S} = 1$ likely results from the residual spectral fluctuation (see last part of App. B.1 and Eq. B.15) as $g^{(2)}(\tau)$ has a strong dependence on dephasing at low powers.⁵⁵

C

Off-resonant drive through the top mirror of the open microcavity

In our system, the only path for the excitation of the quantum dot (QD) with a light field is via the top mirror. Transmission of a light field strongly depends on the detuning of the laser to the cavity mode and the cavity parameters. In order to drive coherently a QD spin, a detuned laser ($\gtrsim 200$ GHz) has to drive a Raman transition (see Ch. 7). In this appendix we derive the enhancement factor of the electric field through a one-sided cavity as a function of the laser detuning Δ_L and the linewidth Δ_f and finesse \mathcal{F} of the cavity. The goal is to find out, if the QD spin transition can be driven coherently through the top mirror in the given experimental conditions. We begin with a simple sketch of an incoming light field with electric field amplitude E_0 scattering of a planar cavity with two flat mirrors as shown in Fig. C.1. The derivation follows Ch. 3 of Ref. ²³⁸

The ratio of the electric field at the centre of the cavity and the input field can be calculated

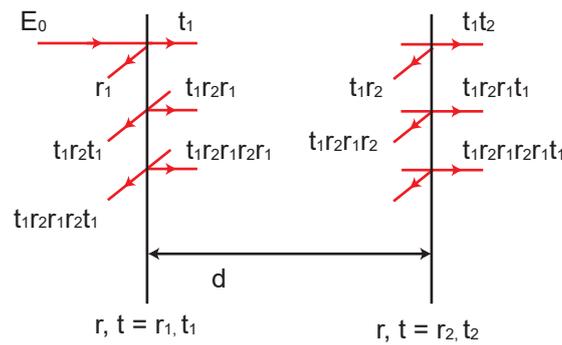


Figure C.1: Illustration of the transmission t_i and reflection r_i coefficients of an incoming electric field E_0 scattering of a cavity consisting of two planar mirrors with distance d between them. The sketch shows the first few components.

by adding up all left and right propagating components inside the cavity

$$\begin{aligned}\frac{E_c}{E_0} &= t_1 e^{-i\delta/4} + t_1 \cdot r_2 e^{-3i\delta/4} + t_1 \cdot r_2 \cdot r_1 e^{-5i\delta/4} + t_1 \cdot r_2 \cdot r_1 \cdot r_2 e^{-7i\delta/4} + \dots \\ &= t_1 e^{-i\delta/4} \left[\frac{1 + r_2 e^{-i\delta/2}}{1 - r_1 r_2 e^{-i\delta}} \right],\end{aligned}\quad (\text{C.1})$$

where δ is the phase change acquired on a round-trip and r_i/t_i are the reflection/transmission coefficients of the two mirrors. For simplifications in the derivation of the detuning dependence of the field enhancement in the cavity later on in this appendix, it is useful to define the electric field ratio in the cavity right after the first mirror only propagating in the direction of the incoming field:

$$\begin{aligned}\frac{E_{c,\rightarrow}}{E_0} &= t_1 + t_1 \cdot r_2 \cdot r_1 e^{-i\delta} + t_1 \cdot r_2 \cdot r_1 \cdot r_2 \cdot r_1 e^{-2i\delta} + \dots \\ &= \frac{t_1}{1 - r_1 r_2 e^{-i\delta}} \approx \frac{t_1}{(1 - r_1 r_2) + ir_1 r_2 \delta}.\end{aligned}\quad (\text{C.2})$$

Furthermore, from Eq. C.1 we can calculate the ratio of the full field intensity at the centre of the cavity and the intensity of the input field:

$$\frac{I_c}{I_0} = \left| \frac{E_c}{E_0} \right|^2 = \frac{(1 - r_1^2)(r_2^2 + 1 + 2r_2 \cos(\delta/2))}{(1 - r_1 r_2)^2 + 4r_1 r_2 \sin^2(\delta/2)} \approx \frac{t_1^2 (r_2 + 1)^2}{(1 - r_1 r_2)^2 + r_1 r_2 \delta^2}.\quad (\text{C.3})$$

Several parameters can be extracted from Eq. C.3. The resonances of the intensity in the cavity are found at $\sin(\delta/2) = 0$, hence $\delta = j \cdot 2\pi$ ($j \in \mathbb{N}$) and the free spectral range (FSR) of the cavity $\text{FSR} = 2\pi$. Using the small angle approximation we find the half of the maximum intensity at $(1 - r_1 r_2)^2 = r_1 r_2 \delta^2$. Therefore, $\delta = \frac{1 - r_1 r_2}{\sqrt{r_1 r_2}}$ leading to a full-width-at-half-maximum (FWHM) $\approx 2(1 - r_1 r_2)$.

Using these equations for FWHM and FSR, we define the finesse of the cavity in terms of the cavity mirrors reflection and transmission coefficients:

$$\mathcal{F} = \frac{\text{FSR}}{\text{FWHM}} = \frac{\pi}{1 - r_1 r_2}.\quad (\text{C.4})$$

Further, some experimental parameters are connected with these expressions. According to Ref. ⁹⁴ and Eq. C.3, the $\text{FWHM} = \Delta\delta = 2(1 - r_1 r_2) = \frac{4\pi d}{c} \Delta f$, with c the speed of light and Δf the cavity linewidth. Therefore, $\delta = \frac{2d}{\lambda} 2\pi = \frac{4\pi d}{c} f$, where f is the laser frequency. Further, $\text{FSR}_f = \mathcal{F} \cdot \Delta f = \frac{c}{4\pi d} 2\pi$ (FSR_f is the FSR in frequency domain).

In order to estimate the detuning dependence of the field enhancement in the cavity we plug these relations into Eq. C.2:

$$\frac{E_{c,\rightarrow}}{E_0} = \frac{t_1}{(1 - r_1 r_2) + ir_1 r_2 \delta} = \frac{t_1 \mathcal{F} (\Delta f / 2\pi)}{(\Delta f / 2) + i(f - f_0)}.\quad (\text{C.5})$$

This leads to a intensity ratio of:

$$\begin{aligned} \frac{I_{c,\rightarrow}}{I_0} &= \frac{t_1^2 \mathcal{F}(\Delta f/2\pi)^2}{(\Delta f/2)^2 + (f - f_0)^2} = \left(\frac{t_1 \mathcal{F}}{\pi}\right)^2 \frac{(\Delta f/2)^2}{(\Delta f/2)^2 + (f - f_0)^2} \\ &= X_{\rightarrow} \frac{(\Delta f/2)^2}{(\Delta f/2)^2 + (f - f_0)^2}. \end{aligned} \quad (\text{C.6})$$

The resonance condition of Eq. C.6 is the enhancement factor of the field intensity in the cavity, X_{\rightarrow} . Note that we can use the simplified scenario (Eq. C.2 instead of Eq. C.1) because the detuning dependence of the enhancement factor should not be influenced by the counter-propagating part of the electric field.

Finally, we can calculate the full enhancement of the electric field in our experimental configuration, a one-sided cavity, where $r_2 = 1$, and $r_1 = r$. On resonance of Eq. C.3 ($\delta = 0$):

$$\frac{I_c}{I_0} = \frac{4(1 - r_1^2)}{(1 - r_1)^2} = \frac{4(1 + r_1)}{(1 - r_1)} \approx 8\mathcal{F}/\pi = X. \quad (\text{C.7})$$

The enhancement at resonance with the cavity, X , is given by $8\mathcal{F}/\pi$. Note that in comparison to the derivation in Ref. ²³⁸ there is an additional factor of 8. A factor of 2 comes from the the one-sided nature of our cavity in comparison to a two-sided cavity. Another factor of two arises from the derivation with the full electric field in the centre of the cavity rather than only using the simplified scenario in Eq. C.2 ($x = 2X_{\rightarrow}$). This results in a factor of four enhancement in the intensity of the field leading to an overall factor of 8.

In our experiments, $\mathcal{F} = 506$, hence $X = 1285$. In order to look at the detuning dependence of the enhancement in our experimental case, we take Eq. C.6 and calculate the detuning at which the cavity enhancement cancels out the losses due to detuning of the laser with respect to the cavity. We assume $|f - f_0| \gg \Delta f$. In that case

$$\frac{I_c}{I_0} \approx X \cdot \frac{(\Delta f/2)^2}{(f - f_0)^2}, \quad (\text{C.8})$$

i.e. $I_c = I_0$ for

$$f - f_0 = \sqrt{\frac{8\mathcal{F}}{\pi}}(\Delta f/2) = \sqrt{\frac{2\mathcal{F}}{\pi}}\Delta f = 12.6\Delta f = 448\text{GHz}. \quad (\text{C.9})$$

Hence, for our $\Delta f = 25$ GHz, we observe this condition at a detuning of 448 GHz, as can be observed in Fig. 7.1b.

As the spin can be driven by Raman transitions with a detuning of $\gtrsim 200$ GHzⁱ, this derivation shows how a Raman drive can be implemented in our cavity by driving through the top mirror. In fact, at all Raman laser detunings used in Ch. 7, the field intensity is still enhanced compared to the laser input, which allows for faster spin rotations (~ 1 GHz) than without the cavity.

ⁱThis is an estimate based on previous experiments. In order to avoid populating the excited state in the Raman process, the detuning should be much higher than the spin Rabi frequency.

Bibliography

- [1] Einstein, A., Podolsky, B. & Rosen, N. Can Quantum-Mechanical Description of Physical Reality Be Considered Complete? *Phys. Rev.* **47**, 777–780 (1935).
- [2] Aspect, A., Dalibard, J. & Roger, G. Experimental Test of Bell’s Inequalities Using Time-Varying Analyzers. *Phys. Rev. Lett.* **49**, 1804–1807 (1982).
- [3] Hensen, B. *et al.* Loophole-free bell inequality violation using electron spins separated by 1.3 kilometres. *Nature* **526**, 682–686 (2015).
- [4] Symul, T., Assad, S. M. & Lam, P. K. Real time demonstration of high bitrate quantum random number generation with coherent laser light. *APL* **98**, 231103 (2011).
- [5] Degen, C. L., Poggio, M., Mamin, H. J., Rettner, C. T. & Rugar, D. Nanoscale magnetic resonance imaging. *PNAS* **106**, 1313–1317 (2009).
- [6] Grinolds, M. S. *et al.* Nanoscale magnetic imaging of a single electron spin under ambient conditions. *Nat. Phys.* **9**, 215–219 (2013).
- [7] Vahlbruch, H. *et al.* The GEO 600 squeezed light source. *Class. Quantum Gravity* **27**, 084027 (2010).
- [8] Aasi, J. *et al.* Enhanced sensitivity of the LIGO gravitational wave detector by using squeezed states of light. *Nat. Photon.* **7**, 613–619 (2013).
- [9] Kimble, H. J. The quantum internet. *Nature* **453**, 1023–1030 (2008).
- [10] Kołodyński, J. *et al.* Device-independent quantum key distribution with single-photon sources. *Quantum* **4**, 260 (2020).
- [11] Hermans, S. L. N. *et al.* Qubit teleportation between non-neighbouring nodes in a quantum network. *Nature* **605**, 663–668 (2022).
- [12] Lu, C.-Y. & Pan, J.-W. Quantum-dot single-photon sources for the quantum internet. *Nat. Nanotechnol.* **16**, 1294–1296 (2021).
- [13] Nielsen, M. A. & Chuang, I. L. *Quantum computation and quantum information* (Cambridge university press, 2010).
- [14] Raussendorf, R. & Briegel, H. J. A one-way quantum computer. *Phys. Rev. Lett.* **86**, 5188–5191 (2001).
- [15] Nielsen, M. A. Cluster-state quantum computation. *Rep. Math. Phys.* **57**, 147–161 (2006).
- [16] Russo, A., Barnes, E. & Economou, S. E. Generation of arbitrary all-photon graph states from quantum emitters. *New J. Phys.* **21**, 055002 (2019).
- [17] Tiurev, K. *et al.* High-fidelity multiphoton-entangled cluster state with solid-state quantum emitters in photonic nanostructures. *Phys. Rev. A* **105**, L030601 (2022).
- [18] Devoret, M. H. & Schoelkopf, R. J. Superconducting circuits for quantum information: An outlook. *Science* **339**, 1169–1174 (2013).
- [19] Tomm, N. *et al.* A bright and fast source of coherent single photons. *Nat. Nanotechnol.* **16**, 399–403 (2021).
- [20] Camenzind, L. C. *et al.* A hole spin qubit in a fin field-effect transistor above 4 kelvin. *Nat. Electron.* **5**, 178–183 (2022).
- [21] Leibfried, D., Blatt, R., Monroe, C. & Wineland, D. Quantum dynamics of single trapped ions. *Rev. Mod. Phys.* **75**, 281–324 (2003).

- [22] Duan, L.-M. & Monroe, C. Colloquium: Quantum networks with trapped ions. *Rev. Mod. Phys.* **82**, 1209–1224 (2010).
- [23] Senellart, P., Solomon, G. & White, A. High-performance semiconductor quantum-dot single-photon sources. *Nat. Nanotechnol.* **12**, 1026–1039 (2017).
- [24] Chuang, I. L. & Yamamoto, Y. Simple quantum computer. *Phys. Rev. A* **52**, 3489–3496 (1995).
- [25] Turchette, Q. A., Hood, C., Lange, W., Mabuchi, H. & Kimble, H. J. Measurement of conditional phase shifts for quantum logic. *Phys. Rev. Lett.* **75**, 4710 (1995).
- [26] Duan, L.-M. & Kimble, H. J. Scalable photonic quantum computation through cavity-assisted interactions. *Phys. Rev. Lett.* **92**, 127902 (2004).
- [27] Awschalom, D. *et al.* Development of Quantum Interconnects (QuICs) for Next-Generation Information Technologies. *PRX Quantum* **2**, 017002 (2021).
- [28] Loss, D. & DiVincenzo, D. P. Quantum computation with quantum dots. *Phys. Rev. A* **57**, 120 (1998).
- [29] Ruf, M., Wan, N. H., Choi, H., Englund, D. & Hanson, R. Quantum networks based on color centers in diamond. *J. Appl. Phys.* **130**, 070901 (2021).
- [30] Bradac, C., Gao, W., Forneris, J., Trusheim, M. E. & Aharonovich, I. Quantum nanophotonics with group IV defects in diamond. *Nat. Commun.* **10**, 5625 (2019).
- [31] Stas, P.-J. *et al.* Robust multi-qubit quantum network node with integrated error detection. *Science* **378**, 557–560.
- [32] Weiss, L., Gritsch, A., Merkel, B. & Reiserer, A. Erbium dopants in nanophotonic silicon waveguides. *Optica* **8**, 40–41 (2021).
- [33] McKeever, J. *et al.* Deterministic generation of single photons from one atom trapped in a cavity. *Science* **303**, 1992–1994 (2004).
- [34] Wilk, T., Webster, S. C., Specht, H. P., Rempe, G. & Kuhn, A. Polarization-controlled single photons. *Phys. Rev. Lett.* **98**, 063601 (2007).
- [35] Ritter, S. *et al.* An elementary quantum network of single atoms in optical cavities. *Nature* **484**, 195–200.
- [36] Reiserer, A., Kalb, N., Rempe, G. & Ritter, S. A quantum gate between a flying optical photon and a single trapped atom. *Nature* **508**, 237 (2014).
- [37] Meraner, M. *et al.* Indistinguishable photons from a trapped-ion quantum network node. *Phys. Rev. A* **102**, 052614 (2020).
- [38] Warburton, R. J. *et al.* Optical emission from a charge-tunable quantum ring. *Nature* **405**, 926–929 (2000).
- [39] Warburton, R. J. Single spins in self-assembled quantum dots. *Nat. Mater.* **12**, 483–493 (2013).
- [40] Reilly, D. J. *et al.* Suppressing Spin Qubit Dephasing by Nuclear State Preparation. *Science* **321**, 817–821 (2008).
- [41] Foletti, S., Bluhm, H., Mahalu, D., Umansky, V. & Yacoby, A. Universal quantum control of two-electron spin quantum bits using dynamic nuclear polarization. *Nat. Phys.* **5**, 903–908 (2009).
- [42] Bluhm, H., Foletti, S., Mahalu, D., Umansky, V. & Yacoby, A. Enhancing the Coherence of a Spin Qubit by Operating it as a Feedback Loop That Controls its Nuclear Spin Bath. *Phys. Rev. Lett.* **105**, 216803 (2010).
- [43] Gangloff, D. A. *et al.* Quantum interface of an electron and a nuclear ensemble. *Science* **364**, 62–66 (2019).
- [44] Jackson, D. M. *et al.* Optimal Purification of a Spin Ensemble by Quantum-Algorithmic Feedback. *Phys. Rev. X* **12**, 031014 (2022).
- [45] Arcari, M. *et al.* Near-unity coupling efficiency of a quantum emitter to a photonic crystal waveguide. *Phys. Rev. Lett.* **113**, 093603 (2014).
- [46] Somaschi, N. *et al.* Near-optimal single-photon sources in the solid state. *Nat. Photon.* **10**, 340–345 (2016).

- [47] Wang, H. *et al.* Towards optimal single-photon sources from polarized microcavities. *Nat. Photon.* **13**, 770–775 (2019).
- [48] Najer, D. *et al.* A gated quantum dot strongly coupled to an optical microcavity. *Nature* **575**, 622–627 (2019).
- [49] Chen, S. *et al.* Heralded three-photon entanglement from a single-photon source on a photonic chip. arXiv:2307.02189(2023).
- [50] Shen, J.-T. & Fan, S. Strongly correlated two-photon transport in a one-dimensional waveguide coupled to a two-level system. *Phys. Rev. Lett.* **98**, 153003 (2007).
- [51] Shen, J.-T. & Fan, S. Theory of single-photon transport in a single-mode waveguide. I. Coupling to a cavity containing a two-level atom. *Phys. Rev. A* **79**, 023837 (2009).
- [52] Lodahl, P. *et al.* Chiral quantum optics. *Nature* **541**, 473–480 (2017).
- [53] Yurgens, V. *et al.* Spectrally stable nitrogen-vacancy centers in diamond formed by carbon implantation into thin microstructures. *APL* **121**, 234001 (2022).
- [54] Toninelli, C. *et al.* Single organic molecules for photonic quantum technologies. *Nat. Mater.* **20**, 1615–1628 (2021).
- [55] Lodahl, P., Mahmoodian, S. & Stobbe, S. Interfacing single photons and single quantum dots with photonic nanostructures. *Rev. Mod. Phys.* **87**, 347–400 (2015).
- [56] Lodahl, P., Ludwig, A. & Warburton, R. J. A deterministic source of single photons. *Phys. Today* **75**, 44–50 (2022).
- [57] Stranski, I. N. & Krastanov, L. Zur Theorie der orientierten Ausscheidung von Ionenkristallen aufeinander. *Sitz. Ber. Akad. Wiss. Math.-Naturwiss. Kl. Abt. IIB* **146**, 797–810 (1938).
- [58] Slater, J. C. & Koster, G. F. Simplified LCAO Method for the Periodic Potential Problem. *Phys. Rev.* **94**, 1498–1524 (1954).
- [59] Harrison, W. A. *Electronic Structure and the Properties of Solids: The Physics of the Chemical Bond* (Dover Publications, 1989).
- [60] Yu, P. Y. & Cardona, M. *Fundamentals of Semiconductors* (Springer, 2010), 4th edn.
- [61] Aharonovich, I., Englund, D. & Toth, M. Solid-state single-photon emitters. *Nat. Photon.* **10**, 631–641 (2016).
- [62] Zrenner, A. A close look on single quantum dots. *J. Chem. Phys.* **112**, 7790–7798 (2000).
- [63] Dalgarno, P. A. *et al.* Coulomb interactions in single charged self-assembled quantum dots: Radiative lifetime and recombination energy. *Phys. Rev. B* **77**, 245311 (2008).
- [64] Smith, J. M. *et al.* Voltage Control of the Spin Dynamics of an Exciton in a Semiconductor Quantum Dot. *Phys. Rev. Lett.* **94**, 197402 (2005).
- [65] Kuhlmann, A. V. *et al.* Transform-limited single photons from a single quantum dot. *Nat. Commun.* **6** (2015).
- [66] Kuhlmann, A. V. *et al.* Charge noise and spin noise in a semiconductor quantum device. *Nat. Phys.* **9**, 570–575 (2013).
- [67] Iles-Smith, J., McCutcheon, D. P. S., Nazir, A. & Mork, J. Phonon scattering inhibits simultaneous near-unity efficiency and indistinguishability in semiconductor single-photon sources. *Nat. Photon.* **11**, 521 (2017).
- [68] Denning, E. V., Iles-Smith, J., Gregersen, N. & Mork, J. Phonon effects in quantum dot single-photon sources. *Opt. Mater. Express* **10**, 222–239 (2020).
- [69] Bester, G. & Zunger, A. Compositional and size-dependent spectroscopic shifts in charged self-assembled $\text{In}_x\text{Ga}_{1-x}\text{As}/\text{GaAs}$ quantum dots. *Phys. Rev. B* **68**, 073309 (2003).
- [70] Bayer, M. *et al.* Fine structure of neutral and charged excitons in self-assembled $\text{In}(\text{Ga})\text{As}/(\text{Al})\text{GaAs}$ quantum dots. *Phys. Rev. B* **65**, 195315 (2002).
- [71] Messiah, A. *Quantum Mechanics* (Dover, 1999).
- [72] Tischler, J., Gammon, D. & Bracker, A. Single Exciton Magneto-Photoluminescence in GaAs Quantum Wells. *Phys. Status Solidi B* **230**, 315–320 (2002).

- [73] Bayer, M. & Forchel, A. Temperature dependence of the exciton homogeneous linewidth in $\text{In}_{0.60}\text{Ga}_{0.40}\text{As}/\text{GaAs}$ self-assembled quantum dots. *Phys. Rev. B* **65**, 041308(R) (2002).
- [74] Kroner, M. *et al.* Optical detection of single-electron spin resonance in a quantum dot. *Phys. Rev. Lett.* **100**, 156803 (2008).
- [75] Högele, A. *et al.* Spin-selective optical absorption of singly charged excitons in a quantum dot. *APL* **86**, 221905 (2005).
- [76] Belhadj, T. *et al.* Impact of heavy hole-light hole coupling on optical selection rules in GaAs quantum dots. *APL* **97**, 051111 (2010).
- [77] Fischer, J., Trif, M., Coish, W. A. & Loss, D. Spin interactions, relaxation and decoherence in quantum dots. *Solid State Commun.* **149**, 1443–1450 (2009).
- [78] Stockill, R. *et al.* Quantum dot spin coherence governed by a strained nuclear environment. *Nat. Commun.* **7**, 12745 (2016).
- [79] Högele, A. *et al.* Voltage-controlled optics of a quantum dot. *Phys. Rev. Lett.* **93**, 217401 (2004).
- [80] Latta, C. *et al.* Confluence of resonant laser excitation and bidirectional quantum-dot nuclear-spin polarization. *Nat. Phys.* **5**, 758–763 (2009).
- [81] Coish, W. A. & Baugh, J. Nuclear spins in nanostructures. *Phys. Status Solidi B* **246**, 2203–2215 (2009).
- [82] Abragam, A. & Hebel, L. C. The Principles of Nuclear Magnetism. *Am. J. Phys.* **29**, 860–861 (1961).
- [83] Press, D. *et al.* Ultrafast optical spin echo in a single quantum dot. *Nat. Photon.* **4**, 367–370 (2010).
- [84] Xu, X. *et al.* Coherent population trapping of an electron spin in a single negatively charged quantum dot. *Nat. Phys.* **4**, 692–695 (2008).
- [85] Kroner, M. *et al.* Resonant two-color high-resolution spectroscopy of a negatively charged exciton in a self-assembled quantum dot. *Phys. Rev. B* **78**, 075429 (2008).
- [86] Press, D., Ladd, T. D., Zhang, B. & Yamamoto, Y. Complete quantum control of a single quantum dot spin using ultrafast optical pulses. *Nature* **456**, 218–221 (2008).
- [87] Brunner, D. *et al.* A coherent single-hole spin in a semiconductor. *Science* **325**, 70–72 (2009).
- [88] Fischer, J., Coish, W. A., Bulaev, D. V. & Loss, D. Spin decoherence of a heavy hole coupled to nuclear spins in a quantum dot. *Phys. Rev. B* **78**, 155329 (2008).
- [89] Fallahi, P., Yilmaz, S. T. & Imamoğlu, A. Measurement of a Heavy-Hole Hyperfine Interaction in InGaAs Quantum Dots Using Resonance Fluorescence. *Phys. Rev. Lett.* **105**, 257402 (2010).
- [90] Luo, J.-W., Bester, G. & Zunger, A. Supercoupling between heavy-hole and light-hole states in nanostructures. *Phys. Rev. B* **92**, 165301 (2015).
- [91] Ribeiro, H., Maier, F. & Loss, D. Inhibition of dynamic nuclear polarization by heavy-hole noncollinear hyperfine interactions. *Phys. Rev. B* **92**, 075421 (2015).
- [92] Uppu, R. *et al.* Scalable integrated single-photon source. *Sci. Adv.* **6**, eabc8268 (2020).
- [93] Javadi, A. *et al.* Single-photon non-linear optics with a quantum dot in a waveguide. *Nat. Commun.* **6**, 8655 (2015).
- [94] Fox, M. *Quantum optics: an introduction* (Oxford University Press, 2006).
- [95] Cui, G. & Raymer, M. G. Quantum efficiency of single-photon sources in the cavity-QED strong-coupling regime. *Opt. Express* **13**, 9660–9665 (2005).
- [96] Brokmann, X., Bawendi, M., Coolen, L. & Hermier, J.-P. Photon-correlation Fourier spectroscopy. *Opt. Express* **14**, 6333–6341 (2006).
- [97] Scheucher, M., Hilico, A., Will, E., Volz, J. & Rauschenbeutel, A. Quantum optical circulator controlled by a single chirally coupled atom. *Science* **354**, 1577–1580 (2016).
- [98] Mahmoodian, S., Lodahl, P. & Sørensen, A. S. Quantum Networks with Chiral-Light–Matter Interaction in Waveguides. *Phys. Rev. Lett.* **117**, 240501 (2016).
- [99] Prasad, A. S. *et al.* Correlating photons using the collective nonlinear response of atoms weakly coupled to an optical mode. *Nat. Photon.* **14**, 719–722 (2020).

- [100] Antoniadis, N. O. *et al.* A chiral one-dimensional atom using a quantum dot in an open microcavity. *npj Quantum Inf.* **8**, 27 (2022).
- [101] Kimble, H. J. Strong interactions of single atoms and photons in cavity qed. *Phys. Scr.* **T76**, 127 (1998).
- [102] Witthaut, D., Lukin, M. D. & Sørensen, A. S. Photon sorters and QND detectors using single photon emitters. *EPL* **97**, 50007 (2012).
- [103] Hartmann, M. J., ao, F. G. S. L. B. & Plenio, M. B. Strongly interacting polaritons in coupled arrays of cavities. *Nat. Phys.* **2**, 849 (2006).
- [104] Chang, D. E., Vuletić, V. & Lukin, M. D. Quantum nonlinear optics — photon by photon. *Nat. Photon.* **8**, 685 – 694 (2014).
- [105] Chang, D. E., Douglas, J. S., González-Tudela, A., Hung, C.-L. & Kimble, H. J. Colloquium: Quantum matter built from nanoscopic lattices of atoms and photons. *Rev. Mod. Phys.* **90**, 031002 (2018).
- [106] Le Jeannic, H. *et al.* Dynamical photon-photon interaction mediated by a quantum emitter. *Nat. Phys.* **18**, 1191–1195 (2022).
- [107] Sørensen, H. *et al.* Coherent Backscattering of Light Off One-Dimensional Atomic Strings. *Phys. Rev. Lett.* **117**, 133604 (2016).
- [108] Goban, A. *et al.* Atom–light interactions in photonic crystals. *Nat. Commun.* **5**, 3808 (2014).
- [109] Tiecke, T. G. *et al.* Nanophotonic quantum phase switch with a single atom. *Nature* **508**, 241–244 (2014).
- [110] Luan, X. *et al.* The Integration of Photonic Crystal Waveguides with Atom Arrays in Optical Tweezers. *Adv. Quantum Technol.* **3**, 2000008 (2020).
- [111] Takahashi, H., Kassa, E., Christoforou, C. & Keller, M. Strong Coupling of a Single Ion to an Optical Cavity. *Phys. Rev. Lett.* **124**, 013602 (2020).
- [112] Pscherer, A. *et al.* Single-molecule vacuum Rabi splitting: four-wave mixing and optical switching at the single-photon level. *Phys. Rev. Lett.* **127**, 133603 (2021).
- [113] Rakher, M. T., Stoltz, N. G., Coldren, L. A., Petroff, P. M. & Bouwmeester, D. Externally mode-matched cavity quantum electrodynamics with charge-tunable quantum dots. *Phys. Rev. Lett.* **102**, 097403 (2009).
- [114] Bakker, M. A., Mehl, S., Hiltunen, T., Harju, A. & DiVincenzo, D. P. Validity of the single-particle description and charge noise resilience for multielectron quantum dots. *Phys. Rev. B* **91**, 155425 (2015).
- [115] De Santis, L. *et al.* A solid-state single-photon filter. *Nat. Nanotechnol.* **12**, 663–667 (2017).
- [116] Shen, J. T. & Fan, S. Coherent photon transport from spontaneous emission in one-dimensional waveguides. *Opt. Lett.* **30**, 2001–2003 (2005).
- [117] Chang, D. E., Sorensen, A. S., Demler, E. A. & Lukin, M. D. A single-photon transistor using nanoscale surface plasmons. *Nat. Phys.* **3**, 807–812 (2007).
- [118] Stiesdal, N. *et al.* Observation of three-body correlations for photons coupled to a Rydberg superatom. *Phys. Rev. Lett.* **121**, 103601 (2018).
- [119] Liang, Q.-Y. *et al.* Observation of three-photon bound states in a quantum nonlinear medium. *Science* **359**, 783–786 (2018).
- [120] Tomm, N. *et al.* Photon bound state dynamics from a single artificial atom. *Nat. Phys.* **19**, 857–862 (2023).
- [121] Carmichael, H. J., Brecha, R. J., Raizen, M. G., Kimble, H. J. & Rice, P. R. Subnatural linewidth averaging for coupled atomic and cavity-mode oscillators. *Phys. Rev. A* **40**, 5516 (1989).
- [122] Auffèves-Garnier, A., Simon, C., Gérard, J.-M. & Poizat, J.-P. Giant optical nonlinearity induced by a single two-level system interacting with a cavity in the purcell regime. *Phys. Rev. A* **75**, 053823 (2007).
- [123] Rice, P. R. & Carmichael, H. J. Single-atom cavity-enhanced absorption. I. Photon statistics in the bad-cavity limit. *IEEE J. Quantum Electron.* **24**, 1351–1366 (1988).
- [124] Carmichael, H. *Statistical Methods in Quantum Optics 2: Non-Classical Fields. Cavity QED I: Simple Calculations* (Springer Berlin Heidelberg, 2008).

- [125] Mahmoodian, S., Calajó, G., Chang, D. E., Hammerer, K. & Sørensen, A. S. Dynamics of many-body photon bound states in chiral waveguide QED. *Phys. Rev. X* **10**, 031011 (2020).
- [126] Noh, C. & Angelakis, D. G. Quantum simulations and many-body physics with light. *Rep. Prog. Phys.* **80**, 016401 (2016).
- [127] Ralph, T. C., Söllner, I., Mahmoodian, S., White, A. G. & Lodahl, P. Photon sorting, efficient Bell measurements, and a deterministic controlled- z gate using a passive two-level nonlinearity. *Phys. Rev. Lett.* **114**, 173603 (2015).
- [128] Yang, F., Lund, M. M., Pohl, T., Lodahl, P. & Mølmer, K. Deterministic Photon Sorting in Waveguide QED Systems. *Phys. Rev. Lett.* **128**, 213603 (2022).
- [129] Shomroni, I. *et al.* All-optical routing of single photons by a one-atom switch controlled by a single photon. *Science* **345**, 903–906 (2014).
- [130] Chen, Z., Zhou, Y., Shen, J.-T., Ku, P.-C. & Steel, D. Two-photon controlled-phase gates enabled by photonic dimers. *Phys. Rev. A* **103**, 052610 (2021).
- [131] Brod, D. J. & Combes, J. Passive CPHASE Gate via Cross-Kerr Nonlinearities. *Phys. Rev. Lett.* **117**, 080502 (2016).
- [132] Sayrin, C. *et al.* Nanophotonic Optical Isolator Controlled by the Internal State of Cold Atoms. *Phys. Rev. X* **5**, 041036 (2015).
- [133] Söllner, I. *et al.* Deterministic photon–emitter coupling in chiral photonic circuits. *Nat. Nanotechnol.* **10**, 775–778 (2015).
- [134] Coles, R. J. *et al.* Chirality of nanophotonic waveguide with embedded quantum emitter for unidirectional spin transfer. *Nat. Commun.* **7**, 11183 (2016).
- [135] Hurst, D. L. *et al.* Nonreciprocal Transmission and Reflection of a Chirally Coupled Quantum Dot. *Nano Lett.* **18**, 5475–5481 (2018).
- [136] Tomm, N. *et al.* Tuning the mode splitting of a semiconductor microcavity with uniaxial stress. *Phys. Rev. Appl.* **15**, 054061 (2021).
- [137] Kuhlmann, A. V. *et al.* A dark-field microscope for background-free detection of resonance fluorescence from single semiconductor quantum dots operating in a set-and-forget mode. *Rev. Sci. Instrum.* **84**, 073905 (2013).
- [138] Najer, D. *et al.* Suppression of surface-related loss in a gated semiconductor microcavity. *Phys. Rev. Appl.* **15**, 044004 (2021).
- [139] Wang, D. *et al.* Turning a molecule into a coherent two-level quantum system. *Nat. Phys.* **15**, 483–489 (2019).
- [140] Snijders, H. *et al.* Purification of a single-photon nonlinearity. *Nat Commun.* **7**, 12578 (2016).
- [141] Javadi, A. *et al.* Spin–photon interface and spin-controlled photon switching in a nanobeam waveguide. *Nat. Nanotechnol.* **13**, 398–403 (2018).
- [142] O’Shea, D., Junge, C., Volz, J. & Rauschenbeutel, A. Fiber-Optical Switch Controlled by a Single Atom. *Phys. Rev. Lett.* **111**, 193601 (2013).
- [143] Hafezi, M., Lukin, M. D. & Taylor, J. M. Non-equilibrium fractional quantum Hall state of light. *New J. Phys.* **15**, 063001 (2013).
- [144] Gullans, M. *et al.* Efimov States of Strongly Interacting Photons. *Phys. Rev. Lett.* **119**, 233601 (2017).
- [145] Maghrebi, M. F. *et al.* Coulomb bound states of strongly interacting photons. *Phys. Rev. Lett.* **115**, 123601 (2015).
- [146] Frey, J. A. *et al.* Electro-optic polarization tuning of microcavities with a single quantum dot. *Opt. Lett.* **43**, 4280–4283 (2018).
- [147] Boyd, R. W. *Nonlinear Optics* (Academic Press, 2020), 4th edn.
- [148] Rolston, S. & Phillips, W. Nonlinear and quantum optics. *Nature* **416**, 219–224 (2002).
- [149] Rupasov, V. I. Complete integrability of the quasi-one-dimensional quantum model of Dicke superradiance. *JETP Letters* **36**, 115–118 (1982).

- [150] Rupasov, V. I. & Yudson, V. I. Exact Dicke superradiance theory: Bethe wavefunctions in the discrete atom model. *Zh. Eksp. Teor. Fiz* **86**, 825 (1984).
- [151] Firstenberg, O. *et al.* Attractive photons in a quantum nonlinear medium. *Nature* **502**, 71–75 (2013).
- [152] Le Jeannic, H. *et al.* Experimental reconstruction of the few-photon nonlinear scattering matrix from a single quantum dot in a nanophotonic waveguide. *Phys. Rev. Lett.* **126**, 023603 (2021).
- [153] Shi, T., Fan, S. & Sun, C. P. Two-photon transport in a waveguide coupled to a cavity in a two-level system. *Phys. Rev. A* **84**, 063803 (2011).
- [154] Rephaeli, E. & Fan, S. Few-photon single-atom cavity QED with input-output formalism in fock space. *IEEE J. Quantum Electron.* **18**, 1754–1762 (2012).
- [155] Saleh, B. E. A. & Teich, M. C. *Fundamentals of photonics* (John Wiley & Sons, 2019).
- [156] Rephaeli, E. & Fan, S. Stimulated emission from a single excited atom in a waveguide. *Phys. Rev. Lett.* **108**, 143602 (2012).
- [157] Wigner, E. P. Lower limit for the energy derivative of the scattering phase shift. *Phys. Rev.* **98**, 145–147 (1955).
- [158] Bourgain, R., Pellegrino, J., Jennewein, S., Sortais, Y. R. P. & Browaeys, A. Direct measurement of the Wigner time delay for the scattering of light by a single atom. *Opt. Lett.* **38**, 1963–1965 (2013).
- [159] Leong, V., Seidler, M. A., Steiner, M., Cerè, A. & Kurtsiefer, C. Time-resolved scattering of a single photon by a single atom. *Nat. Commun.* **7**, 13716 (2016).
- [160] Strauß, M. *et al.* Wigner time delay induced by a single quantum dot. *Phys. Rev. Lett.* **122**, 107401 (2019).
- [161] Chen, Z., Zhou, Y. & Shen, J.-T. Correlation signatures for a coherent three-photon scattering in waveguide quantum electrodynamics. *Opt. Lett.* **45**, 2559–2562 (2020).
- [162] Lamas-Linares, A., Simon, C., Howell, J. C. & Bouwmeester, D. Experimental quantum cloning of single photons. *Science* **296**, 712–714 (2002).
- [163] Giovannetti, V., Lloyd, S. & Maccone, L. Advances in quantum metrology. *Nat. Photon.* **5**, 222–229 (2011).
- [164] Muthukrishnan, A., Scully, M. O. & Zubairy, M. S. Quantum microscopy using photon correlations. *J. Opt., B Quantum Semiclass. Opt.* **6**, S575–S582 (2004).
- [165] Boto, A. N. *et al.* Quantum interferometric optical lithography: Exploiting entanglement to beat the diffraction limit. *Phys. Rev. Lett.* **85**, 2733–2736 (2000).
- [166] Elzerman, J. M. *et al.* Single-shot read-out of an individual electron spin in a quantum dot. *Nature* **430**, 431–435 (2004).
- [167] Neumann, P. *et al.* Single-shot readout of a single nuclear spin. *Science* **329**, 542–544 (2010).
- [168] Fowler, A. G., Mariantoni, M., Martinis, J. M. & Cleland, A. N. Surface codes: Towards practical large-scale quantum computation. *Phys. Rev. A* **86**, 032324 (2012).
- [169] Ristè, D., Bultink, C. C., Lehnert, K. W. & DiCarlo, L. Feedback control of a solid-state qubit using high-fidelity projective measurement. *Phys. Rev. Lett.* **109**, 240502 (2012).
- [170] Campagne-Ibarcq, P. *et al.* Persistent control of a superconducting qubit by stroboscopic measurement feedback. *Phys. Rev. X* **3**, 021008 (2013).
- [171] Watson, T. F. *et al.* A programmable two-qubit quantum processor in silicon. *Nature* **555**, 633–637 (2018).
- [172] Hendrickx, N. W. *et al.* A four-qubit germanium quantum processor. *Nature* **591**, 580–585 (2021).
- [173] Philips, S. G. J. *et al.* Universal control of a six-qubit quantum processor in silicon. *Nature* **609**, 919–924 (2022).
- [174] Wang, H. *et al.* Boson sampling with 20 input photons and a 60-mode interferometer in a 10^{14} -dimensional hilbert space. *Phys. Rev. Lett.* **123**, 250503 (2019).
- [175] Atatüre, M. *et al.* Quantum-Dot Spin-State Preparation with Near-Unity Fidelity. *Science* **312**, 551–553 (2006).

- [176] Xu, X. *et al.* Fast spin state initialization in a singly charged InAs-GaAs quantum dot by optical cooling. *Phys. Rev. Lett.* **99**, 097401 (2007).
- [177] Bodey, J. H. *et al.* Optical spin locking of a solid-state qubit. *npj Quantum Inf.* **5**, 95 (2019).
- [178] Lindner, N. H. & Rudolph, T. Proposal for pulsed On-demand sources of photonic cluster state strings. *Phys. Rev. Lett.* **103**, 113602 (2009).
- [179] Tiurev, K. *et al.* High-fidelity multiphoton-entangled cluster state with solid-state quantum emitters in photonic nanostructures. *Phys. Rev. A* **105**, L030601 (2022).
- [180] Schwartz, I. *et al.* Deterministic generation of a cluster state of entangled photons. *Science* **354**, 434–437 (2016).
- [181] Cogan, D., Su, Z.-E., Kenneth, O. & Gershoni, D. Deterministic generation of indistinguishable photons in a cluster state. *Nat. Photon.* **17**, 324–329 (2023).
- [182] Coste, N. *et al.* High-rate entanglement between a semiconductor spin and indistinguishable photons. *Nat. Photon.* 1–6 (2023).
- [183] Borregaard, J. *et al.* One-way quantum repeater based on near-deterministic photon-emitter interfaces. *Phys. Rev. X* **10**, 021071 (2020).
- [184] Walther, P. *et al.* Experimental one-way quantum computing. *Nature* **434**, 169–176 (2005).
- [185] Weiss, K. M., Elzerman, J. M., Delley, Y. L., Miguel-Sanchez, J. & Imamoglu, A. Coherent two-electron spin qubits in an optically active pair of coupled InGaAs quantum dots. *Phys. Rev. Lett.* **109**, 107401 (2012).
- [186] Prechtel, J. H. *et al.* Decoupling a hole spin qubit from the nuclear spins. *Nat. Mater.* **15**, 981–986 (2016).
- [187] Lu, C.-Y. *et al.* Direct measurement of spin dynamics in InAs/GaAs quantum dots using time-resolved resonance fluorescence. *Phys. Rev. B* **81**, 035332 (2010).
- [188] Lochner, P. *et al.* Real-time detection of single auger recombination events in a self-assembled quantum dot. *Nano Lett.* **20**, 1631–1636 (2020).
- [189] Mannel, H. *et al.* Auger and spin dynamics in a self-assembled quantum dot. arXiv:2110.12213(2022).
- [190] Vamivakas, A. N. *et al.* Observation of spin-dependent quantum jumps via quantum dot resonance fluorescence. *Nature* **467**, 297–300 (2010).
- [191] Delteil, A., Gao, W.-b., Fallahi, P., Miguel-Sanchez, J. & Imamoglu, A. Observation of quantum jumps of a single quantum dot spin using submicrosecond single-shot optical readout. *Phys. Rev. Lett.* **112**, 116802 (2014).
- [192] Gillard, G., Clarke, E. & Chekhovich, E. A. Harnessing many-body spin environment for long coherence storage and high-fidelity single-shot qubit readout. *Nat. Commun.* **13**, 4048 (2022).
- [193] Evans, R. E. *et al.* Photon-mediated interactions between quantum emitters in a diamond nanocavity. *Science* **362**, 662–665 (2018).
- [194] Raha, M. *et al.* Optical quantum nondemolition measurement of a single rare earth ion qubit. *Nat. Commun.* **11**, 1605 (2020).
- [195] Kindem, J. M. *et al.* Control and single-shot readout of an ion embedded in a nanophotonic cavity. *Nature* **580**, 201–204 (2020).
- [196] Riedel, D. *et al.* Deterministic enhancement of coherent photon generation from a nitrogen-vacancy center in ultrapure diamond. *Phys. Rev. X* **7**, 031040 (2017).
- [197] Bergquist, J. C., Hulet, R. G., Itano, W. M. & Wineland, D. J. Observation of Quantum Jumps in a Single Atom. *Phys. Rev. Lett.* **57**, 1699–1702 (1986).
- [198] Verberk, R., van Oijen, A. M. & Orrit, M. Simple model for the power-law blinking of single semiconductor nanocrystals. *Phys. Rev. B* **66**, 233202 (2002).
- [199] Yilmaz, S. T., Fallahi, P. & Imamoglu, A. Quantum-dot-spin single-photon interface. *Phys. Rev. Lett.* **105**, 033601 (2010).
- [200] Dreiser, J. *et al.* Optical investigations of quantum dot spin dynamics as a function of external electric and magnetic fields. *Phys. Rev. B* **77**, 075317 (2008).

- [201] Gaebel, T. *et al.* Stable single-photon source in the near infrared. *New J. Phys.* **6**, 98–98 (2004).
- [202] Zhai, L. *et al.* Quantum interference of identical photons from remote GaAs quantum dots. *Nat. Nanotechnol.* **17** (2022).
- [203] Muller, A. *et al.* Resonance fluorescence from a coherently driven semiconductor quantum dot in a cavity. *Phys. Rev. Lett.* **99**, 187402 (2007).
- [204] Thomas, P., Ruscio, L., Morin, O. & Rempe, G. Efficient generation of entangled multiphoton graph states from a single atom. *Nature* **608**, 677–681 (2022).
- [205] DiVincenzo, D. P. The physical implementation of quantum computation. *Fortschr. Phys.* **48**, 771–783 (2000).
- [206] Raussendorf, R., Browne, D. E. & Briegel, H. J. Measurement-based quantum computation on cluster states. *Phys. Rev. A* **68**, 022312 (2003).
- [207] Briegel, H. J., Browne, D. E., Dür, W., Raussendorf, R. & Van den Nest, M. Measurement-based quantum computation. *Nat. Phys.* **5**, 19–26 (2009).
- [208] Azuma, K., Tamaki, K. & Lo, H.-K. All-photonic quantum repeaters. *Nat. Commun.* **6**, 6787 (2015).
- [209] Buterakos, D., Barnes, E. & Economou, S. E. Deterministic generation of all-photonic quantum repeaters from solid-state emitters. *Phys. Rev. X* **7**, 041023 (2017).
- [210] Togan, E. *et al.* Quantum entanglement between an optical photon and a solid-state spin qubit. *Nature* **466**, 730–734 (2010).
- [211] Bernien, H. *et al.* Heralded entanglement between solid-state qubits separated by three metres. *Nature* **497**, 86–90 (2013).
- [212] Gao, W. B., Fallahi, P., Togan, E., Miguel-Sanchez, J. & Imamoglu, A. Observation of entanglement between a quantum dot spin and a single photon. *Nature* **491**, 426–430 (2012).
- [213] Appel, M. H. *et al.* Entangling a hole spin with a time-bin photon: A waveguide approach for quantum dot sources of multiphoton entanglement. *Phys. Rev. Lett.* **128**, 233602 (2022).
- [214] De Greve, K. *et al.* Ultrafast coherent control and suppressed nuclear feedback of a single quantum dot hole qubit. *Nat. Phys.* **7**, 872–878 (2011).
- [215] Huthmacher, L. *et al.* Coherence of a dynamically decoupled quantum-dot hole spin. *Phys. Rev. B* **97**, 241413 (2018).
- [216] Éthier-Majcher, G. *et al.* Improving a solid-state qubit through an engineered mesoscopic environment. *Phys. Rev. Lett.* **119**, 130503 (2017).
- [217] Nguyen, G. N. *et al.* Enhanced electron spin coherence in a GaAs quantum emitter (2023). arXiv:2307.02323.
- [218] Jackson, D. M. *et al.* Quantum sensing of a coherent single spin excitation in a nuclear ensemble. *Nat. Phys.* **17**, 585–590 (2021).
- [219] Coish, W. A., Fischer, J. & Loss, D. Exponential decay in a spin bath. *Phys. Rev. B* **77**, 125329 (2008).
- [220] Harris, R. K., Becker, E. D., Menezes, S. M. C. d., Goodfellow, R. & Granger, P. NMR nomenclature. Nuclear spin properties and conventions for chemical shifts (IUPAC Recommendations 2001). *Pure Appl. Chem.* **73**, 1795–1818 (2001).
- [221] Fischer, J., Coish, W. A., Bulaev, D. V. & Loss, D. Spin decoherence of a heavy hole coupled to nuclear spins in a quantum dot. *Phys. Rev. B* **78**, 155329 (2008).
- [222] Machnikowski, P., Gawarecki, K. & Cywiński, L. Hyperfine interaction for holes in quantum dots: k - p model. *Phys. Rev. B* **100**, 085305 (2019).
- [223] Appel, M. H. *et al.* Coherent Spin-Photon Interface with Waveguide Induced Cycling Transitions. *Phys. Rev. Lett.* **126**, 013602 (2021).
- [224] Zhai, L. *et al.* Low-noise GaAs quantum dots for quantum photonics. *Nat. Commun.* **11**, 4745 (2020).
- [225] Nawrath, C. *et al.* High emission rate from a purcell-enhanced, triggered source of pure single photons in the telecom c-band. arXiv:2207.12898(2022).
- [226] Flågan, S. *et al.* A diamond-confined open microcavity featuring a high quality-factor and a small mode-volume. *J. Appl. Phys.* **131**, 113102 (2022).

- [227] Feuchtmayr, F. *et al.* Enhanced spectral density of a single germanium vacancy center in a nanodiamond by cavity integration. *APL* **123**, 024001 (2023).
- [228] Ribeiro, H. & Clerk, A. A. Accelerated adiabatic quantum gates: Optimizing speed versus robustness. *Phys. Rev. A* **100**, 032323 (2019).
- [229] Béguin, L. *et al.* On-demand semiconductor source of 780-nm single photons with controlled temporal wave packets. *Phys. Rev. B* **97**, 205304 (2018).
- [230] Antoniadis, N. O. *et al.* Cavity-enhanced single-shot readout of a quantum dot spin within 3 nanoseconds. *Nat. Commun.* **14**, 3977 (2023).
- [231] Wasilewski, Z., Fafard, S. & McCaffrey, J. Size and shape engineering of vertically stacked self-assembled quantum dots. *J. Cryst. Growth* **201-202**, 1131–1135 (1999).
- [232] Casey, H. C., Sell, D. D. & Wecht, K. W. Concentration dependence of the absorption coefficient for n- and p-type GaAs between 1.3 and 1.6 eV. *J. Appl. Phys.* **46**, 250–257 (1975).
- [233] Guha, B. *et al.* Surface-enhanced gallium arsenide photonic resonator with quality factor of 6×10^6 . *Optica* **4**, 218–221 (2017).
- [234] Hunger, D., Deutsch, C., Barbour, R. J., Warburton, R. J. & Reichel, J. Laser micro-fabrication of concave, low-roughness features in silica. *AIP Adv.* **2**, 012119 (2012).
- [235] Greuter, L. *et al.* A small mode volume tunable microcavity: Development and characterization. *Appl. Phys. Lett.* **105**, 121105 (2014).
- [236] Lalanne, P., Hugonin, J.-P. & Gérard, J.-P. Electromagnetic study of the quality factor of pillar microcavities in the small diameter limit. *Appl. Phys. Lett.* **84**, 4726–4728 (2004).
- [237] Gregersen, N. *et al.* Numerical and experimental study of the Q factor of high- Q micropillar cavities. *IEEE J. Quantum Electron.* **46**, 1470–1483 (2010).
- [238] Nagourney, W. *Quantum Electronics for Atomic Physics* (Oxford University Press, 2010).
- [239] Barbour, R. J. *et al.* A tunable microcavity. *J. Appl. Phys.* **110**, 053107 (2011).
- [240] Greuter, L., Starosielec, S., Kuhlmann, A. V. & Warburton, R. J. Towards high-cooperativity strong coupling of a quantum dot in a tunable microcavity. *Phys. Rev. B* **92**, 045302 (2015).
- [241] Benelajla, M., Kammann, E., Urbaszek, B. & Karrai, K. Physical Origins of Extreme Cross-Polarization Extinction in Confocal Microscopy. *Phys. Rev. X* **11**, 021007 (2021).

Acknowledgements

First of all, I want to thank Richard Warburton for the great opportunity to perform the PhD in the *Nano-photonics* group. It has been a pleasure working under his supervision. Conversations with Richard always taught me something new and I felt supported from him in every aspect of the project as well as on personal topics. I also want to thank the rest of my PhD committee. Thank you, Philipp Treutlein, for all your interesting questions and inputs in our annual meetings, they always gave me a lot to think about. A big thank you also to Alexander Kubanek for agreeing to be the external referee of this thesis and travelling to Basel for my defence. I really enjoyed our conversations in Benasque and am happy to have him in my committee.

Next, I want to thank Alisa Javadi. He has been something like my second mentor during my PhD and took me under his supervision from day one. The way he pushed me, I had the change of learning all tasks of a project within the first year of my PhD: experiments, theory and writing of a paper. Conversations with him always lead to new understanding and he never seemed annoyed by my overload of questions. Without Alisa, many of the exciting results presented in this thesis would not have been possible.

Big thanks also go to the second post-doc I had the pleasure of working with, Mark Hogg. Marks extensive knowledge of spin physics and electronics and his drive in the lab benefited the cavity team immensely. It was also great to have a native speaker in the team – I think my English skills have profited a lot from it! Mark and I managed to be a great team in many shared projects with a great outcome. I wish him all the best with the future of this project. I am sure he will make cluster-states work with our system!

Biggest part of my time in the *Nano-photonics* group, I had a pleasure to work with Natasha Tomm in the cavity team. Thank you, Natasha, for all the good times we have spent, the hours aligning setups, writing papers and running between the labs as well as Rhine swimming, skiing, (hosing and) BBQing on the terrace and so much more. With you, work always felt more fun and we have been a really amazing team! Our trip to Australia was an adventure that I will never forget. I am very happy that our paths will cross again soon when you come back to Switzerland and look forward to future cocktail evenings and other happenings.

I further want to thank Malwina Marczak and Timon Baltisberger for the great teamwork in the cavity-team, all the nice and fun conversations and their enthusiasm about the project. I learned so much when teaching them our system. They are both very bright students and I am sure they will continue rocking this project in the future. I wish them all the best for their PhDs!

Willy Stehl and Sebastián (Sebu) Leni have been my Master's student and the first people I had to supervise in the lab. Thank you both for all the fun times in and outside the lab

and I wish you all the best for your future.

Even though we didn't have an overlap in my time as a PhD student, I want to thank Daniel Najer for his support on the project during my Master's thesis. His optimism has shaped the way I think about research and it has been great working with him for a few months.

During my time in the *Nano-photonics* group I got to spend time with several amazing people. Thank you, Viktoria Yurgens, Clemens Spinnler, Nam Nguyen and Yannik Fontana for being such amazing office-mates. With you guys, we always had the best discussions about all sorts of things and it always brightened up the working days. In particular, thank you Viktoria for all our Monday morning discussions, uncountable skiing trips, BBQs, Rhine swims, drinks, CrossFit and more. You have not only been a co-worker to me, but a real friend for life. Thanks Clemens for bringing Mathias and me to the Genossenschaft and being a great neighbour, fondue host and gossiping partner. Thanks Nam for introducing me to the real Asian cuisine on all our conference-trips. Thanks, Yannik for bringing me back to skiing and teaching me all the deep-snow skills (not that I have many at this point). Apart from the office- and lab-buddies I want to thank a few more of the people of the *Corona*-generation that made live during the lock-down bearable and since then have turned into good friends. Thank you, Lukas Sponfeldner, for being the social glue of our group. Beers, Skiing, CrossFit and so much more has always been a pleasure with you and you always spread a good mood! Thanks Simon Geyer, mainly for the similar things as Lukas. I am very happy to have you left over in the group with me and have had you here as mental support in the last parts of the PhD. Thank you to Sigurd Flågan for the many beer-evenings and late-night chats about life.

Thanks also to Nadine Leisgang for introducing me to the *Nano-photonics* group. Even though she originally convinced me to join the 2D project and I left her for the bright side of the group, her recommendation was of big value. Further I want to thank all the people that prove-read this thesis: Mark, Malwina, Timon, Simon, Clemens and Mathias. I also want to thank the rest of the *Nano-photonics* group – current and former generations – that have not been named yet for an always encouraging and fun environment.

Most of the work in this thesis would not have been possible without theoretical support. In that regard I want to thank our in-house theoreticians Patrick Potts and his group members Marcelo Janovitch and Matteo Brunelli as well as Sahand Mahmoodian from Sydney University for their amazing input. In particular all the conversations with Marcelo have been an interesting experience and a clash of the two worlds of physics has taught both of us a lot. Thank you also to Arne Ludwig and his team in Bochum for all the great conversations about the QD fabrication and the origin of our hole and of course for the fabrication of our magic samples that enabled all these exciting experiments! Also, thanks to the mechanical and electrical workshops as well as the administrative staff for keeping the department running. Nothing would work without all of you!

The time of a PhD can be challenging and it has been important to me, to have a place to go to and forget about work for a few hours. In that regard, thanks to all people of both the Dreirosen CrossFit group as well as the University Choir Basel for contributing in keeping me sane. In particular, thank you Meret Zimmermann for dragging me into CrossFit – these evenings have been keeping me going for the last years. Also thank you for being my Soprano II buddy and support. Also big thanks to the Vorstand during my time of presidency of the University Choir: Chris Peyer, Larissa Hofer and Alexandra Von Gatterburg, you guys

rock and it was really great working with you. Thanks also to our conductor Olga Pavlu for making this side-job a fun experience!

In the private context, I want to thank my family for their support and encouragement during this time. In particular to my parents, Eleni Panoussis and Antonis Antoniadis: thanks for never stopping to believe in me and for your support in all these years. To my brother Christos – thank you for your humour enlightening each of our conversations, your comments made the experience of a PhD much more realistic and was often much needed. Thanks to my cousin Dimitra Vlahou for giving me the joy of being a godmother to this wonderful boy Thanasaki. It brought so much love into my life!

I am also enormous thankful to all my close friends for believing in me, and being understanding whenever I was too stressed to keep in touch regularly: Corinna Althaus, Vicky Stalder, Nathalie Reichel, Raphaela Keller and Julia Reiman.

Last but certainly not least, a huge thank you to Mathias Claus. You have been the biggest support over all these years: constantly believing in me, cheering me up, listen to all my complains on the daily basis, pushing me to my limits and supporting me; especially in the last few stressful months. I wouldn't have made it without you.

Thank you!

List of publications

- N. Tomm*, A. Javadi*, N. O. Antoniadis, D. Najer, M. C. Löbl, A. R. Korsch, R. Schott, S. R. Valentin, A. D. Wieck, A. Ludwig and R. J. Warburton, *A bright and fast source of coherent single photons*, Nat. Nanotechnol. **16**, 399 (2021)
- N. O. Antoniadis, N. Tomm, T. Jakubczyk, R. Schott, S. R. Valentin, A. D. Wieck, A. Ludwig, R. J. Warburton and A. Javadi *A chiral one-dimensional atom using a quantum dot in an open microcavity*, npj Quantum Inf. **8**, 27 (2022)
- N. Bart, C. Dangel, P. Zajac, N. Spitzer, J. Ritzmann, M. Schmidt, H. G. Babin, R. Schott, S. R. Valentin, S. Scholz, Y. Wang, R. Uppu, D. Najer, M. C. Löbl, N. Tomm, A. Javadi, N. O. Antoniadis, L. Midolo, K. Müller, R. J. Warburton, P. Lodahl, A. D. Wieck, J. J. Finley and A. Ludwig, *Wafer-scale epitaxial modulation of quantum dot density*, Nat. Commun. **13**, 1633 (2022)
- N. Tomm*, S. Mahmoodian*, N. O. Antoniadis, R. Schott, S. R. Valentin, A. D. Wieck, A. Ludwig, A. Javadi and R. J. Warburton, *Direct observation of photon bound-state dynamics using a single artificial atom*, Nat. Phys. **19**, 857-862 (2023)
- N. O. Antoniadis, N. Tomm, A. Javadi, R. Schott, S. R. Valentin, A. D. Wieck, A. Ludwig and R. J. Warburton, *Measurement of the efficiency of a bright quantum-dot-based single-photon source*, Proc. SPIE 12446, Quantum Computing, Communication, and Simulation III, 124460S (2023)
- N. O. Antoniadis*, M. R. Hogg*, W. F. Stehl, A. Javadi, N. Tomm, R. Schott, S. R. Valentin, A. D. Wieck, A. Ludwig and R. J. Warburton *Cavity-enhanced single-shot readout of a quantum dot spin within 3 nanoseconds*, Nat. Commun. **14**, 3977 (2023)
- A. Javadi, N. Tomm, N. O. Antoniadis, A. J. Brash, R. Schott, S. R. Valentin, A. D. Wieck, A. Ludwig and R. J. Warburton *Cavity-enhanced excitation of a quantum dot in the picosecond regime*, New J. Phys. **25**, 093027 (2023)

*Equal contribution

Publications in preparation:

- N. Tamm*, N. O. Antoniadis*, M. Janovitch*, M. Brunelli, R. Schott, S. R. Valentin, A. D. Wieck, A. Ludwig, P. P. Potts, A. Javadi, and R. J. Warburton *A tunable coherent and efficient light-matter interface based on a single quantum emitter in a microcavity* (2023), *in preparation*.
- Mark R. Hogg*, N. O. Antoniadis*, M. Marczak, A. Javadi, R. Schott, S. R. Valentin, A. D. Wieck, A. Ludwig and R. J. Warburton, *Fast optical manipulation of a coherent hole spin in a microcavity* (2023), *in preparation*.
- Mark R. Hogg*, S. Leni*, N. O. Antoniadis*, N. Tamm, A. Javadi, R. Schott, S. R. Valentin, A. D. Wieck, A. Ludwig and R. J. Warburton, *Studying single-photon source emitter dynamics using photon-correlation Fourier spectroscopy* (2023), *in preparation*.

*Equal contribution

Curriculum vitae

Nadia Olympia Antoniadis

Personal information

Email address: n.antoniadis@gmx.ch

Date of birth: 12th March 1995

Place of birth: Basel, Switzerland

Citizenship: Swiss, Greek

Education

- 2020-2023, **Ph.D. in Experimental Physics**
PhD School "Quantum Computing and Quantum Technology"
Universität Basel, Switzerland

Thesis: "*A quantum dot in a microcavity as a coherent spin-photon interface*"

Advisors: Prof. Dr. Richard J. Warburton, Prof. Dr. Philipp Treutlein

- 2018-2020, **M.Sc. in Physics**
Universität Basel, Switzerland

Thesis: "*An efficient source of indistinguishable single photons: a gated InAs quantum dot in a tunable microcavity*"

Advisors: Prof. Dr. Richard J. Warburton, Dr. Alisa Javadi

Project: "*Strain-effects on optical properties of MoSe₂*"

Advisors: Prof. Dr. Richard J. Warburton, Dr. Nadine Leisgang

- 2015-2018, **B.Sc. in Nanoscience**
Universität Basel, Switzerland